

ABSTRACT

WANNA, NADIM GEORGE. Design of Reflective Optical Systems. (Under the direction of Thomas A. Dow).

The primary objective of this research is to develop optical and opto-mechanical design procedures for reflective optical systems. Challenges in fabrication and testing have limited the choice of surfaces used in the design of reflective optical systems to rotationally symmetric surfaces. Freeform surfaces or non-rotationally symmetric surfaces are necessary to meet challenging performance and packaging requirements. To gain familiarity with optical and opto-mechanical design techniques, two systems were considered: a two mirror Ritchey-Chrétien telescope and a Three Mirror Anastigmat.

The two mirror Ritchey-Chrétien optical system using rotationally symmetric hyperbolic surfaces is designed. The opto-mechanical design incorporates the use of radial and axial fiducial surfaces to locate the two mirrors onto a tube relating the optical surfaces to each other and to the detector through a spacer plate.

Optical performance improvement over the two mirror telescope is achieved with the addition of a third mirror. The Three Mirror Anastigmat (TMA) optical design uses off-axis conic sections of a rotationally symmetric system. Further improvement to the optical performance is achieved with a freeform TMA optical system and optical surface fabrication feedback to the designer. Opto-mechanical design of the TMA incorporates the use of a telescope frame to constrain each mirror in six degrees of freedom and relate the optical surfaces to each other and to the detector. The mirrors are held in place

through independent mounting clamps to sustain high gravitational acceleration with minimum optical surface distortion.

The two mirror telescope optical performance is limited by optical aberrations especially at high field angles. Locating the mirrors on a tube over-constrains the components and distorts the optical surfaces. Multiple assembly configurations or non-repeatability is due to symmetry of mounting screws. Impressive optical performance, 58 times wavefront error improvement over the two mirror system, is achieved with an unobstructed TMA optical system using freeform surfaces. A snap-together repeatable assembly without adjustments is designed using conventional fiducial techniques and independent mounting clamps minimizing optical surface distortion.

DESIGN OF REFLECTIVE OPTICAL SYSTEMS

by

NADIM G. WANNA

A thesis submitted to the Graduate Faculty of
North Carolina State University
in partial fulfillment of the
requirements for the Degree of
Master of Science

**MECHANICAL AND AEROSPACE ENGINEERING
NORTH CAROLINA STATE UNIVERSITY**

Raleigh, NC
2006

APPROVED BY:


Dr. Ron Scattergood


Dr. Jeffrey Eischen


Advisory Committee Chair
Dr. Thomas Dow

BIOGRAPHY

Nadim Wanna was born and raised in Beirut, Lebanon. He graduated from Saint Joseph School in 2000 and then entered the American University of Beirut before transferring to the Department of Mechanical and Aerospace Engineering at North Carolina State University in Raleigh, NC. While an undergraduate at North Carolina State University, Nadim participated in research on object transportation theory in the Precision Engineering Center under the direction of Dr. Ro for six months. Nadim also interned at Lebanon Chemicals Company in Beirut, Lebanon during the summer of 2004. After completing his Bachelor of Science in Mechanical Engineering with High Distinction in 2004, Nadim pursued his Masters in the spring of 2004 at North Carolina State University.

ACKNOWLEDGEMENTS

I would like to express my sincere gratitude to the invaluable experience gained with pursuing my Masters. I would like to individually thank:

- Dr. Dow, my advisor for his great knowledge, constant pursue of excellent, and his support and guidance.
- Dr. Eischen and Dr. Scattergood, my committee members, for being part of this research.
- Alex Sohn and Ken Garrard, for all the help, support, and knowledge.
- Lucas Lamonds and Rob Woodside, for making this project a wonderful experience.
- Lara Masters, Roxie Gold, and Donna Irwin, for answering all the questions.
- The rest of the students at the PEC, Brett, Nathan, Kara, Dave, Yanbo, Tim, Quenyi, and Arun.
- Tarek Salloum and Nabil Attallah for all the support throughout the years.
- To my parents, George and Amal Wanna, and my brother Bassam for always being there for me and their endless support. Thank you for everything.

TABLE OF CONTENTS

LIST OF FIGURES	vii
LIST OF TABLES	x
1 INTRODUCTION.....	1
1.1 BACKGROUND.....	1
1.1.1 <i>Two Mirror Optical Designs</i>	2
1.1.2 <i>Three Mirror Optical Designs</i>	2
1.2 PREVIOUS RESEARCH.....	3
1.2.1 <i>Freeform Optics</i>	3
1.2.2 <i>Freeform Fabrication</i>	4
1.2.3 <i>Freeform Metrology</i>	5
1.2.4 <i>Opto-Mechanical Design</i>	6
1.3 PROBLEM STATEMENT	8
2 OPTICAL DESIGN OF TWO MIRROR TELESCOPE.....	9
2.1 INTRODUCTION	9
2.2 CONFIGURATION	10
2.2.1 <i>Size and Shape</i>	10
2.2.2 <i>Detector</i>	12
2.2.3 <i>Optimization</i>	13
2.3 THEORETICAL PERFORMANCE.....	17
2.3.1 <i>Aberrations</i>	18
2.3.1.1 <i>Astigmatism</i>	18
2.3.1.2 <i>Coma</i>	19
2.3.1.3 <i>Spherical Aberration</i>	22
2.3.2 <i>Wavefront Analysis</i>	23
2.3.3 <i>Modulation Transfer Function</i>	26
2.3.4 <i>Spot Diagram</i>	28
2.4 SENSITIVITY ANALYSIS.....	29
3 OPTOMECHANICAL DESIGN OF TWO MIRROR TELESCOPE	32
3.1 INTRODUCTION	32
3.2 MATERIAL	32
3.3 STRUCTURE.....	32
3.3.1 <i>Telescope Support</i>	33
3.3.2 <i>Camera Support</i>	37
3.3.3 <i>Manufacturing Feasibility</i>	38
3.4 TWO MIRROR DESIGN CONCLUSION	39
3.4.1 <i>Dual Pass Measurements</i>	39
3.4.2 <i>Aspect Ratio</i>	42
3.4.3 <i>Primary Mirror Structure</i>	43
3.4.4 <i>Secondary Mirror Structure</i>	47

4	OPTICAL DESIGN OF TMA	49
4.1	INTRODUCTION	49
4.2	CONFIGURATION	50
4.2.1	<i>TMA using Conic Surfaces.....</i>	<i>50</i>
4.2.1.1	Size and Shape of Conic Surfaces	50
4.2.1.2	Detector.....	51
4.2.1.3	Optimization of Conic Surfaces.....	53
4.2.2	<i>TMA using Zernike Surfaces.....</i>	<i>56</i>
4.2.2.1	Size and Shape of Freeform Surfaces	56
4.2.2.2	Optimization of Freeform Surfaces	58
4.3	THEORETICAL PERFORMANCE OF CONIC AND FREEFORM TMA SYSTEMS.....	62
4.3.1	<i>Aberrations</i>	<i>62</i>
4.3.1.1	Astigmatism	63
4.3.1.2	Coma.....	65
4.3.1.3	Spherical Aberration	66
4.3.2	<i>Wavefront Analysis of Conic and Freeform TMA Systems.....</i>	<i>68</i>
4.3.3	<i>Modulation Transfer Function.....</i>	<i>70</i>
4.3.4	<i>Spot Diagram of Conic and Freeform TMA Systems.....</i>	<i>72</i>
4.4	SENSITIVITY ANALYSIS.....	74
4.5	SURFACE DECOMPOSITION.....	79
4.5.1	<i>Off-axis Conic TMA</i>	<i>80</i>
4.5.2	<i>On-axis Zernike Polynomial TMA</i>	<i>84</i>
4.6	COMPARISON OF CONIC AND FREEFORM TMA SYSTEMS	88
5	OPTOMECHANICAL DESIGN OF TMA.....	89
5.1	INTRODUCTION	89
5.2	MATERIAL	90
5.3	MIRROR STRUCTURE.....	90
5.3.1	<i>Lightweight Design for Fabrication</i>	<i>90</i>
5.3.2	<i>Fiducialization Techniques.....</i>	<i>95</i>
5.3.2.1	Conventional.....	95
5.3.2.2	Kinematic Coupling.....	97
5.3.3	<i>Mounting Features.....</i>	<i>102</i>
5.4	TELESCOPE FRAME	110
5.4.1	<i>Structure.....</i>	<i>110</i>
5.4.2	<i>Frame Structural Analysis.....</i>	<i>113</i>
5.4.2.1	Launch Acceleration	113
5.4.2.2	Gravity Loading.....	116
5.4.2.3	Modal Analysis	117
5.5	MANUFACTURING FEASIBILITY.....	118
5.6	ASSEMBLY PROCEDURE.....	119
6	CONCLUSION AND FUTURE WORK	121
6.1	TWO MIRROR TELESCOPE.....	121

6.2	THREE MIRROR TELESCOPE	122
6.3	FUTURE WORK	126
7	REFERENCES.....	127
8	APPENDIX.....	131
	<i>APPENDIX A – Fabrication Date Tables</i>	<i>132</i>
	<i>APPENDIX B – Sensitivity Analysis.....</i>	<i>140</i>
	<i>APPENDIX C – Detail Drawings of the Two Mirror Telescope.....</i>	<i>160</i>
	<i>APPENDIX D – Detail Drawings of the Three Mirror Anastigmat.....</i>	<i>169</i>
	<i>APPENDIX E – Zernike Polynomial Surface</i>	<i>186</i>
	<i>APPENDIX F – Kinematic Coupling Design Table</i>	<i>189</i>

LIST OF FIGURES

FIGURE 1-1: CASSEGRAIN REFLECTOR BASIC LAYOUT	2
FIGURE 1-2: DECOMPOSITION OF A BICONIC MIRROR SURFACE (A) INTO SYMMETRIC (B) AND NON-SYMMETRIC AND (C) COMPONENTS FOR ON-AXIS FABRICATION	5
FIGURE 1-3: EXAMPLE OF A KINEMATIC LOCATING FIXTURE.....	7
FIGURE 2-1: TWO MIRROR OPTICAL SYSTEM	10
FIGURE 2-2: CANON DIGITAL EOS 300D	12
FIGURE 2-3: CODE V OPTIMIZATION OR AUTOMATIC DESIGN DIALOG BOX	14
FIGURE 2-4: PARAXIAL MARGINAL EXIT ANGLE FROM THE SECONDARY MIRROR.....	15
FIGURE 2-5: FIELD CURVES SHOWING FOCUS ERRORS ON THE TANGENTIAL (DOTTED LINE) AND SAGITTAL (SOLID LINE) PLANES	17
FIGURE 2-6: FIELD MAP OF ASTIGMATISM FOR OPTIMIZED TWO MIRROR SYSTEM.....	19
FIGURE 2-7: FIELD MAP OF COMA FOR OPTIMIZED TWO MIRROR SYSTEM	21
FIGURE 2-8: RELATIONSHIP BETWEEN RAY POSITION AND ITS RESPECTIVE POSITION IN THE COMA PATCH.....	21
FIGURE 2-9: SCHEMATIC OF SPHERICAL ABERRATION THAT VARIES WITH APERTURE	22
FIGURE 2-10: FIELD MAP OF SPHERICAL ABERRATION FOR OPTIMIZED TWO MIRROR SYSTEM	23
FIGURE 2-11: RMS WAVEFRONT ERROR MAP ACROSS THE FIELD OF VIEW OF THE TELESCOPE	25
FIGURE 2-12: WAVEFRONT ERROR FOR THE OPTIMIZED SYSTEM AT THREE FIELD POSITIONS	26
FIGURE 2-13: MTF FOR THE OPTIMIZED TWO MIRROR SYSTEM PRESENTED ON-AXIS AND AT TWO LOCATIONS OFF-AXIS (0.35° AND 0.5°).	27
FIGURE 2-14: SPOT DIAGRAM FOR THE OPTIMIZED TWO MIRROR SYSTEM	29
FIGURE 2-15: RMS WAVEFRONT ERROR SENSITIVITY ANALYSIS.....	31
FIGURE 3-1: TWO MIRROR TELESCOPE COMPONENTS	33
FIGURE 3-2: DETAIL DRAWING OF THE TELESCOPE	35
FIGURE 3-3: ASSEMBLY OF OPTICAL COMPONENTS INTO THE TUBE	36
FIGURE 3-4: DISPLACEMENT PLOTS TO DETERMINE AXIAL STIFFNESS	37
FIGURE 3-5: FABRICATION OF TWO-MIRROR TELESCOPE ON A DIAMOND TURNING MACHINE	39
FIGURE 3-6: DUAL PASS SETUP FOR TELESCOPE MEASUREMENT, SHOWING ON-AXIS RAYS	40
FIGURE 3-7: WAVEFRONT ERROR FOR THE DUAL PASS MODEL IN CODE V WITH BEST FOCUS AT 0.35°	41
FIGURE 3-8: DEFLECTION OF A 150 MM DIA. ALUMINUM PLATE VS. ASPECT RATIO (DIAMETER/THICKNESS).....	43
FIGURE 3-9: MEASUREMENT OF THE PRIMARY MIRROR OPTICAL SURFACE WHEN IT IS ASSEMBLED ON THE TUBE	44
FIGURE 3-10: PRIMARY AND TUBE AXIAL FIDUCIAL FORM ERROR RELATIONSHIP	45
FIGURE 3-11: PRIMARY MIRROR OPTICAL SURFACE EDGE DISPLACEMENT	46
FIGURE 3-12: PRIMARY MIRROR DEFORMATION DUE TO THE RADIAL INTERFERENCE FIT ...	47
FIGURE 3-13: SECONDARY MIRROR STRUCTURE DEFLECTION DUE TO MOUNTING ONTO THE TUBE	48

FIGURE 3-14: SCHEMATIC OF THE SECONDARY MIRROR STRUCTURE WITH INTERFERENCE PRESSURE APPLIED COLLINEAR TO THE NEUTRAL AXIS.....	48
FIGURE 4-1: TMA USING CONIC SECTIONS LAYOUT	51
FIGURE 4-2: STARLIGHT XPRESS SXV-M25	52
FIGURE 4-3: TMA USING ROTATIONALLY SYMMETRIC CONIC SURFACES.....	55
FIGURE 4-4: TMA USING ON-AXIS ZERNIKE SURFACES	57
FIGURE 4-5: TMA USING ZERNIKE SURFACES OPTICAL SYSTEM	61
FIGURE 4-6: FIELD MAP OF ASTIGMATISM (Z5 AND Z6) FOR ZERNIKE POLYNOMIAL TMA	63
FIGURE 4-7: ASTIGMATISM ACROSS THE FIELD OF VIEW PLOTTED ON THE SAME SCALE.....	64
FIGURE 4-8: FIELD MAP OF COMA (Z7 AND Z8) FOR THE ON-AXIS ZERNIKE POLYNOMIAL TMA.....	65
FIGURE 4-9: COMA ACROSS THE FIELD OF VIEW PLOTTED ON THE SAME SCALE	66
FIGURE 4-10: FIELD MAP OF SPHERICAL ABERRATION (Z9) FOR ON-AXIS ZERNIKE POLYNOMIAL SYSTEM	67
FIGURE 4-11: SPHERICAL ABERRATION ACROSS THE FIELD OF VIEW PLOTTED ON THE SAME SCALE	68
FIGURE 4-12: RMS WAVEFRONT ERROR FOR ZERNIKE TMA ACROSS THE FIELD OF VIEW.	69
FIGURE 4-13: RMS WAVEFRONT ERROR AS FIELD ANGLE OVER THE APERTURE OF THE TELESCOPE.....	70
FIGURE 4-14: MTF FOR BOTH TMA OPTICAL SYSTEMS	72
FIGURE 4-15: RMS SPOT DIAGRAM ACROSS THE FIELD OF VIEW FOR THE ZERNIKE POLYNOMIAL SYSTEM	73
FIGURE 4-16: RMS SPOT DIAGRAM FOR BOTH TMA SYSTEMS PLOTTED USING THE SAME SCALE	74
FIGURE 4-17: RMS WAVEFRONT ERROR SENSITIVITY ANALYSIS FOR THE OFF-AXIS CONIC TMA.....	77
FIGURE 4-18: RMS WAVEFRONT ERROR SENSITIVITY ANALYSIS FOR THE ON-AXIS ZERNIKE POLYNOMIAL TMA	79
FIGURE 4-19: NRS COMPONENT (P-V = 186 MM) OF OFF-AXIS CONIC TMA PRIMARY MIRROR	83
FIGURE 4-20: NRS COMPONENT (P-V = 191 MM) OF OFF-AXIS CONIC TMA SECONDARY MIRROR	83
FIGURE 4-21: NRS COMPONENT (P-V = 21 MM) OF OFF-AXIS CONIC TMA TERTIARY MIRROR	84
FIGURE 4-22: NRS COMPONENT (P-V = 84 MM) OF ZERNIKE TMA PRIMARY MIRROR.....	86
FIGURE 4-23: NRS COMPONENT (P-V = 110 MM) OF ZERNIKE TMA SECONDARY MIRROR	87
FIGURE 4-24: NRS COMPONENT (P-V = 41 MM) OF ZERNIKE TMA TERTIARY MIRROR.....	87
FIGURE 5-1: SCHEMATIC OF A MIRROR SUBSTRATE WITH A REDUCED MOUNTING AREA	92
FIGURE 5-2: DISTORTION OF THE OPTICAL SURFACE WHEN THE ENTIRE BACK IS USED (LEFT) AND WHEN ONLY A REGION IS USED (RIGHT) TO MOUNT ONTO THE VACUUM CHUCK .	92
FIGURE 5-3: LIGHTWEIGHT PRIMARY MIRROR.....	93
FIGURE 5-4: CUTTING FORCES SIMULATION AND EFFECT ON THE OPTICAL SURFACE	94
FIGURE 5-5: MIRROR SUBSTRATE VACUUM MOUNTING SIMULATION	95
FIGURE 5-6: MIRROR BLANK WITH PINS INSTALLED IN THE FIDUCIAL PLANE THAT FIT INTO A PIN HOLE AND SLOT ON THE TELESCOPE FRAME	97

FIGURE 5-7: KELVIN COUPLING (LEFT) AND KINEMATIC COUPLING (RIGHT) CONSTRAIN A RIGID BODY IN SIX DEGREES OF FREEDOM	98
FIGURE 5-8: DEFINITION OF THE CONTACT RADII ON THE HOUSING (H) AND THE BALL FEATURES (B).....	100
FIGURE 5-9: SKETCH OF THE MIRROR SURFACE SHOWING THE BALL FEATURES MACHINED ON THE OUTSIDE FIDUCIAL RING.....	100
FIGURE 5-10: DETAILS OF THE THREE BALL FEATURES ON THE MIRROR FIDUCIAL SURFACE	101
FIGURE 5-11: MIRROR WITH FIDUCIAL AND MOUNTING TABS	103
FIGURE 5-12: DISTORTION OF THE OPTICAL SURFACE WITH INTEGRATED FLEXURE MOUNTING TABS	104
FIGURE 5-13: DOUBLE-JOINTED CLAMP DESIGN.....	106
FIGURE 5-14: DEFLECTION OF THE MOUNTING TAB (LEFT) AND THE STRESS DISTRIBUTION (RIGHT)	107
FIGURE 5-15: DEFLECTION (LEFT) AND STRESS DISTRIBUTION (RIGHT) FOR THE SECONDARY AND TERTIARY MIRRORS MOUNTING CLAMP	108
FIGURE 5-16: SCHEMATIC OF LOCATING AND MOUNTING MIRROR ON THE TELESCOPE HOUSING	109
FIGURE 5-17: DISPLACEMENT OF THE LIGHTWEIGHT PRIMARY MIRROR DUE TO CLAMPING FORCES.....	109
FIGURE 5-18: TELESCOPE FRAME WITHOUT THE SIDE PLATES ATTACHED	111
FIGURE 5-19: SECTION OF THE HOUSING WITH HOLE-SLOT-FLAT TO LOCATE MIRROR AND CLAMP LOADING HOLES	112
FIGURE 5-20: ASSEMBLING TWO SIDE PLATES ON THE TELESCOPE FRAME	112
FIGURE 5-21: TELESCOPE FRAME WITH DIMENSIONS (IN MM) AND LOADING-RESTRAINT CONDITIONS	114
FIGURE 5-22: FRAME DISPLACEMENT WITH 15 MM THICK MIRROR MOUNTING SURFACES	115
FIGURE 5-23: FRAME DISPLACEMENT WITH THE FINAL MOUNTING SURFACE WALL THICKNESSES	116
FIGURE 5-24: FRAME DISPLACEMENT DUE TO WEIGHT OF COMPONENTS IN DIFFERENT DIRECTIONS.....	117
FIGURE 5-25: FIRST MODE SHAPE OF THE TELESCOPE FRAME STRUCTURE	118
FIGURE 5-26: FINAL TELESCOPE ASSEMBLY AND TELESCOPE FRAME DIMENSIONS (IN MM)	120

LIST OF TABLES

TABLE 2-1: TWO MIRROR OPTIMIZATION ROUTINE CONSTRAINTS	15
TABLE 2-2: TWO MIRROR OPTICAL SYSTEM SPECIFICATIONS	16
TABLE 2-3: CHANGE IN RMS WAVEFRONT ERROR WITH MANUFACTURING TOLERANCES (λ = 632.8 nm)	30
TABLE 4-1: OFF-AXIS CONIC OPTIMIZATION ROUTINE CONSTRAINTS	54
TABLE 4-2: OFF-AXIS CONIC OPTICAL SYSTEM SPECIFICATIONS.....	55
TABLE 4-3: ZERNIKE SURFACE OPTIMIZATION ROUTINE CONSTRAINTS	60
TABLE 4-4: TMA USING ZERNIKE SURFACES OPTICAL SYSTEM SPECIFICATIONS	61
TABLE 4-5: CHANGE IN RMS WAVEFRONT ERROR WITH MANUFACTURING TOLERANCES (λ = 632.8nm), FOR OFF-AXIS CONIC TMA	76
TABLE 4-6: RMS WAVEFRONT ERROR CHANGE (λ = 632.8 nm), FOR ON-AXIS ZERNIKE POLYNOMIAL TMA.....	78
TABLE 4-7: OFF-AXIS CONIC TMA DECOMPOSITION.....	82
TABLE 4-8: ZERNIKE POLYNOMIAL TMA DECOMPOSITION (COEFFICIENTS DEFINED IN APPENDIX E).....	85
TABLE 5-1: BALL AND GROOVE FEATURES ON THE FIDUCIAL SURFACES SHOWN IN FIGURE 5-8	102
TABLE 5-2: MIRROR MOUNTING TAB AND OPTICAL SURFACE DISPLACEMENT RESULTS (MM)	116
TABLE 5-3: FIRST MODE FREQUENCIES FOR THE COMPONENTS AND FRAME STRUCTURE..	117
TABLE 8-1: STANDARD ZERNIKE POLYNOMIALS.....	187
TABLE 8-2: CONSTANTS (M AND N) FOR DIFFERENT θ VALUES.....	189

1 INTRODUCTION

1.1 BACKGROUND

Optical systems play a crucial role in a wide variety of products from camera phones to seeker missile guidance systems to free-space optical interconnects on computer chips. The field is divided into two major categories: Geometrical Optics is the study of light without diffraction or interference and Physical Optics expands the scope to include diffraction effects. Whereas some optical systems use reflective, refractive and diffractive elements, the emphasis in this project will be on reflective systems that perform at multiple wavelengths.

Optical systems have been around since early 17th century. Galileo is credited for building the first telescope in 1609 for astronomical purposes using convex object lens and concave eye lens. The early history era, from 1608 up to 1672, is particularly instructive where the basic theory of reflecting telescopes and all its basic forms is explored. Optical theory of compound telescope consisting of two curved mirrors is developed through the work of Descartes, Mersenne, Gregory, Newton and Cassegrain. Through the period between 1672 and 1840, intensive development of the refractor is accomplished and complemented by major improvements in manufacturing capabilities [15]. A refracting telescope is another type of optical telescope that refracts or bends light at each end utilizing lenses. Due to aperture size limits, reflective telescopes gained familiarity over refractive telescopes.

1.1.1 Two Mirror Optical Designs

Rotationally symmetric and unobstructed reflective multi-mirror optical systems have been published in technical literature patents. In reviewing these systems, three or four mirror unobstructed telescopes are often derived from previous rotationally symmetric obstructed designs [16]. The most basic configuration providing a compact form is the Cassegrain or its variations, Ritchey-Chrétien for example. Cassegrain two-mirror telescopes consist of two rotationally symmetric conic surfaces with the image plane easily accessible behind the primary mirror, shown in Figure 1-1 [2]. Cassegrain's typical operating conditions are limited by third order aberrations, usually astigmatism that increases with field angle.

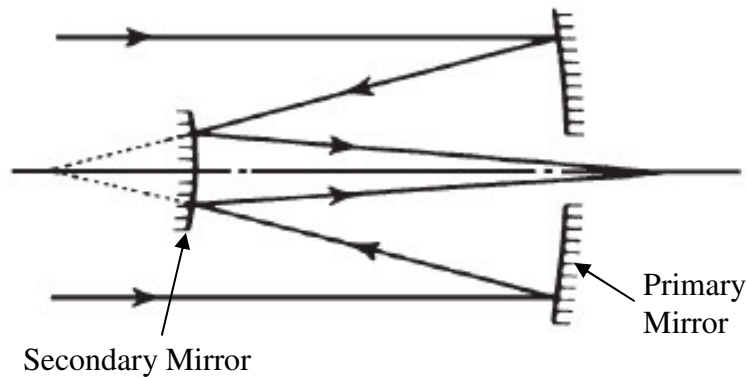


Figure 1-1: Cassegrain reflector basic layout

1.1.2 Three Mirror Optical Designs

Improvement to the Cassegrain designs or two mirror rotationally symmetric designs, which significantly improves the performance, are the three mirror anastigmat (TMA) optical system with a Cassegrain-type fore-optics plus a concave relay. With three conic

or aspheric optical surfaces, all performance degrading third order aberrations can be corrected and higher order aberrations can be controlled. Three mirror anastigmat variations are among the widely used unobstructed telescope systems. Offner's patents describe a TMA used as an afocal beam reducer to illuminate the entire detector for measurements of parameters such as quantum efficiency and pixel-to-pixel non-uniformity [24]. Cook's patents illustrate multiple variations of unobstructed three mirror designs using on-axis or off-axis segments of rotationally symmetric surfaces for different applications [25]. The degree of optical aberration correction attainable with three mirrors versus two mirrors is remarkable. Korsch presents the majority of three mirror anastigmat configurations using on-axis and off-axis segments of rotationally symmetric aspheres [26]. Rodgers reviews multiple-mirror unobscured designs in his paper "Unobscured Mirror Designs" ranging from two to many mirrors with different operating conditions and limitations [16].

1.2 PREVIOUS RESEARCH

1.2.1 Freeform Optics

The first widely used freeform optics formed part of the viewing optics of the Polaroid SX-70 camera in the early 1970s [30]. The freeform surface corrected for aberration errors across the field of view. Astigmatic contact lenses or freeform lenses are used for different power correction along different directions [31]. The first reflective optical system using a freeform surface is designed for an InfraRed Multi-Object Spectrometer (IRMOS). Optical astronomy has long been based on optical designs with rotationally

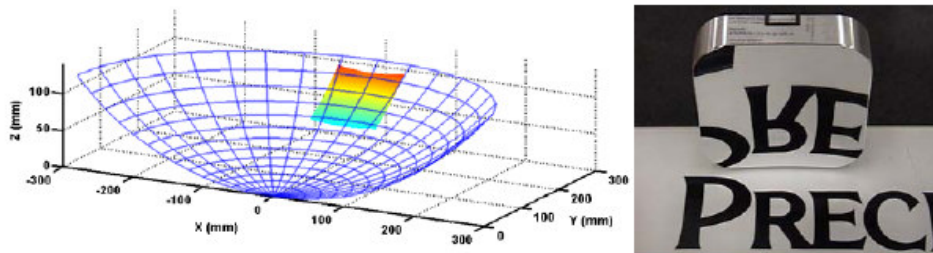
symmetric surfaces. The biconic freeform surface allows for a substantial reduction in the overall size and weight of the instrument while meeting the system requirements [32].

Typical aerial defense optical systems use reflective optical components to image light onto a detector. Three Mirror Anastigmat (TMA) has an advantage over rotationally symmetric two mirror systems, since the third mirror corrects for aberrations at the image plane. Rotationally symmetric conic surfaces are common, but more degrees of freedom are necessary to meet challenging performance and packaging requirements. Current TMA optical systems use a combination of on-axis and off-axis rotationally symmetric aspheric segments as documented by Rodgers [16]. To avoid astigmatism at a single off-axis field angle, a locally anamorphic surface is needed, with a longer radius in the field angle direction than in the orthogonal direction. Non-rotationally symmetric surfaces, or freeform surfaces, open a new window for optical design by adding degrees of freedom to the optical surface that can correct optical errors. In this case, oblique ray incident angles introduce aberrations that are correctable by surface shapes that have different local base radii of curvature in the orthogonal directions as discussed by Thompson [13]. Thus, benefit of using freeform surfaces is controlling aberration nodes in the field of view, which consequently allows reduction of the wavefront error.

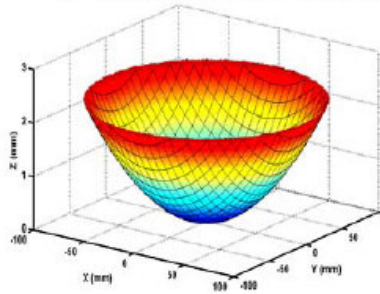
1.2.2 Freeform Fabrication

Freeform surfaces are typically machined using a diamond turning machine (DTM) with a fast tool servo (FTS). This concept, patented by the PEC [14], decomposes the surface into rotationally symmetric and non-rotationally symmetric components. The main axes of the DTM are used to create the best-fit asphere and a piezoelectrically driven tool

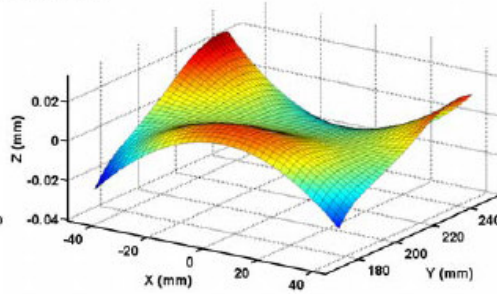
holder adds the non-rotationally symmetric component, as shown in Figure 1-2. A number of different FTS designs are now commercially available with different strokes and bandwidths ranging from low-amplitude, high-speed designs (30 μ m at 10 kHz) to long-range, low-speed design (1 mm at 100 Hz). The FTS must be synchronized to the rotation of the spindle of the DTM to create a surface height that is a function of both radius and angular position.



a) Off-axis biconic mirror segment



b) Rotationally symmetric component of mirror



c) NRS component of the mirror

Figure 1-2: Decomposition of a biconic mirror surface (a) into symmetric (b) and non-symmetric and (c) components for on-axis fabrication

1.2.3 Freeform Metrology

One way of measuring freeform surfaces are using a coordinate measuring machine (CMM). Cylindrical machines are also used to measure freeform surfaces where the surface is mounted on an air-bearing spindle (θ) and a non-contact optical sensor is moved radially over the surface by an r-z mechanism. An optical probe is used for non-

contact measurement protecting the optical surface and should be positioned perpendicular to the surface (ϕ -axis) [33].

Computer generated holograms (CGH) mounted onto a phase shifting laser interferometer is another way to measure freeform surfaces where the CGH is used to adapt the wavefront to the freeform surfaces measured. The measurement uncertainty depends on the calibrated null lenses and CGH [34].

1.2.4 Opto-Mechanical Design

Mechanical design of the shape and position of the optical components in an optical system is very critical in achieving the predicted optical performance. Opto-mechanical design consists of positioning the mirrors without distorting the optical surfaces [17]. With fabrication capabilities developed at the PEC, described in Section 1.2.2, optical surfaces and fiducial features are machined using the diamond turning machine and fast tool servo. Handbook of Optomechanical Engineering describes the use of clamps, bonding, or flexure mounts as a way of mounting mirrors onto a telescope frame [17]. Kinematic support for a component is constraining it in six degrees of freedom, shown in Figure 1-3. At A the ball end rod fits in a conical depression, V-groove at B eliminates two rotations about a vertical axis at A and about the axis AC, while the contact at C eliminate the final rotation about the AB axis as described by Smith [2]. Previous researchers have applied this kinematic support concept by using two pins that fit into a hole and slot constraining a mirror component in six degrees of freedom [19]. Clearance between pins and the mating hole and slot is increasing assembly tolerances ($\sim 5 \mu\text{m}$); thus, degrading the optical performance of the system. Different alignment

methodologies can precisely locate mirror components on a telescope frame to less than 1 μm while assembly cost increase exponentially [35]. Contact between the mirror component and the telescope frame and mounting forces should be collinear to eliminate any moments that would affect the optical surface. A semi-kinematic system is more desirable in practice than a kinematic system. Semi-kinematic design is defined as a substitution of the point and line contact into small area contacts to reduce the Hertzian contact stress and plastic deformation of mating surfaces [18].

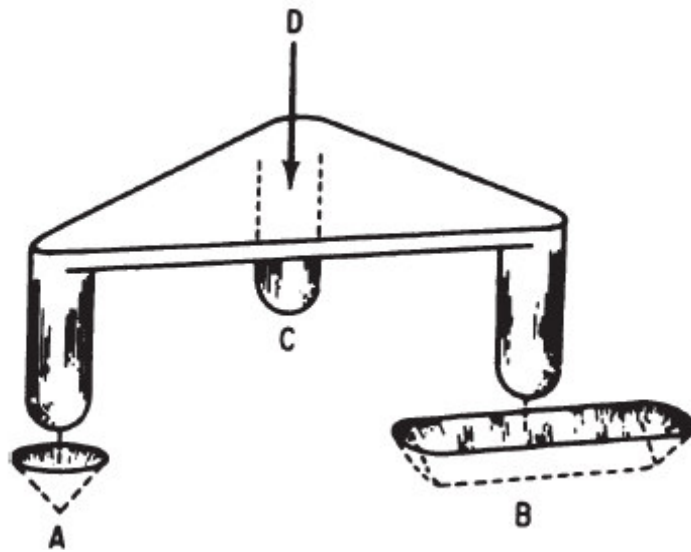


Figure 1-3: Example of a kinematic locating fixture

Different telescope frame designs have been used to constrain mirrors in six degrees of freedom using fiducial features and referencing the optical surfaces to each other. Designs varied from one piece telescope housing finished to sub-micron geometry for local surface co-planarity and parallelism [19], to a multiple piece design assembled together [20]. To further improve this research, a conventional two-mirror optical system is designed and tested to serve as a learning exercise, then ensued by a three mirror anastigmat using freeform surfaces is designed.

1.3 PROBLEM STATEMENT

The primary objective of this research is to demonstrate the power of freeform optical systems used in military applications, especially missile defense optical systems. Freeform surfaces are defined as surfaces without an axis of symmetry. Use of freeform surfaces in reflective optical systems allows improved system performance with substantial aberration reduction in the system, improving the image quality. This research focuses on optical and optomechanical design techniques of multi-mirror reflective optical systems.

2 OPTICAL DESIGN OF TWO MIRROR TELESCOPE

2.1 INTRODUCTION

A telescope system using two mirrors is selected for the first prototype because it is the simplest example of a reflecting telescope. The goal is to gain familiarity with optical design, fabrication, assembly and performance evaluation for telescope systems. Because changes are most efficiently made during the design process, an understanding of the whole phase (design, fabrication, assembly and metrology) must be addressed and is a key to cost effective deployment of systems.

The classic Cassegrain uses a two mirror layout that consists of a primary and a secondary mirror as shown in Figure 2-1. The mirrors are coaxial and each mirror is rotationally symmetric about this axis. For a Cassegrain design the primary is parabolic and the secondary is hyperbolic. Light enters the system, first encountering the primary mirror, which then reflects the light to the secondary mirror. The secondary mirror reflects light through a hole in the center of the primary to the image plane as shown in Figure 2-1. Cassegrain telescope systems suffer from optical aberrations, especially astigmatism and coma that increase with increasing field angles. The image is aberration-free only on-axis [2].

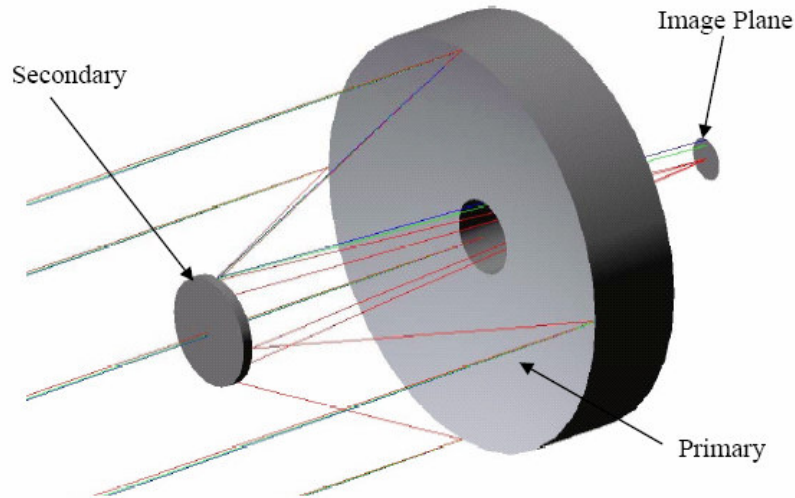


Figure 2-1: Two mirror optical system

2.2 CONFIGURATION

Ritchey-Chrétien design, first introduced in a 1904 paper “On the Modern Reflecting Telescope, and the Making and Testing of Optical Mirrors” [1], is a modification of the Cassegrain design. In this configuration, both aspheres are hyperbolic. The Hubble Space Telescope is a Ritchey-Chrétien (RC) design. Ritchey-Chrétien designs use the hyperbolic primary mirror to correct both coma and spherical aberration that are inherent in the Cassegrain configuration [2].

2.2.1 Size and Shape

Ritchey-Chrétien designs [2, 3] typically have an f-number range between 4 and 6 and full field angles from 0.75° to 2° . F-number is defined as focal length divided by aperture diameter. Initial design specifications are chosen realizing these limits. Since astigmatism is a function of field height in all two-mirror designs, the system was specified as a 1° field angle optical system.

The optical system overall size is determined by optical, fabrication, and mechanical design issues. A primary aperture diameter of 150 mm served as the starting point of the optical design. Many of the optical choices are centered on the primary's speed, that is, light gathering ability. The primary is set at $f/1$; thus, the focal length is 150 mm and radius of curvature is twice the focal length, or 300 mm. Initially, the conic constant was set at -1 (parabola) and allowed to vary in the optimization. The diameter of the center hole was set to 26 mm to allow light reflected from the secondary mirror to form the image at the detector.

Specification of the secondary is largely based on its function to reflect light from the primary and to correct the primary's optical defects. Its aperture diameter is solved by the height of the marginal rays reflected from the primary. Marginal rays are the rays that start from the point where the object crosses the optical axis and reflect from the outer edge of the primary mirror or aperture stop. In accordance with the Ritchey-Chrétien prescription, the conic constant was set for a hyperboloid at -2 and allowed to vary in the optimization. The radius of curvature was initially set to be 90 mm, but was also allowed to vary.

Mirror spacing is measured as a percentage of the secondary distance from the primary's focal point. Small percentages, below 15%, increase alignment sensitivity and large percentages, above 30%, increase obscuration. Spacing in this system is initially set at 20%. Spacing of the secondary affects the radius of curvature and thereby substantially affecting the focal point of the secondary and thus, the location of the detector. Therefore,

small adjustments or 0.25% step increments to the initial spacing were used to finalize the distance from the secondary to the image plane.

2.2.2 Detector

A Canon digital EOS (300D) SLR camera was chosen for its high resolution, 6-megapixel, CMOS sensor, USB interface with remote capture and data transfer function, availability and low cost. The detector size is 22.7 mm by 15.1 mm. To image the full field of the optical system onto this detector, the image size in the optical design was held to 15 mm. The CMOS array in this camera has 3072 x 2048 effective pixels; thereby yielding a square pixel pitch of 7.4 μm . The camera and CMOS sensor are shown in Figure 2-2.

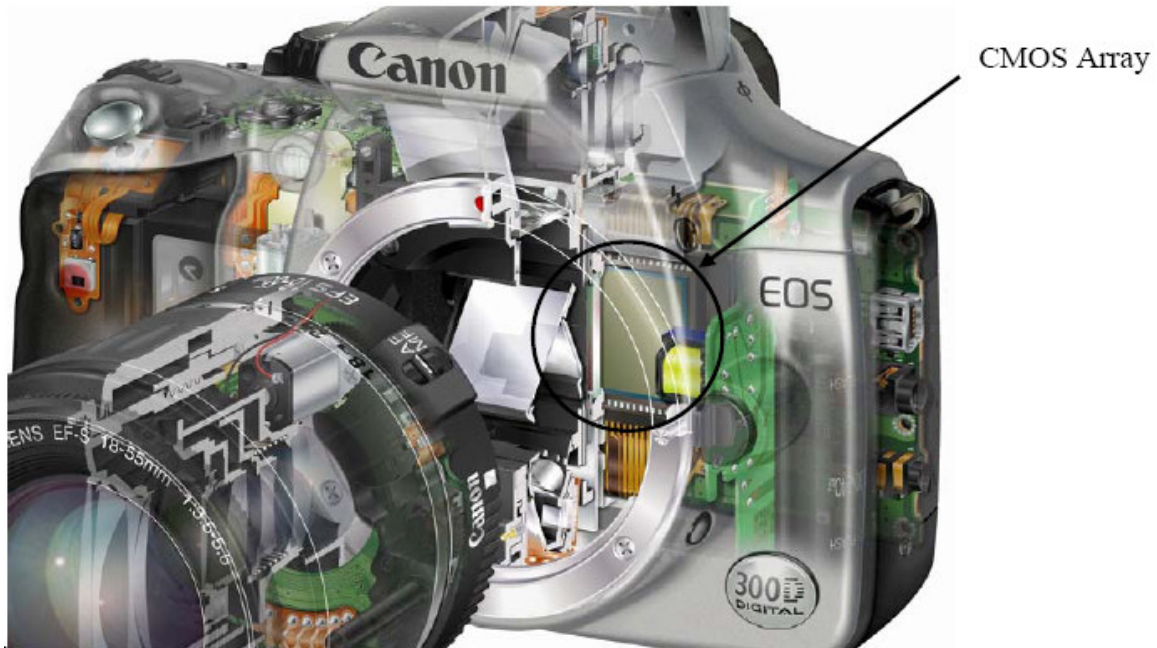


Figure 2-2: Canon digital EOS 300D

Ritchey-Chrétien telescope's image plane is situated behind the primary mirror. Given the system layout, distance from the CMOS array to the lens mounting flange (44 mm) is taken into consideration during the optical design.

2.2.3 Optimization

Global system specifications are used in Code V to initialize the system and solve basic system parameters. The Entrance Pupil Diameter or EPD is set at 150 mm, or the size of the primary mirror. Analysis wavelength is set at HeNe (632.8 nm). Because astigmatism is a function of field height in all two-mirror designs, this system is specified to be 1° field angle. Paraxial image solve is enabled such that the image surface is set at the system paraxial image focus, or the point where the rays parallel to the system axis converge.

Optical Research Associates (ORA) provides an optimization routine in Code V that is fully customizable as shown in Figure 2-3. The optimizer uses an accelerated damped least square (DLS) algorithm to generate changes in variables that improve the system. Two categories of settings define boundary conditions or constraints customizable through the tabs shown in Figure 2-3. General constraints are general boundary conditions that control thickness values and glass map boundaries to avoid unrealistic designs. Specific constraints are entered by the user to physically or optically constraint the whole system or a range of surfaces [7]. Since reflecting telescopes can be nearly diffraction limited, the error function type is set to wavefront error variance. Constraints applied in the optimization routine are shown in Table 2-1. Third order spherical aberration and third order tangential coma are both targeted to zero. Additionally, the YZ

paraxial marginal exit angle, shown in Figure 2-4, between the secondary mirror and the detector is set to 0.08726. This value is calculated by dividing the inverse of the system's f-number by 2. The system f-number is set by a combination of the detector height, field angle, and aperture diameter as shown in Equations 1 and 2.

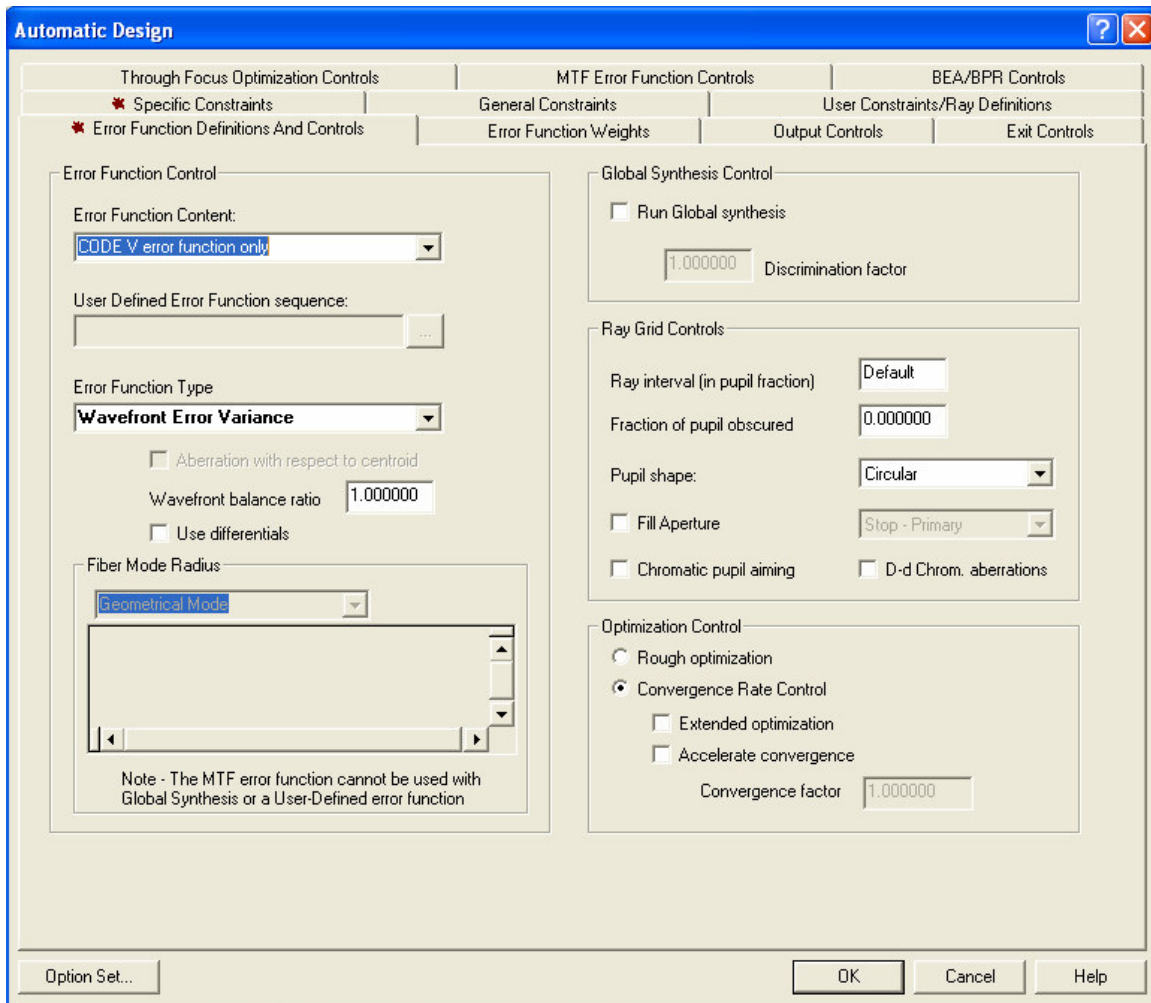


Figure 2-3: Code V optimization or automatic design dialog box

$$f \# = \frac{h_{\text{detector}}}{\theta_{\text{field}} \cdot d_{\text{aperture}}} = \frac{15\text{mm}}{\left(\frac{1^\circ}{57.3}\right) 150\text{mm}} = 5.73 \quad (1)$$

$$\theta_{\text{Paraxial Marginal Exit}} = \frac{1}{2 \times f \#} \quad (2)$$

Table 2-1: Two mirror optimization routine constraints

Constraint	Tab	Description
3rd order Spherical Aberration	Specific Constraints	Constrain to 0 minimizing spherical aberration over the field of view
3rd order Coma	Specific Constraints	Constrain to 0 minimizing coma over the field of view
YZ Paraxial Marginal Exit Angle	Specific Constraints	Set the exit angle at 0.0872645 to constrain the f-number to 5.73 and the EFL to 859.873 mm

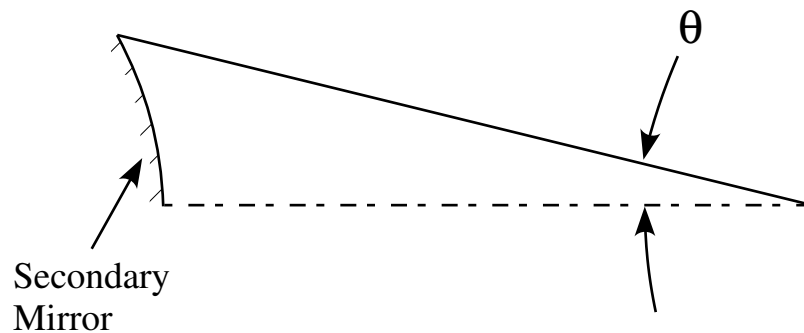


Figure 2-4: Paraxial marginal exit angle from the secondary mirror

All specifications not explicitly selected are allowed to vary during optimization. The final conic constant of the primary is -1.0195 and the secondary is -2.1666. Radius of curvature of the secondary is 88.1225 mm and the aperture diameter is 38.9395 mm. Distance between the primary and secondary vertices was adjusted by trial and error to accommodate the 44 mm spacing from mount to film plane of the Canon EOS camera

used as the detector. The final distance between the primary and secondary vertices is set to 113.625 mm. Paraxial image solve positions the image plane 208.519 mm away from the secondary mirror vertex.

The optical specifications for the optimized two mirror Ritchey-Chrétien design is tabulated in Table 2-2, full fabrication data tables can be found in Appendix A. The Effective Focal Length or EFL of the finalized system is 859.873 mm, computed using Equation 3.

$$EFL = f / \# \cdot EPD \quad (3)$$

Table 2-2: Two mirror optical system specifications

	Radius of curvature (mm)	Conic constant	Aperture diameter (mm)	Distance to next surface (mm)
Primary	-300	-1.0195	150	113.625
Secondary	-88.1225	-2.1666	38.9395	208.519

To minimize the wavefront error over the full field of view, the image plane is linearly translated to the best focus position. Figure 2-5 shows the image plane (vertical line) at the on-axis focus (a) and best focus position (b). Best focus is the optimum position of the image plane in the field of view where focus error is minimized over the whole field. For the on-axis focus position, focus error increases with field angle to reach a maximum of 0.826 mm at the 0.5° field angle. For the best focus position, focus error is compensated over the field of view and is 0.481 mm at the 0.5° field angle and 0.345 mm at the 0° field angle. For the two mirror telescope, the best focus position is 0.345 mm in a direction towards the secondary mirror. This shift changes the distance from the

secondary mirror to the image's best focus position to 208.174 mm, different from the on-axis focus position given in Table 2-2. Difference between on-axis and best focus image position will be explained in further detail in the wavefront analysis Section 2.3.2.

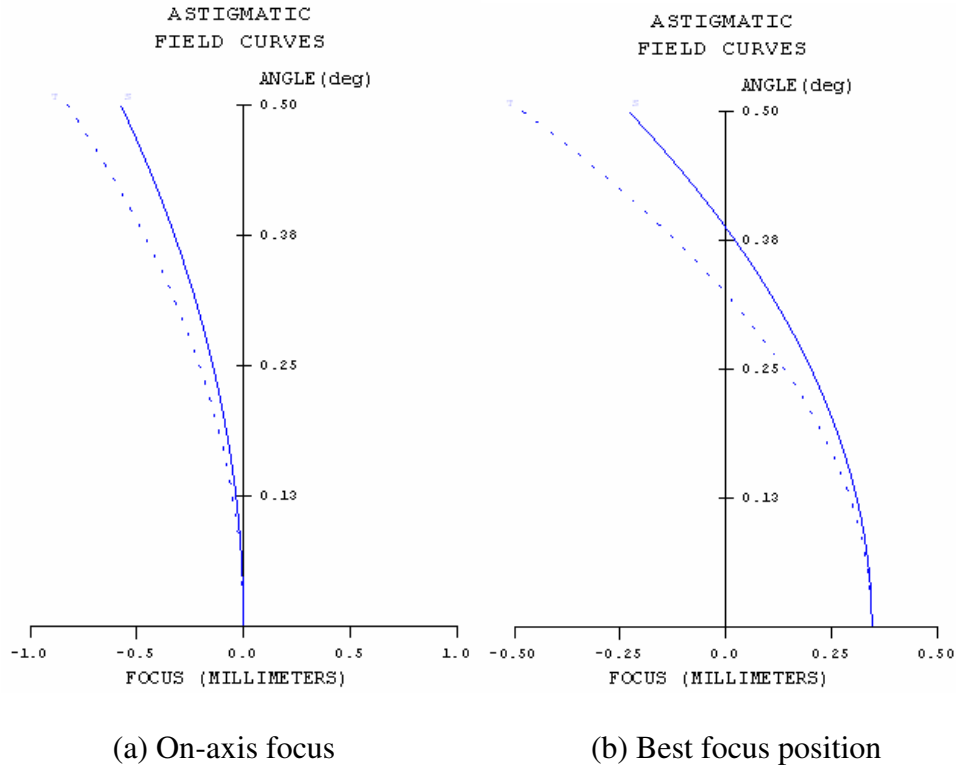


Figure 2-5: Field curves showing focus errors on the tangential (dotted line) and sagittal (solid line) planes

2.3 THEORETICAL PERFORMANCE

The performance of the two-mirror system is performed using tools in Code V. The fundamental aberration in a Ritchey-Chrétien (RC) design is uncorrectable astigmatism. Both hyperbolic mirrors correct for spherical aberration and coma. For a rotationally symmetric two mirror system, astigmatism is zero on-axis and increases with the field angle. The following section illustrates different ways to assess the system's performance including

- Aberrations
- Wavefront Analysis
- Modulation Transfer Function
- Spot Diagram

2.3.1 Aberrations

Aberrations define the extent to which the quality of an image is affected [6]. The most important optical aberrations affecting image quality are the third-order terms. In an axially symmetrical system, only odd-order terms exist. First-order terms describe the position and size of the image. Third-order terms were first codified by Seidel and include spherical aberration, coma, astigmatism, Petzval curvature, and distortion [2]. Fifth and higher order terms are extremely complex and are not used to quantify aberrations affecting image quality. Code V optical design software produces plots of field-dependent performance parameters, through the Field Map option, that presents these third-order errors. Of the five terms listed above, astigmatism, coma, and spherical aberration are the most fundamental and they give the best description of system performance. Each is discussed in the following sections.

2.3.1.1 Astigmatism

Astigmatism occurs when the tangential and sagittal images do not coincide at the image plane. The image of a point source takes the form of two separate foci, the vertical fan has a point focus in the tangential direction but this point is a line when viewed in the sagittal direction and vice versa [2]. Between these foci, the image is an elliptical or circular blur. For the rotationally symmetric two mirror system, astigmatism is zero on-

axis and increases with field angle as shown in Figure 2-6. The line lengths represent the magnitude of the error and the angle shows the relative size of the tangential and sagittal fringe Zernike components (Z5 and Z6). Astigmatic error line representation points towards the center of the field. Maximum error is 0.747 waves at edge of the field, with an average error of 0.388 waves over the full field.

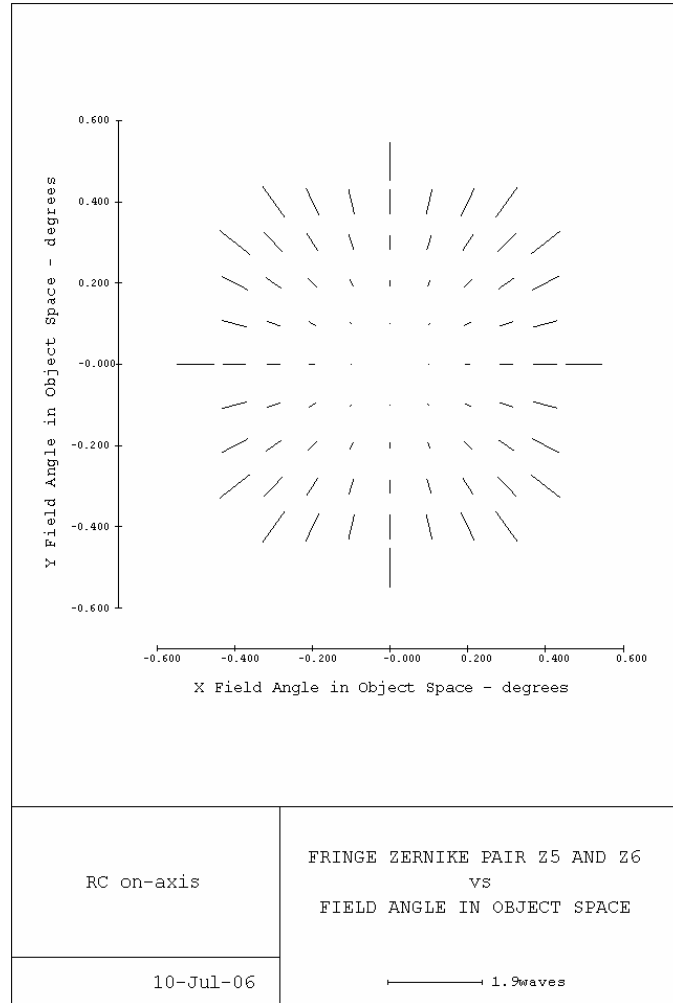


Figure 2-6: Field map of astigmatism for optimized two mirror system

2.3.1.2 Coma

Coma is defined as the variation in magnification with aperture; that is, rays passing through the top and bottom of the lens may focus at a different height than the focus of

those passing through the center [2]. In an axially symmetrical system, there is no coma for the on-axis field but coma magnitude increases with field angle in a direction away from the optical axis as shown in Figure 2-7. The shape of the error resembles an “ice cream cone” where the image of oblique rays at a specific field angle spread out into a comet-shaped flare. Figure 2-8 shows the relationship between rays passing through a circular aperture and their location in the coma patch [2]. Rays forming a circular aperture form a circle in the coma patch. Distance from P to AB is the tangential coma and distance from P to CD is called the sagittal coma and is one-third the tangential coma. The size of the “ice cream cone” in Figure 2-7 represents the magnitude of the components of the coma in the sagittal and tangential directions ($Z7$ and $Z8$). The maximum error is 0.015 waves at the edge of the field with an average error of 0.012 waves over the full field of view.

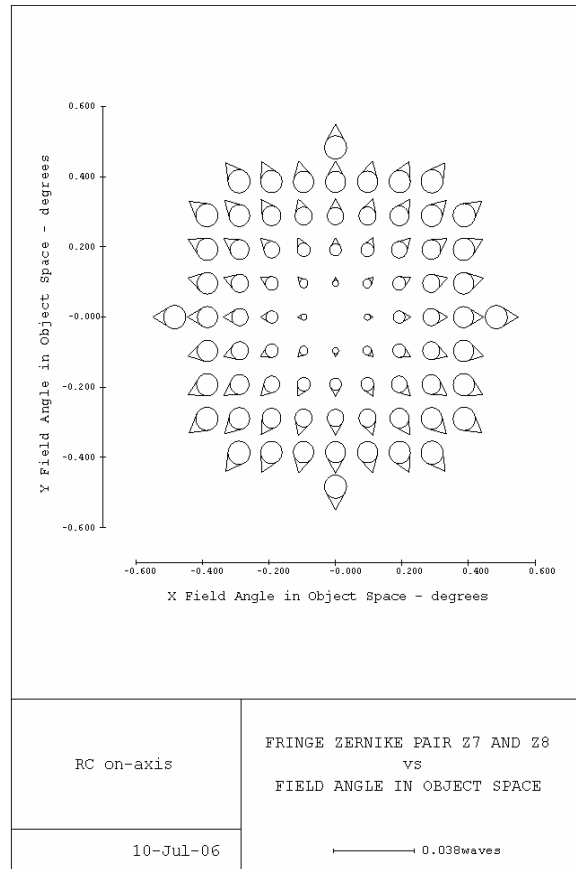
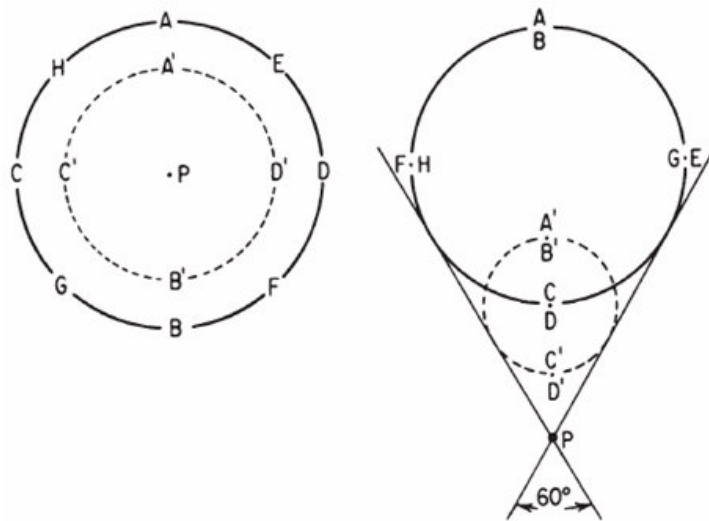


Figure 2-7: Field map of coma for optimized two mirror system



(a) Circular lens aperture (b) Position of rays on the image plane

Figure 2-8: Relationship between ray position and its respective position in the coma patch

2.3.1.3 Spherical Aberration

Spherical aberration errors involve a change in the focus point of an optical system for off-axis rays as shown in Figure 2-9. Rays at different heights in the aperture will focus at different locations. The distance from the paraxial focus to the axial intersection of the off-axis ray is called longitudinal spherical aberration (LA'). Transverse spherical aberration (TA') is the vertical distance measured on the paraxial focus line [2]. For this rotationally symmetric design, the spherical aberration, shown in Figure 2-10, is minimum on-axis, -0.0018 waves, and increases with aperture away from the optical axis to reach a maximum value of -0.0092 waves at the edge of the field. The average error over the full field is -0.0056 waves. Negative spherical aberration magnitudes indicate that the off-axis rays focus closer to the secondary mirror or in the negative z -direction.

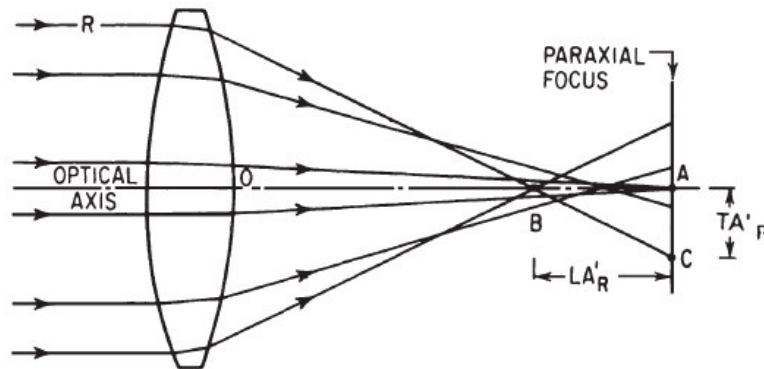


Figure 2-9: Schematic of spherical aberration that varies with aperture

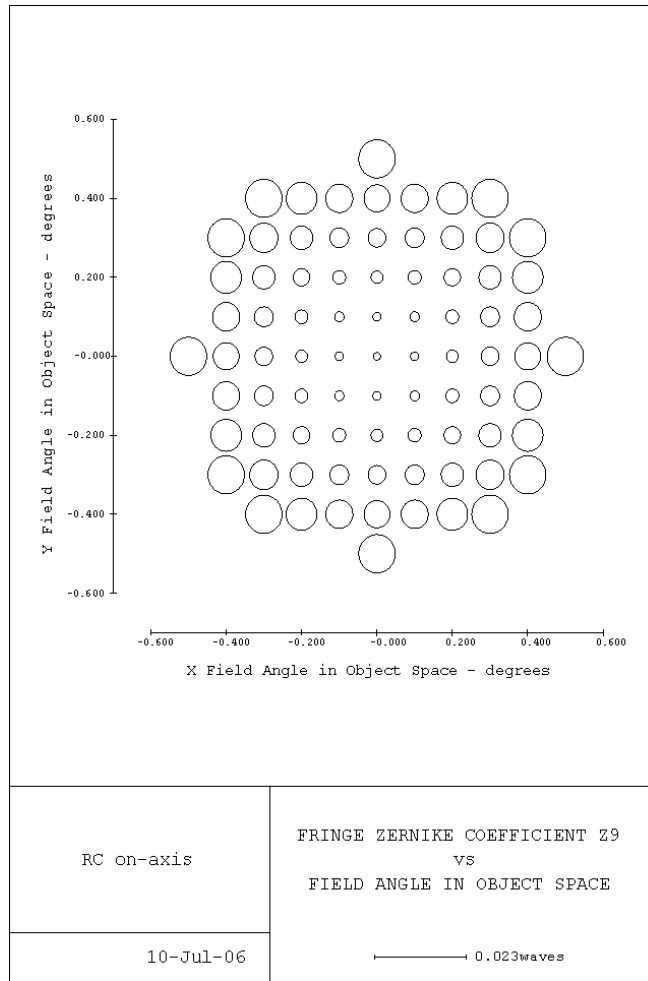
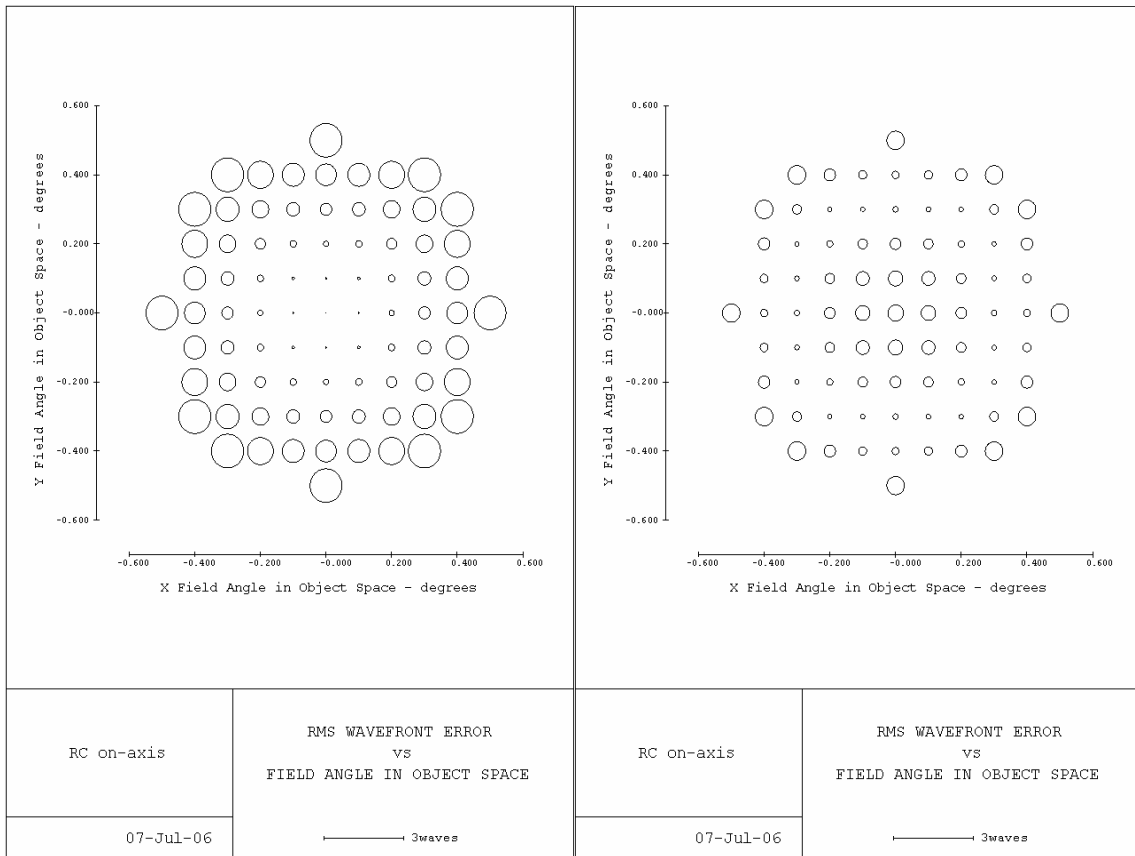


Figure 2-10: Field map of spherical aberration for optimized two mirror system

2.3.2 Wavefront Analysis

One way to evaluate the effect of optical aberrations in an optical system is performed by plotting the RMS wavefront error over field of view of the system through the Field Map option in Code V. Wavefront aberration or wavefront error is an aberration function published by Hamilton containing all aberration terms [6]. The general form of the aberration function is in terms of three fundamental parameters: the aperture radius, the field radius and the azimuth angle of the plane containing the principal ray in the image forming wavefront. Total wavefront aberration of the image is the sum of the surface

contributions. Figure 2-11(a) shows a plot for the RMS wavefront error the RC design over the $\pm 0.5^\circ$ circular field of view with the image plane at the on-axis focus position. The diameter of the circles indicates the magnitude of the error at each field position in waves. At the on-axis focus position, the minimum error occurs at the center of the field and error increases with astigmatism as the field of view increases. To minimize the error over the entire field of view, Code V optical software creates a best focus position for the system – in this case at the 0.35° field angle (70% of the range). Figure 2-11(b) shows the RMS wavefront error with the minimum error now at an intermediate position. Both figures are plotted using the same scale. RMS wavefront error, for the on-axis focus position, is 0.001 waves at the center of the field and increases to 1.199 waves at 0.5° with an average of 0.626 waves over the full field. The optimum focus position wavefront error is 0.582 waves on-axis while 0.658 waves at 0.5° with an average of 0.367 waves over the full field. Image plane translation to best focus position minimizes the average wavefront error over the whole field by decreasing the error at the outer field angles and increasing the error at the center of the field. Best focus average wavefront error is 58.6 % of the error at the on-axis position.



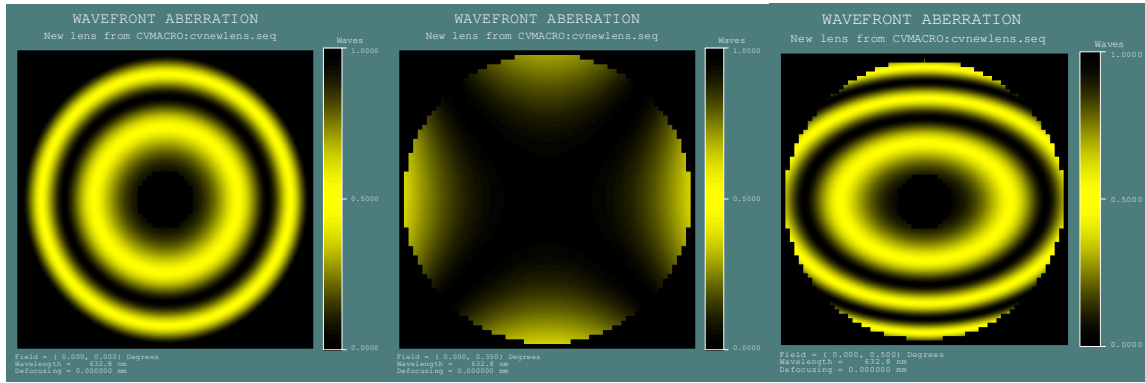
a) Best focus on-axis

b) Best focus at 0.35° (70% of max field)

Figure 2-11: RMS wavefront error map across the field of view of the telescope

Another way to view the system aberrations is to plot the interferometric fringe pattern departure from an ideal spherical wavefront sent through the telescope. Code V Pupil Map plot options include presentation of the interferogram fringe pattern for three different field positions with the best focus at 0.35° illustrated in Figure 2-12. Shapes of the fringes indicate the aberrations present at that region of the system. The only aberration present on-axis is spherical aberration as shown by the circular interference fringes that is caused by the defocus needed to optimize the system over the field of view. The aberrations are smallest at the 0.35° field angle and the fringe pattern is typical of

astigmatism with different radii of curvature in the orthogonal directions [27]. The interference plot for the 0.5° half-field shows focus and astigmatic errors produce the oval wavefront with more fringes vertically than horizontally.



a) Error at 0°

b) Error at 0.35°

c) Error at 0.5°

Figure 2-12: Wavefront error for the optimized system at three field positions

2.3.3 Modulation Transfer Function

Another measure of the optical quality of the RC telescope is the Modulation Transfer Function (MTF). The MTF is used to determine the frequency response of a system or its ability to render spatial frequencies on the image plane. Characteristic such as sharpness and resolution can be related to MTF. Diffraction is an optical effect that limits the resolution of a system and is a function of the numerical aperture and the wavelength of light. Numerical aperture is defined as half the inverse of the f-number of the system. Diffraction sets the upper limit of contrast for all diffraction-limited systems and is plotted as the right-most dotted line in Figure 2-13. The MTF plot gives a modulation value for contrast with 1.0 being perfect black and white boundaries and 0.0 being totally gray as a function of the spatial frequency. MTF plot for the RC design displays the best performance at the 0.35° field angle as a result of the image plane focus compensation.

There are two traces for each field angle that show the MTF along the tangential (solid line) and radial (or sagittal, dotted line). The best focus field angle (0.35°) exhibits a smooth transition to the cutoff frequency (275 cycles/mm) and shows 60 cycles/mm at 50 % modulation. The other two field angles (0° and 0.5°) experience a sudden drop in the MTF and exhibit a much lower frequency, 15 cycles/mm at 50 % modulation, due to the lack of focus. The highest achievable resolution is on white-black cycle, two pixels wide, also known as the Nyquist frequency. The Canon CMOS detector Nyquist frequency is 68 cycles/mm, determined by dividing twice the pixel size by 1. The MTF for the different field angles varies at this frequency from 0 % for the on-axis and edge fields to 45 % for the best focus position. The best modulation at this frequency is 64 % determined by the diffraction limit.

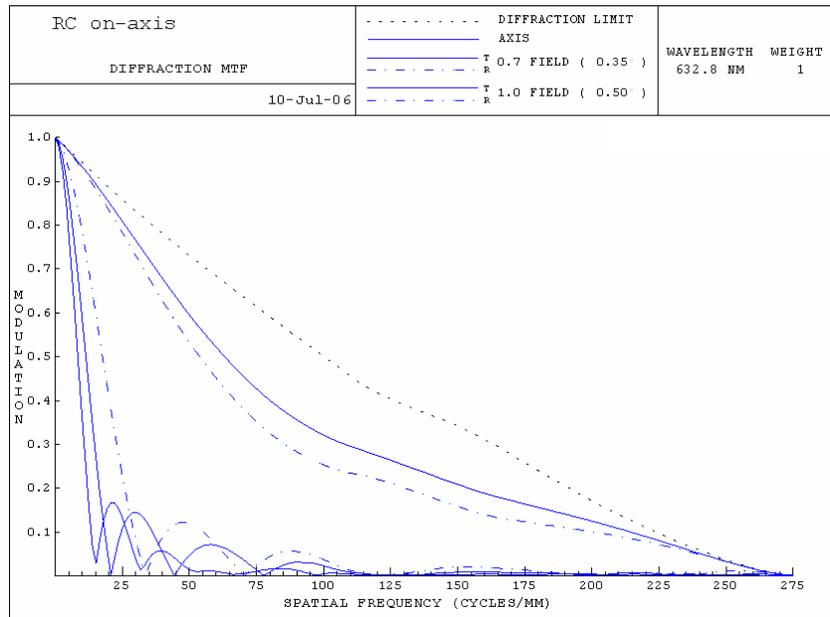
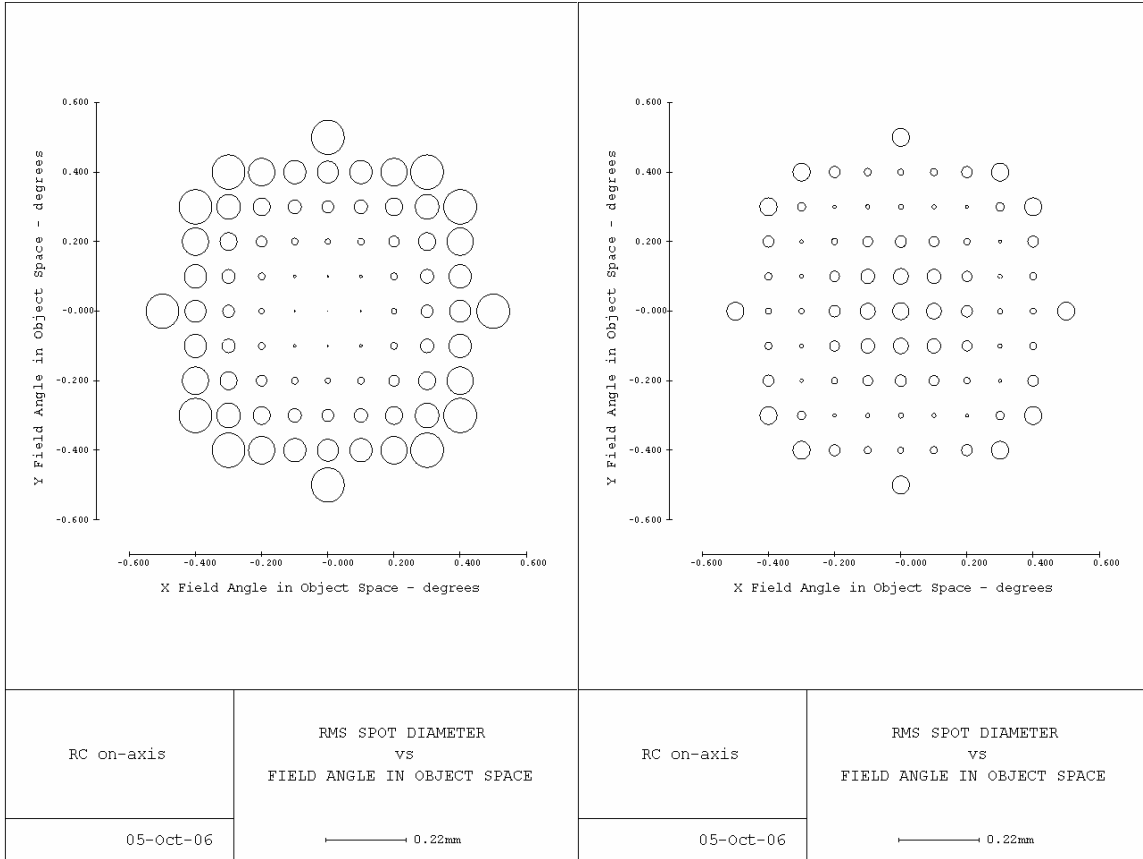


Figure 2-13: MTF for the optimized two mirror system presented on-axis and at two locations off-axis (0.35° and 0.5°).

2.3.4 Spot Diagram

Spot diagrams show the ray-based geometrical shape of the image distribution for each field angle. Rays reflected from the primary mirror at a specific field angle will intersect the image plane forming a circular spot. The spot diameter gives a good visual impression of image quality and its size can be used to identify optical characteristics and aberrations. The spot diagrams at the on-axis and best focus positions are plotted on the same scale in Figure 2-14. The best focus position is determined by Code V through the image plane compensation. For the on-axis focus position, the smallest RMS spot size is $0.18\ \mu\text{m}$ at the center of field and increases radially outwards to reach a maximum of $89.5\ \mu\text{m}$ at the edge of the field (0.5°), with an average of $46.4\ \mu\text{m}$ over the field of view. The smallest RMS spot size for the best focus position is $8.4\ \mu\text{m}$ at 0.35° and it increases to approximately $47\ \mu\text{m}$ at the edge of the field, with an average of $25.5\ \mu\text{m}$ over the full field. The spot diagrams at both positions resemble the RMS wavefront error plots respectively. Aberrations affecting image quality influence the spot diagram by increasing the spot diameter or blur. Image plane compensation to best focus position decreases the spot diameter of the outer edge field angles by increasing the diameter of the center field angles. Best focus position average spot diameter is 55 % of the average on-axis focus position.



(a) On-axis focus position

(b) Best focus position

Figure 2-14: Spot diagram for the optimized two mirror system

2.4 SENSITIVITY ANALYSIS

The telescope is designed based on a snap-together assembly and, as a result, the imaging performance is affected by the magnitude of the optical and fiducial surface fabrication errors discussed by Woodside [4]. The shape error created by the Rank-Pnemo ASG 2500 diamond turning machine (DTM) on flat and spherical components is on the order of $\lambda/4$ (150 nm). This tolerance consists of radius and astigmatic error on both optical surfaces. Tolerance on length dimensions is $\pm 2 \mu\text{m}$. This includes spacing between the two mirrors, decentration of the mirrors in 2 dimensions (x and y), and tip and tilt of the

mirrors about x and y axes. A Code V tool called ‘sensitivity analysis’ predicts the effect of manufacturing tolerances on image quality.

Results of the sensitivity analysis simulation are shown in Table 2-3 and complete results can be found in Appendix B. Average RMS wavefront error (waves) over the field of view is used to evaluate the effect of tolerances on image quality. Theoretical RMS wavefront error due to the uncorrectable astigmatism inherent in the two mirror optical system is listed for each field angle. Predicted wavefront error due to fabrication tolerances is computed without compensation and the subsequent error with compensation. Image plane focus shift serves as a compensating factor for the system’s tolerance. Figure 2-15 shows the variation in wavefront error due to manufacturing tolerances for the different field angles. The predicted wavefront error with and without compensation are almost identical and overlap in Figure 2-15. The predicted wavefront error with compensation experiences very small variation compared to the error without compensation. The image plane focus shift (4.086 μm) compensates for the radius error on both mirrors and z-displacement error between the mirrors. The system’s predicted RMS wavefront error experiences very small changes due to the small contribution of the radius and spacing errors of the mirrors.

Table 2-3: Change in RMS wavefront error with manufacturing tolerances ($\lambda = 632.8 \text{ nm}$)

Field Angle	Theoretical Wavefront	Predicted Error without Compensation	Predicted Error with Compensation	Compensation (focus change)(μm)
0°	0.582	0.6219	0.6210	4.086
0.35°	0.154	0.3261	0.3261	4.086
0.5°	0.668	0.7652	0.7650	4.086

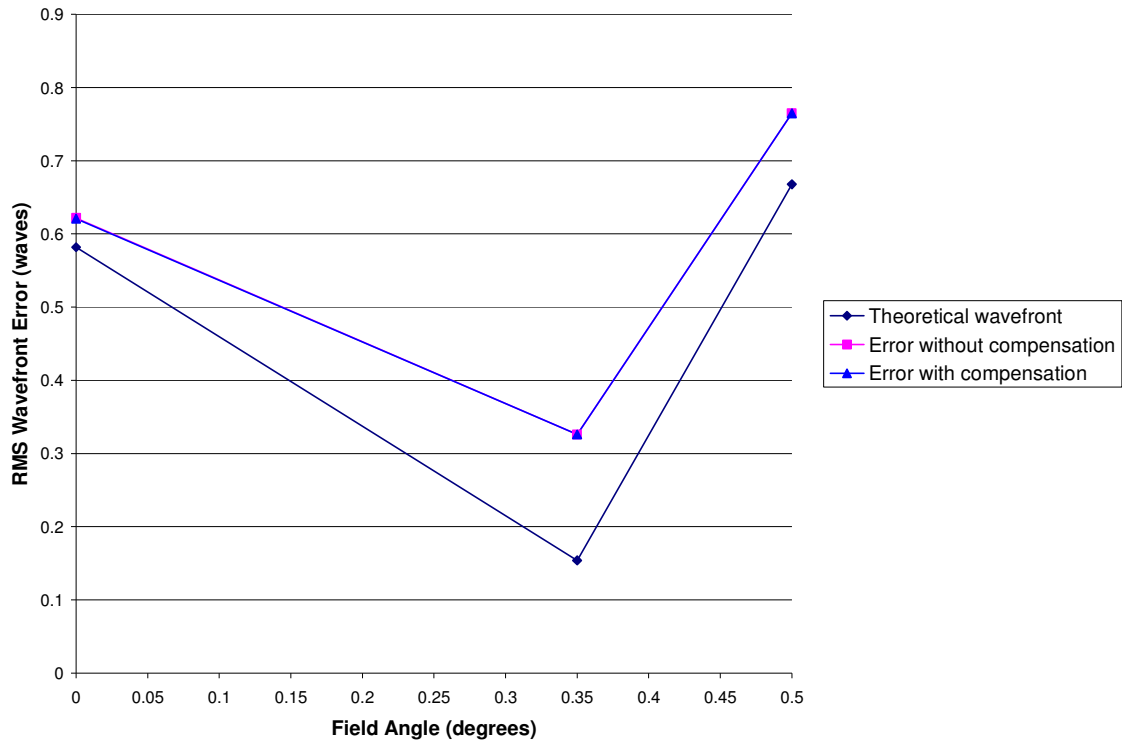


Figure 2-15: RMS wavefront error sensitivity analysis

3 OPTOMECHANICAL DESIGN OF TWO MIRROR TELESCOPE

3.1 INTRODUCTION

Design of the structure to support the imaging optics is extremely important in delivering an image quality within the tolerances specified. Design issues to be considered are the following: material selection, mirror substrate design, mechanical support of the mirrors in the system, and assembly fiducials. Several designs of the crucial connection between the primary and secondary mirror were considered. A bracket press fit into the primary mirror hole and holding the secondary mirror at the other end was designed. The tube design, described in this section, is chosen due to its simplicity and fabrication feasibility.

3.2 MATERIAL

All components of the telescope are Aluminum 6061-T6. This material combines high strength, low weight, and good machineability with diamond tools, excellent coating adhesion and high resistance to corrosion [5]. Also, by using a single material, no distortion of the components will occur for an environmental temperature change. One problem with 6061 aluminum is second-phase impurities would tend to reduce the surface finish of the optical surfaces to the order of 6 nm RMS [28].

3.3 STRUCTURE

The optomechanical design consists of separate primary and secondary optics with a cylindrical tube connecting them. This tube, shown in Figure 3-1, provides reference surfaces that locate the two optical surfaces in the axial, radial and tilt directions. The

different telescope components, shown in Figure 3-1, are the primary mirror, secondary mirror, connecting tube, spacer, gussets and base plate.

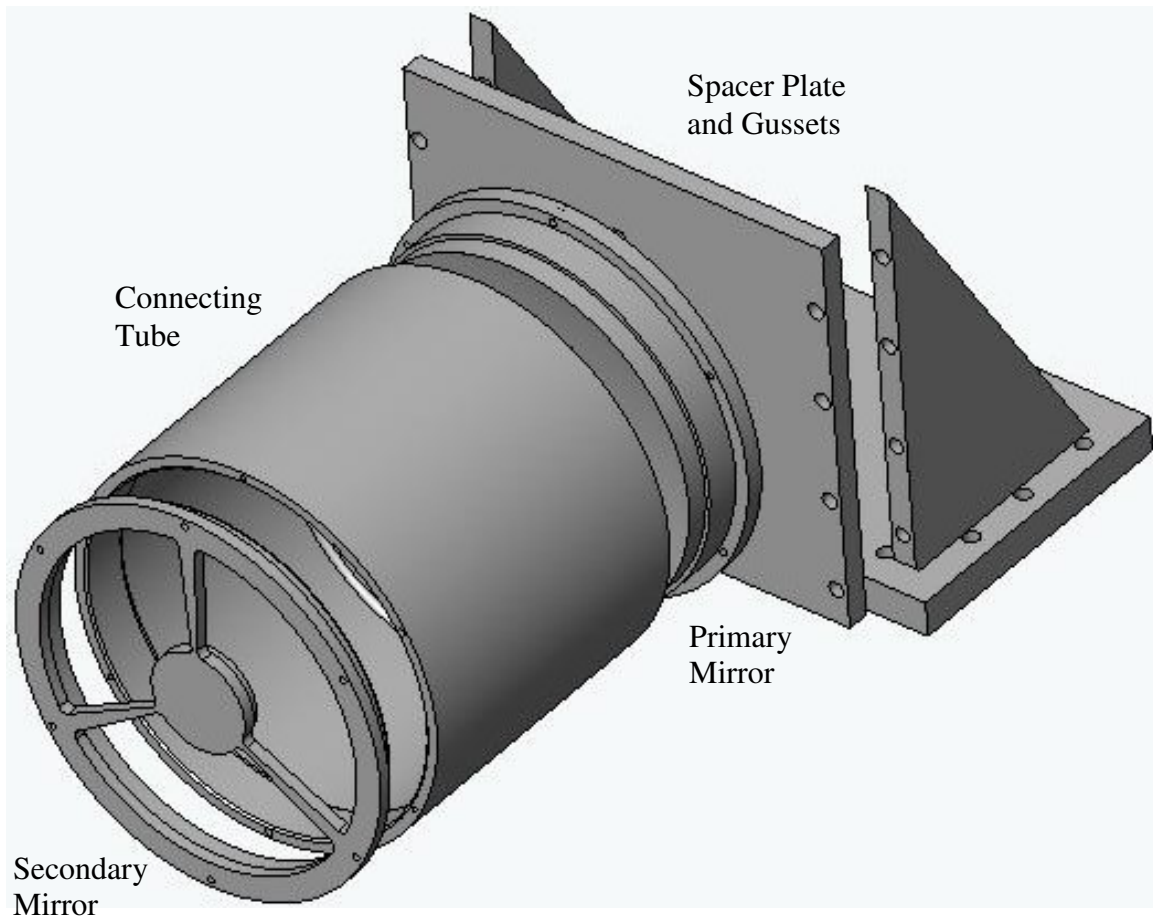


Figure 3-1: Two mirror telescope components

3.3.1 Telescope Support

The optomechanical design concept for the two mirror telescope incorporates axial and radial fiducial features to relate the primary and secondary optical surfaces to the image plane (detector). Both optical components are mounted on the tube relating the optical surfaces to each other. The outer diameter (OD) of the cylindrical tube is 164.2 mm. Aspect ratio is the mirror aperture diameter divided by the thickness. The 39.4 mm secondary mirror has an average thickness of 10 mm for an aspect ratio of 4 and is

supported by three radial struts from the outer ring to the mirror. The average thickness of the primary is 27 mm and the OD is 150 mm for an aspect ratio of 5.5. Detail drawings of the telescope components can be found in Appendix C.

A radial interference surface on the primary mirror, shown in Figure 3-2, locates the axis of the tube to be coincident with the axis of the primary. This radial interference surface constrains the mirror component from translating in the radial direction. The axial reference ring sets the distance along the axis constraining the mirror along the axial direction and tilt about the radial direction. Three symmetric screws hold the mirror component on the tube constraining the rotation about the optical axis (axial direction). The secondary mirror structure also has a radial interference surface that ensures that the primary and secondary mirrors are coaxial. While the secondary axial stop positions the secondary mirror at the correct axial distance from the primary mirror. Flatness and roundness of the reference surfaces ensures that the primary-tube-secondary interface is coaxial.

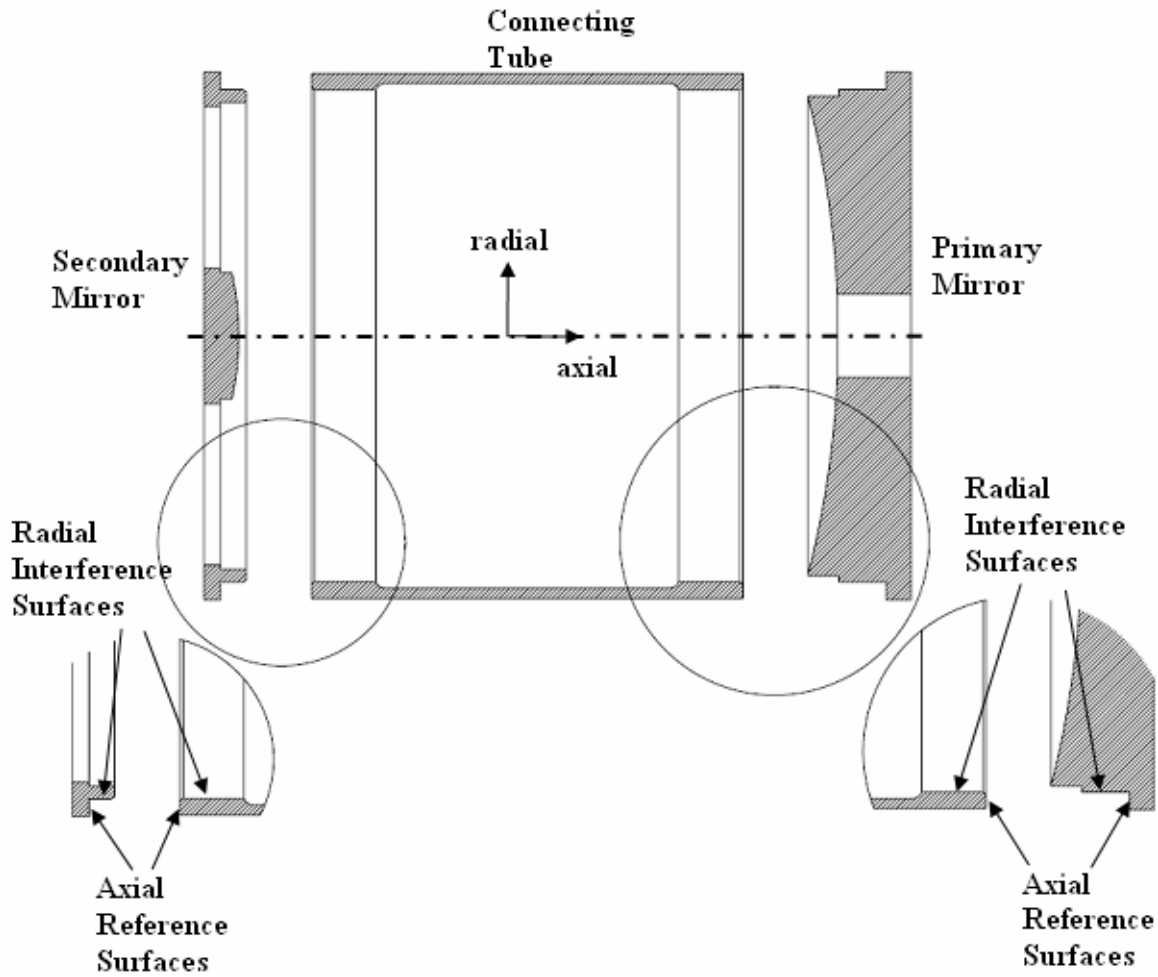


Figure 3-2: Detail drawing of the telescope

The optomechanical design is based on a snap-together assembly without any adjustments. The primary and secondary structures have a small radial interference fit to the tube ($\sim 6 \mu\text{m}$) and three 4-40 screws are employed to hold the optical structures in place. The assembly process is to heat the tube by holding it in bare hands to eliminate the thermal interference, inserting the optical structure into the tube, shown in Figure 3-3, and then tighten the screws to 2 in-lbs. This torque should produce a force of 90 lbs or 400 N. A detailed assembly procedure of the two mirror telescope can be found in Appendix C.

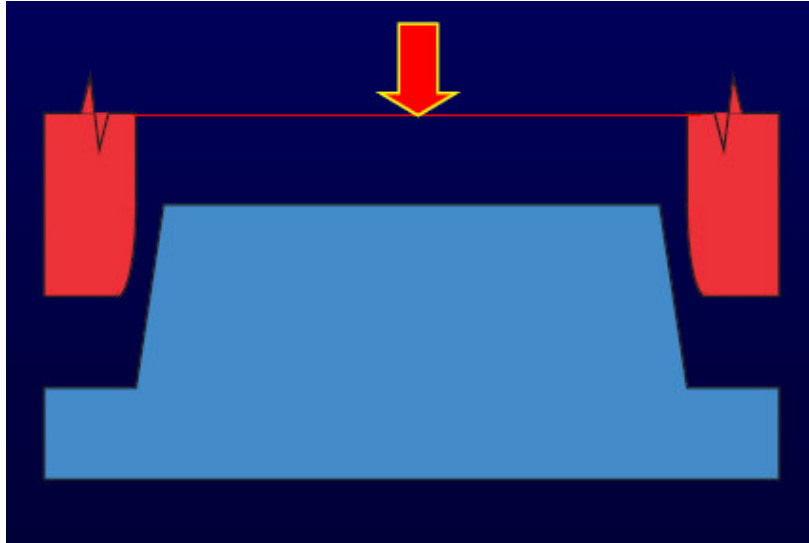
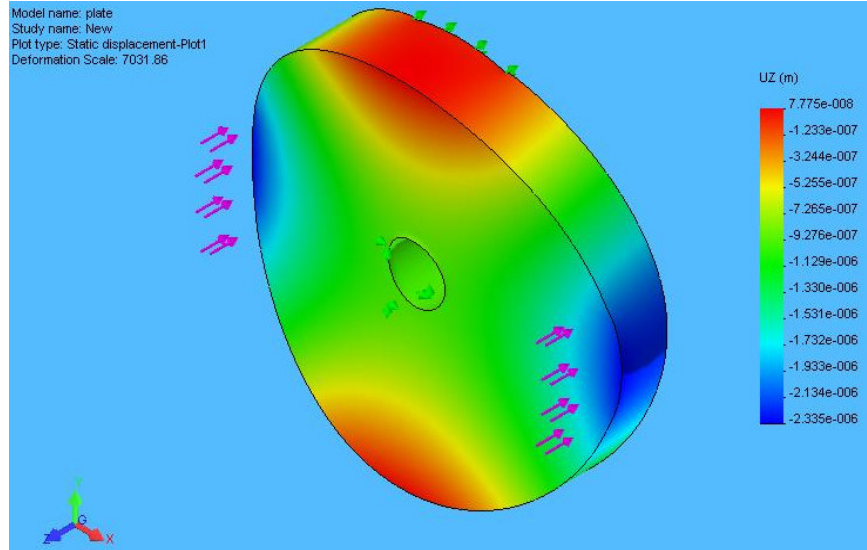
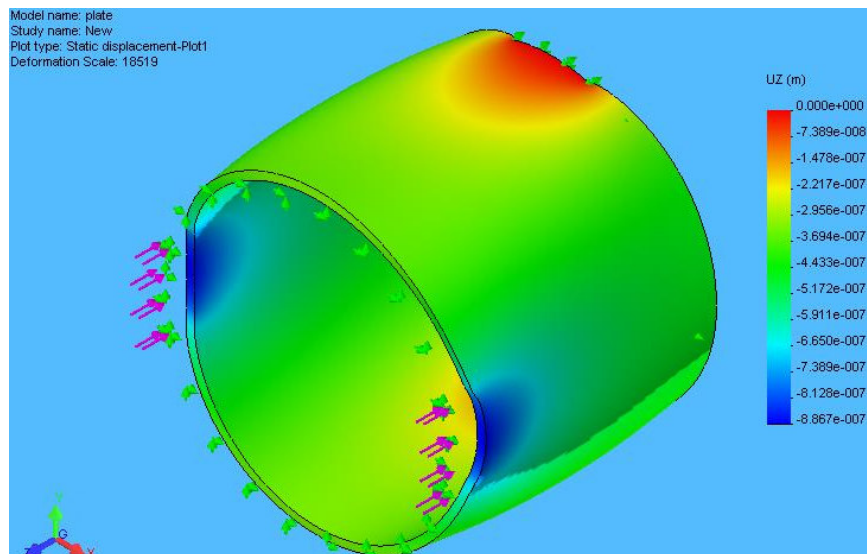


Figure 3-3: Assembly of optical components into the tube

Since the tube is stiffer in the axial direction than the optical components, application of these three forces on the components is found to cause distortion to the optical surfaces. When the primary is assembled to the tube, configuration of the assembled parts will be a function of the shape and stiffness of the mating components. The tube and a circular plate were modeled in SolidWorks/Cosmos to find the stiffness of the two components in the axial direction. Both components are analyzed under the same loading-restraint conditions. Distributed load, equivalent to 100 N, is applied at two equal areas on one end of the part. The part is restrained in six degrees of freedom using similar areas at the opposite end. Inside surface of the parts is restrained from expanding in the radial direction. Results of the simulation, shown in Figure 3-4, determine the plate's axial stiffness is 42.83 N/ μm , while the tube's stiffness is 112.77 N/ μm . The tube is more than two times stiffer than the plate; thus, mounting the primary and secondary on the tube would deform the mirrors under the assembly conditions.



(a) Circular plate displacement in the z-direction



(b) Tube displacement in the z-direction

Figure 3-4: Displacement plots to determine axial stiffness

3.3.2 Camera Support

The telescope is tested by mounting it on the tripod for photography or the laser interferometer for dual pass measurements through the camera support structure, shown in Figure 3-1. The camera support structure consists of a spacer plate, gussets, and a base

plate. The spacer plate connects to the primary mirror structure through three ¼” socket head cap screws. To minimize the distortion of the primary mirror’s back optical reference surface, three 0.5 mm thick shim washers are used between the two mating surfaces to minimize the contact surface. The washers would also provide adjustability when needed. The camera is mounted on the opposite side of the spacer plate through a lens mounting flange. Two gussets and a base plate facilitate mounting the telescope onto the tripod. A Hewlett-Packard laser tripod served as the mounting device for the telescope. Testing the telescope using dual pass measurements in the laser interferometer is carried out without using the camera support structure.

3.3.3 Manufacturing Feasibility

Fabrication of the telescope was performed using a Rank Pneumo ASG 2500 Diamond Turning Machine (DTM) as shown in Figure 3-5. The ASG 2500 X and Z axes have 250 mm and 150 mm ranges of motion. The DMI position feedback resolution for the axes is 2.5 nm and the spindle has a 5000 line encoder with 4x quadrature interpolation. The primary-tube-secondary optical axis is collinear; therefore, each structure is machined using the face of the spindle as a reference surface and the spindle axis as the optical axis. For the primary and secondary mirror structures, the optical surface is machined during the same machining setup as the flat fiducial surface. The distance between the fiducial surface and apex of the optical surface is set during this machining operation and determines the spacing between the elements. Next, the radial fiducial surfaces are machined. Then, the tube’s outer radial surface and inner radial fiducial surfaces are machined for concentricity. Next, the tube’s axial reference surfaces are machined to ensure length and parallelism aligning the two optical elements. Finally, the camera

mounting surface on the spacer plate is machined to place the detector at the best focus position.

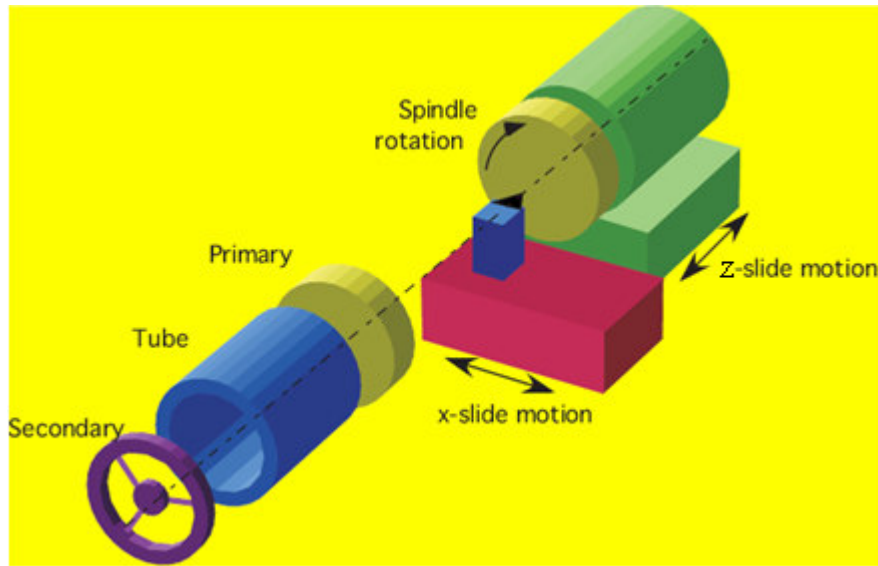


Figure 3-5: Fabrication of two-mirror telescope on a diamond turning machine

3.4 TWO MIRROR DESIGN CONCLUSION

The two-mirror telescope system is fabricated at the Precision Engineering Center (PEC) using the ASG 2500 DTM, described by Lamonds [10]. Optical components and the system performance were measured and described by Woodside [4]. Errors due to optical component fabrication and post-assembly design issues have an impact on the optical performance. System and component errors affecting optical performance are discussed in the following section.

3.4.1 Dual Pass Measurements

The telescope was measured using the Zygo-GPI laser interferometer as discussed by Woodside [4]. The dual pass measurement was setup in Code V to visualize the wavefront error plots generated in the experiment. The wavefront error for this

measurement is twice that of the RC telescope because the spherical wavefront passes through the telescope twice. A schematic of the system is shown in Figure 3-6. The two telescopes are on top of each other but the optical path in Code V goes from left to right and returns from right to left. A spherical wavefront is generated from the focus point at the left, passes through the telescope and creates collimated light that impinges onto the flat mirror. Light is collimated because the system is designed for infinite conjugates. Light from the flat mirror is reflected back through an identical telescope and focused onto the original point. To test the system for the 0.35° and 0.5° fields, the telescope is translated from the nominal optical axis, shown in Figure 3-6 as the centerline, in the z-direction. The telescope is decentered until the off-axis focus coincides with the optical axis, where each field angle corresponds to a different off-axis focus. Then, the flat mirror is tilted to reflect the collimated light back through the telescope. The wavefront error for the different fields is shown in Figure 3-7.

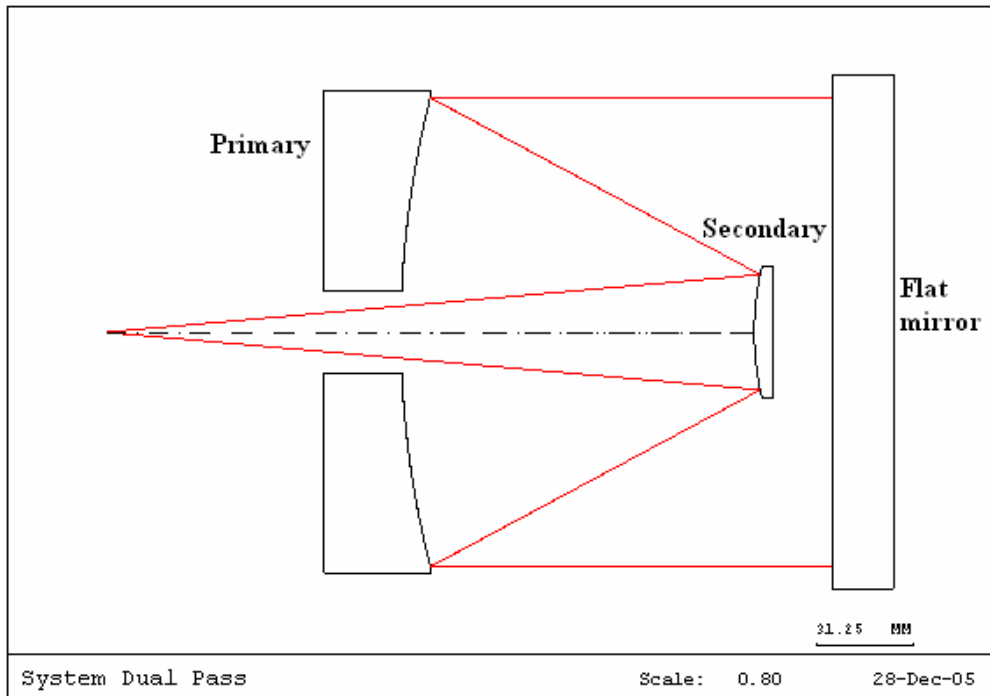
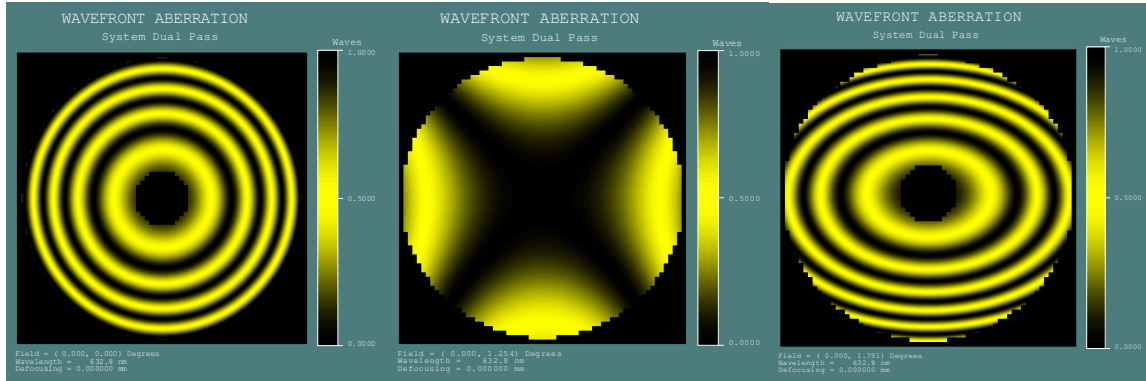


Figure 3-6: Dual pass setup for telescope measurement, showing on-axis rays



a) Error at 0°

b) Error at 0.35°

c) Error at 0.5°

Figure 3-7: Wavefront error for the dual pass model in Code V with best focus at 0.35°

The spherical wavefront passes through the system twice, since there are two telescopes concatenated on each other. Therefore, theoretical wavefront error from the dual pass model, Figure 3-7, is double the theoretical wavefront error for the system, Figure 2-12. The wavefront error for the 0° field shows circular interference fringes, maximum of 4 waves, which indicates that the system is out of focus due to image plane compensation. Aberrations are minimum at the 0.35° field angle where astigmatism dominates the wavefront, peak-to-valley of 1.4 waves, because image plane compensation corrects the focus error at this field angle. Wavefront error for the 0.5° field shows both focus and astigmatic error with oval interference fringes and a maximum error of 5.5 waves. Twice the wavefront error is expected when measuring the performance of the telescope on the Zygo-GPI interferometer and should be considered when interpreting the results.

3.4.2 Aspect Ratio

Distortions of the optical surfaces can occur when a part is mounted on the vacuum chuck for machining. The compliance of the mirror blanks are related to the aspect ratio between the diameter and the thickness. To keep the mirror blank as stiff as possible and the distortion as small as possible, the aspect ratio should be small. One way to evaluate the effect of a change in either dimension is to consider the problem of a plate with diameter (d) and thickness (t) that is simply supported on the outer diameter and loaded with uniform pressure over the surface. This is analogous to the part being vacuumed onto a chuck but where contact only occurs at the outer diameter. For this condition, the deflection at the center can be written as [3]:

$$\delta_{\max} = 0.7 \left(\frac{qr^4}{Et^3} \right) \quad (3)$$

where q is the pressure, r is the outside radius, E is the elastic modulus of the material and t is the plate thickness. Figure 3-8 shows the deflection of the 150 mm diameter plate as a function of the aspect ratio for a typical vacuum loading of 10 psi (70 kPa). Note that the deflection is not just a function of the aspect ratio but also depends on the radius because the ratio is r^4/t^3 . The aspect ratio of the primary is about 5.5 so it will deflect more than 1 μm for the vacuum loading. For the same loading-restraint conditions, the secondary mirror, with an aspect ratio of about 4, would only have 0.1 μm deflection at the center. These results had an impact on the optical surfaces; thus, on the optical performance of the system, measured and discussed by Woodside [4]. Therefore, a circular plate with an aspect ratio of 3 has an acceptable deflection when mounted on the

vacuum chuck for machining. Results of this simulation are taken into consideration when designing the mirror components for the three mirror anastigmat (TMA).

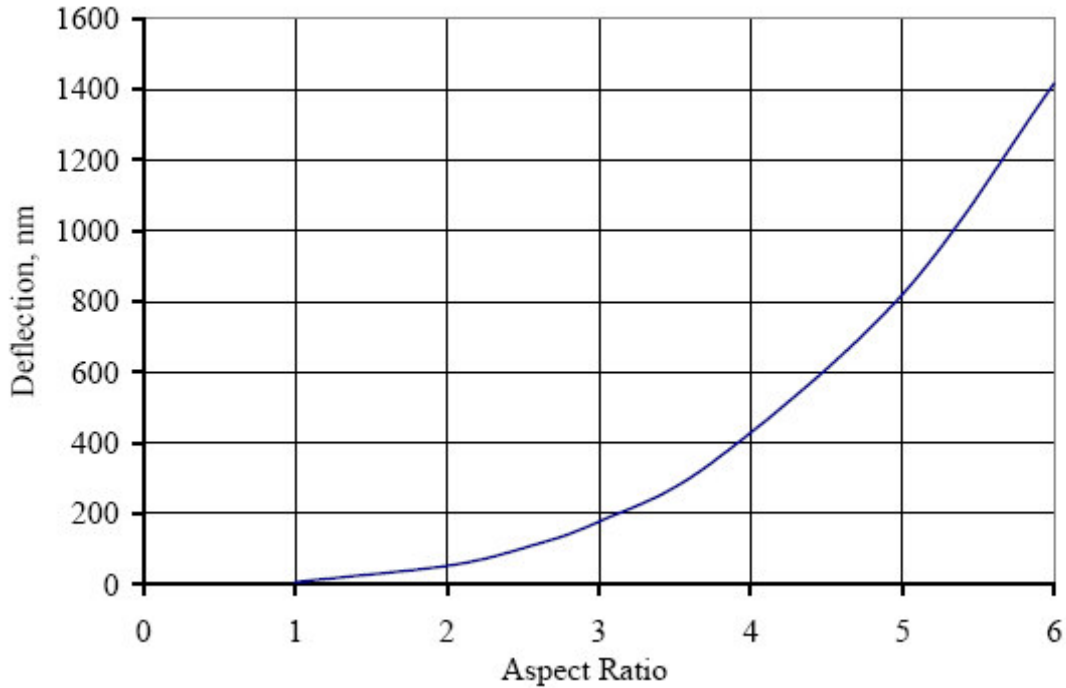


Figure 3-8: Deflection of a 150 mm dia. aluminum plate vs. Aspect Ratio
(diameter/thickness)

3.4.3 Primary Mirror Structure

The primary mirror optical surface is measured on the Zygo-GPI laser interferometer using dual pass interferometry due to its hyperbolic surface. The primary mirror measurement, shown in Figure 3-9, is taken when the component is assembled onto the tube. The measurement shows trefoil symmetry with a peak-to-valley of $0.3 \mu\text{m}$ and spherical aberration as discussed by Woodside [4]. The primary mirror optical surface measurement without assembly to the tube shows no trefoil symmetry. The primary mirror structure is press fit into the tube with a radial interference of $6 \mu\text{m}$ applied 6.5 mm from the axial fiducial surface. Assembly process is to seat the primary on the tube,

then by applying the screw forces both pieces are pulled together ensuring the axial reference surfaces meet.

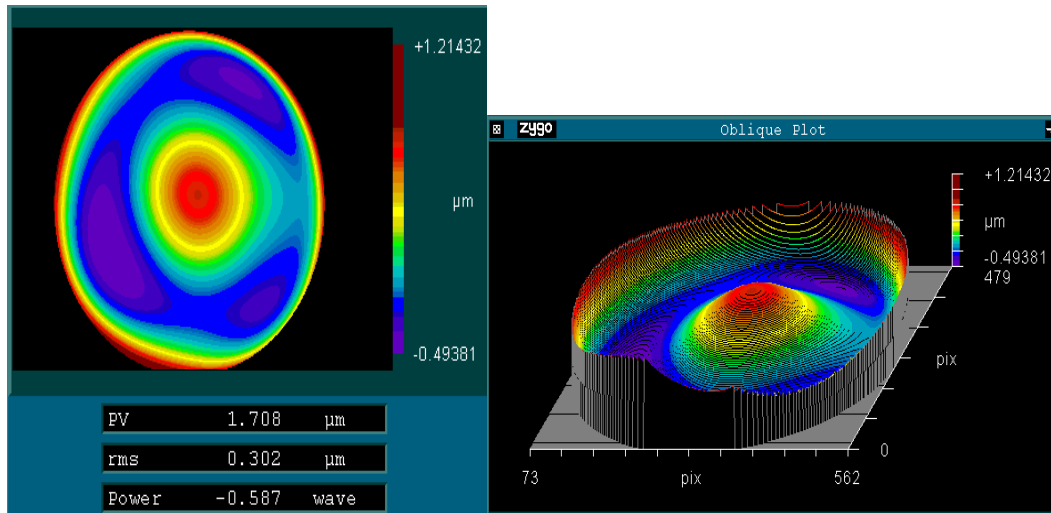


Figure 3-9: Measurement of the primary mirror optical surface when it is assembled on the tube

The primary mirror and tube axial fiducial surfaces were measured and shown in Figure 3-10 including the screw hole locations [4]. Both fiducial surfaces have two peaks and two valleys where the primary fiducial surface has a 5 μm peak-to-valley while the tube fiducial surface has a 3 μm peak-to-valley. During the assembly process, contact between the two fiducial surfaces first occurs at the two points shown in Figure 3-10 then the screws force contact at the screw location indicated. The force applied at each screw location depends on the gap between the fiducial surfaces and the relative stiffness of both components discussed in Section 3.3.1. Screw forces at the three locations are 78.9 N, 125.34 N and 49.05 N respectively. The primary mirror is modeled in SolidWorks/Cosmos to determine the effect of the varying screw forces. Translation of two pads on the axial fiducial surface, 180° out of phase, is constrained in the axial

direction. The other four degrees of freedom are constrained at the ¼” mounting screw holes on the back of the primary. The primary mirror’s optical surface outer edge displacement plot, Figure 3-11, shows trefoil symmetry with a 0.283 μm peak-to-valley corresponding to the 0.3 μm measured peak-to-valley. Optical surface trefoil deformation is a result of the distortion of the mating axial fiducial surfaces. Contact between fiducial surfaces should be over a small area to avoid the influence of fabrication errors on optical surfaces. The modeled and measured trefoil symmetry deformation exceeds the fabrication tolerance and its influence on the optical performance is discussed by Woodside [4].

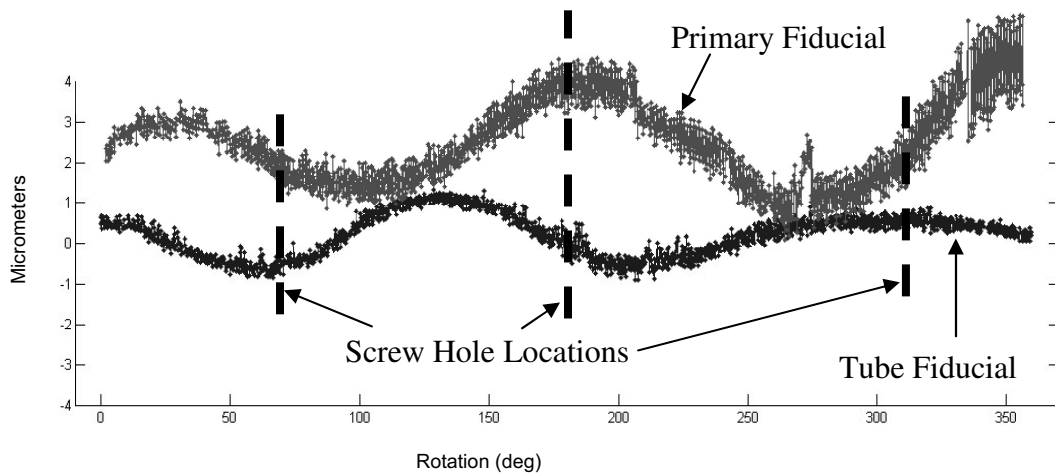


Figure 3-10: Primary and tube axial fiducial form error relationship

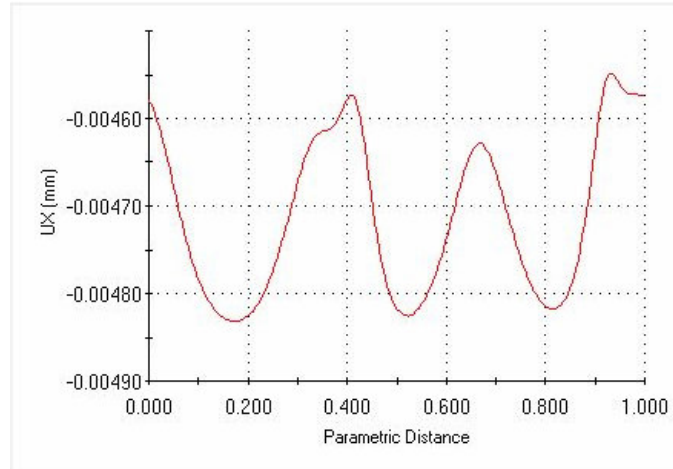


Figure 3-11: Primary mirror optical surface edge displacement

Uniform pressure due to the radial interference fit is modeled in SolidWorks/Cosmos. The part is restrained in six degrees of freedom at the 1/4" mounting screw holes on the back of the primary. Interference pressure, equivalent to 59 MPa, is applied 6.5 mm from the axial fiducial surface. Displacement plot is shown in Figure 3-12 and optical surface displacement is 3 μm due to the interference pressure. This displacement decreases the optical surface radius of curvature by 96 μm causing a focus error in the system. Effect of this interference pressure can be eliminated by applying the pressure through the neutral axis of the component.

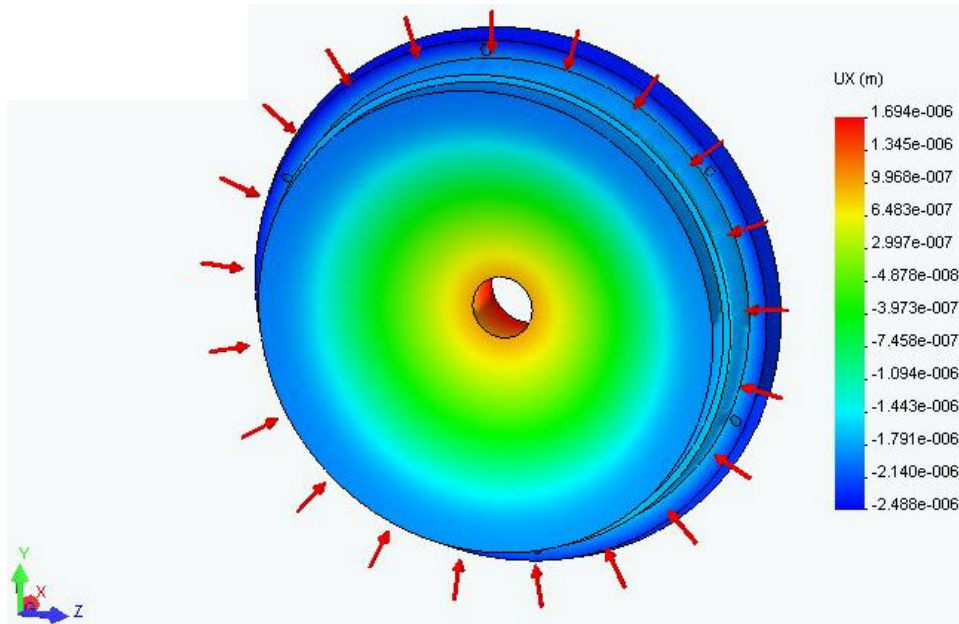


Figure 3-12: Primary mirror deformation due to the radial interference fit

3.4.4 Secondary Mirror Structure

The secondary mirror structure is press fit into the tube with a radial interference of $6\ \mu\text{m}$ applied 5 mm from the axial fiducial surface. As modeled in Section 3.3.1, the tube is stiffer than the optical components. The secondary mirror structure press fit into the tube generates a radial interference force of 90 lbs which creates a bending moment on the mirror. This bending moment displaces the secondary mirror $9.26\ \mu\text{m}$ away from the primary mirror as shown by the model setup in SolidWorks/Cosmos, Figure 3-13. This displacement causes focus error in the system and will shift the image plane as discussed by Woodside [4]. The moment can be eliminated if the radial interference pressure is applied at the neutral axis of the component as shown in Figure 3-14.

The opto-mechanical design concept is based on the use of radial and axial fiducial surfaces to reference optical surfaces and the detector to each other and constraint the

optical components in six degrees of freedom. To ensure that optical surfaces are coaxial, the two mirror components are press fit into a connecting tube at opposite ends. Simulations of the interference forces generated between the components exhibit optical surface distortions on both the primary and secondary mirror surfaces. Therefore, press fitting optical components into structures is not an ideal design and should be avoided in the non-rotationally symmetric three mirror anastigmat design.

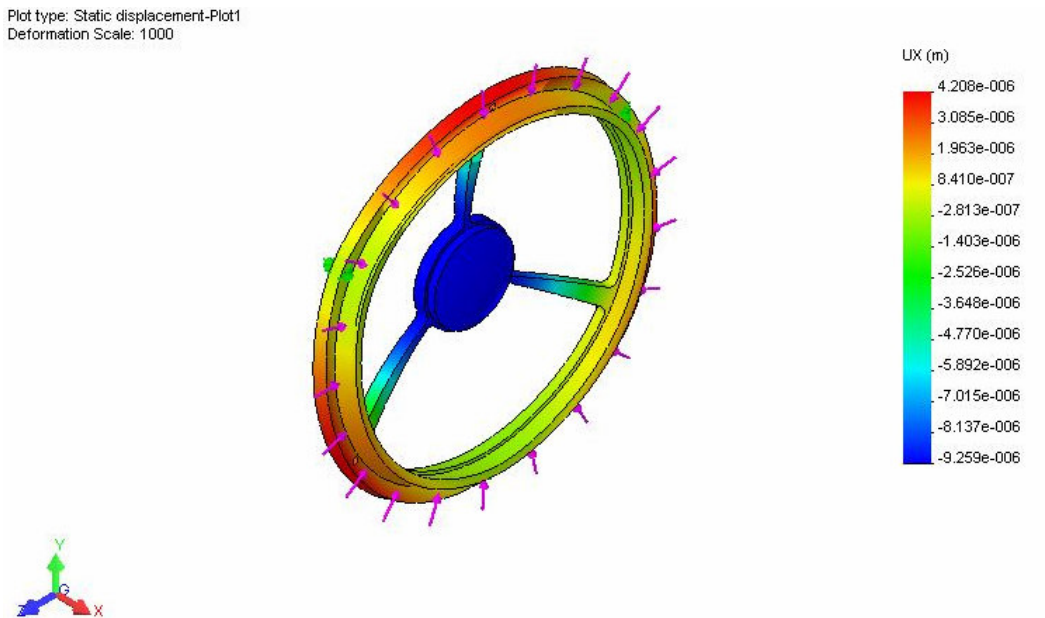


Figure 3-13: Secondary mirror structure deflection due to mounting onto the tube

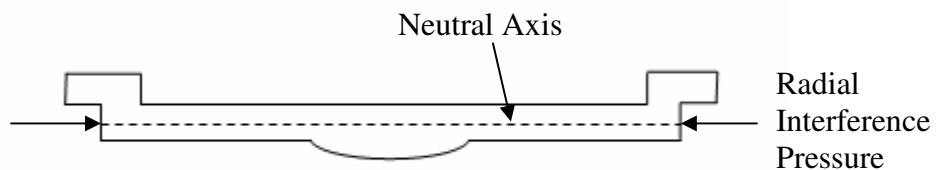


Figure 3-14: Schematic of the secondary mirror structure with interference pressure applied collinear to the neutral axis

4 OPTICAL DESIGN OF TMA

4.1 INTRODUCTION

For rotationally symmetric systems, there is no astigmatism for the on-axis field. As the field angle moves further from the axis, the amount of astigmatism linearly increases. To avoid astigmatism at an off-axis field angle, two unobstructed three mirror telescopes were investigated. First, a traditional Three Mirror Anastigmat (TMA) is designed with a single axis of symmetry and the surfaces are off-axis sections of rotationally symmetric conic surfaces. An alternative design was also investigated for the TMA using freeform surfaces, where the surfaces are converted to Zernike surfaces.

The two Three Mirror Anastigmat (TMA) designs have an f-number of 6.139 with an unobstructed entrance pupil diameter of 140 mm, a 1° circular field of view and an effective focal length of 859.5 mm. These specifications are close to the two mirror telescope. The entrance pupil diameter (EPD) was reduced from 150 mm to 140mm to allow the fiducial ring to be measured in the laser interferometer. The interferometer can accommodate flat parts with aperture diameter up to 150 mm. Ability to measure fiducial as well as optical surfaces is important and led to changing the EPD to accommodate a 10 mm fiducial ring. Changing the EPD and keeping the effective focal length constant changes the f-number from 5.73 to 6.139 following Equation 3.

4.2 CONFIGURATION

The traditional unobstructed telescope design uses off-axis conical surfaces. This system will be an improvement over the two-mirror telescope that suffers from astigmatism at high field angles. The telescope using off-axis conic surfaces optical performance was further improved by making the optical surfaces on-axis Zernike polynomials.

4.2.1 TMA using Conic Surfaces

4.2.1.1 Size and Shape of Conic Surfaces

The TMA system was designed to improve on the performance of the two mirror telescope. The primary mirror is the corner stone of the design and its radius of curvature is set at 1000 mm. The state of the art is a primary mirror with an f-number between 0.75 and 1.25. The conic constant is set to -1 (parabola) in the initial layout, shown in Figure 4-1, but it was allowed to vary in the optimization. The entrance pupil diameter (stop surface) was decentered by 220 mm, setting the f-number of the primary mirror in the range specified above.

The secondary mirror shares the same optical axis as the primary mirror. The distance between the primary and the secondary is specified to be 260 mm, ensuring the incoming rays are unobstructed. The radius of curvature is initially set at 400 mm, but allowed to vary in the optimization. Following the initial specifications, the conic constant was initially set to -2 (hyperbolic) and allowed to vary.

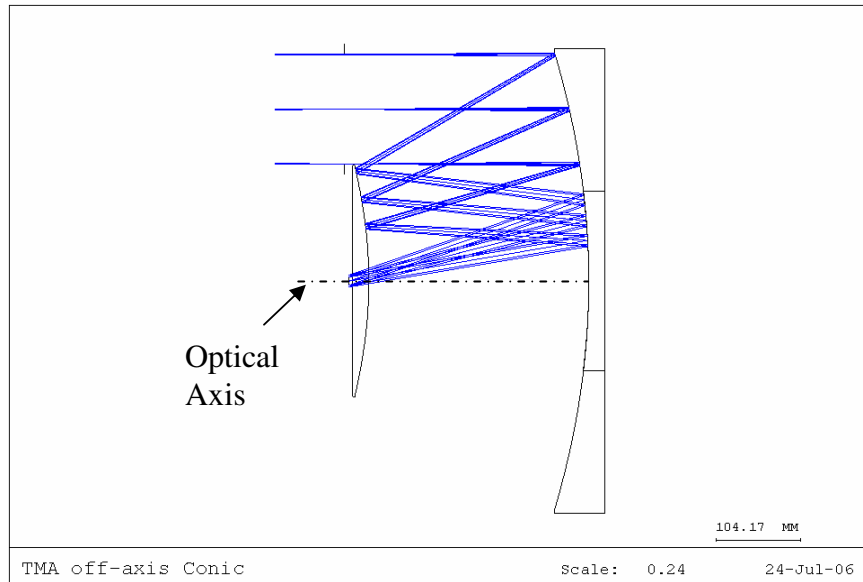


Figure 4-1: TMA using conic sections layout

The tertiary mirror is placed coplanar with the primary mirror. This might be an advantage where the primary and tertiary mirror could be machined from the same blank. The radius of curvature is calculated in Code V by the YZ paraxial marginal exit angle given in Equation 1. The conic constant is initially set at -2 (hyperbola) and allowed to vary in the optimization. The distance from the tertiary mirror to the image plane is determined by the paraxial image distance solve. This option sets the distance to the image surface such that the paraxial marginal rays or rays parallel to the optical axis intersect the image plane at the center.

4.2.1.2 Detector

The Canon digital camera with a CMOS detector was used to capture the images produced by the two mirror telescope. The detector is 44 mm behind the lens mounting flange in the camera. Optomechanical design of the two mirror telescope is geared towards accommodating that distance. Since the image is located behind the primary

mirror, the camera is mounted co-axially to the system with enough space to house the camera's configuration. For the TMA optical system, the image is below the secondary mirror and slightly behind it. Due to geometrical constraints, the detector's location with respect to the mounting flange and the lack of focus shift with the lens mounting flange, an astronomical camera, shown in Figure 4-2, was chosen for the TMA.

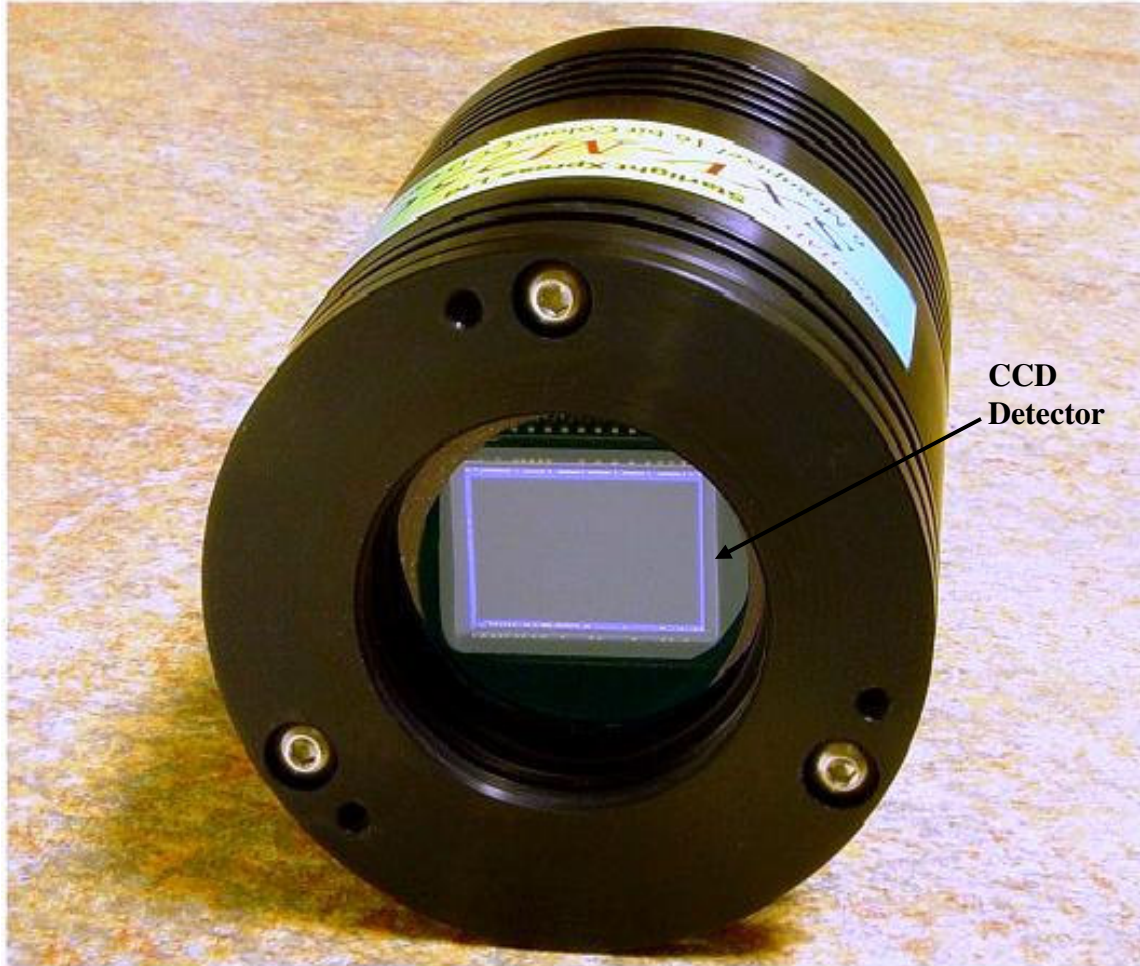


Figure 4-2: Starlight Xpress SXV-M25

The Starlight Xpress SXV-M25 has a high resolution, 6-megapixel CCD sensor with USB interface, single cable control. The detector is a 23.4 mm by 15.6 mm sensor with a square pixel size of 7.8 μm . The CCD detector has very similar specification to the

Canon CMOS detector. The camera is mounted on the telescope structure using a T-42 thread mount with the advantage of linear translation of the detector, or focus compensation.

4.2.1.3 Optimization of Conic Surfaces

The purpose of optimization is to generate the best optical design within a given set of physical and other constraints. The error function combines image error data into a single number that is minimized in the optimization routine. Code V provides four error function types, wavefront error variance is chosen in this case since the system performance will be measured using dual pass interferometry.

The image plane position is constrained to be behind the secondary mirror by at least 25 mm for mounting clearance of the Starlight detector. The effective focal length and f-number of the system are calculated by the paraxial marginal exit angle reflected from the third mirror using Equations 1 and 2. For this system, the detector and entrance pupil diameter set the f-number at 6.139 and the effective focal length at 859.5 mm. All specifications not explicitly selected are allowed to vary during optimization.

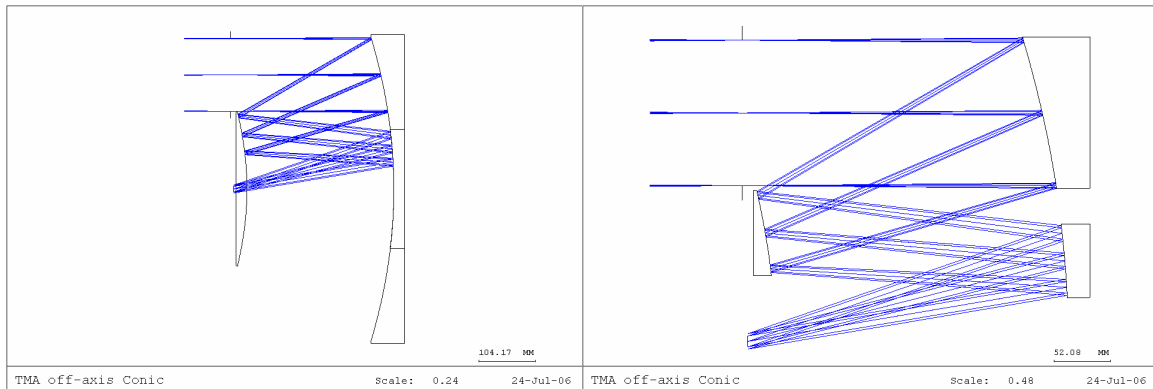
The optimization process produces a telescope with improved system performance. Table 4-1 shows the specific constraints applied in the optimization routine of the system and set through the automatic design dialog box shown in Figure 2-3 and discussed in Section 2.2.3. The system is evaluated using the field map option. This option presents various analysis results as a grid of field points, helping to visualize the variation of performance across the field of view or image format [7]. Plotting the wavefront

polynomial fit for coma and spherical aberration, shows a node for each option that is above the center of the field. A node or an aberration node, in the field of view represents a point where the particular aberration plotted is zero. The wavefront polynomial fit plot for astigmatism shows a node very close to the center. For optical systems without symmetry, Thompson [8] shows that two nodes exist in the astigmatism plot; the other node is outside the field of view. Constraints are added to the system by targeting the single coma and spherical aberration nodes on-axis and targeting the astigmatic nodes to the top and bottom of the field. Running the optimization routine, with the added constraints, does not improve the optical performance of the system due to the lack of variables in the conic surfaces.

Table 4-1: Off-axis conic optimization routine constraints

Constraint	Tab	Description - Code
Image Plane	Specific Constraints	Geometrically constrain the image plane to be at least 25 mm behind the secondary mirror $@g11 == (oal\ s'm-2'..'m-3') + (oal\ s'm-3'..i)$ $@g11 < -25$
Paraxial marginal exit angle	Specific Constraints	Set the exit angle at 0.08145 to constrain the f-number to 6.139 and the EFL to 859.5 mm
Coma node	User Constraints/Ray Definitions	Constrain the coma node to the center of the field of view $@z8 == ZFRCOEF(1,1,1,8,61,16,'enp')$ $@z8 = 0$
Astigmatic nodes	User Constraints/Ray Definitions	Constrain the astigmatic nodes to top and bottom of the field $@z5t == ZFRCOEF(1,3,1,5,61,9,'enp')$ $@z5t = 0;wtc\ 10$ $@z6t == ZFRCOEF(1,3,1,6,61,9,'enp')$ $@z6t = 0;wtc\ 10$

The 2-D plot of the three mirror anastigmat is shown in Figure 4-3, for the parent system (a) and the used apertures (b). The optical specifications of the three mirrors are tabulated in Table 4-2 and the full telescope fabrication data table output from Code V can be found in Appendix A. Distance between the primary-secondary and secondary-tertiary is set to 270 mm for clearance of incoming beams. The decenter and aperture of each surface is solved for in Code V real ray tracing data. The image plane is 294.860 mm away from the tertiary mirror where the chief ray has a zero height. To minimize the wavefront error over the field of view, the image plane is linearly translated to the best focus position. The distance between the tertiary mirror and the image plane best focus position is 295 mm, different from the on-axis focus position given in Table 4-2. The effective focal length of the finalized system is 859.5 mm.



a) Parent system

b) Used apertures only

Figure 4-3: TMA using rotationally symmetric conic surfaces

Table 4-2: Off-axis conic optical system specifications

	Radius of curvature (mm)	Conic Constant	Aperture Diameter (mm)	Surface decenter (mm)	Distance to next surface (mm)
Primary	-1000	-1.755	140	220	270
Secondary	-587.151	-5.801	79.5	104.409	270
Tertiary	-939.433	-5.197	68	77.508	294.86

4.2.2 TMA using Zernike Surfaces

4.2.2.1 Size and Shape of Freeform Surfaces

An alternative design for the three mirror anastigmat using freeform surfaces is shown in Figure 4-4. This design maintains the f-number, field of view, entrance pupil diameter, and focal length of the conic TMA. The optical surfaces in this design are converted to on-axis Zernike polynomial surface types. The Zernike surface is a 10th order standard Zernike polynomial added to a base conic and the equation used is the following:

$$z = \frac{cr^2}{1 + \sqrt{1 - (1+k)c^2r^2}} + \sum_{j=1}^{66} C_{j+1}Z_j \quad (4)$$

Where z is the sag of the surface parallel to the z-axis

c is the vertex curvature

k is the conic constant

Z_j is the j-th Zernike polynomial (range of j: 1 to 66)

C_{j+1} is the coefficient for Z_j

The set of Zernike polynomials through the 10th order can be found in Appendix E.

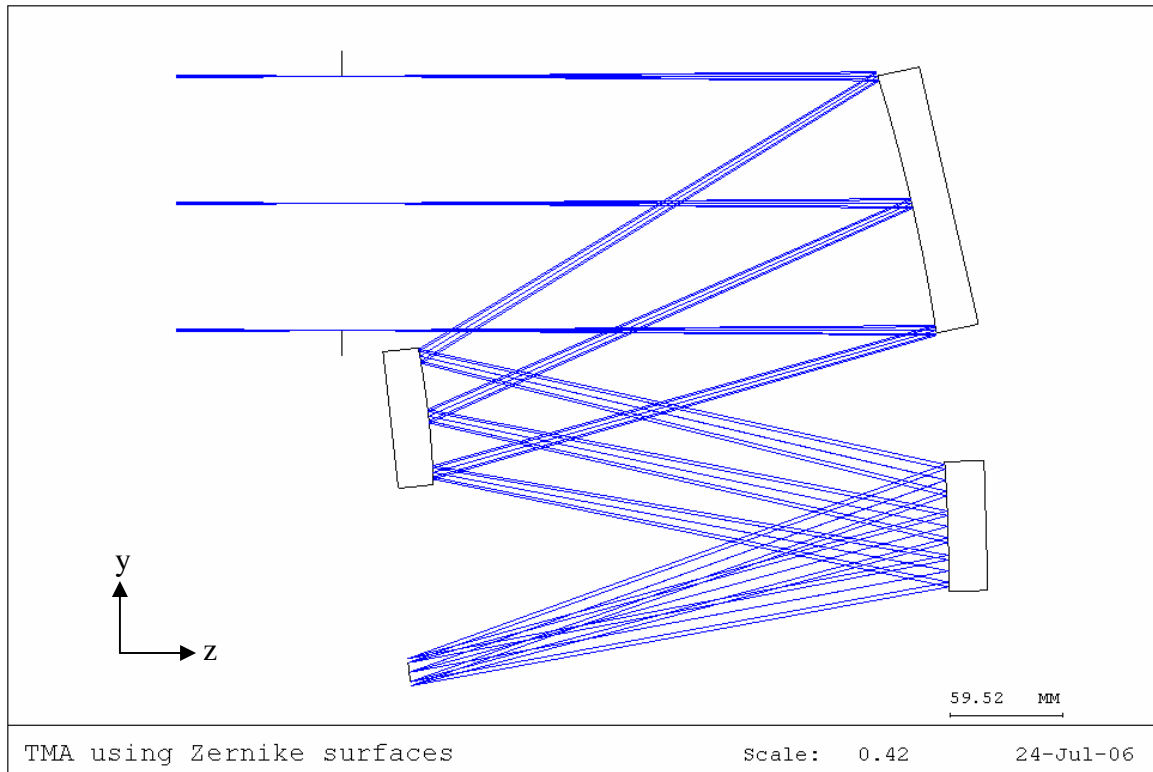


Figure 4-4: TMA using on-axis Zernike surfaces

Using the TMA off-axis conic design as a baseline, entrance pupil diameter decenter is deleted leading to an on-axis rotationally symmetric system. Then, surface properties of the three mirrors are changed from conical surfaces to freeform surfaces or Zernike polynomial surfaces keeping the same radius of curvatures and conic constant values. Zernike polynomial coefficients (C_{j+1}), 4th to 26th terms, are set to variable. Primary and secondary mirrors radii of curvature are set as variable, while the tertiary mirror's radius of curvature is solved for by paraxial marginal exit angle given in Equation 1 to set the f-number of the system at 6.139 and the EFL at 859.5 mm.

To realize an unobstructed telescope design, the mirrors are tilted about their optical axis. “Decenter and Bend” option in Code V tilts the optical components about their optical axis with the new optical axis collinear with the normal vector at the vertex of the surface [9]. Positive α -tilt is rotation about the x-axis in the counter-clockwise direction. First, the primary mirror is tilted by 12.7° , placing the secondary mirror below the entrance pupil. Next, the secondary mirror is tilted by -15.3° , placing the tertiary mirror below the primary mirror. Finally, the tertiary mirror is tilted by 10.2° , placing the image below the secondary mirror. The image plane α -tilt is set as variable to solve for the best orientation minimizing the wavefront error in the optimization routine. Distance between primary-secondary and secondary-tertiary mirrors is set to 280 mm. Distance between tertiary mirror and image is variable.

4.2.2.2 Optimization of Freeform Surfaces

The starting point of each optical design is a design goal and initial specifications set prior to running an optimization routine that leads to a finalized system. Using the off-axis conic TMA design as a starting point with the changes to on-axis freeform surfaces provide the baseline for optimization of the TMA using Zernike surfaces. Of the four error function types provided by Code V, wavefront error variance is chosen since the system is diffraction limited.

The system is optimized by minimizing the wavefront error and geometrically constraining the vertical distance between the secondary mirror and the entrance pupil diameter to be at least 10 mm. Table 4-3 shows the specific constraints applied in the optimization routine of the system and set through the automatic design dialog box

shown in Figure 2-3 and discussed in Section 2.2.3. The field map option, in Code V, is used to evaluate the system at the image plane. The wavefront polynomial fit for spherical aberration displays a node located on the horizontal axis. The polynomial fit for coma shows a node located below the axis at $(-0.1^\circ, 0.2^\circ)$ field angle. Polynomial fit for astigmatism displays two nodes, as shown in Thompson's paper [8], for non-rotationally symmetric systems. The two nodes are in the field of view and are located on the horizontal axis at $(\pm 0.2^\circ, 0^\circ)$. To minimize these optical aberrations thus the wavefront error, further optimization is executed with additional constraints applied to the system.

Improving the performance of the TMA, more constraints are added to the optimization routine. To minimize the coma and spherical aberration over the field of view, the coma node is constrained to be at the origin of the circular field of view. This also constrains the spherical aberration node to be at the center of field. Astigmatic nodes are shifted from their original location to $(\pm 0.35^\circ, 0^\circ)$ on the horizontal axis. Astigmatism increases radially outwards from both nodal positions. Placing the nodes at this intermediate position decreases the astigmatic average over the field of view while placing the nodes at the edge increases the average.

The 3-D wireframe plot of the optimized TMA using on-axis freeform optics is shown in Figure 4-5. Optical specifications of the system are tabulated in Table 4-4 and the full telescope fabrication data tables output from Code V can be found in Appendix A. The primary and secondary base optical surfaces are hyperboloids while the tertiary mirror

base is an ellipsoid. The values of Zernike coefficients will be discussed in the surface decomposition Section 4.5.2. Distance between tertiary mirror and the image plane on-axis focus position is 294.453 mm. To minimize the wavefront error over the field of view, the image plane is linearly translated to the best focus position. Distance between the tertiary mirror and the image plane best focus position is 294.596 mm, different from the on-axis focus position given in Table 4-4. The mirror tilts are shown in Table 4-4, and the image is tilted by -9.574° to compensate for optical aberrations.

Table 4-3: Zernike surface optimization routine constraints

Constraint	Tab	Description - Code
Vertical distance between secondary mirror and EPD	User Constraints/Ray Definitions	Geometrically constrain the secondary mirror to be at least 10 mm away from the EPD $@slope == (m\ r3\ f9\ s2\ g2)/(n\ r3\ f9\ s2\ g2)$ $@b == -@slope*(z\ r3\ f9\ s2\ g2)+(y\ r3\ f9\ s2\ g2)$ $@clear == @slope*(z\ r2\ f3\ s4\ g2) +@b - (y\ r2\ f3\ s4\ g2)$ $@\ clear = 10\ mm$
Coma node	User Constraints/Ray Definitions	Constrain the coma node to the center of the field of view $@z8 == ZFRCOEF(1,1,1,8,61,16,'enp')$ $@z8 = 0$
Astigmatic nodes	User Constraints/Ray Definitions	Constrain the astigmatic nodes to $(\pm 0.35^\circ, 0^\circ)$ of the field $@z5t == ZFRCOEF(1,7,1,5,61,9,'enp')$ $@z5t = 0;wtc\ 10$ $@z6t == ZFRCOEF(1,8,1,6,61,9,'enp')$ $@z6t = 0;wtc\ 10$

Table 4-4: TMA using Zernike surfaces optical system specifications

	Radius of curvature (mm)	Conic Constant	Aperture Diameter (mm)	Distance to next surface (mm)	α -tilt (°)
Primary	-1003.328	-1.613	140	280	12.374
Secondary	-556.276	-5.769	72	280	-18.646
Tertiary	-865.999	1.399	68	294.453	14.184
Image	-	-	15.1	-	-9.571

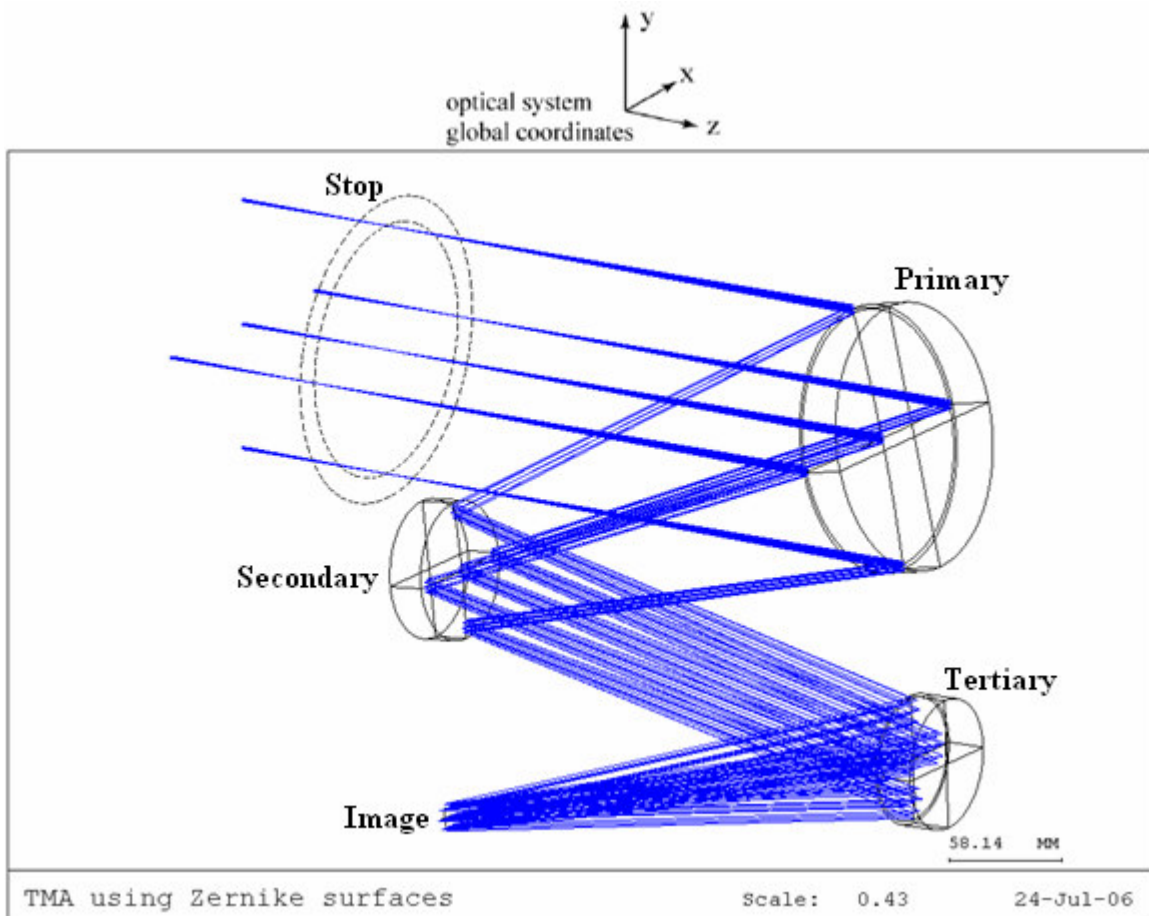


Figure 4-5: TMA using Zernike surfaces optical system

4.3 THEORETICAL PERFORMANCE OF CONIC AND FREEFORM TMA SYSTEMS

Both TMA systems are evaluated in Code V to predict theoretical performance of the telescopes. Helium-Neon light ($\lambda = 632.8$ nm) is used for analysis. Performance measures used to evaluate the two mirror telescope will also be used to assess both TMA systems and compare them to each other. The performance of either TMA is at least 3 times better than the two-mirror telescope described earlier. Both telescopes have different characteristics, the on-axis Zernike polynomial system shows impressive improvement in performance over the off-axis conic system. The following section illustrates different ways to assess performance of both systems including

- Aberrations
- Wavefront Analysis
- Modulation Transfer Function
- Spot Diagram

4.3.1 Aberrations

System performance is depicted using field map option plots of specific aberrations provided in Code V. Aberrations express system performance by isolating each of the specific errors (Seidel aberrations) that have an impact on the wavefront error. Seidel aberrations or third-order aberrations are derived from Hamilton's Characteristic Function (wavefront aberration function) and are the dominant errors of optical systems [6]. Similar to the two mirror telescope, astigmatism, coma, and spherical aberration are

the Seidel terms that will be discussed and compared for both TMA systems in the following sections.

4.3.1.1 Astigmatism

For the on-axis Zernike polynomial TMA, the field map plot for astigmatism is shown in Figure 4-6. Astigmatism, for a non-rotationally symmetric system, has two nodes or point of zero aberration error. The two nodes can either be located in the field of view or outside the field. For the on-axis Zernike polynomial TMA system, astigmatic nodes are located at $(\pm 0.35^\circ, 0^\circ)$ field angles. Astigmatic error increases from these points outward with a maximum value of 0.012 waves at the top edge of the field. Average astigmatic error is 0.0056 waves over the field of view.

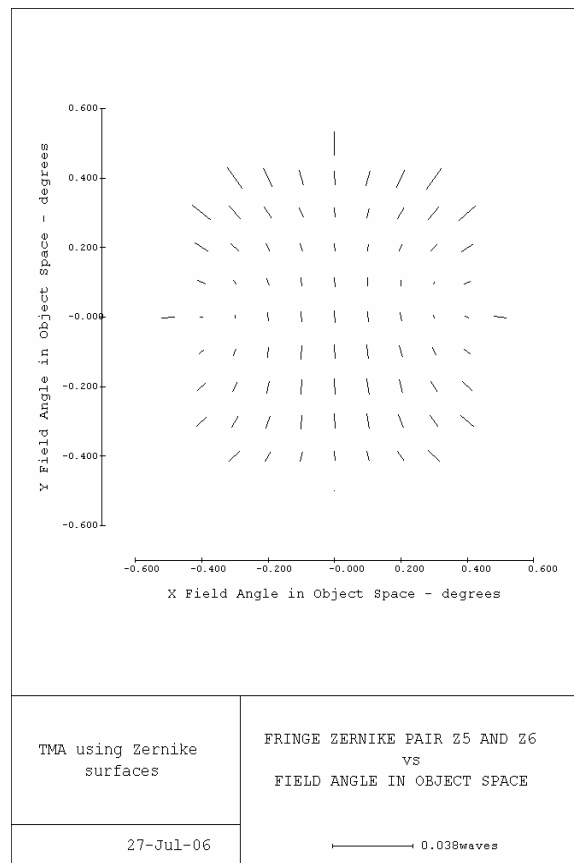
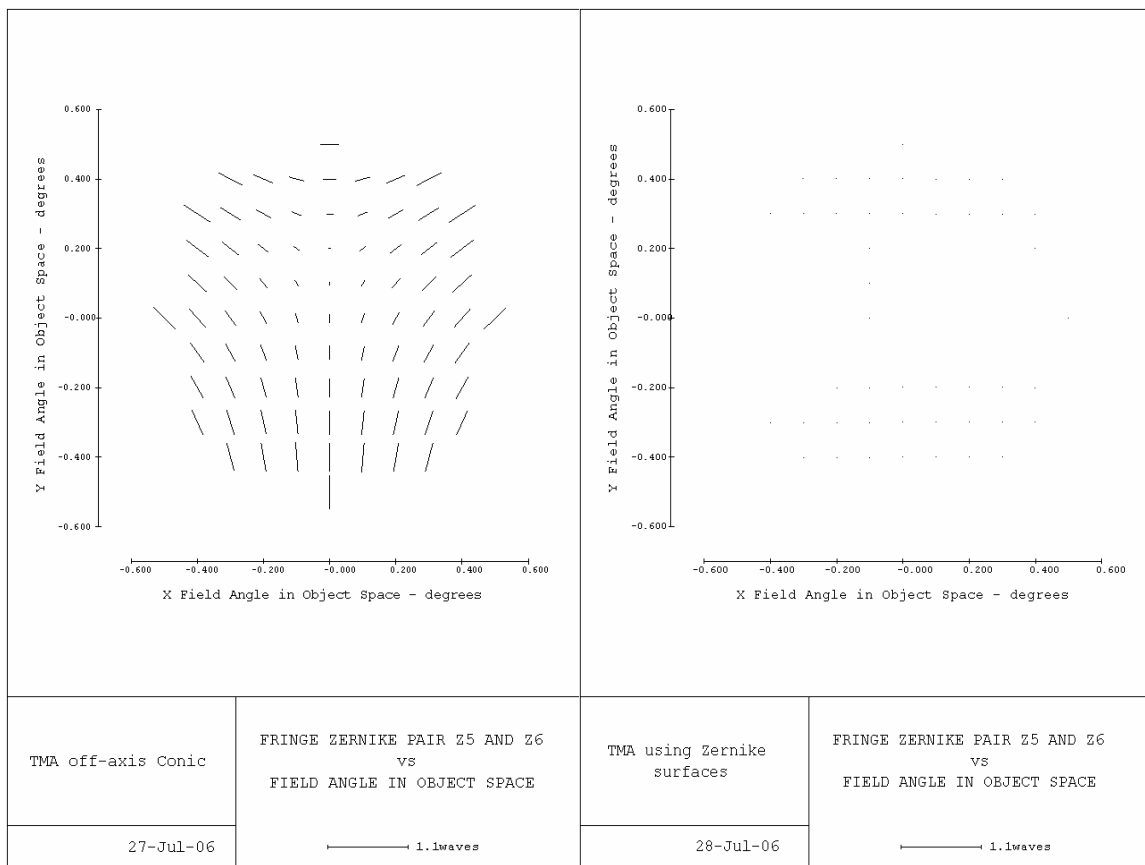


Figure 4-6: Field map of astigmatism (Z5 and Z6) for Zernike polynomial TMA

Astigmatic error for both systems is compared in Figure 4-7, using the same scale. Compared to the off-axis conic system, the on-axis Zernike polynomial astigmatism is nearly imperceptible. TMA using off-axis conics is also non-rotationally symmetric but only one node is in the field of view located at $(0^\circ, 0.2^\circ)$ field angle. The second node is outside the field of view. In the optimization routine, placing the second node in the field of view didn't improve the optical performance due to the lack of variables in the system. Astigmatic error increases outward from the node to reach a maximum of 0.437 waves at -0.5° vertical field angle, with an average error of 0.27 waves over the field of view.



(a) Off-axis conic TMA

(b) On-axis Zernike polynomial TMA

Figure 4-7: Astigmatism across the field of view plotted on the same scale

4.3.1.2 Coma

Coma is the variation of magnification with aperture, as described in the two mirror telescope Section 2.3.1.2. Comatic error for the on-axis Zernike polynomial TMA over the field of view is shown in Figure 4-8. The coma node (zero error) is at the center of the field as intended in the optimization routine. Error increases from that point outwards to reach a maximum of 0.0056 waves at the top of the field. The average error is 0.00186 waves over the field of view.

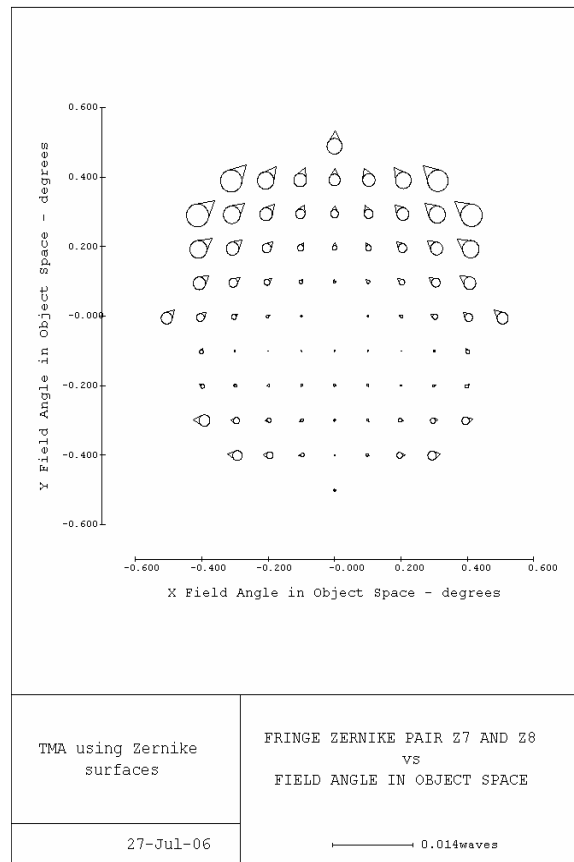
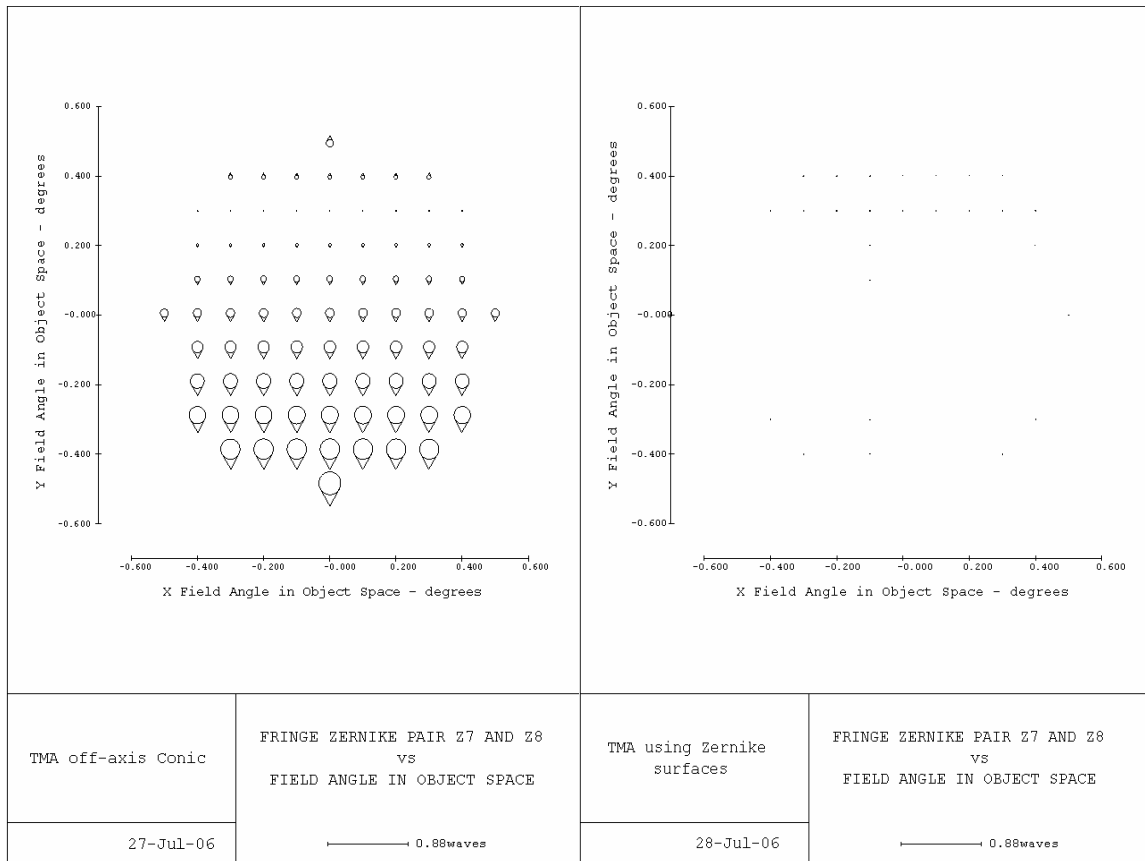


Figure 4-8: Field map of coma (Z7 and Z8) for the on-axis Zernike polynomial TMA

Comatic error for both TMA systems is compared in Figure 4-9. Off-axis conic TMA average error is 0.15 waves over the field of view. The average comatic error for the off-

axis conic system is 80 times the average error for the on-axis Zernike system. The improvement in comatic error is easily noticed in Figure 4-9 where the on-axis Zernike coma error is almost invisible or the image is coma-free. Minimum error of 0.008 waves occurs above the center of the field, coincident with other aberration nodes as expected. Error increases from that point outwards to reach a maximum of 0.358 waves at -0.5° , bottom of the field.



(a) Off-axis conic TMA

(b) On-axis Zernike polynomial TMA

Figure 4-9: Coma across the field of view plotted on the same scale

4.3.1.3 Spherical Aberration

Spherical aberration is change in the focus point for off-axis rays in an optical system.

Figure 4-10 shows spherical aberration for the on-axis Zernike polynomial TMA.

Spherical node is located on the horizontal axis as constrained in the optimization routine. Spherical aberration increases in the y-direction to reach a maximum of 0.00293 waves at 0.5°, top of the field. Average error over the field of view is 0.00008 waves.

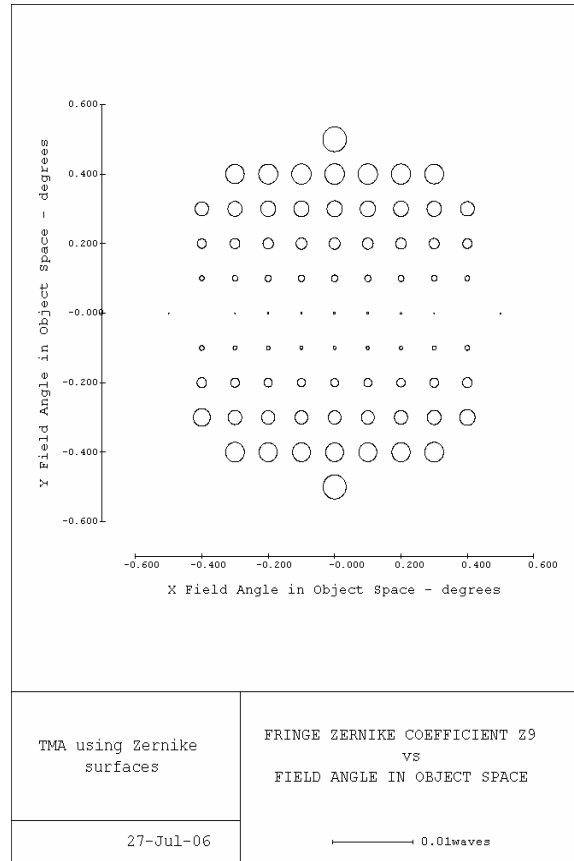
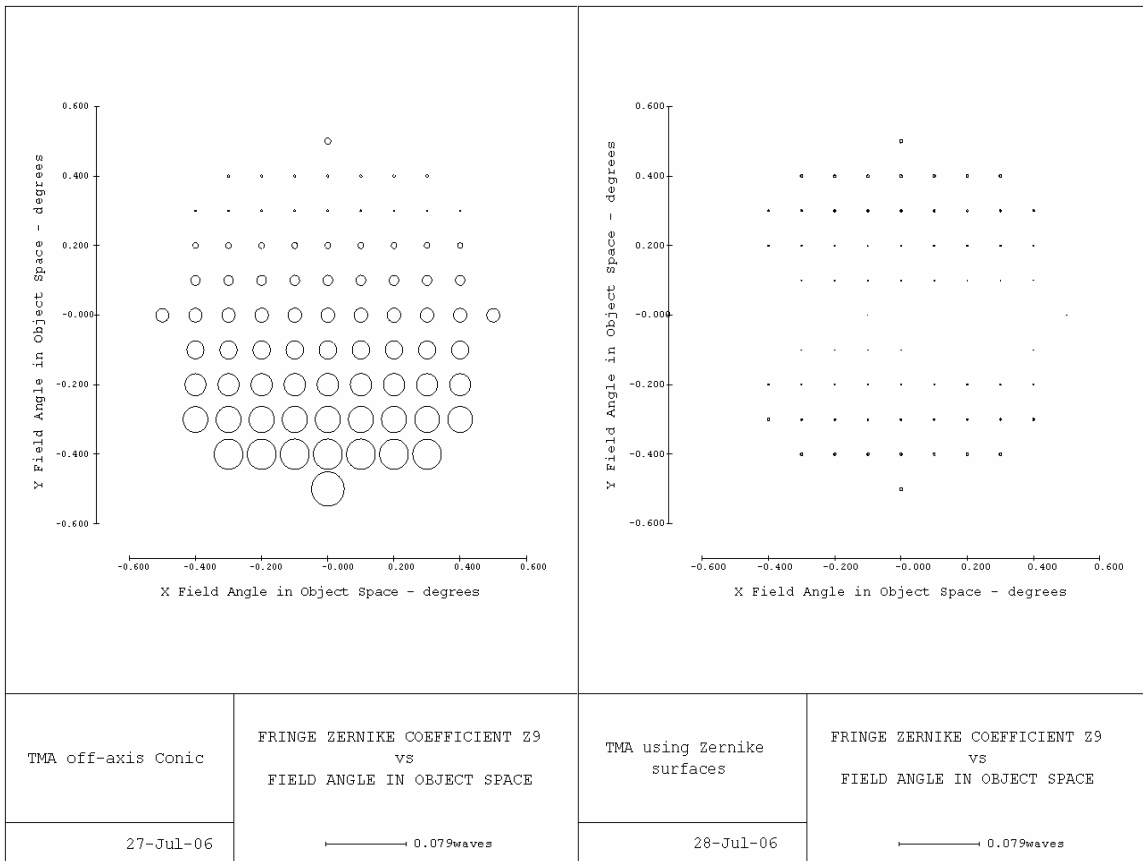


Figure 4-10: Field map of spherical aberration (Z9) for on-axis Zernike polynomial system

Spherical aberration for both systems is compared in Figure 4-11, utilizing the same scale. Improvement from off-axis conic TMA to on-axis Zernike polynomial TMA is apparent in the spherical aberration plots. Average error over the field of view for off-axis conic system is 0.013 waves, 157 times worse than on-axis Zernike system. Minimum

spherical error, for off-axis conic system, is above the center field at the 0.3° horizontal line. Error increases to reach a maximum of 0.032 waves at the bottom of the field.



(a) Off-axis conic TMA

(b) On-axis Zernike polynomial TMA

Figure 4-11: Spherical aberration across the field of view plotted on the same scale

4.3.2 Wavefront Analysis of Conic and Freeform TMA Systems

Wavefront error plot for Zernike polynomial TMA over the full field of view, shown in Figure 4-12, gives the best description of the performance of the system. Wavefront error is a combination of the errors as the light moves through the system from stop surface to the image plane. Minimum error is 0.003 waves located at $(\pm 0.4^\circ, 0^\circ)$ near the location of astigmatic nodes. Error increases from these points inward, towards the center of the field, and outwards away from both field points. The error at the worst point in the field

is 0.011 waves at the center of the field, with an average of 0.0063 waves over the field of view.

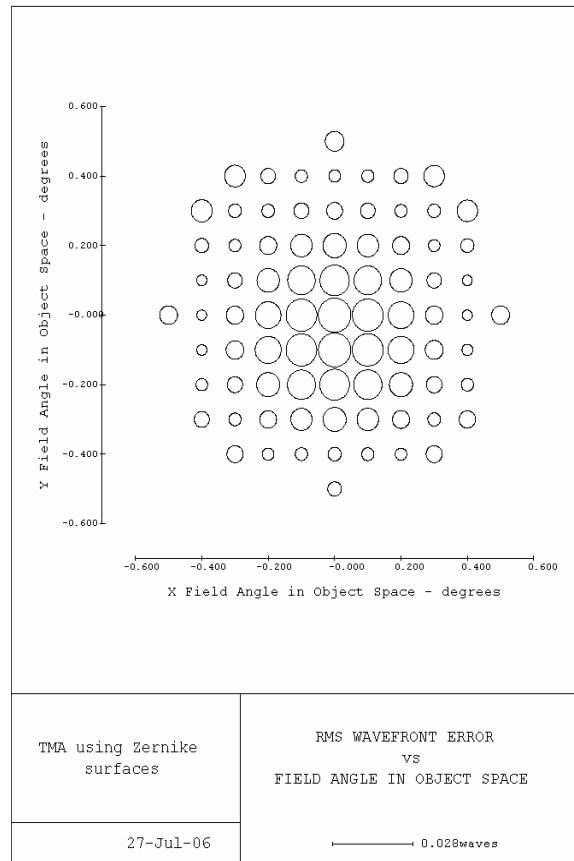
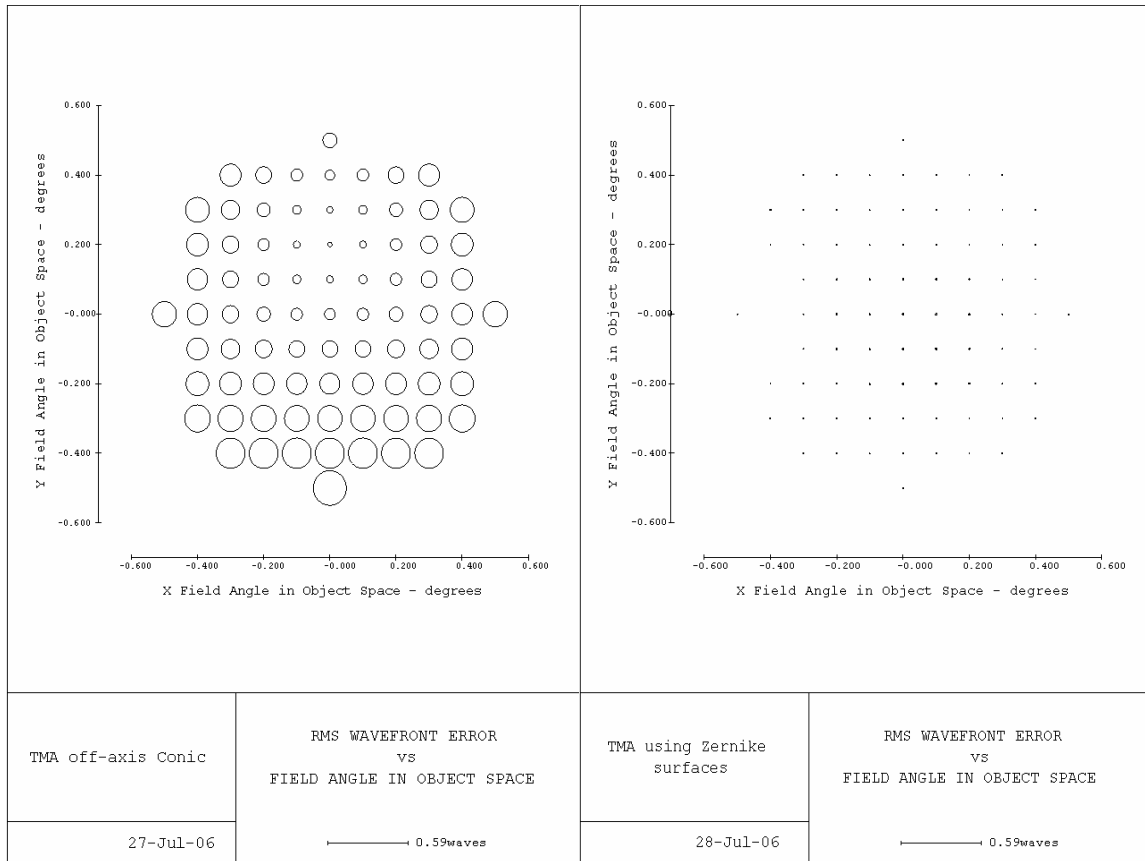


Figure 4-12: RMS wavefront error for Zernike TMA across the field of view

The wavefront error over the full field of the two TMA systems is compared in Figure 4-13 with both plots having the same scale. The diameters of the circles indicated the magnitude of the error at each field location. For the off-axis conic TMA, wavefront error is shown in Figure 4-13(a). The smallest error occurs in the center of the field at (0°, 0.2°) and the minimum error is 0.032 waves. The location of the minimum error is due to the system being off-axis where the different aberration nodes for this system are located above the optical axis. The error increases radially outwards to reach a maximum of

0.242 waves at -0.5° . The average wavefront error over the field of view is 0.134 waves. Compared to the on-axis Zernike system, average wavefront error over the field of view is 0.0063 waves or 21 times improvement over the off-axis conic TMA. This is noticed in Figure 4-13, where at the common scale, wavefront error magnitudes of freeform design are nearly invisible.



(a) Off-axis conic TMA

(b) On-axis Zernike polynomial TMA

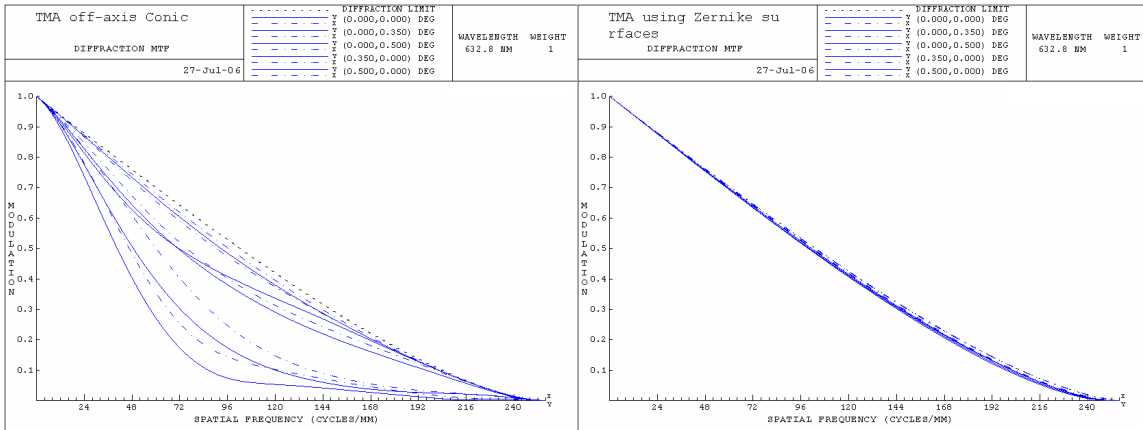
Figure 4-13: RMS wavefront error as field angle over the aperture of the telescope

4.3.3 Modulation Transfer Function

Modulation Transfer Function (MTF) is another measure of the performance of optical systems consisting of a series of alternating light and dark bars [2]. The MTF plot gives a modulation value for contrast with 1.0 being perfectly black and white boundaries and

0.0 being totally gray as a function of the spatial frequency. As described in Section 2.3.3, diffraction is an optical effect that limits the resolution or optical performance of a system and is plotted as the right-most dotted line in Figure 4-14. The off-axis conic system MTF plot is shown in Figure 4-14(a) and the best performance is the center of the field where it is almost diffraction limited, or 96 cycles/mm at 50% modulation. Other field angles in the system do not exhibit a sudden drop-off in modulation found in the RC design as shown in Figure 2-13. The lowest MTF is at the 0.5° field angle showing 33 cycles/mm at 50% modulation. The Starlight Xpress CCD detector threshold or Nyquist frequency (64 cycles/mm) is determined by dividing twice the pixel size by 1. Nyquist frequency is the highest resolution the CCD sensor can detect. At this frequency, modulation varies between 23% for the worst field (0.5°) to 67% at the best field (0°) for the off-axis conic TMA system.

The on-axis Zernike polynomial system MTF plot is shown in Figure 4-14(b). Performance is essentially perfect; even at the worst location in the field it is diffraction limited. At 50% modulation, system frequency varies between 99 – 104 cycles/mm. At the Nyquist frequency of the detector (64 cycles/mm), modulation varies between 68% and 69%. Compared to the off-axis conic system, the on-axis Zernike system MTF shows an impressive improvement in overall performance.



(a) Off-axis conic TMA

(b) On-axis Zernike polynomial TMA

Figure 4-14: MTF for both TMA optical systems

4.3.4 Spot Diagram of Conic and Freeform TMA Systems

The spot diagram shows the dispersion of rays at different field angles on the image plane. The spot diameter gives a visual impression of image quality for each field angle. Image quality is related to the spot size at a particular field angle where the smaller the spot diameter the better image quality. The spot diagram of the on-axis Zernike polynomial TMA at best focus position is shown in Figure 4-15. The smallest RMS spot diameter is $0.336 \mu\text{m}$ at $(\pm 0.4, 0^\circ)$ field angles in the field of view, coincident with the location of the minimum wavefront error. The RMS spot size is highest at the center of the field, $0.876 \mu\text{m}$, with an average of $0.551 \mu\text{m}$ over the field of view.

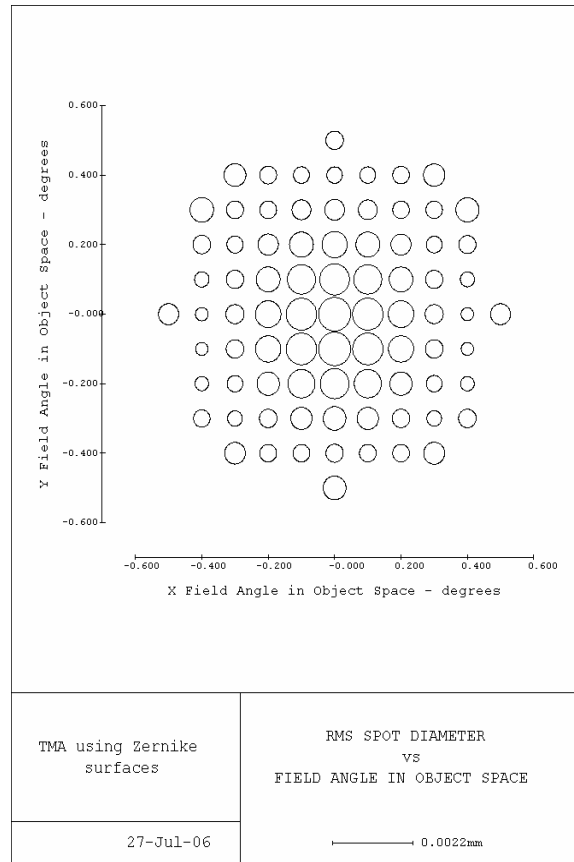
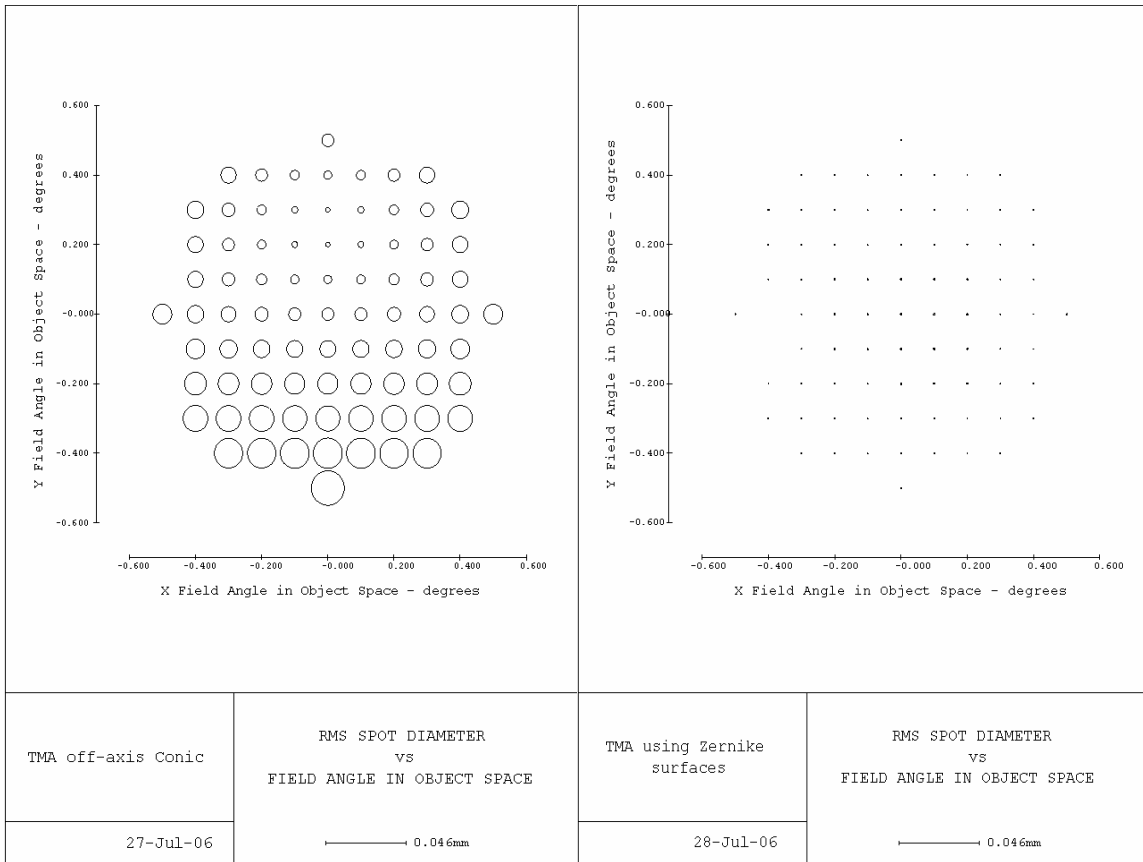


Figure 4-15: RMS spot diagram across the field of view for the Zernike polynomial system

RMS spot diagram for both TMA systems is compared in Figure 4-16, using the same scale. The on-axis Zernike polynomial system shows smaller spot diameters compared to the off-axis conic system demonstrating an improved system performance. Spot diagram of the off-axis conic system at best focus position is shown in Figure 4-16(a). The smallest RMS spot diameter is 2.5 μm at the location of the best focus (0° , 0.2°), and it increases radially outward to reach a value of 18.8 μm the bottom of the field (-0.5°). The average spot diameter over the field of view is 9.4 μm compared to 0.551 μm for the on-axis Zernike polynomial system.



(a) Off-axis conic TMA

(b) On-axis Zernike polynomial TMA

Figure 4-16: RMS spot diagram for both TMA systems plotted using the same scale

4.4 SENSITIVITY ANALYSIS

The goal of the design is to create a snap-together assembly to simplify the assembly task as was done for the two mirror system in Section 3.3. The Rayleigh criterion or limit is when the wavefront error does not exceed one-quarter wave about a selected image point for the image to be perfect [2]. To achieve Rayleigh criterion with a snap-together assembly, sensitivity analysis for both TMA systems is conducted in Code V.

The telescope system will be machined using a diamond turning machine (DTM) with a fast tool servo (FTS). Both TMA systems will be analyzed using the same degrees of

freedom. Linear translation of the detector is used as a compensator. Manufacturing errors and their perturbations will affect the performance of the system and an estimate of the sources and magnitudes of these errors are as follows:

- Radius error on three optical surfaces due to surface fabrication error on DTM, equivalent to half-wave ($\pm \lambda/4$)
- Astigmatic error on three optical surfaces due to surface fabrication error on DTM with FTS, equivalent to half-wave ($\pm \lambda/4$)
- Spacing error between primary-secondary and secondary-tertiary mirrors due to telescope frame fiducial surface fabrication error on DTM, equivalent to $\pm 2 \mu\text{m}$
- Tip and tilt of three mirrors due to telescope frame fiducial surface fabrication error on DTM, equivalent to $\pm 2 \mu\text{m}$ at edge of mirrors
- Decentration of three mirrors in 2 dimensions (x and y) due to fiducial features fabrication error on the mirror substrates and telescope frame, equivalent to $\pm 2 \mu\text{m}$
- Rotation of three mirrors about z-axis due to fiducial features fabrication error on the mirror substrates and telescope frame, equivalent to three times spindle encoder resolution of the diamond turning machine ($\pm 0.027^\circ$)

Sensitivity analysis is run in Code V with the tolerances specified above and image plane translation as a compensator. Results of the simulation for the off-axis conic TMA at different field angles is shown in Table 4-5, and complete sensitivity analysis Code V output can be found in Appendix B. For each field angle, theoretical wavefront error measured in waves is listed. Additionally, the predicted wavefront error due to

manufacturing errors is computed and subsequent error with image plane focus shift as a compensator. The effect of manufacturing tolerances on the RMS wavefront error is shown in Figure 4-17. The predicted wavefront error with and without compensation are almost identical and overlap in Figure 4-17. If the image plane is linearly translated by 14.5 μm in a direction towards the tertiary mirror, radius error on the three optical surfaces will be compensated. Image compensation slightly reduces the predicted wavefront error; thus, radius fabrication errors have small influence on the wavefront error. While analyzing the sensitivity analysis output found in Appendix B, astigmatic errors on the three optical surfaces have the highest impact on the predicted RMS wavefront error for the different field angles.

Table 4-5: Change in RMS wavefront error with manufacturing tolerances ($\lambda = 632.8\text{nm}$),
for off-axis conic TMA

Field Number	Field Angle	Theoretical Wavefront	Predicted Error without Compensation	Predicted Error with Compensation	Compensation (focus change)(μm)
1	0°, 0°	0.0777	0.233	0.2326	14.5
2	0°, 0.35°	0.058	0.2294	0.2291	14.5
3	0°, 0.5°	0.1035	0.2644	0.2642	14.5
4	0.35°, 0°	0.1322	0.2855	0.2852	14.5
5	0.5°, 0°	0.1762	0.33	0.3297	14.5
6	0.35°, 0.35°	0.1638	0.3241	0.3239	14.5
7	0.35°, -0.35°	0.1963	0.3373	0.3371	14.5
8	0°, -0.35°	0.1948	0.337	0.3368	14.5
9	0°, -0.5°	0.2416	0.383	0.3828	14.5
10	-0.35°, 0°	0.1322	0.2855	0.2852	14.5
11	-0.5°, 0°	0.1762	0.33	0.3297	14.5
12	-0.35°, 0.35°	0.1638	0.3241	0.3239	14.5
13	-0.35°, -0.35°	0.1963	0.3373	0.3371	14.5

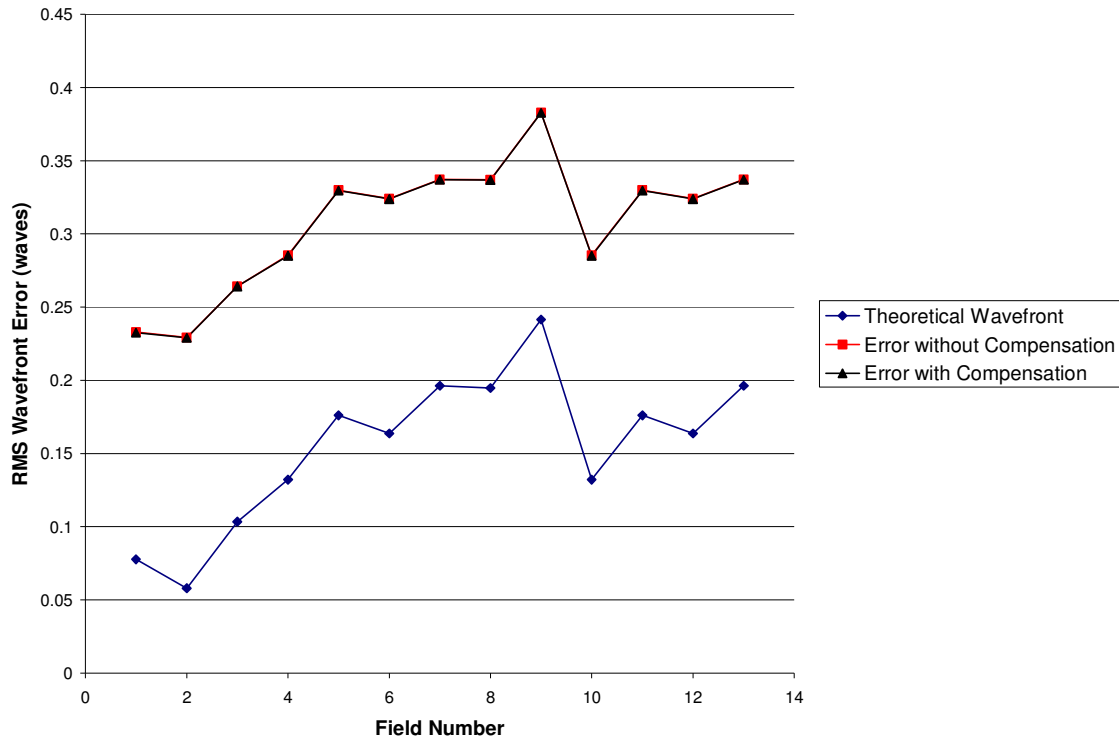


Figure 4-17: RMS Wavefront Error sensitivity analysis for the off-axis conic TMA

Sensitivity analysis is also performed for the on-axis Zernike polynomial TMA using the same manufacturing tolerances and image plane compensation described earlier in this section. Results of the simulation for different field angles is shown in Table 4-6 following the same format used to present the off-axis conic TMA results, with complete sensitivity analysis Code V output found in Appendix B. Effect of fabrication tolerances on the RMS wavefront error is also shown in Figure 4-18. The predicted wavefront error with and without compensation are almost identical and overlap in Figure 4-18. A 7.352 μm image plane translation in a direction towards the tertiary mirror compensates for the radius errors on the three optical surfaces, where the influence is small compared to other fabrication errors. Compensation optimizes focus for the different field angles and the

small change in focus has a minimal effect on the predicted wavefront error. Analyzing the sensitivity analysis output found in Appendix B, astigmatic errors on the three optical surfaces have the highest impact on the predicted wavefront error.

Table 4-6: RMS wavefront error change ($\lambda = 632.8$ nm), for on-axis Zernike polynomial TMA

Field Number	Field Angle	Theoretical Wavefront	Predicted Error without Compensation	Predicted Error with Compensation	Compensation (focus change)(μm)
1	0°, 0°	0.0112	0.2214	0.2213	7.352
2	0°, 0.35°	0.0045	0.2203	0.2203	7.352
3	0°, 0.5°	0.0065	0.2195	0.2194	7.352
4	0.35°, 0°	0.0045	0.2177	0.2176	7.352
5	0.5°, 0°	0.0061	0.2167	0.2166	7.352
6	0.35°, 0.35°	0.007	0.2197	0.2196	7.352
7	0.35°, -0.35°	0.0054	0.2175	0.2174	7.352
8	0°, -0.35°	0.0062	0.2188	0.2187	7.352
9	0°, -0.5°	0.0047	0.219	0.2189	7.352
10	-0.35°, 0°	0.0044	0.2177	0.2177	7.352
11	-0.5°, 0°	0.0061	0.2167	0.2166	7.352
12	-0.35°, 0.35°	0.0071	0.2192	0.2191	7.352
13	-0.35°, -0.35°	0.0053	0.2178	0.2177	7.352

The on-axis Zernike polynomial TMA average RMS wavefront error, theoretical performance, shows 21 times performance improvement over the off-axis conic TMA. Off-axis conical system fabrication error analysis shows the sensitivity of the system interpreted in the RMS wavefront error and the predicted error exceeds the Rayleigh criterion. The on-axis Zernike polynomial system fabrication error analysis is more sensitive than the off-axis conic TMA where the predicted RMS wavefront error increases by an average of 38 times from the theoretical performance. Although the on-

axis Zernike polynomial system is more sensitive to fabrication errors, the predicted wavefront error is below the Rayleigh criterion yielding a perfect image.

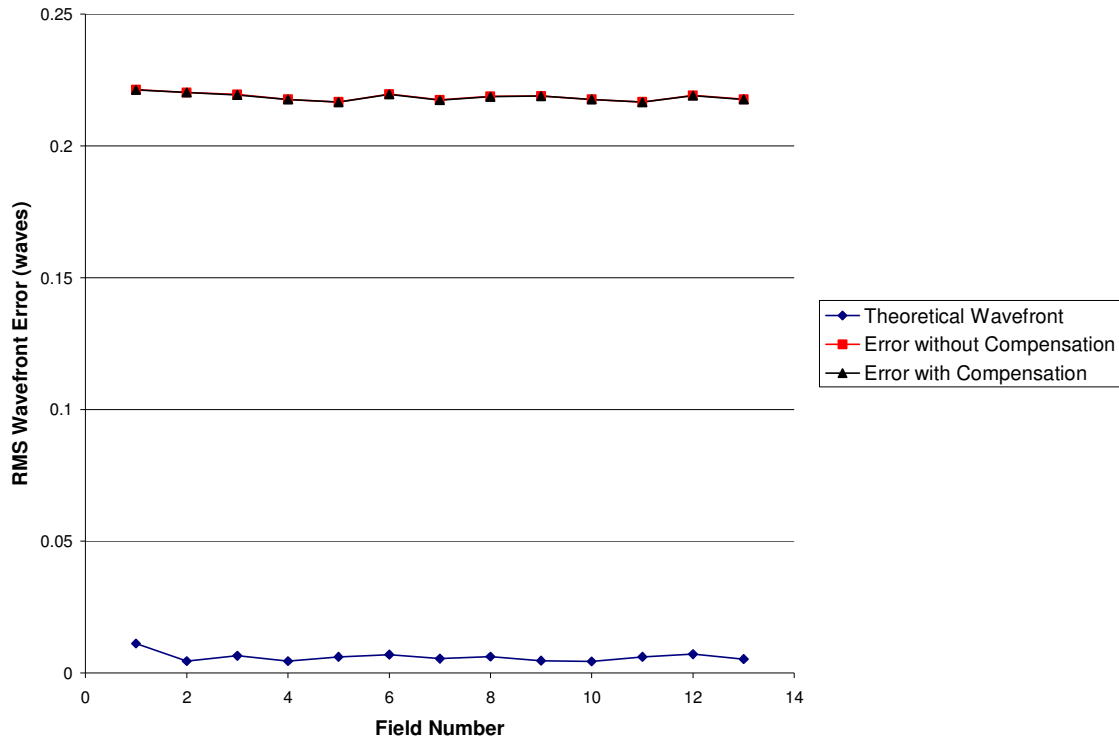


Figure 4-18: RMS Wavefront Error sensitivity analysis for the on-axis Zernike Polynomial TMA

4.5 SURFACE DECOMPOSITION

The Precision Engineering Center (PEC) has two diamond turning machines, a Rank-Pnemo ASG 2500 and a Rank Taylor Hobson Nanoform 600. Both are hydrostatic oil bearing T-lathes with an air bearing spindle mounted on one of the linear axes. Two fast tool servos are available to supplement either machine for non-rotationally symmetric turning. A 400 μm range Variform and a 40 μm FLATS (Fast Linear Actuating Tool Servo, a PEC design) are available. Surface decomposition into a rotationally symmetric

and non-rotationally symmetric component provides feedback to the designer on surface fabrication with the machine capabilities provided at the PEC.

4.5.1 Off-axis Conic TMA

Off-axis conic surfaces are not rotationally symmetric about the center of their respective apertures, except their defining optical axis. The optical surfaces can either be machined off-axis around their defining optical axis or machined on-axis around the center of their respective apertures. Off-axis machining is constrained by the machine's ability to accommodate the off-axis aperture diameters and the need for a different mounting fixture for each mirror. Machining the optical surfaces on the diamond turning machine with a fast tool servo requires a description of the conical surface translated on-axis and tilted. Decomposition of off-axis conic segment of a conic surface into a rotationally symmetric component and a non-rotationally symmetric residual has been developed by the PEC [11]. The result is a functional description of the conical surfaces, along with coefficients to a radial polynomial that is the best-fit asphere minimizing the Non-Rotationally Symmetric (NRS) sag.

NRS sag of a surface is a direct measure of the difficulty of its fabrication using this fabrication technology. It is the difference between the conical surface and the best fit asphere. A decomposition program, nrsgen, written in C by Garrard [12], creates a sag table for the entire surface. Table 4-7 shows the decomposition parameters and results for the off-axis conics. The asphere error values in Table 4-7 give an estimate of the maximum sag difference between the true best fit asphere and surface generated by

connecting the points of the asphere grid sag table with straight lines. The general equation of an optical surface of revolution about the z-axis can be written as [29]

$$z = \frac{cs^2}{1 + \sqrt{1 - (k+1)c^2s^2}} + A_4s^4 + A_6s^6 + A_8s^8 + A_{10}s^{10} + \dots \quad (5)$$

where $s^2 = x^2 + y^2$ and $c = \frac{1}{r} = \frac{1}{\text{radius of curvature}}$. Also, A_i are the aspheric

deformation constants, and K is the conic constant. The NRS shape is described in cylindrical coordinates by substituting the NRS coefficients from Table 4-7 into Equation 6.

$$z_{NRS} = d_1 + d_2\rho\cos(\theta) - \sqrt{d_3 + d_4\rho\cos(\theta) + d_5\rho^2 + d_6\cos^2(\theta)} \quad (6)$$

The shapes of the NRS components of the primary, secondary, and tertiary mirrors are shown in Figure 4-19 through Figure 4-21. For all three mirrors the FTS will reverse directions twice per spindle revolution. The Variform FTS has a maximum speed capacity of 140 mm/sec. By calculating the maximum slope in the circumferential direction along the surfaces in Figure 4-19 through Figure 4-21 and dividing these quantities into 140, the maximum rotational speed for machining can be determined. For all three mirrors, the slopes are less than 2 mm/sec. Therefore, the Variform limit is not reached until the spindle speed exceeds 4200 rpm ($140/2*60$), which is more than twice as fast as the maximum Nanoform spindle speed.

Table 4-7: Off-axis conic TMA decomposition

	Off-Axis Conic TMA		
	Primary	Secondary	Tertiary
R (radius of curvature)(mm)	-1000	-587.151127	-939.432788
K (conic constant)	-1.754657	-5.801289	-5.197043
Aperture radius (mm)	70	39.75	34
Decenter (Y) (mm)	220	104.40911	77.50807
NRS Sag (mm)	0.186188	0.19121	0.021322
Tilt (YZ)	0.212065	-0.162682	0.080917
Decenter (Z)(mm)	23.982967	-8.955286	3.174892
Asphere Sag (mm)	2.350362	-1.231344	0.603868
Asphere Error	0.000004	0.000002	0.000001
Asphere Coefficients			
A2	4.800E-04	-7.830E-04	5.231E-04
A4	-7.488E-11	2.230E-09	-5.958E-10
A6	2.336E-17	-1.270E-14	1.357E-15
A8	-9.109E-24	9.049E-20	-3.865E-21
A10	3.978E-30	-7.218E-25	1.232E-26
A12	-1.862E-36	6.169E-30	-4.211E-32
A14	9.127E-43	-5.523E-35	1.508E-37
A16	-4.627E-49	5.114E-40	-5.581E-43
NRS Coefficients			
D1	-1.539E+03	1.374E+02	-2.296E+02
D2	-5.333E-01	1.994E-01	-1.006E-01
D3	2.368E+06	1.888E+04	5.272E+04
D4	1.644E+03	5.522E+01	4.630E+01
D5	1.477E+00	2.151E-01	2.402E-01
D6	1.696E-01	7.041E-03	1.959E-03

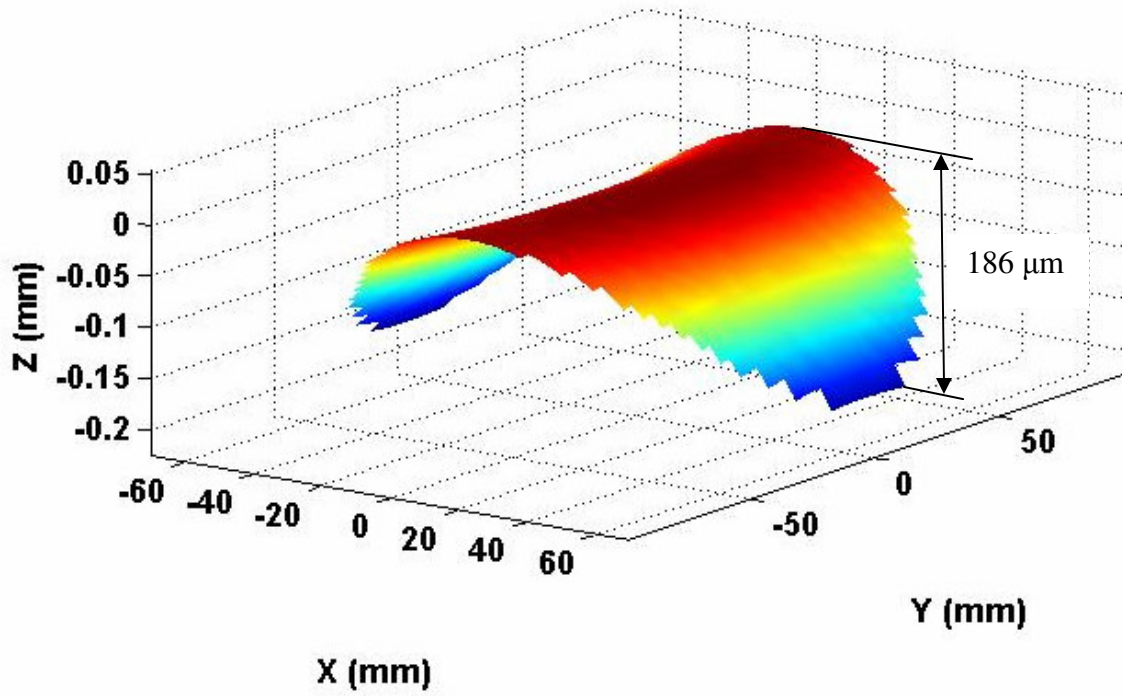


Figure 4-19: NRS component (P-V = $186 \mu\text{m}$) of off-axis conic TMA Primary mirror

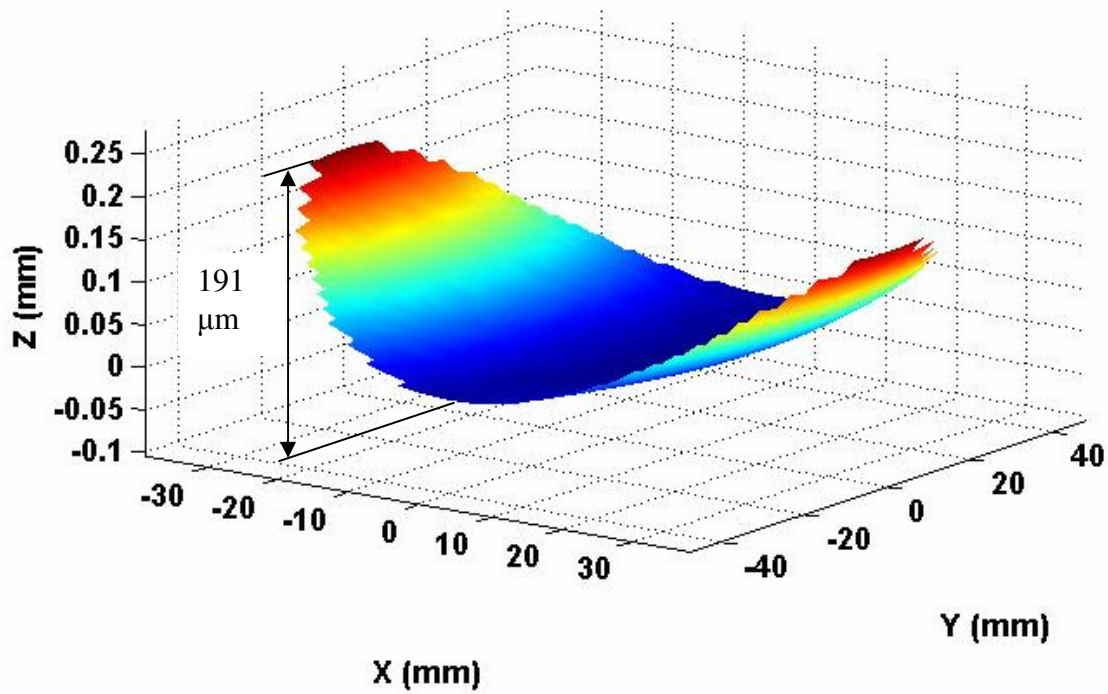


Figure 4-20: NRS component (P-V = $191 \mu\text{m}$) of off-axis conic TMA Secondary mirror

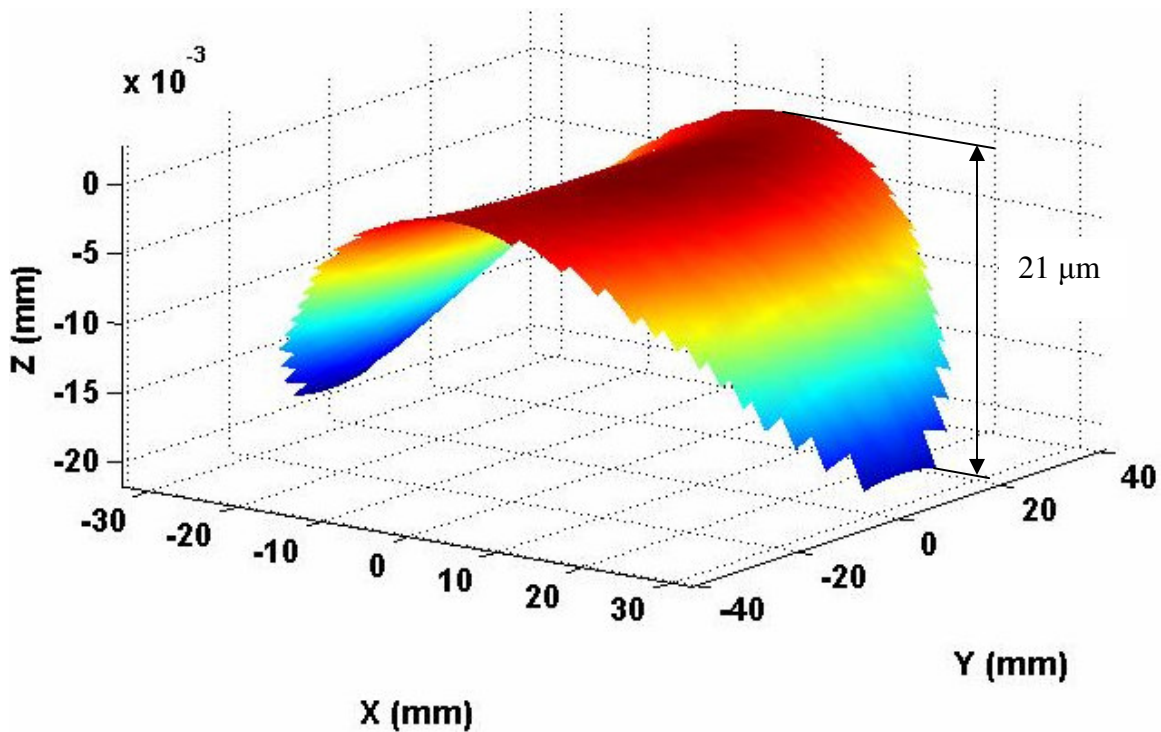


Figure 4-21: NRS component ($P-V = 21 \mu\text{m}$) of off-axis conic TMA Tertiary mirror

4.5.2 On-axis Zernike Polynomial TMA

The on-axis Zernike polynomial TMA mirrors are analyzed using the fabrication table output of Code V. The data output reveals a maximum sag difference from a base radius sphere. The machining process of the mirrors would be to machine this base radius sphere into each mirror, check the optical surface on the laser interferometer, then add the non-rotationally symmetric (NRS) sag on the surface through the Fast Tool Servo (FTS). The shape and location parameters of the three mirrors are given in Table 4-8. Primary and secondary mirrors are hyperboloids while the tertiary mirror is an oblate ellipsoid deformed by Zernike coefficients 4 through 26 discussed in the optical surface Equation 4, Section 4.2.2.1. The tilt (YZ) angle (radians) specifies the pointing angle of the normal vector from the vertex of each mirror surface in the YZ plane.

Table 4-8: Zernike polynomial TMA decomposition (Coefficients defined in Appendix E)

	Zernike Polynomial		
	Primary	Secondary	Tertiary
R (radius of curvature)(mm)	-1003.328496	-556.27642	-865.999075
K (conic constant)	-1.61273	-5.768838	1.39954
Aperture radius (mm)	70	36	34
Zernike Coefficients			
Z4 (Z1=Z2=Z3=0)	-3.350E-06	1.300E-05	1.544E-05
Z5	6.809E-07	-1.015E-05	-5.148E-06
Z6	-2.562E-07	-9.782E-07	5.433E-07
Z7	1.850E-10	2.217E-09	1.596E-09
Z8	-2.308E-11	-4.659E-10	-5.083E-10
Z9	4.150E-08	3.109E-07	5.289E-08
Z10	-2.446E-08	-3.817E-07	-2.182E-07
Z11	3.361E-12	-1.021E-10	-2.906E-11
Z12	6.338E-12	2.783E-10	7.073E-11
Z13	-2.719E-12	-2.123E-10	2.114E-10
Z14	-2.759E-14	1.854E-12	1.087E-12
Z15	6.004E-14	2.851E-13	4.866E-13
Z16	-3.891E-17	-1.190E-15	7.848E-16
Z17	2.013E-17	-2.549E-16	1.157E-15
Z18	-2.994E-17	-1.624E-15	-2.034E-15
Z19	-8.724E-16	-6.149E-13	-2.136E-13
Z20	-2.772E-15	1.230E-13	-1.432E-13
Z21	-1.355E-15	-7.020E-15	-4.419E-14
Z22	-6.216E-18	-7.045E-16	-7.105E-16
Z23	-2.017E-18	-1.950E-16	-7.307E-16
Z24	-6.394E-19	-7.824E-16	-3.212E-17
Z25	4.183E-18	1.271E-15	8.669E-17
Z26	-9.923E-20	-1.951E-17	-1.902E-17
NRS Sag (mm)	0.084049	0.109937	0.040490
Tilt (YZ)	0.215964	-0.325427	0.247554
Sphere Radius (mm)	-1003.328496	-556.276472	-865.999075

Fitting a sphere to each surface reduces the NRS sag to a maximum of 109.9 μm for the secondary mirror. Figure 4-22 through Figure 4-24 show the NRS component remaining

after removal of the sphere. The NRS sag plots provide freeform surfaces fabrication feedback to the designer within the capabilities at the PEC using the diamond turning machine and the Variform fast tool servo (400 μm range). NRS sag plot of tertiary mirror, shown in Figure 4-24, resembles a saddle shape or astigmatism. Additional tilt of the mirrors may further reduce the NRS sag. This would change the mounting plane angle with respect to the optical housing by an equal amount.

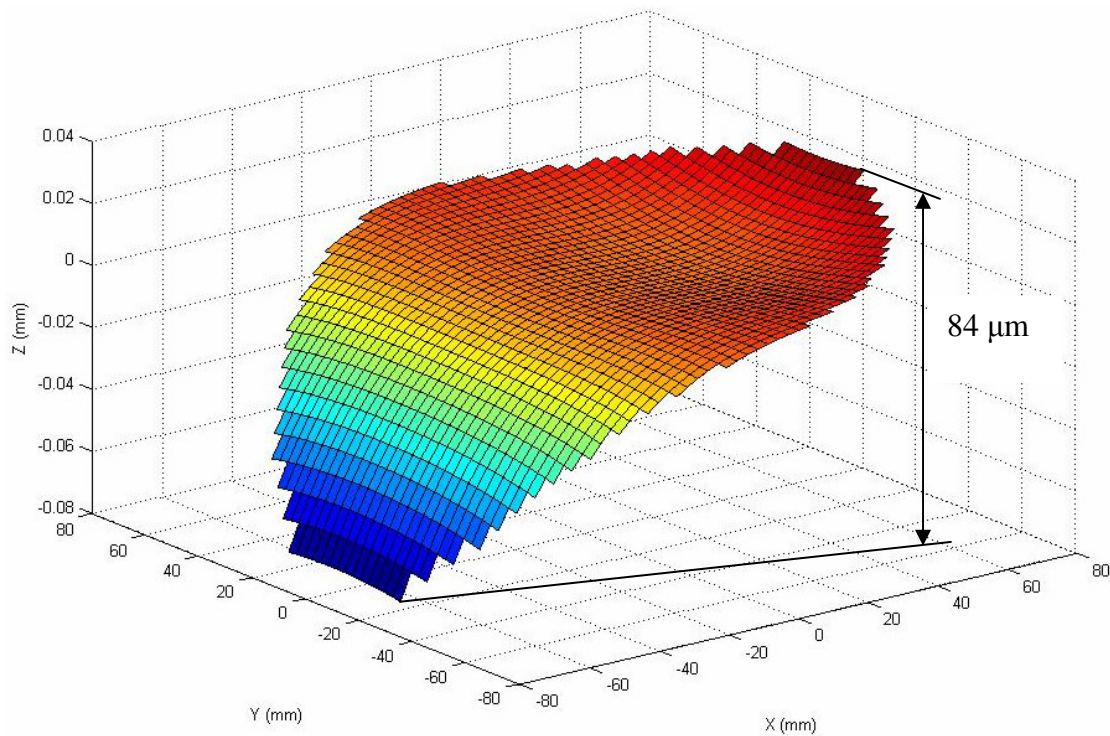


Figure 4-22: NRS component (P-V = 84 μm) of Zernike TMA Primary mirror

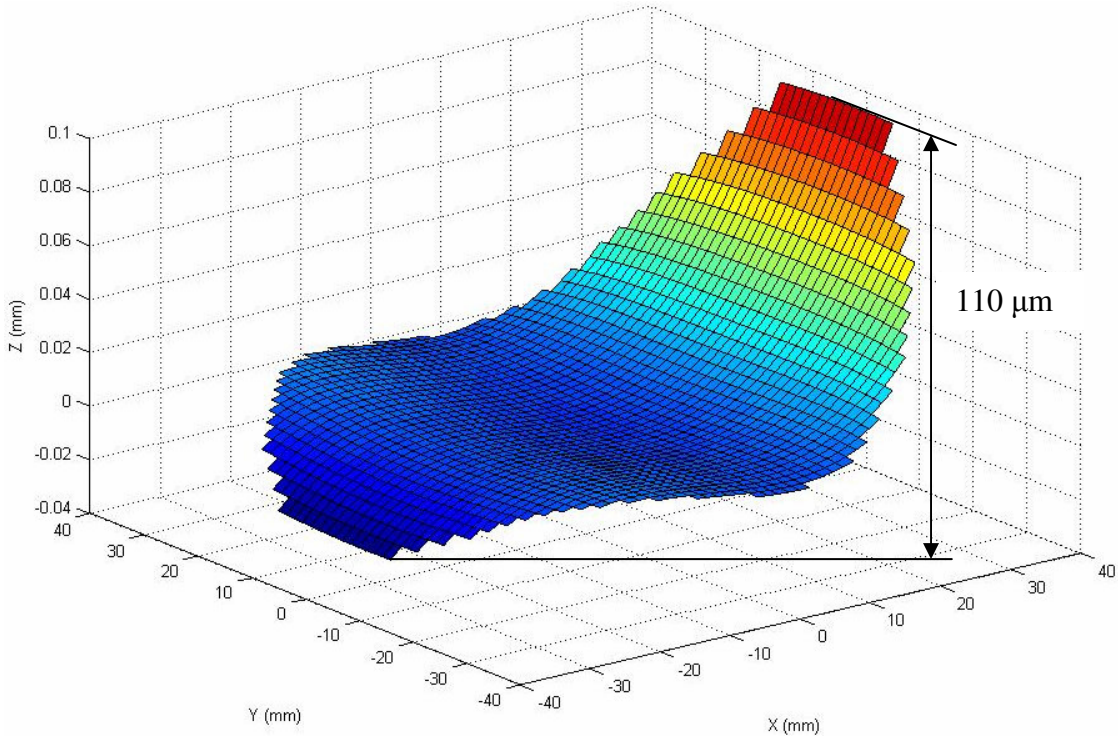


Figure 4-23: NRS component (P-V = 110 μm) of Zernike TMA Secondary mirror

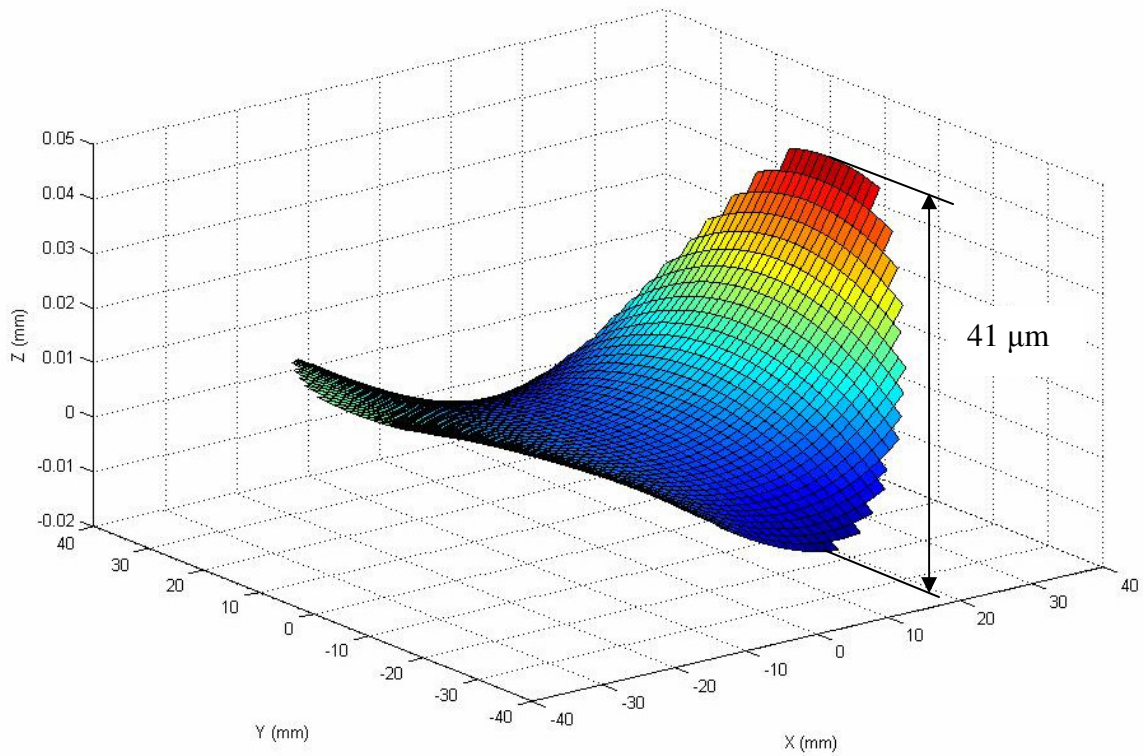


Figure 4-24: NRS component (P-V = 41 μm) of Zernike TMA Tertiary mirror

4.6 COMPARISON OF CONIC AND FREEFORM TMA SYSTEMS

The eccentric conic TMA has the advantage that its surfaces may be tested with the laser interferometer, using relatively simple test configurations. The on-axis Zernike polynomial freeform surfaces require a computer generated hologram (CGH) to be tested using interferometric equipment. Stylus profilometer or an ultra-precision CMM can measure freeform surfaces, provided machines have sufficient accuracy. Freeform surfaces present a more challenging task to measure than off-axis conics.

Both TMA systems optical surfaces can be machined on the diamond turning machine with a Fast Tool Servo (FTS) to compensate for the sag difference. Fast tool servos that have a small range produce better surface finish over the same range than using a FTS with a longer range. On-axis Zernike polynomial surfaces require smaller servo excursions (110 μm) than the off-axis conical surfaces (191 μm). In addition, performance of the on-axis Zernike TMA shows impressive improvement over the off-axis conic TMA as described in the theoretical performance Section 4.3. Although, sensitivity analysis shows the on-axis Zernike system more sensitive to fabrication errors, overall performance is remarkably better than the off-axis conic system. Therefore, the opto-mechanical TMA design is directed towards designing the structure that maintains the optical elements aligned during ground tests and launch for the on-axis Zernike polynomial system.

5 OPTOMECHANICAL DESIGN OF TMA

5.1 INTRODUCTION

Non-rotationally symmetric optical surfaces for telescope objectives have been shown to produce remarkable improvements in performance over off-axis conic sections and rotationally symmetric surfaces. However, non-rotationally symmetric surfaces add complexity to the opto-mechanical design because of the added degree of freedom over rotationally symmetric two mirror systems that come with performance gain.

Based on the on-axis Zernike polynomial optical system, opto-mechanical design concept for the three mirror telescope is a snap-together telescope with diamond machined optical surfaces with special emphasis on the component orientation and assembly onto the housing. The opto-mechanical design specifications are based on a missile application and must withstand vibration and high acceleration loading. Standard methods use pins, holes, slots and machined flats to locate the optical component on an intermediate plate. Flexure mounts integrated in the component mount the optical structure onto the housing [23].

The goal is to package the optical elements such that the appropriate degrees of freedom are constrained but the elements are not over constrained and thus prone to distortion. The implementation of snap-together systems using conventional methods requires high assembly tolerances. Integrating the machining of fiducial and optical surfaces with a fast tool servo should permit tolerances of less than 5 μm that is in conjunction with

Raytheon's assembly tolerances. Industry practice can produce on the order from 5 μm to 1 μm assembly tolerances with measurement and tweaking. The following section addresses the issues of material, fiducial and mounting features and telescope frame.

5.2 MATERIAL

Similar to the two-mirror telescope, components of the TMA system are to be machined from aluminum 6061-T6 alloys. Aluminum alloys are lightweight, strong and are widely used in optical instrument structures [18]. This material presents a balanced compromise between material strength necessary for structural rigidity and material properties to create surface finishes adequate for infrared imaging. Optical and fiducial surfaces are machined utilizing diamond turning process capable of producing high fidelity optical surfaces in many non-ferrous materials. The potential surface finish of 6061 Aluminum is not as good as Aluminum electrodeposited plated surfaces but is acceptable for the infrared needs of this telescope [28]. Fabrication of mirrors and telescope frame from 6061-T6 aluminum allows system expansion and contraction proportionally with a temperature gradient. Thus, thermal instability does not affect the optical performance of the system.

5.3 MIRROR STRUCTURE

5.3.1 Lightweight Design for Fabrication

The design of the mirror structure is crucial in achieving a snap-together telescope. Each of the three mirrors is designed to incorporate the same fiducial and mounting features. The thickness of each mirror structure is based on the aspect ratio; that is, the ratio of the

mirror diameter to the thickness. Using the aspect ratio simulation conclusions discussed in the two-mirror optomechanical Section 3.4.2, a part with an aspect ratio between 3 and 4 provides minimal distortion values when mounted on the vacuum chuck for machining. Distortions of the optical surfaces can occur when the mirror component is mounted on the vacuum chuck of a diamond turning machine for fabrication.

The primary mirror has an aperture diameter of 150 mm and 10 psi vacuum pressure is used to mount the part on the chuck. This pressure is equivalent to 1218 N mounting force applied on the back surface of the primary mirror and can cause significant amount of distortion if both mounting surfaces are not flat. Reducing the vacuum pressure is an option but not recommended since damage can occur to the part while machining. Another way of reducing the optical surface distortion is to apply the same pressure (10 psi) over a smaller contact area. Thus, a 75 mm diameter raised mounting plane on the back of the primary mirror minimizes the distortion of the optical surface when mounted on the vacuum chuck as shown in Figure 5-1. Aspect ratio is reduced from 6 to 3 by using a 75 mm raised mounting plane, for a 25 mm thick part, instead of the whole aperture. Figure 5-2 shows a comparison between a 25 mm thick primary mirror using its full aperture (150 mm) mounted on the vacuum chuck and a 75 mm diameter region. Optical surface distortion is reduced from 891 nm to 99.7 nm respectively.

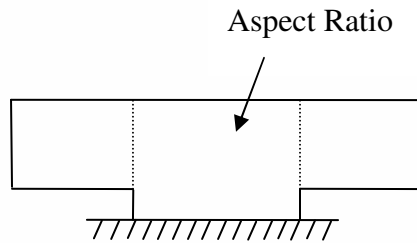


Figure 5-1: Schematic of a mirror substrate with a reduced mounting area

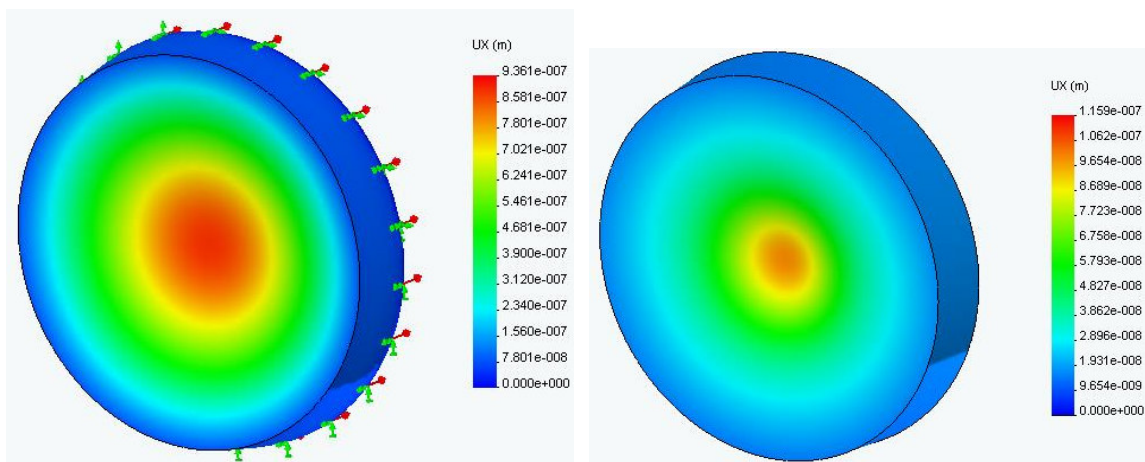


Figure 5-2: Distortion of the optical surface when the entire back is used (left) and when only a region is used (right) to mount onto the vacuum chuck

Figure 5-3 shows the primary mirror structural design. The part is 150 mm in diameter and 25 mm thick at the center and increases to reach a maximum thickness of 27.45 mm at the edge. The raised mounting plane is 75 mm in diameter. Light-weighting the part reduces the mass and therefore the deflection due to gravitational loading. Radial struts connect the outer fiducial ring to the inner mounting plane. Two different thickness struts are used; the 10mm thick strut provides support for the mounting clamp contact area.

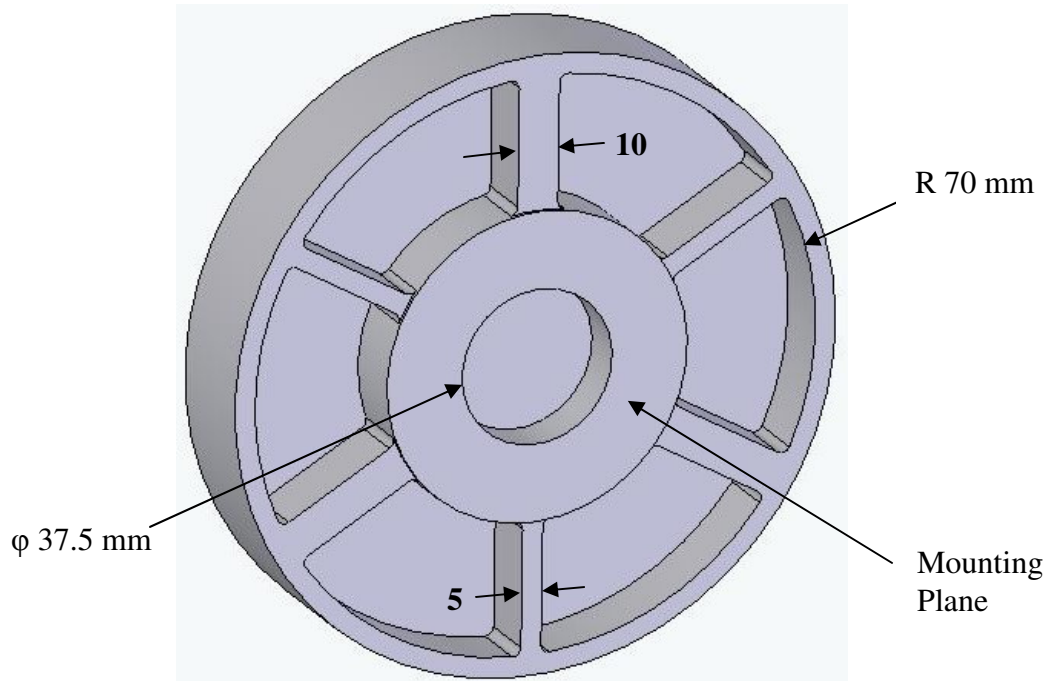
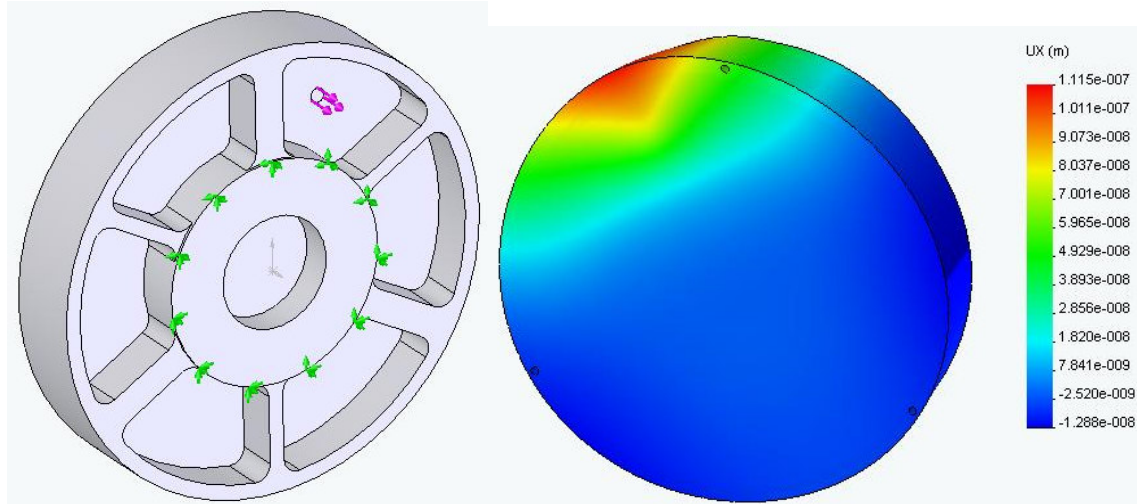


Figure 5-3: Lightweight primary mirror

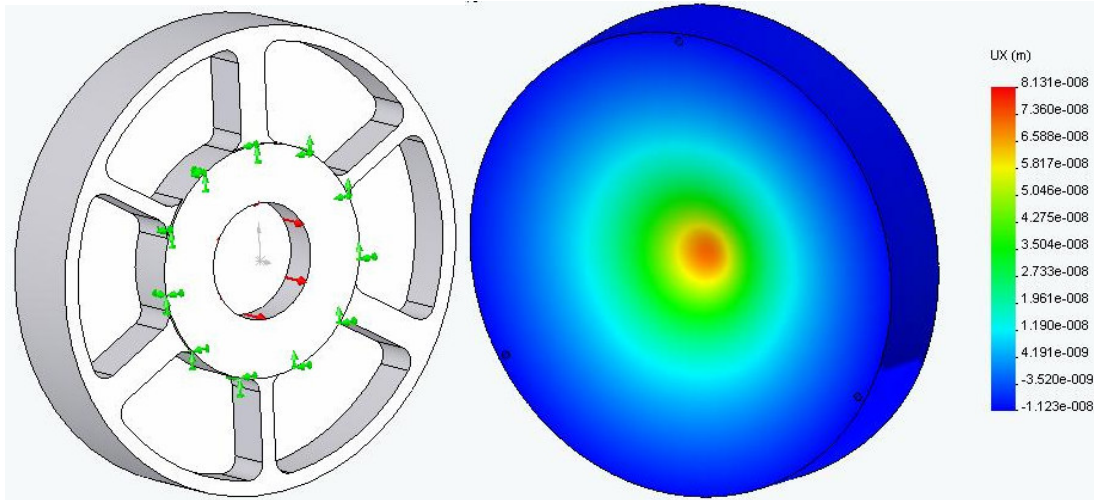
Groove depth is defined as the depth of the material removed from the back of the mirror substrate measured from the mounting plane. Groove depth depends on the cutting force, maximum of 10 N, modeled in Solidworks/Cosmos as a load acting on the middle of the grooves as shown in Figure 5-4 (a). Optical surface deflection is shown in Figure 5-4 (b) and maximum displacement of 100 nm at the edge of the optical surface corresponds to a groove depth of 16 mm. The displacement due to the cutting forces is within the tolerance range specified in the sensitivity analysis Section 4.4.



(a) Mirror substrate loading/restraint (b) Optical surface displacement plot

Figure 5-4: Cutting forces simulation and effect on the optical surface

Further weight reduction is accomplished by boring a hole in the middle of the structure. Depth of the hole depends on the optical surface deflection due to the 10 psi mounting vacuum pressure. The part is modeled in Solidworks/Cosmos with the edge of the mounting plane fixed and uniform pressure applied on the critical area as shown in Figure 5-5 (a). Displacement is shown in Figure 5-5 (b) where 71.6 nm optical surface displacement corresponds to 11 mm depth measured from the mounting plane. The mass of the primary mirror is reduced from 1.27 kg to 0.85 kg, or 33 percent weight reduction. The secondary and tertiary mirror structures incorporate the same lightweight structural design concept and are stiffness scaled to their respective aperture. Detail drawings of the three mirrors structures can be found in Appendix D.



(a) Mirror structure loading/restraint (b) Optical surface displacement plot

Figure 5-5: Mirror substrate vacuum mounting simulation

5.3.2 Fiducialization Techniques

For a rigid body, six degrees of freedom must be constrained by no more than six forces or these additional forces will distort the optical surfaces. Therefore, six forces are employed to constrain each mirror. The two mirror optical system only requires five forces due to the rotational symmetry. Rotation about the optical axis, or z-axis, does not need to be constrained. If the surfaces are not rotationally symmetric, the final degree of freedom, rotation about the z-axis must be constrained. The following sections discuss techniques to locate the mirror components onto an optical housing with the proper orientation.

5.3.2.1 Conventional

The conventional technique involves locating the mirrors on a planar surface on the face of the housing using the reference fiducial surfaces machined onto the face of the mirror and a pair of pins that fit into a hole and a slot on the telescope frame. For the on-axis

Zernike polynomial optical design, the optical axis of each mirror is normal to the surface at the center along the z-direction as shown in Figure 5-6. The fiducial surface creates a plane that mates to the plane created on the telescope frame through contact pads and positions the optical axis of the mirror in the correct direction with respect to the other mirrors in the system. The fiducial plane constrains the optical component in three degrees of freedom but will allow translation in the x and y directions and rotation about the z axis. These degrees of freedom are constrained by the pair of pins protruding from the fiducial plane on the mirror. One pin will fit into a pin hole constraining linear translation of the mirror in the x and y directions. The other pin will fit into a slot constraining the mirror from rotating about the z-axis, thus all six degrees of freedom of the mirror are constrained. Orientation of each optical surface depends on the orientation of the fiducial plane on the telescope frame and the location of the hole and slot in the contact pads. Fabrication of the optical surface will be created with respect to the fiducial plane and the location of the two pins.

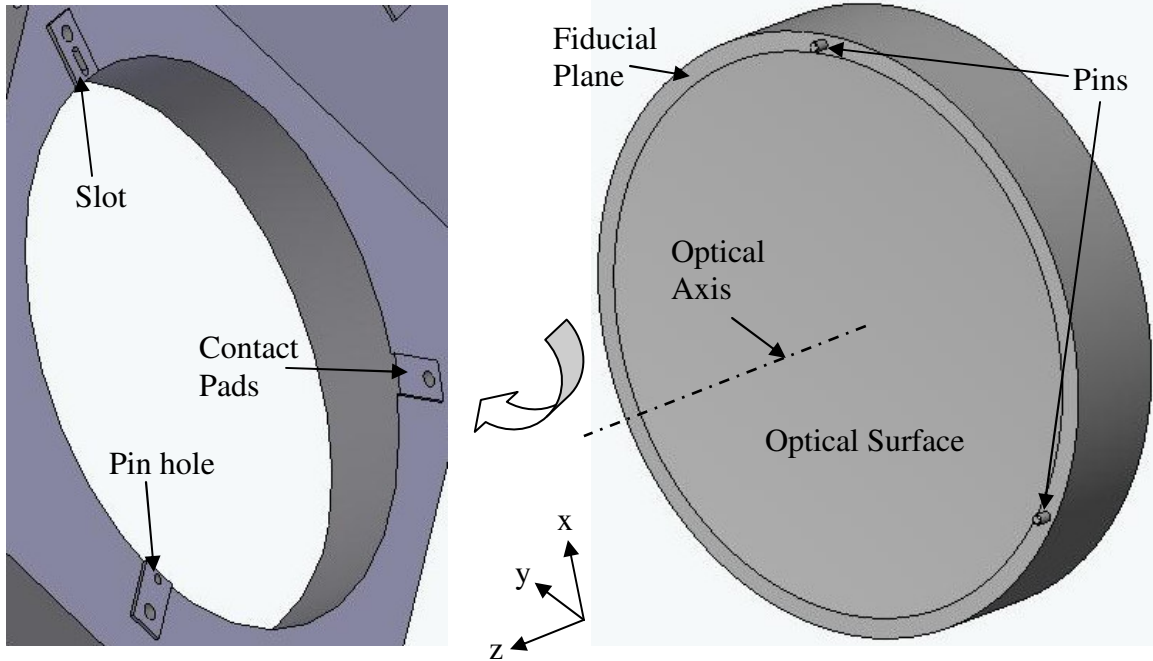


Figure 5-6: Mirror blank with pins installed in the fiducial plane that fit into a pin hole and slot on the telescope frame

5.3.2.2 Kinematic Coupling

Kinematic or Kelvin coupling provides deterministic location in all six degrees of freedom of two components in relation to each other without over-constraining them. Avoiding over-constrain is necessary since it causes stress in the structural component that results in optical surface distortion and non-repeatable location [21]. Ideally, three points on a structure that are rigidly coupled to each other locate with six planes rigidly connected on another component. Ignoring contact stress, this locating technique provides a unique and critical constraint with respect to both mating components.

Two examples of kinematic coupling are shown in Figure 5-7. Spheres attached on one component either mate with a trihedral hole, groove and flat shown on the left, or in three V-grooves shown on the right. Components are kept in contact through gravitational

force or an external force applied through flexures or clamping components together. Contact stress inherent in kinematic design is a concern due to the significant influence on the placement of the components or plastic deformation of the mating surfaces.

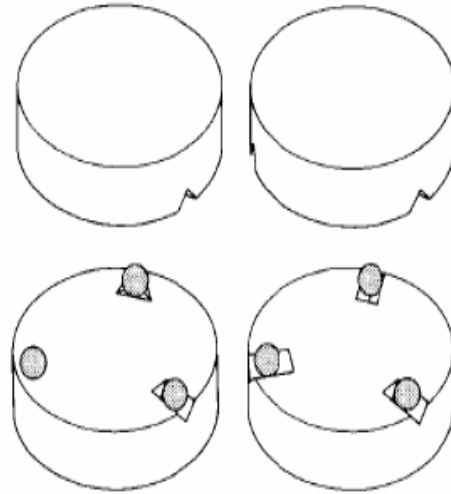


Figure 5-7: Kelvin coupling (left) and kinematic coupling (right) constrain a rigid body in six degrees of freedom

Elastic contact stress between the ball features on the mirror fiducial surface and the V-grooves machined into the housing must be less than the bearing yield stress, 386 MPa, of 6061-T6 aluminum material selected for the system [5]. The stress will depend on the load and geometry of the mating surfaces. Equations to calculate the Hertz contact stress for the generalized case of two mating surfaces each defined by a radius of curvature in two orthogonal planes are given in Equation 7 and 8 [22]. At the contact point, relative sizes of the radii control the contact stress, shown in Figure 5-8. The smaller the surface radius, the larger the contact stress for a given load. Dimensions of the contact surface are an ellipse with a major radius “a” and a minor radius “b”.

$$a = m \sqrt[3]{1.5 \frac{P(1-\nu^2)}{E(A+B)}} \quad (7)$$

$$b = n \sqrt[3]{1.5 \frac{P(1-\nu^2)}{E(A+B)}} \quad (8)$$

in which the constants A and B are geometry factors dependent on the two radii of each component and are determined from Equations 9 and 10. The coefficients m and n are parameters dependent on the radii shown in Figure 5-8 and the values depend on the angle θ , given in Equation 11, where various values of θ are found in Appendix F. P is the load applied to a single contact, E is the elastic modulus and ν is the Poisson's ratio of the material.

$$A + B = \frac{1}{2} \left(\frac{1}{R_{bxz}} + \frac{1}{R_{byz}} + \frac{1}{R_{hxz}} + \frac{1}{R_{hyz}} \right) \quad (9)$$

$$B - A = \frac{1}{2} \left[\left(\frac{1}{R_{bxz}} - \frac{1}{R_{byz}} \right)^2 + \left(\frac{1}{R_{hxz}} - \frac{1}{R_{hyz}} \right)^2 + 2 \left(\frac{1}{R_{bxz}} - \frac{1}{R_{byz}} \right) \left(\frac{1}{R_{hxz}} - \frac{1}{R_{hyz}} \right) \cos 2\psi \right]^{\frac{1}{2}} \quad (10)$$

$$\cos \theta = \frac{B - A}{A + B} \quad (11)$$

Based on the calculated maximum stress given in Equation 12 for different ball and groove shapes, an acceptable feature size is determined that can be fabricated with the equipment at the PEC. Figure 5-9 shows a schematic of how the ball features are machined in the same process as the optical surface using the fast tool servo.

$$\sigma_{\max} = \frac{1.5P}{\pi ab} \quad (12)$$

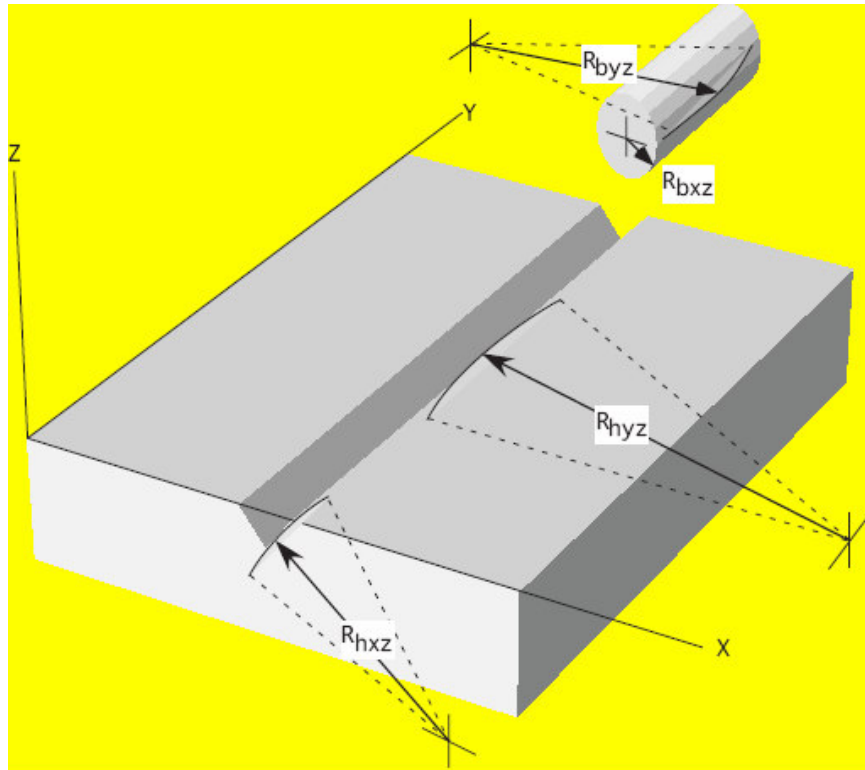


Figure 5-8: Definition of the contact radii on the housing (h) and the ball features (b)

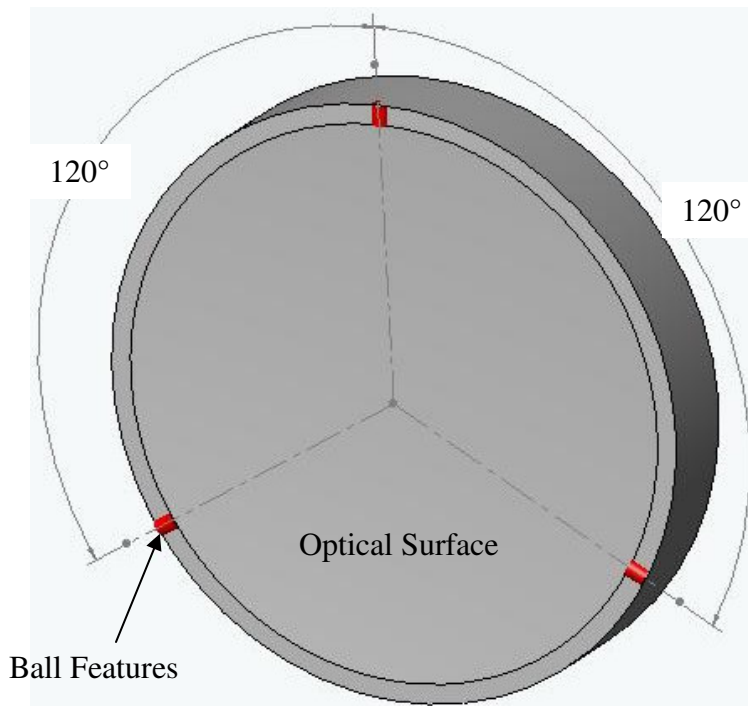


Figure 5-9: Sketch of the mirror surface showing the ball features machined on the outside fiducial ring

Figure 5-10 shows the detailed shape of the ball features. The optical surface is machined using the FTS to generate both the NRS optical surface and the alignment ball features. The ball features have a height of only a few hundred micrometers. The features will be created using the Variform FTS having a 400 μm range of motion at 140 mm/sec maximum speed. The same tool will be used for the optical surface and fiducials to guarantee relative placement. Table 5-1 shows the radius and contact stress for each ball-groove contact. Providing sufficient load without yielding at the contact could be a problem. The housing V-groove surfaces are nearly flat and are machined using a flycutter with a dead sharp diamond tool. The modeled load is equivalent to ten times the weight of the primary mirror and the maximum stress does not exceed the bearing yield stress of the contacting material.

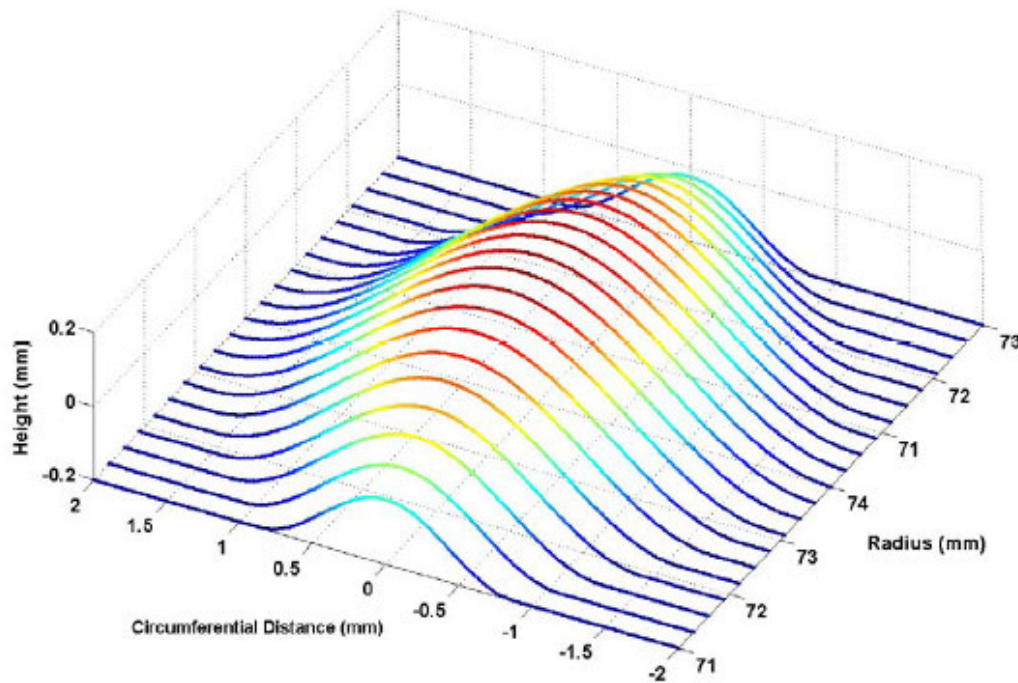


Figure 5-10: Details of the three ball features on the mirror fiducial surface

Table 5-1: Ball and groove features on the fiducial surfaces shown in Figure 5-8

Mirror		
R _{bxz}	40	mm
R _{byz}	6	mm
Housing		
R _{hxz}	1,000,000	mm
R _{hyz}	1,000,000	mm
Load	30	N
Max Stress	375	MPa

The conventional pin-hole-slot locating method limits the optical performance of the system to the predicted wavefront error described in the sensitivity analysis Section 4.4. This limit in optical performance is due to the inaccuracy of locating the optical surface with respect to the pins while machining, in addition to the clearance tolerance between the pins and the holes and slots. Utilizing the fast tool servo to machine the fiducial features and the optical surface during the same setup should significantly improve assembly tolerances to less than 2 μm and is limited by the machine resolution to less than 1 μm , thus increasing the optical performance.

5.3.3 Mounting Features

Using the primary and secondary mirror two mirror system simulation conclusions discussed in Sections 3.4.3 and 3.4.4, different locating and mounting features are incorporated into the mirror substrates as shown in Figure 5-11 to reduce the influence of mounting stresses on the optical system. Instead of a radial interference fit around the periphery of the entire mirror, the mirrors will be located on the telescope frame using the pin-hole-slot fiducialization technique described in Section 5.3.2.1. Each mirror substrate incorporates a fiducial plane mating with fiducial contact pads and two pins that fit into a

hole and a slot on the telescope frame that constrains each mirror substrate in six degrees of freedom. To reduce the influence of mounting stresses on the optical surface, three flexures or mounting tabs, shown in Figure 5-11, apply the mounting forces necessary to sustain ten times gravitational acceleration holding the mirror substrates on the telescope frame.

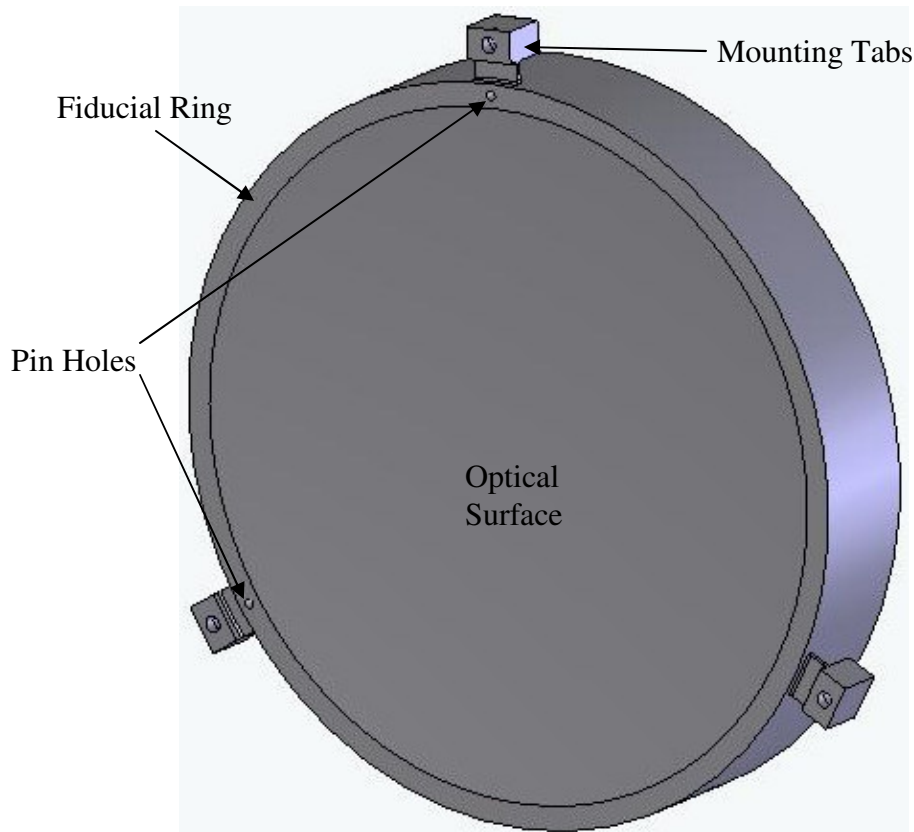


Figure 5-11: Mirror with fiducial and mounting tabs

The mounting tabs are designed where a thin flexure is attached to the outside of the mirror blank and a screw applies the mounting load to hold the mirror on the telescope frame. The primary mirror mass is 0.85 kg and required at least 85 N of mounting force to sustain ten times gravitational loading. The length and thickness of each flexure have been designed such that it will deflect approximately 10 μm when a force of 30 N is

applied on the mounting tab. The face of the three tabs will be machined 10 μm below the surface of the fiducial plane. That fiducial plane will be the face of the ring for the pin-slot design. Figure 5-12 shows that there is significant distortion (200 nm peak-to-valley) of the optical surface with this mounting arrangement. The mounting forces are applied 10.25 mm away from the fiducial contact tabs. These forces create a moment on the optical surface that causes unnecessary distortion.

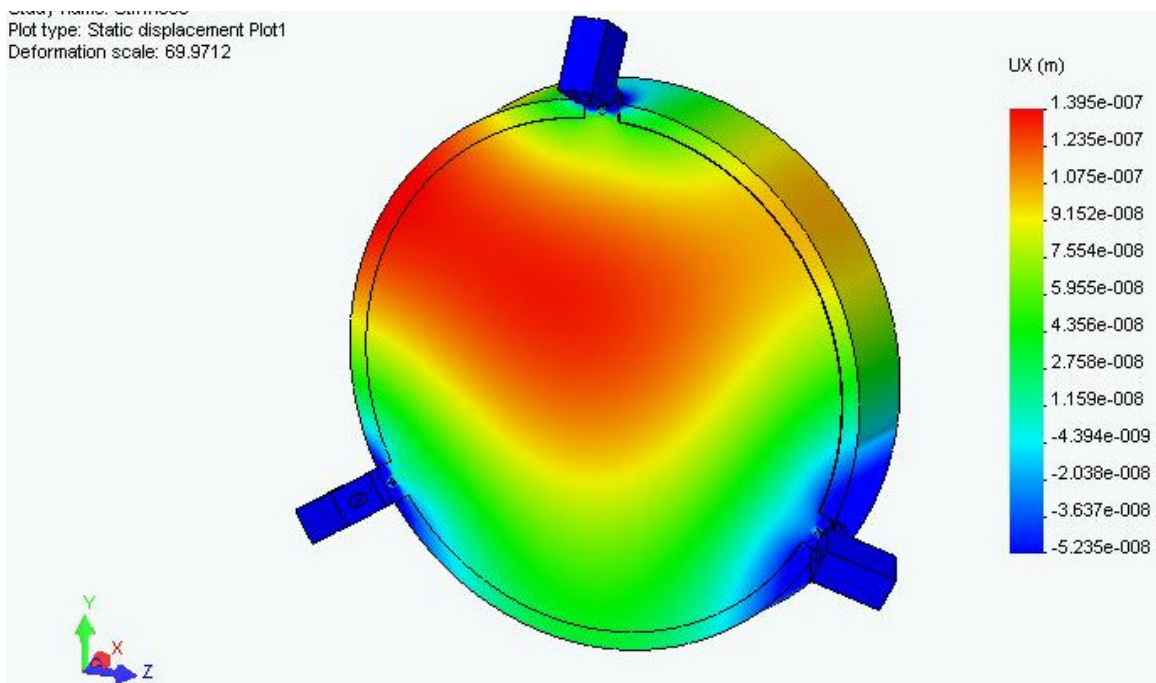


Figure 5-12: Distortion of the optical surface with integrated flexure mounting tabs

A set of independent mounting flexures or clamps are designed due to the fragile nature of the flexure elements (1 mm thick) that could ruin the mirror substrate if damaged during the assembly process. Additionally, these flexures presented a manufacturing challenge, requiring a combination of conventional milling, die-sink EDM and wire-cut EDM. The mounting flexures or clamps are designed to meet the following criteria:

- Clamping force of 30 N for the primary mirror and 10 N for the secondary and tertiary mirrors
- Machined from 6061-T6 Aluminum (yield strength = 276 MPa)
- Maximum stress not to exceed 50% of yield strength
- Deflection at least 10 times the fabrication tolerance (12 μm)

Each mirror is held in place using three clamps. Additional advantage of the clamps is the mounting load is applied directly over the fiducial pad, eliminating the moments that cause distortion of the optical surface. Two different sets of clamps were designed since the primary mirror requires higher mounting force to sustain 10 times gravitational loading. The secondary and tertiary mirrors are lighter and require 10 N of mounting force, and they have a different geometry than the primary mirror. The clamp design for the primary is shown in Figure 5-13 with a 10 mm radius contact region. The clamp has two flexures in series, 4.5 mm top and 3.5 mm thick bottom, making the clamp more compliant to the mounting loads. The primary clamp has an overall height of 33.32 mm and 10 mm depth. M4 socket head cap screws are utilized to apply the axial clamping load and a lip (1mm long and 1 mm thick) at the bottom prevents rotation of the post. The clamps are to be cut using wire EDM technology.

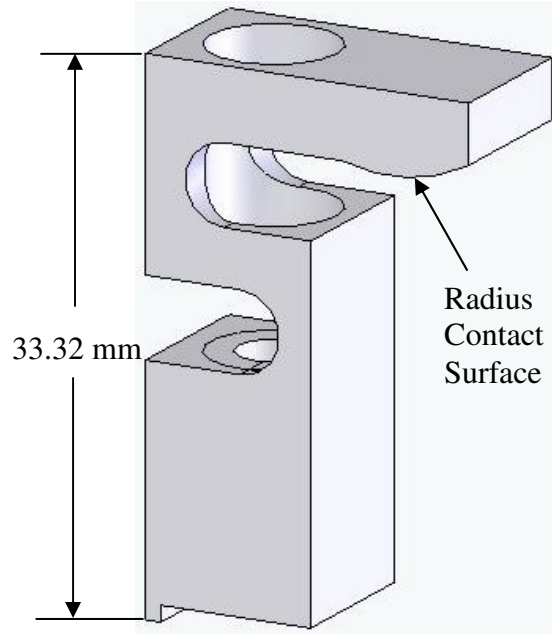


Figure 5-13: Double-jointed clamp design

The modeling was performed in Solidworks/Cosmos, where the base of the post is fixed and a uniform load of 30 N applied to the radius contact surface in the vertical direction. Figure 5-14 shows the displacement plot and stress distribution for the clamp. Displacement at the radius contact point is 125 μm and this represents at least 10 times the tolerance for wire EDM. Having the contact radius displacement be at least 10 times the fabrication tolerance ensures that the mounting load is applied and will sustain 10 times gravitational acceleration. Maximum stress of 122.1 MPa occurs at the bottom flexure or 44% of the yield stress of 6061-T6 Aluminum, satisfying the stress criterion.

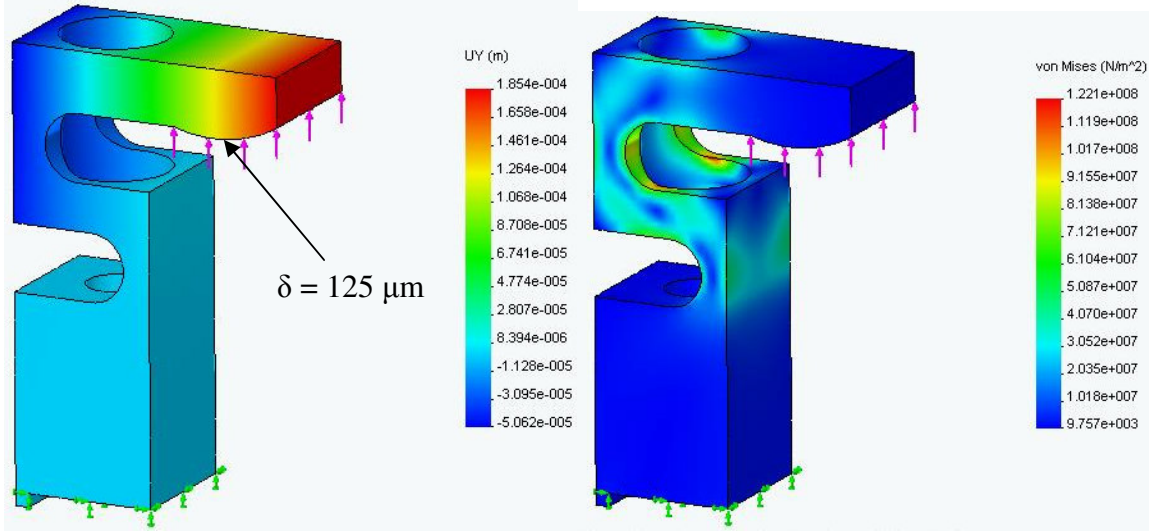


Figure 5-14: Deflection of the mounting tab (left) and the stress distribution (right)

The secondary and tertiary mirror clamps have a similar design concept to that of the primary with a 10 mm radius contact surface. The clamps are 19.275 mm long, with 2 mm top and 2.5 mm bottom thick flexures. Figure 5-15 shows the deflection of the radius contact point (125 μm) with 10 N loading and the stress distribution for the clamps. Maximum stress of 95 MPa, or 34.4% of yield strength, occurs at the top flexure under the loading requirements. Detail drawings of the final clamp designs can be found in Appendix D.

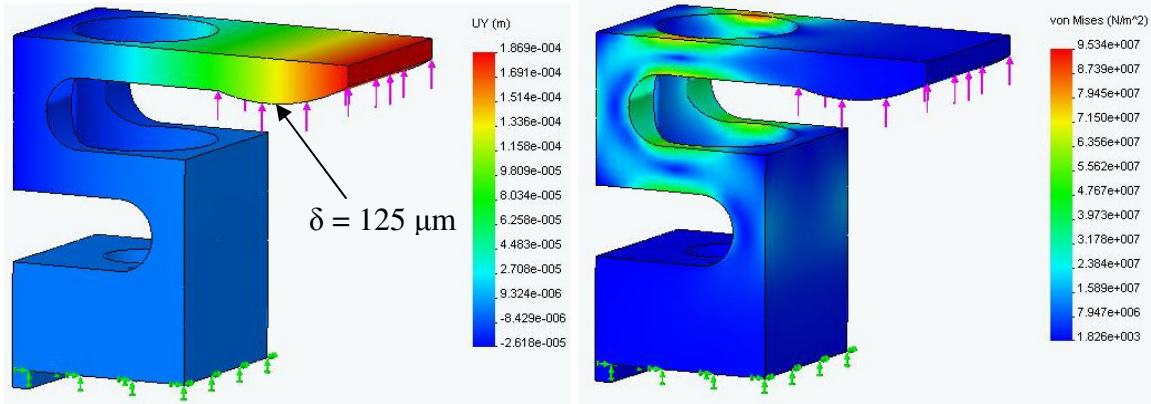


Figure 5-15: Deflection (left) and stress distribution (right) for the secondary and tertiary mirrors mounting clamp

Modeling the effect of clamping force on the optical surface of the lightweight primary mirror, shown in Figure 5-3, is simulated by restraining the optical structure in 6 degrees of freedom through the fiducial features. Clamping force, equivalent to 30 N, is applied opposing the fiducial features assuming a circular contact region 10 mm in diameter, schematic shown in Figure 5-16. Optical surface distortion, shown in Figure 5-17, varies with a peak-to-valley of 95 nm. Therefore, eliminating the moments created by the flexural mounting tabs and the advantage of applying the mounting load co-linear with the fiducial contact tabs reduces the optical surface distortion by more than half compared to the flexural mounting tab simulation. This optical surface distortion is taken into consideration in the sensitivity analysis Section 4.4.

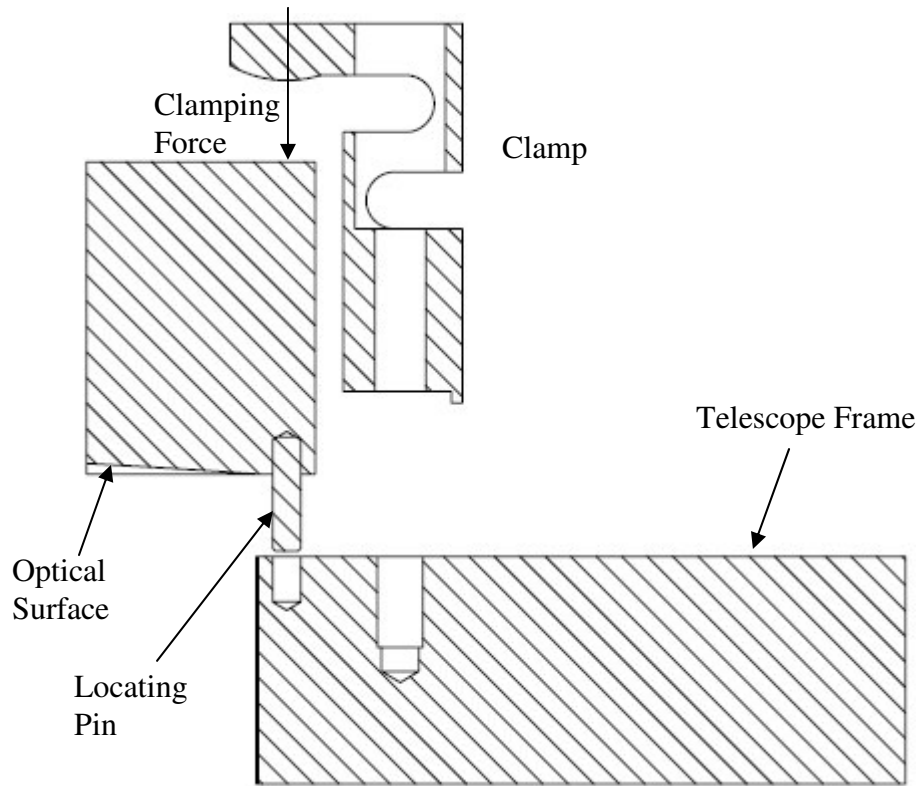


Figure 5-16: Schematic of locating and mounting mirror on the telescope housing

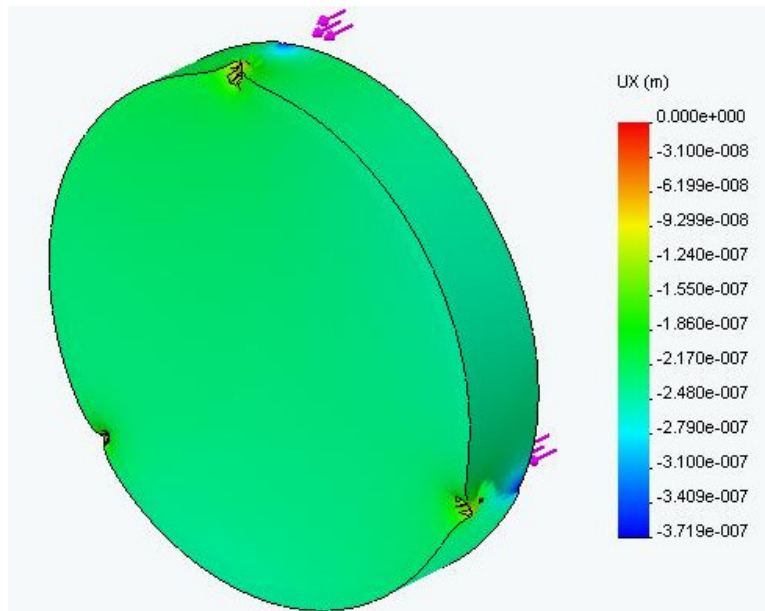


Figure 5-17: Displacement of the lightweight primary mirror due to clamping forces

5.4 TELESCOPE FRAME

To support the mirrors in space, a telescope frame is fabricated to support each optical element in the correct orientation with the other elements without distorting the optical surfaces. The frame facilitates mounting the telescope structure onto an optical bench for testing or to an anti-ballistic missile structure. The TMA optical system consists of on-axis Zernike polynomial surfaces as described in the optical design Section 4.2.2 and the support and orientation of the mirrors will be discussed in this section.

5.4.1 Structure

The frame is a lightweight aluminum structure with mounting surfaces for the three mirrors and the detector. The frame incorporates the mirror and detector tilt angles with respect to the vertical axis. A solid block of 6061-T6 Aluminum will be used for the main structure and wire EDM or water-jet machining will be used to eliminate most of material in the center of the optical frame. Side view of the frame is shown in Figure 5-18 with the primary and tertiary locating and mounting planes. The optical component mounting surfaces consist of three fiducial contact tabs as shown in Figure 5-19. Tabs create the fiducial plane that locates the mirrors on the housing frame in three degrees of freedom. The tabs incorporate a hole and slot where two pins protruding from the mirror fiducial ring locate the mirrors in the correct orientation about the optical axis constraining the mirror in six degrees of freedom as described in the conventional fiducialization technique Section 5.3.2.1. Three clamps using M4 socket head cap screws apply the mounting load through the threaded holes to hold the mirrors in place and sustain 10 times the gravitational acceleration.

Side plates of the housing will be fabricated as solid plates and bolted to the housing using M3 socket head cap screws around the periphery of the frame as shown in Figure 5-20. Side plates are mounted on the frame using bolts instead of pins to increase the structural integrity. Stiffness of the telescope frame under gravitational loading is 70 times higher in the x-direction than in the y-direction. Assembly of the side plates onto the telescope frame has to be carefully conducted to ensure that no permanent distortion of the frame occurs after bolting the parts together [20]. The telescope frame can be mounted to an optical bench for testing or to a missile structure through the three outer tabs using three M6 socket head cap screws and three spherical washers. Detail drawings of the frame, side plates and outer mounts can be found in Appendix D.

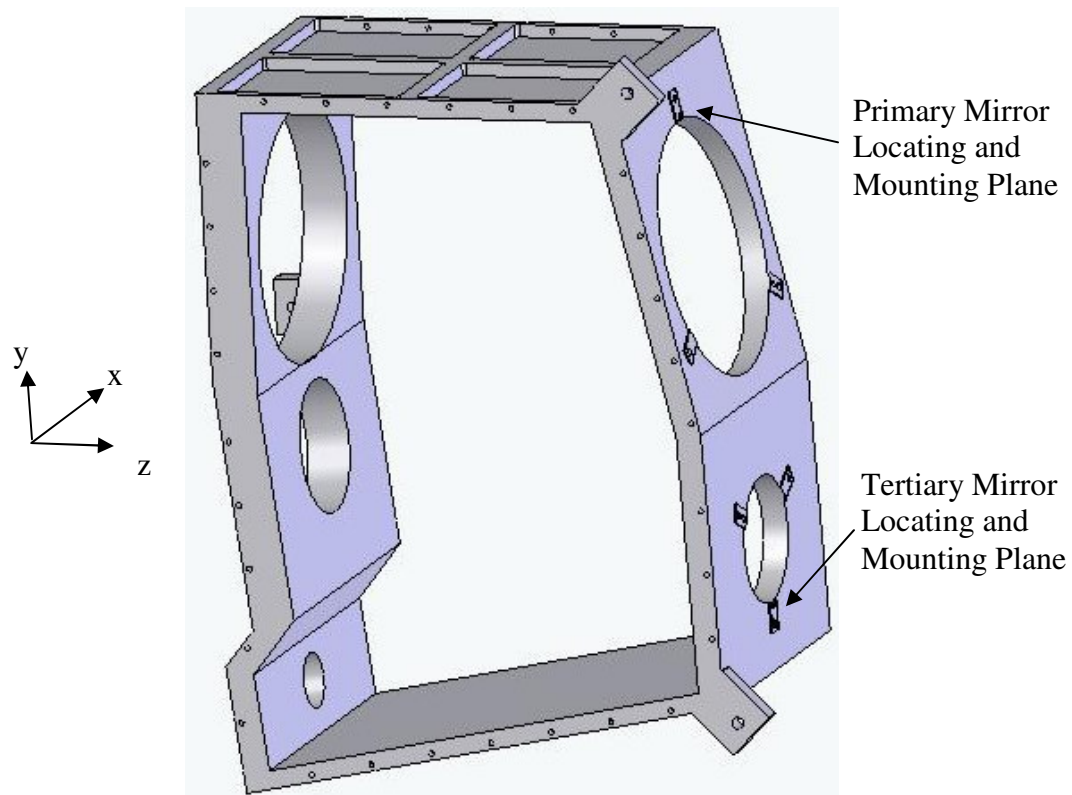


Figure 5-18: Telescope frame without the side plates attached

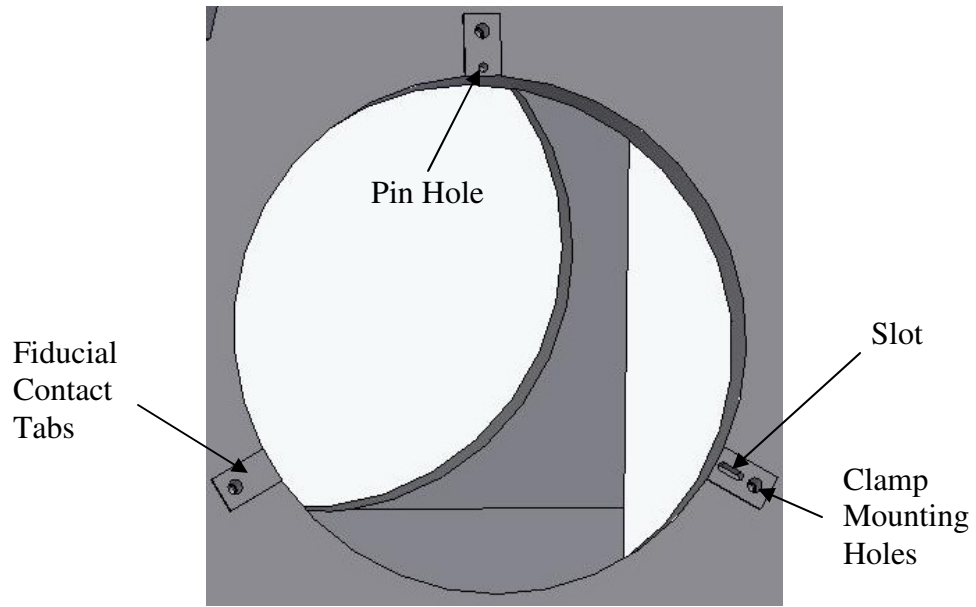


Figure 5-19: Section of the housing with hole-slot-flat to locate mirror and clamp loading holes

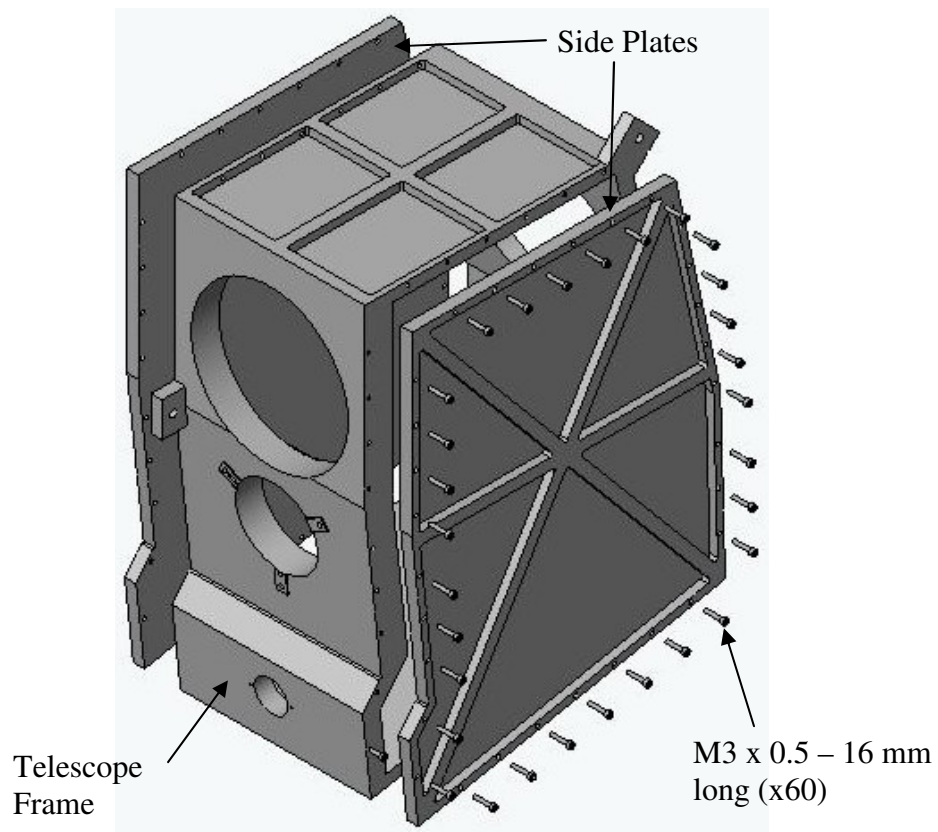


Figure 5-20: Assembling two side plates on the telescope frame

5.4.2 Frame Structural Analysis

5.4.2.1 Launch Acceleration

The telescope frame is modeled in SolidWorks/Cosmos to optimize the wall thicknesses and minimize mass to sustain the missile apparatus launch requirements. Initial wall thickness of 10 mm was chosen for mirror and detector mounting surfaces and 10 mm was used for non-mounting surfaces. The telescope frame is shown in Figure 5-21 with final wall thicknesses (in mm) and 10 mm for non-mounting surfaces. The frame is analyzed in SolidWorks/Cosmos to minimize the fiducial contact tabs distortion using the following loading-restraint conditions, shown in Figure 5-21. The frame is constrained in six degrees of freedom using the three outer tab mounting holes. Launch acceleration or ten times gravitational acceleration is applied in the z-direction, perpendicular to the entrance aperture (vertical axis). On each mirror mounting surface, clamping load is applied on the threaded holes (30 N for primary mirror and 10 N for secondary and tertiary mirror). Fiducial contact pads are loaded with a normal force equivalent to 10 times the mirror weight in addition to the clamping force (58.5 N for primary, 16.5 N for secondary and 15.5 N for tertiary mirror). The detector mounting holes are loaded with 10 times the detector weight (50 N). The outer mounting tabs are located at the edge of the frame, as shown in Figure 5-21, to support the telescope frame with the three mirrors and the detector. Multiple tab positions were modeled in SolidWorks/Cosmos to find the tab location where minimum mounting surface distortion under gravitational loading occurred.

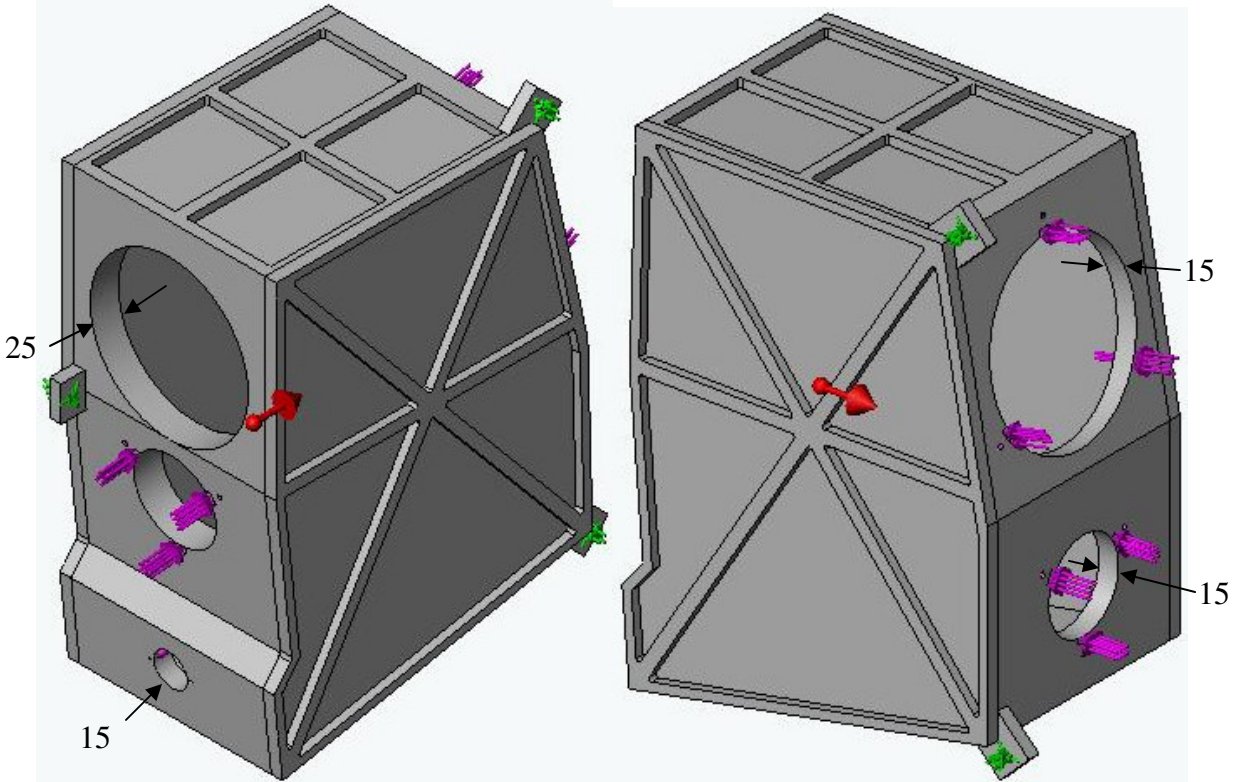


Figure 5-21: Telescope frame with dimensions (in mm) and loading-restraint conditions

Using finite element analysis, results of the simulation using the initial wall thicknesses reveal mirror mounting surfaces distortion that exceeds the tolerances ($2\ \mu\text{m}$) specified in the sensitivity analysis Section 4.4. To decrease the distortion of these surfaces, mirror and detector mounting wall thickness was increased to 15 mm. This increase reduces the displacement of the primary and tertiary mounting surfaces below $2\ \mu\text{m}$ while the secondary mounting surface distortion is $2.6\ \mu\text{m}$ as shown in Figure 5-22.

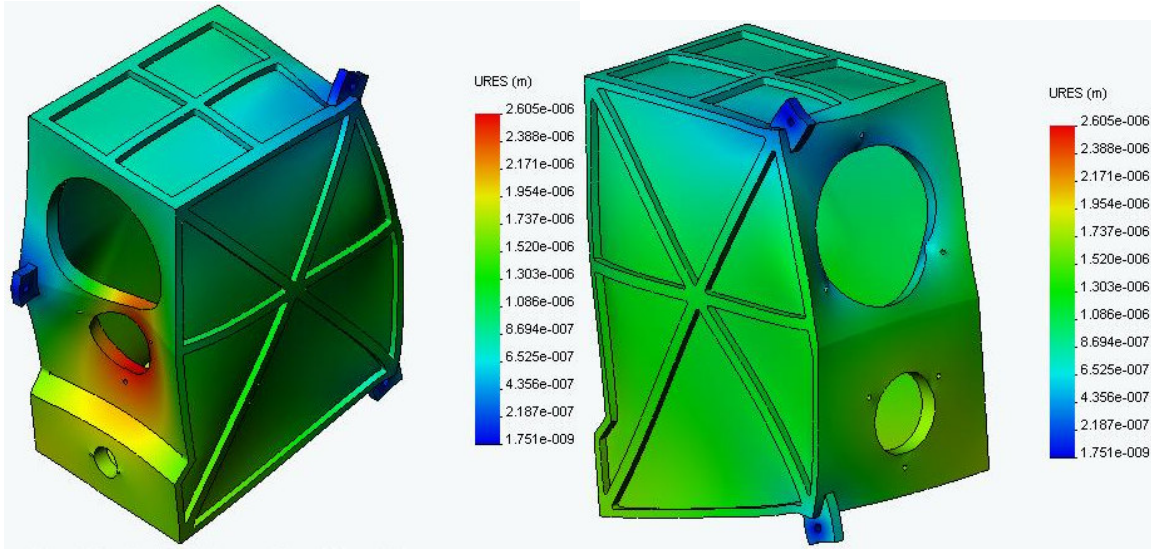


Figure 5-22: Frame displacement with 15 mm thick mirror mounting surfaces

Multiple secondary mirror wall thicknesses were simulated to reduce the mounting surface distortion below the 2 μm tolerance. Distortion of the final implementation of the frame is shown in Figure 5-23 and mirror mounting plane displacements are tabulated in Table 5-2. The table also includes the maximum optical surface displacement results for the three mirror components under launch acceleration requirements. Each mirror component is constrained in six degrees of freedom at the pin hole edges with ten times gravitational loading in the z-direction in addition to the clamping force discussed earlier in this section. Total displacement of each mirror component is included in Table 5-2 which is addition of the mounting tab and the maximum optical surface displacement. The total displacement does not exceed the 2 μm tolerance specified in the sensitivity analysis Section 4.4. Non-mounting plates are lightweight to reduce the mass of the frame from 11.035 kg (24.328 lbs) to 7.148 kg (15.76 lbs) or 35 % reduction without any significant effect on the mounting planes.

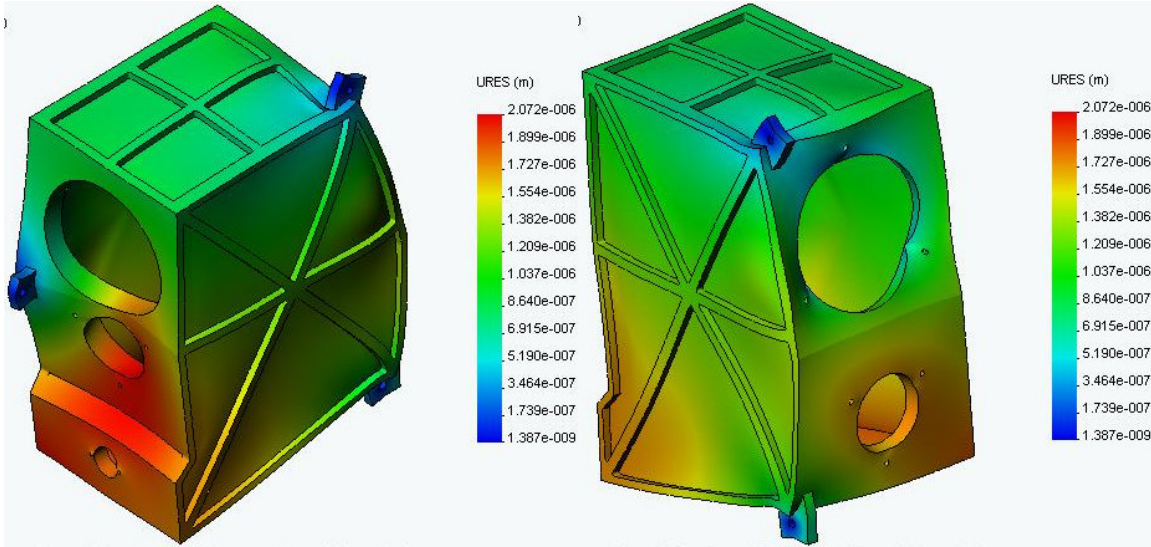


Figure 5-23: Frame displacement with the final mounting surface wall thicknesses

Table 5-2: Mirror mounting tab and optical surface displacement results (μm)

	Primary	Secondary	Tertiary
Mounting Plane	0.627	1.844	1.689
Optical Surface	-0.330	0.141	-0.021
Total Displacement	0.297	1.985	1.668

5.4.2.2 Gravity Loading

The frame gravity loading condition is simulated in SolidWorks/Cosmos using the loading-restraint specifications described in Section 5.4.2.1 except (1g) gravitational acceleration is applied in three directions. Distortion of the frame is shown in Figure 5-24 with 1.85 μm displacement at the primary mirror mounting plane, 0.403 μm at the secondary mirror and 1.43 μm at the tertiary mirror.

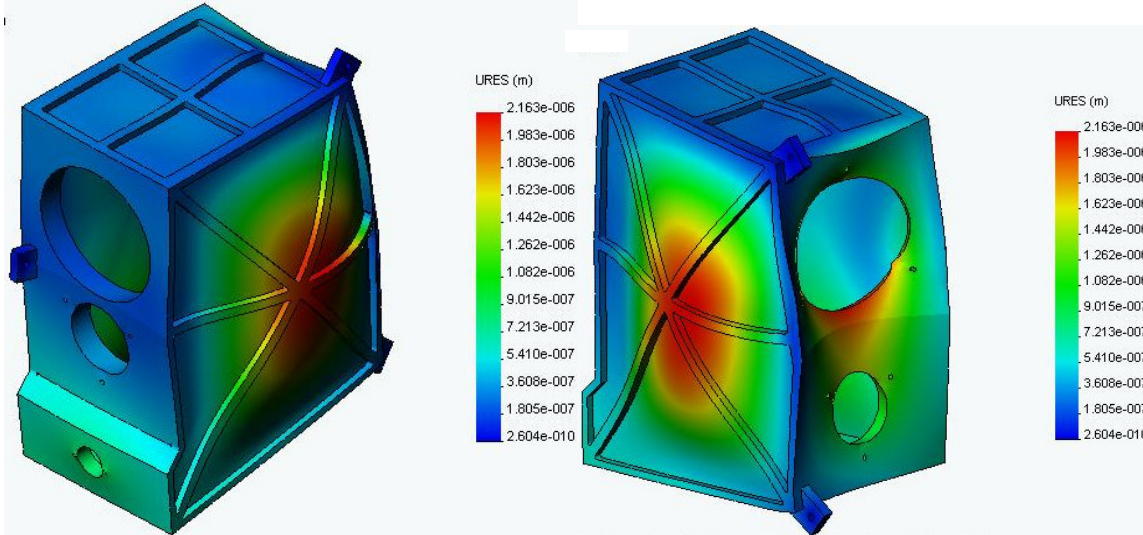


Figure 5-24: Frame displacement due to weight of components in different directions

5.4.2.3 Modal Analysis

Finite element analysis was used to evaluate the first mode of the mirror components and the telescope frame structure. The first mode shape of the telescope structure is illustrated below in Figure 5-25 and results of the simulation are tabulated in Table 5-3. The lowest frequency of the system is 575 Hz which is higher than the missile launch excitation peak frequency of 400 Hz.

Table 5-3: First mode frequencies for the components and frame structure

	1st Mode
Primary Mirror	1579.7 Hz
Secondary Mirror	3488.5 Hz
Tertiary Mirror	3641.4 Hz
Telescope Frame	575 Hz

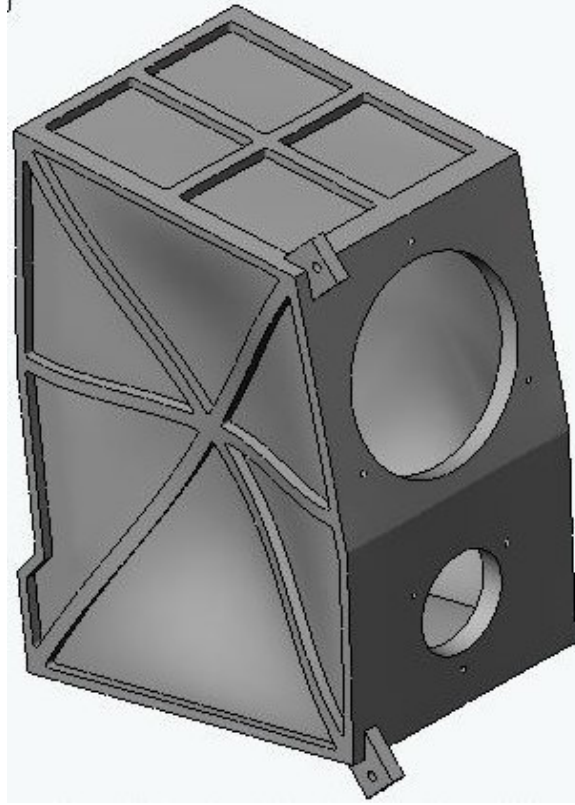


Figure 5-25: First mode shape of the telescope frame structure

5.5 MANUFACTURING FEASIBILITY

Fabrication of the TMA telescope could be carried out at the Precision Engineering Center (PEC) using the Rank Pneumo ASG 2500 and the Nanoform 600 Diamond Turning Machines. The three optical surfaces as well as the fiducial ring on each mirror component will be diamond turned in one setup utilizing the Fast Tool Servo. The freeform optical surfaces have been decomposed into rotationally symmetric and non-rotationally symmetric shapes to determine if the equipment available are capable of fabricating the mirror surfaces as discussed in the surface decomposition Section 4.5.2. The Variform fast tool servo with 400 μm range has the capacity to machine the freeform optical surfaces on the DTM. The telescope frame will be machined on the Nanoform

600 3-axis diamond turning machine. The frame will be mounted on the positioning spindle that is equipped with a high-torque motor and an angular encoder that can place it at a specific angular location. A diamond flycutter is mounted on a vertical y-axis that is mounted on the z-axis that moves along the spindle axis. The axis of the flycutter is along the x-axis direction. The fiducial mounting surfaces on the telescope frame will be diamond flycut by moving the flycutter across the face of the frame, then the frame is rotated to the appropriate location and the next mounting surface is machined. The telescope frame is finished in one machining setup to ensure accurate location of the optical surfaces and the detector with respect to each other.

5.6 ASSEMBLY PROCEDURE

The overall dimensions of the Three Mirror Anastigmat are 190 mm x 281 mm x 385 mm with a total weight of 8.404 kg (18.528 lbs). A final assembly isometric view and dimensions is shown in Figure 5-26. Detailed assembly instructions for the telescope can be found in Appendix D.

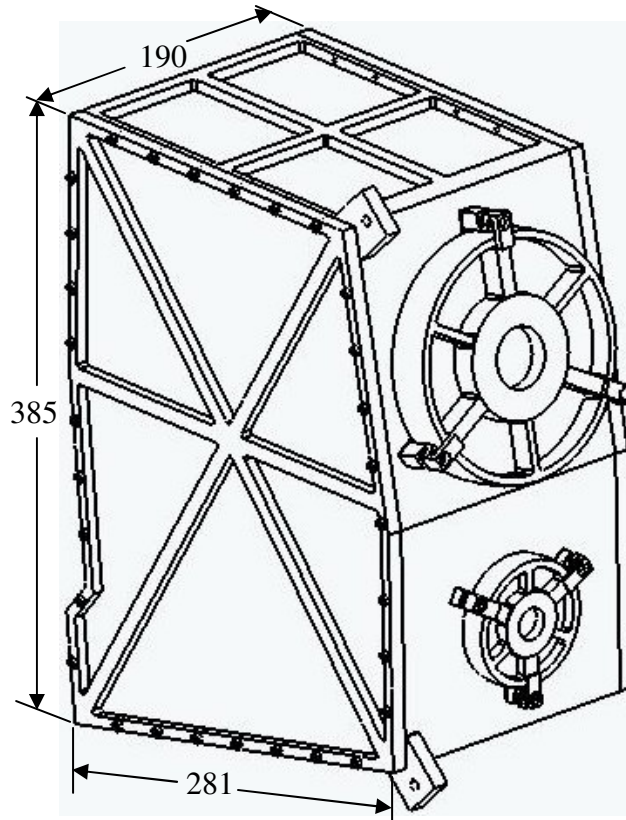


Figure 5-26: Final telescope assembly and telescope frame dimensions (in mm)

6 CONCLUSION AND FUTURE WORK

6.1 TWO MIRROR TELESCOPE

A two mirror Ritchey-Chrétien (RC) optical system has been designed and optimized using rotationally symmetric conic surfaces.

- Canon EOS 300D digital camera equipped with a CMOS detector is used to capture the image.
- Optical performance of the RC design is dominated by astigmatism that increases with field angle.
- Image plane translation compensates for optical aberrations and the average RMS wavefront error is 0.367 waves over the field of view.
- Effect of fabrication tolerances on optical performance modeled in Code V show 44 % increase in RMS wavefront error at specific field angles.

Opto-mechanical design concept for this telescope is a snap-together assembly; that is, optical components, connecting tube and spacer are diamond turned and bolted together without adjustments or shims.

- Radial interference between mirror components and tube (6 μm interference) locates the optical components in the radial direction in conjunction with an axial fiducial ring providing axial location constraining the components in six degrees of freedom.
- Three symmetric screw locations at each end of the tube warrants multiple mirror orientations and lack of assembly repeatability.

Fabrication and assembly of the telescope was completed at the PEC and the optical components and system performance were measured. Errors due to optical component fabrication and post-assembly design issues having an impact on the optical performance are the following:

- Primary mirror with a high aspect ratio (5.5) shows more than 1 μm optical surface distortion when mounted on the vacuum chuck for machining, while the secondary mirror with a lower aspect ratio (4) has an optical surface distortion of about 0.1 μm .
- Mirror components with an aspect ratio of 3 have an acceptable optical surface distortion.
- Optical surface distortion occurs when radial interference pressure is not applied through the neutral axis of the component affecting the focus of the system.
- Assembling the primary mirror on the tube introduces optical surface trefoil symmetry distortion due to deformation of the mating axial fiducial surfaces.
- Design of the two mirror telescope was a challenge and the issues addressed and solved serve as a background for future designs.

6.2 THREE MIRROR TELESCOPE

Optical performance is improved with the addition of a third mirror. The first Three Mirror Anastigmat (TMA) optical system is designed using off-axis conic sections of rotationally symmetric surfaces.

- The off-axis conic TMA optical design follows similar specifications as the RC system with a 15 mm diameter image, 1° circular field of view and an effective focal length of 859.5 mm.
- Entrance pupil diameter reduction to 140 mm to accommodate a 10 mm fiducial ring changes the f-number of the system to 6.139.
- Optical performance of the off-axis conic TMA is 2.7 times better than the RC system but limited aberration node control due to the lack of variables.
- Average RMS wavefront error is 0.134 waves over the field of view.
- Starlight Xpress CCD detector is used to capture the image instead of the Canon detector because of the focus adjustment advantage using a T-thread mount.

A TMA optical system using freeform surfaces is designed following the same specifications as the off-axis conic TMA.

- Freeform surfaces introduce additional variables to the system that can be manipulated in the optimization routine.
- Impressive optical performance improvement is achieved with freeform surfaces due to aberration node control.
- Average RMS wavefront error is 0.0063 waves over the field of view.
- Aberration nodal control achieved with freeform surfaces shows 21 times optical performance improvement over the off-axis conic TMA and 58 times improvement over the RC system.

Sensitivity analysis of fabrication tolerances effect on optical performance is modeled in Code V for off-axis conic and freeform TMA optical designs.

- Average RMS wavefront error for the off-axis conic TMA increases from 0.134 waves to 0.308 waves, while the wavefront error increases from 0.0063 waves to 0.219 waves for the freeform TMA.
- Off-axis conic TMA is less sensitive to fabrication tolerances than the freeform TMA noticed in the predicted wavefront error increase.
- Although the freeform TMA is more sensitive to fabrication tolerances, optical performance is below the Rayleigh criterion (0.25 waves) where the image is perfect.

Optical surfaces are decomposed into a rotationally symmetric component (machined by the DTM) and a non-rotationally symmetric component (machined by the FTS) to check the surface fabrication with capabilities available at the PEC and provide feedback to the optical designer.

- Off-axis conic optical surfaces can either be machined off-axis or on-axis utilizing the FTS (191 μm maximum servo excursion).
- On-axis freeform surfaces are machined on-axis utilizing the FTS and require smaller servo excursions (110 μm) to machine the NRS component.
- Ability to integrate freeform surfaces in an optical design with optical surface fabrication feedback to the designer is a great advantage.
- Further improvements could be achieved with implementation of optical surface fabrication feedback in the optical design software (Code V) provided by ORA.

Opto-mechanical design of the TMA focuses on simplifying manufacturing and snap-together assembly processes for freeform optical systems while improving optical performance.

- Mirror components are lightweight structures with a low aspect ratio reducing optical surface distortion below 100 nm while machining.
- Conventional fiducialization techniques is implemented where pins fit in a hole and slot locating the optical components on the telescope frame in six degrees of freedom without using interference surfaces.
- Clearance between the pins and the mating hole and slot limit assembly tolerances.
- Integrating the fabrication of kinematic fiducials with freeform optical surfaces using a fast tool servo permits tolerances less than 1 μm .
- Application of the mounting forces through independent clamps directly over the fiducial contact pad eliminates the moment and reduces the optical surface distortion from 200 nm to 95 nm.
- A lightweight telescope frame facilitates mounting the telescope on an optical testing bench or an anti-ballistic missile structure.
- Mirror mounting surface and optical surface distortions are lower than the 2 μm fabrication tolerance under high gravitational loading (ten times gravitational acceleration) and gravity loading conditions; thus, the telescope delivers an impressive image performance.

6.3 FUTURE WORK

Future work for this project includes fabrication of the Three Mirror Anastigmat utilizing the conventional fiducialization technique. Since the telescope will be mounted onto an anti-ballistic missile structure, optical performance of the system should be tested under high gravitational acceleration required during the missile launch. Assembly procedure and repeatability should also be tested. To further improve assembly tolerances and angular orientation errors, implementation of the new fiducialization technique by taking advantage of the fast tool servo to machine the kinematic coupling features in conjunction with the optical surface. Fabrication and comparison of the new telescope with the conventional assembly procedure should demonstrate improved optical performance with tighter assembly tolerances.

7 REFERENCES

1. Ritchey, G.W. "On the Modern Reflecting Telescope, and the Making and Testing of Optical Mirrors." Smithsonian Contributions to Knowledge. 34:1-51, 1904.
2. Smith, Warren J. Modern Optical Engineering. 3rd Ed. SPIE Press. McGraw Hill, New York, NY, 2000, pg 22, 62-71,152, 355, 366-383.
3. Roark, R. and Young, W. Formulas for Stress and Strain. McGraw Hill, 1975, pg 362.
4. Woodside, R. M., "Metrology of Reflective Optical Systems," MS Thesis, North Carolina State University, 2006, pg 12-33, 56-66.
5. Callister, William. Material Science and Engineering an Introduction. 5th Ed. New York: John Wiley and Sons, 2000, pg 371-373.
6. Wilson, R.N. Reflective Telescope Optics I. 2nd Ed. New York: Springer, 2004, pg 29, 57, 59-63.
7. Irving, B. Code V, Introductory User's Guide. ORA, 2004, pg 44-51.
8. Thompson, K. "Description of the Third-Order Optical Aberrations of Near-Circular Pupil Optical Systems without Symmetry". Optical Society of America, July 2005, pg 1389-1401.
9. Bruegge, T., Corn, E., Hasenauer, D., Kuper, T., Reid, D., Rimmer, M., Stone, B. Code V Application Programming Reference Guide. Pasadena, California: ORA 2005.
10. Lamonds, D.L., "Surface Finish and Form Fidelity in Diamond Turning," MS Thesis, North Carolina State University, 2006.
11. Moorefield II, G.M., Garrard, K.P., Taylor, L.W., Falter, K.J., Dow, T.A., "Generation of Rotationally Asymmetric Optical Surfaces using a Fast Tool Servo,"" PEC 1994 Annual Report, 11, 121-129, 1994.

12. Garrard, K., Sohn, A. "Off-Axis Biconic Mirror Fabrication." Precision Engineering Center 2002 Annual Report . January 2003.
13. Rogers, M. and Thompson K., "Benefits of Freeform Mirror Surfaces in Optical Design," Proceedings of the ASPE Winter Tropical Meeting on Freeform Optics, Chapel Hill, NC, Feb. 2004, pg 73-79.
14. US Patent # 5,467,675 issued November 21, 1995 entitled "Apparatus and Method for Forming a Workpiece Surface into a Non-Rotationally Symmetric Shape," by Dow, Garrard, Moorefield and Taylor.
15. Schroeder, Daniel J. Astronomical Optics. San Diego: Academic Press, 2000, pg 1-6.
16. Rogers, John "Unobscured Mirror Designs." IODC Conference, SPIE, Vol. 4832, 2002.
17. Ahmad, Anees. Handbook of Optomechanical Engineering. New York: CRC Press, 1997, pg 51-55, 197-202.
18. Yoder, Paul R. Opto-Mechanical Systems Design. 3rd Ed. Boca Raton, FL: CRC Press, 2006, pg 124-129, 272-288.
19. Sweeney, Michael "Advanced Manufacturing Technologies for Light-Weight, Post Polished, Snap-together Reflective Optical System Designs." Proceedings of SPIE. Ed. Alson Hatheway. Seattle, USA, 2002. pg. 144-154.
20. Hegge, M.J., Baer, J.W., Hardaway, L.M.R., Taudien, G., Sabatke, D.S., Shidemantli, S.R. "Diamond Turned, Light Weight, Athermal, Visible TMA Telescope for the Planned New Horizons Mission to Pluto." Proceedings of SPIE. Ed. Alson Hatheway. Bellingham, WA, 2005.
21. Solcum, A.H., "Precision Machine Design," Prentice Hall, Englewood Cliffs NJ, pg 401-412, 1992.
22. Timoshenko, S.P., Goodier, J.N., "Theory of Elasticity," McGraw Hill, 3rd Edition, New York, pg 409-417, 1970.
23. Cohen, E.J., Hull, A.B., Escobedo-Torres, J., Barber, D.D., Johnston, R.A., Small, D.W., Prata, A.J., Freniere, E.R., Butcher, H.R. "Optical Design of the Ultra-

- Light-Weight FIRST Telescope.” Proceedings of SPIE. Munich, Germany, 2000, vol. 4015, pg. 559-566.
24. US Patent # 4,296,186 issued October 6, 1982 entitled “Restricted Off-axis Field Optical System,” by Offner.
 25. US Patent # 4,265,510 issued May 5, 1981 entitled “Three Mirror Anastigmat Optical System,” by Cook.
 26. Korsch, Dietrich. Reflective Optics. San Diego: Academic Press, 1991, pg. 207-258.
 27. Malacara, Daniel. Optical Shop Testing. 2nd Ed. New York: John Wiley & Sons, 1992, pg 81-84.
 28. Schaefer, J.P. “Progress in Precision – Single Point Diamond Turning (SPDT) of Optical Components.” Presented at ASPE 2002 Spring Tropical Meeting on Progress in Precision. Raleigh, NC: 2002.
 29. Allen, W.D., Fornaro, R.J., Garrard, K.P., Taylor, L.W. “A High Performance Embedded Machine Tool Controller”, Microprocessors and Microprogramming, 40, pg 179-191, 1994.
 30. Plummer, W.T., “Free-form Optical Components in Some Early Commercial Products,” Proceedings of the ASPE Winter Tropical Meeting on Freeform Optics, Chapel Hill, NC, Feb. 2004, pg 68-71.
 31. Heinrich, M.D., Wildsmith, C., “Need for Precision Engineering in Astigmatic Contact Lenses,” Proceedings of the ASPE Winter Tropical Meeting on Freeform Optics, Chapel Hill, NC, Feb. 2004, pg 18-22.
 32. Winsor, R.S., Ohl, R.G., Connelly, J.A., MacKenty, J.W., “Optical Design of an Infrared Multi-Object Spectrometer Utilizing a Free-Form Optical Surface,” Proceedings of the ASPE Winter Tropical Meeting on Freeform Optics, Chapel Hill, NC, Feb. 2004, pg 79-83.
 33. Henselmans, R., Rosielle, P.C.J.N., Kappelhof, J.P., “NANOMEFOS—Nanometer Accuracy Non-contact Measurement of Freeform Optical Surfaces,” Proceeding of the ASPE Winter Tropical Meeting on Freeform Optics, Chapel Hill, NC, Feb. 2004, pg 97-101.

34. Burge, J.H., Wyant, J.C., "Use of Computer Generated Holograms for Testing Aspheric Surfaces," Proceedings of the ASPE Winter Tropical Meeting on Freeform Optics, Chapel Hill, NC, Feb. 2004, pg 57-62.
35. Schaefer, J., "Assembly and Alignment Capabilities Overview," ELCAN Optical Technologies – Texas, April 14, 2005.

8 LIST OF APPENDICES

A) Fabrication Data Tables.....	132
i) Two-Mirror Optical System	
ii) Three Mirror Anastigmat using Off-axis Conics	
iii) Three Mirror Anastigmat using On-axis Zernike Polynomial	
B) Sensitivity Analysis.....	140
i) Two-Mirror Optical System	
ii) Three Mirror Anastigmat using Off-axis Conics	
iii) Three Mirror Anastigmat using On-axis Zernike Polynomial	
C) Detail Drawings of the Two Mirror Telescope.....	160
i) Primary Mirror	
ii) Secondary Mirror	
iii) Tube	
iv) Spacer	
v) Base Plate	
vi) Gussets	
vii) Two Mirror Telescope Assembly Steps	
D) Detail Drawings of the Three Mirror Anastigmat.....	169
i) Primary Mirror	
ii) Secondary Mirror	
iii) Tertiary Mirror	
iv) Primary Clamp	
v) Secondary Clamp	
vi) Telescope Frame	
vii) Side Plates	
viii) Mounts	
ix) Three Mirror Anastigmat Assembly Steps	
E) Zernike Polynomial Surface.....	186
F) Kinematic Coupling Design Table.....	189

APPENDIX A – Fabrication Date Tables

Fabrication Data for Two Mirror Optical System

FABRICATION DATA

RC on-axis

ELEMENT NUMBER	RADIUS OF CURVATURE		THICKNESS	APERTURE DIAMETER		GLASS
	FRONT	BACK		FRONT	BACK	
OBJECT	INF		INFINITY	C-1		
1	A(1)		-113.6250	C-1		REFL
2	A(2)		208.1761	38.9396		REFL
IMAGE	INF			15.0754		

NOTES - Positive radius indicates the center of curvature is to the right Negative radius indicates the center of curvature is to the left

- Dimensions are given in millimeters
- Thickness is axial distance to next surface
- Image diameter shown above is a paraxial value, it is not a ray traced value

APERTURE DATA

APERTURE ROTATION	SHAPE	DIAMETER		DECENTER	
		X	Y	X	Y
C- 1	CIRCLE	150.000			
0.0	CIRCLE (OBSC)	26.000	26.000	0.000	0.000

ASPHERIC CONSTANTS

$$Z = \frac{Y^2}{R \left(1 + \sqrt{1 - (1+K) \left(\frac{Y}{R} \right)^2} \right)} + (A)Y^2 + (B)Y^4 + (C)Y^6 + (D)Y^8 + (E)Y^{10}$$

D

ASPHERIC CURV	K	A	B	C
A(1)	-0.00333333	-1.019484		
A(2)	-0.01134784	-2.166620		

REFERENCE WAVELENGTH = 632.8 NM

INFINITE CONJUGATES

EFL	=	859.8726
BFL	=	208.5191
FFL	=	-3077.3097
F/NO	=	5.7325

IMAGE DIST = 208.1761
OAL = -113.6250
PARAXIAL
IMAGE HT = 7.5040
SEMI-FIELD
ANGLE = 0.5000
ENTR PUPIL
DIAMETER = 150.0000
DISTANCE = 0.0000
EXIT PUPIL
DIAMETER = 41.9135
DISTANCE = -31.7495

NOTES - FFL is measured from the first surface
- BFL is measured from the last surface

Fabrication Data for Three Mirror Anastigmat using Off-axis Conics

FABRICATION DATA

TMA off-axis conic

ELEMENT NUMBER	RADIUS OF CURVATURE FRONT	RADIUS OF CURVATURE BACK	THICKNESS	APERTURE DIAMETER FRONT	APERTURE DIAMETER BACK	GLASS
OBJECT		INF	INFINITY			
			50.0000	140.8727		
			APERTURE STOP	140.0000		
			300.0000			
		DECENTER (1)		585.2361		
1		A(1)	-270.0000	C-1		REFL
2		A(2)	270.0000	C-2		REFL
3		A(3)	-295.0001	C-3		REFL
IMAGE		INF		14.9921		

NOTES - Positive radius indicates the center of curvature is to the right Negative radius indicates the center of curvature is to the left
 - Dimensions are given in millimeters
 - Thickness is axial distance to next surface
 - Image diameter shown above is a paraxial value, it is not a ray traced value

APERTURE DATA

APERTURE ROTATION	SHAPE	DIAMETER		DECENTER		
		X	Y	X	Y	
0.0	C- 1	CIRCLE	136.856	136.856	0.000	220.000
0.0	C- 2	CIRCLE	78.429	78.429	0.000	104.409
0.0	C- 3	CIRCLE	67.774	67.774	0.000	77.508

ASPHERIC CONSTANTS

2					
(CURV) Y	4	6	8	10	
Z =	+ (A)Y ² + (B)Y ⁴ + (C)Y ⁶ + (D)Y ⁸				
	+ (1-(1+K) (CURV) Y ²) ^{1/2}				
ASPHERIC	CURV	K	A	B	C
D					
A(1)	-0.00100000	-1.754657			
A(2)	-0.00170314	-5.801289			

A(3) -0.00106447 -5.197043

DECENTERING CONSTANTS

DECENTER	X	Y	Z	ALPHA	BETA
GAMMA					

D(1)	0.0000	-220.0000	0.0000	0.0000	0.0000
0.0000					

A decenter defines a new coordinate system (displaced and/or rotated) in which subsequent surfaces are defined. Surfaces following a decenter are aligned on the local mechanical axis (z-axis) of the new coordinate system. The new mechanical axis remains in use until changed by another decenter. The order in which displacements and tilts are applied on a given surface is specified using different decenter types and these generate different new coordinate systems; those used here are explained below. Alpha, beta, and gamma are in degrees.

DECENTERING CONSTANT KEY:

TYPE	TRAILING CODE	ORDER OF APPLICATION
DECENTER		DISPLACE (X, Y, Z) TILT (ALPHA, BETA, GAMMA) REFRACT AT SURFACE THICKNESS TO NEXT SURFACE

REFERENCE WAVELENGTH = 632.8 NM

This is a non-symmetric system. If elements with power are decentered or tilted, the first order properties are probably inadequate in describing the system characteristics.

INFINITE CONJUGATES

EFL	=	-859.5000
BFL	=	-294.8598
FFL	=	142.5075
F/NO	=	6.1393
IMAGE DIST	=	-295.0001
OAL	=	350.0000
PARAXIAL		
IMAGE HT	=	5.2505
SEMI-FIELD		
ANGLE	=	0.3500
ENTR PUPIL		
DIAMETER	=	140.0000
DISTANCE	=	50.0000
EXIT PUPIL		
DIAMETER	=	1300.7597
DISTANCE	=	-8280.5954

NOTES - FFL is measured from the first surface
- BFL is measured from the last surface

Coefficients for a Zernike Surface (SPS ZRN)

6.8094E-07	K (C1) : -1.6127E+00	ZP4 (C5) : -3.3503E-06	ZP5 (C6) :
-2.3077E-11	ZP6 (C7) : -2.5616E-07	ZP7 (C8) : 1.8498E-10	ZP8 (C9) :
3.3611E-12	ZP9 (C10) : 4.1502E-08	ZP10 (C11) : -2.4460E-08	ZP11 (C12) :
-2.7586E-14	ZP12 (C13) : 6.3376E-12	ZP13 (C14) : -2.7193E-12	ZP14 (C15) :
2.0127E-17	ZP15 (C16) : 6.0042E-14	ZP16 (C17) : -3.8906E-17	ZP17 (C18) :
-2.7724E-15	ZP18 (C19) : -2.9944E-17	ZP19 (C20) : -8.7236E-16	ZP20 (C21) :
-2.0165E-18	ZP21 (C22) : -1.3547E-15	ZP22 (C23) : -6.2161E-18	ZP23 (C24) :
-9.9229E-20	ZP24 (C25) : -6.3936E-19	ZP25 (C26) : 4.1826E-18	ZP26 (C27) :

S- 2 Curvature = -0.00179767
Coefficients for a Zernike Surface (SPS ZRN)

-1.0150E-05	K (C1) : -5.7688E+00	ZP4 (C5) : 1.2998E-05	ZP5 (C6) :
-4.6591E-10	ZP6 (C7) : -9.7819E-07	ZP7 (C8) : 2.2167E-09	ZP8 (C9) :
-1.0205E-10	ZP9 (C10) : 3.1088E-07	ZP10 (C11) : -3.8172E-07	ZP11 (C12) :
1.8536E-12	ZP12 (C13) : 2.7830E-10	ZP13 (C14) : -2.1232E-10	ZP14 (C15) :
-2.5488E-16	ZP15 (C16) : 2.8514E-13	ZP16 (C17) : -1.1905E-15	ZP17 (C18) :
1.2300E-13	ZP18 (C19) : -1.6244E-15	ZP19 (C20) : -6.1491E-13	ZP20 (C21) :
-1.9503E-16	ZP21 (C22) : -7.0203E-15	ZP22 (C23) : -7.0447E-16	ZP23 (C24) :
-1.9509E-17	ZP24 (C25) : -7.8242E-16	ZP25 (C26) : 1.2713E-15	ZP26 (C27) :

S- 3 Curvature = -0.00115474

Coefficients for a Zernike Surface (SPS ZRN)

-5.1485E-06	K (C1) : 1.3995E+00	ZP4 (C5) : 1.5436E-05	ZP5 (C6) :
-5.0832E-10	ZP6 (C7) : 5.4332E-07	ZP7 (C8) : 1.5961E-09	ZP8 (C9) :
-2.9057E-11	ZP9 (C10) : 5.2886E-08	ZP10 (C11) : -2.1818E-07	ZP11 (C12) :

```

1.0867E-12      ZP12 (C13) : 7.0733E-11      ZP13 (C14) : 2.1135E-10      ZP14 (C15) :
1.1567E-15      ZP15 (C16) : 4.8658E-13      ZP16 (C17) : 7.8478E-16      ZP17 (C18) :
-1.4320E-13     ZP18 (C19) : -2.0342E-15     ZP19 (C20) : -2.1363E-13     ZP20 (C21) :
-7.3075E-16     ZP21 (C22) : -4.4189E-14     ZP22 (C23) : -7.1055E-16     ZP23 (C24) :
-1.9016E-17     ZP24 (C25) : -3.2117E-17     ZP25 (C26) : 8.6693E-17      ZP26 (C27) :

```

DECENTERING CONSTANTS

DECENTER GAMMA	X	Y	Z	ALPHA	BETA
D (1) 0.0000 (BEND)	0.0000	0.0000	0.0000	12.3738	0.0000
D (2) 0.0000 (BEND)	0.0000	0.0000	0.0000	-18.6456	0.0000
D (3) 0.0000 (BEND)	0.0000	0.0000	0.0000	14.1838	0.0000
D (4) 0.0000 (RETU)	0.0000	0.0000	0.0000	-9.5740	0.0000

A decenter defines a new coordinate system (displaced and/or rotated) in which subsequent surfaces are defined. Surfaces following a decenter are aligned on the local mechanical axis (z-axis) of the new coordinate system. The new mechanical axis remains in use until changed by another decenter. The order in which displacements and tilts are applied on a given surface is specified using different decenter types and these generate different new coordinate systems; those used here are explained below. Alpha, beta, and gamma are in degrees.

DECENTERING CONSTANT KEY:

TYPE	TRAILING CODE	ORDER OF APPLICATION
DECENTER		DISPLACE (X, Y, Z) TILT (ALPHA, BETA, GAMMA) REFRACT AT SURFACE THICKNESS TO NEXT SURFACE
DECENTER & RETURN	RETU	DECENTER (X, Y, Z, ALPHA, BETA, GAMMA) REFRACT AT SURFACE RETURN (-GAMMA, -BETA, -ALPHA, -Z, -Y, -X) THICKNESS TO NEXT SURFACE
DECENTER & BEND	BEND	DECENTER (X, Y, Z, ALPHA, BETA, GAMMA) REFLECT AT SURFACE BEND (ALPHA, BETA, GAMMA) THICKNESS TO NEXT SURFACE

REFERENCE WAVELENGTH = 632.8 NM

This is a non-symmetric system. If elements with power are decentered or tilted, the first order properties are probably inadequate in describing the system characteristics.

INFINITE CONJUGATES	X	Y
EFL	= -859.4968	-859.4968
BFL	= -282.3713	-282.3713

FFL	=	296.3594	296.3594
F/NO	=	6.1393	6.1393
IMAGE DIST	=	-294.5966	-294.5966
OAL	=	350.0000	350.0000
PARAXIAL			
IMAGE HT	=	5.2504	5.2504
SEMI-FIELD			
ANGLE	=	0.3500	0.3500
ENTR PUPIL			
DIAMETER	=	140.0000	140.0000
DISTANCE	=	50.0000	50.0000
EXIT PUPIL			
DIAMETER	=	488.4310	488.4310
DISTANCE	=	-3280.9775	-3280.9775

NOTES - FFL is measured from the first surface
 - BFL is measured from the last surface

APPENDIX B – Sensitivity Analysis

Sensitivity Analysis for Two Mirror Optical System

C O D E V

S E N S I T I V I T Y A N A L Y S I S
P O L Y C H R O M A T I C R M S W A V E F R O N T A B E R R A T I O N

RC on-axis

WEIGHT	NO. OF RAYS	WAVELENGTH
1	FIELD (X,Y) = (0.00, 0.00)MAX, (0.00, 0.00)DEG 764	632.8 NM
FIELD WEIGHT = 1.00		
NOMINAL RMS		= 0.5823

MANUFACTURING ERROR COMPENSATING PARAMETERS		CHANGES IN RMS FOR PLUS AND MINUS			
TYPE	CHANGE	MANUFACTURING ERRORS		DLZ S3	
DLR S1	0.0001580v	0.0000	0.0000	-0.002423	
DLR S2	0.0001580v	0.0000	0.0000	0.001628	
DSZ S1..2	0.0020000v	0.0000	0.0000	0.002000	
DLX S1	0.0020000v	0.0001	0.0001	0.000000	
DLY S1	0.0020000v	0.0001	0.0001	0.000000	
DLX S2	0.0020000v	0.0001	0.0001	0.000000	
DLY S2	0.0020000v	0.0001	0.0001	0.000000	
DLA S1	0.0000267v	0.0004	0.0004	0.000000	
DLB S1	0.0000267v	0.0004	0.0004	0.000000	
DLA S2	0.0001030v	0.0003	0.0003	0.000000	
DLB S2	0.0001030v	0.0003	0.0003	0.000000	
ZFR S1	C5 0.1767700v	0.0124	0.0124	0.000000	
ZFR S1	C6 0.1767700v	0.0123	0.0123	0.000000	
ZFR S2	C5 0.1767700v	0.0098	0.0098	0.000000	
ZFR S2	C6 0.1767700v	0.0097	0.0097	0.000000	
PROBABLE CHANGE IN RMS		0.0387			
PROBABLE CHANGE OF COMPENSATORS (+/-)				0.004086	

Units - linear dimensions in mm. angles in radians,
fringes in wavelengths at 546.1 nm.
RMS is in wavelengths at 632.8 nm.

The probable change and cumulative probability results are based on the assumption that the distribution of the RMS converges to a Gaussian form

	CUMULATIVE PROBABILITY	CHANGE IN RMS	
errors can	50.0 PCT.	0.0150	* If it is assumed that the
values	84.1 PCT.	0.0270	only take on the extreme
percent	97.7 PCT.	0.0387 *	of the tolerances, the 97.7
0.0997	99.9 PCT.	0.0502	probable change in RMS is

WEIGHT	NO. OF RAYS	WAVELENGTH
1	FIELD (X, Y) = (0.00, 0.70)MAX, (0.00, 0.35)DEG 772	632.8 NM
	FIELD WEIGHT = 1.00	
	NOMINAL RMS = 0.1535	

MANUFACTURING ERROR COMPENSATING PARAMETERS		CHANGES IN RMS FOR PLUS AND MINUS MANUFACTURING ERRORS			
TYPE	CHANGE			DLZ S3	
DLR S1	0.0001580v	0.0000	0.0000	-0.002423	
DLR S2	0.0001580v	0.0000	0.0000	0.001628	
DSZ S1..2	0.0020000v	0.0000	0.0000	0.002000	
DLX S1	0.0020000v	0.0004	0.0004	0.000000	
DLY S1	0.0020000v	0.0001	0.0007	0.000000	
DLX S2	0.0020000v	0.0004	0.0004	0.000000	
DLY S2	0.0020000v	0.0007	0.0001	0.000000	
DLA S1	0.0000267v	0.0025	0.0013	0.000000	
DLB S1	0.0000267v	0.0016	0.0016	0.000000	
DLA S2	0.0001030v	-0.0031	0.0059	0.000000	
DLB S2	0.0001030v	0.0013	0.0013	0.000000	
ZFR S1	C5 0.1767700v	0.1217	-0.1202	0.000000	
ZFR S1	C6 0.1767700v	0.0422	0.0422	0.000000	
ZFR S2	C5 0.1767700v	-0.1072	0.1081	0.000000	
ZFR S2	C6 0.1767700v	0.0341	0.0341	0.000000	
PROBABLE CHANGE IN RMS		0.1727			
PROBABLE CHANGE OF COMPENSATORS (+/-)				0.004086	

WEIGHT NO. OF RAYS WAVELENGTH
 1 FIELD (X,Y) = (0.00, 1.00)MAX, (0.00, 0.50)DEG 632.8 NM
 772

FIELD WEIGHT = 1.00

NOMINAL RMS = 0.6676

MANUFACTURING ERROR
 COMPENSATING PARAMETERS

CHANGES IN RMS FOR

PLUS AND MINUS

TYPE	CHANGE	MANUFACTURING ERRORS		DLZ S3
DLR S1	0.0001580v	0.0000	0.0000	-0.002423
DLR S2	0.0001580v	0.0000	0.0000	0.001628
DSZ S1..2	0.0020000v	0.0000	0.0000	0.002000
DLX S1	0.0020000v	0.0001	0.0001	0.000000
DLY S1	0.0020000v	0.0032	-0.0030	0.000000
DLX S2	0.0020000v	0.0001	0.0001	0.000000
DLY S2	0.0020000v	-0.0030	0.0032	0.000000
DLA S1	0.0000267v	-0.0124	0.0132	0.000000
DLB S1	0.0000267v	0.0004	0.0004	0.000000
DLA S2	0.0001030v	0.0047	-0.0040	0.000000
DLB S2	0.0001030v	0.0003	0.0003	0.000000
ZFR S1 C5	0.1767700v	0.0646	-0.0471	0.000000
ZFR S1 C6	0.1767700v	0.0110	0.0110	0.000000
ZFR S2 C5	0.1767700v	-0.0428	0.0566	0.000000
ZFR S2 C6	0.1767700v	0.0087	0.0087	0.000000

PROBABLE CHANGE IN RMS 0.0974

PROBABLE CHANGE OF COMPENSATORS (+/-) 0.004086

P E R F O R M A N C E S U M M A R Y
 POLYCHROMATIC RMS WAVEFRONT ABERRATION

WAVELENGTH WEIGHT
 632.8 NM 1

(+/-) *	RELATIVE FIELD	WEIGHT	DESIGN	DESIGN + TOL *	COMPENSATOR RANGE DLZ S3
	0.00, 0.00	1.00	0.5823	0.6210	0.004086
	0.00, 0.70	1.00	0.1535	0.3261	0.004086
	0.00, 1.00	1.00	0.6676	0.7650	0.004086

* The probable change and cumulative probability

results are based on the assumption that the distribution of the RMS converges to a Gaussian form

The compensator range is a mean plus 2 Sigma value.

Linear compensators are in units of millimeters.

Angular compensators are in radians.

Tolerance coefficients can be saved with the lens to speed up subsequent

Sensitivity Analysis for Three Mirror Anastigmat using Off-Axis Conics

C O D E V

POSITION 1

SENSITIVITY ANALYSIS POLYCHROMATIC RMS WAVEFRONT ABERRATION

TMA using off-axis conics

 FIELD (X,Y) = (0.00, 0.00)MAX, (0.00, 0.00)DEG WAVELENGTH WEIGHT NO. OF RAYS
 FIELD WEIGHT = 1.00 632.8 NM 1 772
 NOMINAL RMS = 0.0777

MANUFACTURING ERROR			CHANGES IN RMS FOR PLUS AND MINUS MANUFACTURING ERRORS		COMPENSATING PARAMETERS
TYPE		CHANGE			DLZ S7
ZFR S4	C5	0.1767700v	0.0910	0.0150	-0.005930
ZFR S4	C6	0.1767700v	0.0561	0.0561	0.000000
ZFR S5	C5	0.1767700v	-0.0033	0.0678	-0.002227
ZFR S5	C6	0.1767700v	0.0370	0.0370	0.000000
ZFR S6	C5	0.1767700v	0.0509	-0.0117	0.002788
ZFR S6	C6	0.1767700v	0.0243	0.0243	0.000000
DSZ S4..5		0.0020000v	0.0000	0.0000	-0.000300
DSZ S5..6		0.0020000v	0.0013	-0.0013	-0.001886
DLA S4		0.0000292v	-0.0057	0.0068	-0.013294
DLB S4		0.0000292v	0.0019	0.0019	0.000000
DLA S5		0.0000510v	-0.0011	0.0011	0.000489
DLB S5		0.0000510v	0.0000	0.0000	0.000000
DLA S6		0.0000590v	0.0025	-0.0024	0.003784
DLB S6		0.0000590v	0.0001	0.0001	0.000000
DLX S4		0.0020000v	0.0001	0.0001	0.000000
DLY S4		0.0020000v	0.0014	-0.0014	0.002602
DLX S5		0.0020000v	0.0001	0.0001	0.000000
DLY S5		0.0020000v	-0.0015	0.0016	-0.002807
DLX S6		0.0020000v	0.0000	0.0000	0.000000
DLY S6		0.0020000v	0.0001	-0.0001	0.000204
DLG S4		0.0004710v	0.0000	0.0000	0.000000
DLG S5		0.0004710v	0.0000	0.0000	0.000000
DLG S6		0.0004710v	0.0000	0.0000	0.000000
DLR S4		0.0001580v	0.0000	0.0000	0.000160
DLR S5		0.0001580v	0.0000	0.0000	-0.000088
DLR S6		0.0001580v	0.0000	0.0000	0.000030

PROBABLE CHANGE IN RMS 0.1550
 PROBABLE CHANGE OF COMPENSATORS (+/-) 0.014500

Units - linear dimensions in mm. angles in radians,
 fringes in wavelengths at 546.1 nm.
 RMS is in wavelengths at 632.8 nm.

The probable change and cumulative probability results are based on the assumption that the distribution of the RMS converges to a Gaussian form

CUMULATIVE PROBABILITY	CHANGE IN RMS	
50.0 PCT.	0.0705	* If it is assumed that the errors can only take on the extreme values of the tolerances, the 97.7 percent probable change in RMS is 0.2875
84.1 PCT.	0.1174	
97.7 PCT.	0.1550 *	
99.9 PCT.	0.1873	

 FIELD (X,Y) = (0.00, 0.70)MAX, (0.00, 0.35)DEG WAVELENGTH WEIGHT NO. OF RAYS
 FIELD WEIGHT = 1.00 632.8 NM 1 764
 NOMINAL RMS = 0.0580

MANUFACTURING ERROR			CHANGES IN RMS FOR PLUS AND MINUS MANUFACTURING ERRORS		COMPENSATING PARAMETERS
TYPE		CHANGE			DLZ S7
ZFR S4	C5	0.1767700v	-0.0008	0.1086	-0.005930
ZFR S4	C6	0.1767700v	0.0645	0.0645	0.000000
ZFR S5	C5	0.1767700v	0.0831	-0.0245	-0.002227

ZFR S5	C6	0.1767700v	0.0439	0.0439	0.000000
ZFR S6	C5	0.1767700v	-0.0387	0.0640	0.002788
ZFR S6	C6	0.1767700v	0.0292	0.0292	0.000000
DSZ S4..5		0.0020000v	0.0000	0.0000	-0.000300
DSZ S5..6		0.0020000v	-0.0019	0.0019	-0.001886
DLA S4		0.0000292v	0.0105	-0.0103	-0.013294
DLB S4		0.0000292v	0.0024	0.0024	0.000000
DLA S5		0.0000510v	0.0015	-0.0015	0.000489
DLB S5		0.0000510v	0.0000	0.0000	0.000000
DLA S6		0.0000590v	-0.0039	0.0039	0.003784
DLB S6		0.0000590v	0.0001	0.0001	0.000000
DLX S4		0.0020000v	0.0001	0.0001	0.000000
DLY S4		0.0020000v	-0.0023	0.0023	0.002602
DLX S5		0.0020000v	0.0001	0.0001	0.000000
DLY S5		0.0020000v	0.0025	-0.0025	-0.002807
DLX S6		0.0020000v	0.0000	0.0000	0.000000
DLY S6		0.0020000v	-0.0002	0.0002	0.000204
DLG S4		0.0004710v	0.0000	0.0000	0.000000
DLG S5		0.0004710v	0.0000	0.0000	0.000000
DLG S6		0.0004710v	0.0000	0.0000	0.000000
DLR S4		0.0001580v	0.0001	-0.0001	0.000160
DLR S5		0.0001580v	-0.0001	0.0001	-0.000088
DLR S6		0.0001580v	0.0000	0.0000	0.000030

PROBABLE CHANGE IN RMS 0.1711
PROBABLE CHANGE OF COMPENSATORS (+/-) 0.014500

FIELD (X,Y) = (0.00, 1.00)MAX, (0.00, 0.50)DEG
FIELD WEIGHT = 1.00
NOMINAL RMS = 0.1035

WAVELENGTH 632.8 NM
WEIGHT 1
NO. OF RAYS 764

MANUFACTURING ERROR			CHANGES IN RMS FOR PLUS AND MINUS MANUFACTURING ERRORS		COMPENSATING PARAMETERS
TYPE		CHANGE			DLZ S7
ZFR S4	C5	0.1767700v	-0.0624	0.1058	-0.005930
ZFR S4	C6	0.1767700v	0.0463	0.0463	0.000000
ZFR S5	C5	0.1767700v	0.0811	-0.0641	-0.002227
ZFR S5	C6	0.1767700v	0.0299	0.0299	0.000000
ZFR S6	C5	0.1767700v	-0.0546	0.0623	0.002788
ZFR S6	C6	0.1767700v	0.0189	0.0189	0.000000
DSZ S4..5		0.0020000v	0.0000	0.0000	-0.000300
DSZ S5..6		0.0020000v	-0.0018	0.0018	-0.001886
DLA S4		0.0000292v	0.0098	-0.0096	-0.013294
DLB S4		0.0000292v	0.0013	0.0013	0.000000
DLA S5		0.0000510v	0.0020	-0.0020	0.000489
DLB S5		0.0000510v	0.0000	0.0000	0.000000
DLA S6		0.0000590v	-0.0039	0.0039	0.003784
DLB S6		0.0000590v	0.0001	0.0001	0.000000
DLX S4		0.0020000v	0.0000	0.0000	0.000000
DLY S4		0.0020000v	-0.0022	0.0022	0.002602
DLX S5		0.0020000v	0.0001	0.0001	0.000000
DLY S5		0.0020000v	0.0024	-0.0024	-0.002807
DLX S6		0.0020000v	0.0000	0.0000	0.000000
DLY S6		0.0020000v	-0.0002	0.0002	0.000204
DLG S4		0.0004710v	0.0000	0.0000	0.000000
DLG S5		0.0004710v	0.0000	0.0000	0.000000
DLG S6		0.0004710v	0.0000	0.0000	0.000000
DLR S4		0.0001580v	0.0001	-0.0001	0.000160
DLR S5		0.0001580v	-0.0001	0.0001	-0.000088
DLR S6		0.0001580v	0.0000	0.0000	0.000030

PROBABLE CHANGE IN RMS 0.1606
PROBABLE CHANGE OF COMPENSATORS (+/-) 0.014500

FIELD (X,Y) = (0.70, 0.00)MAX, (0.35, 0.00)DEG
FIELD WEIGHT = 1.00
NOMINAL RMS = 0.1322

WAVELENGTH 632.8 NM
WEIGHT 1
NO. OF RAYS 764

MANUFACTURING ERROR			CHANGES IN RMS FOR PLUS AND MINUS MANUFACTURING ERRORS		COMPENSATING PARAMETERS
TYPE		CHANGE			DLZ S7
ZFR S4	C5	0.1767700v	0.0519	0.0271	-0.005930
ZFR S4	C6	0.1767700v	-0.0619	0.0987	0.000000
ZFR S5	C5	0.1767700v	0.0132	0.0353	-0.002227
ZFR S5	C6	0.1767700v	0.0755	-0.0560	0.000000

ZFR S6	C5	0.1767700v	0.0241	0.0061	0.002788
ZFR S6	C6	0.1767700v	-0.0476	0.0585	0.000000
DSZ S4..5		0.0020000v	0.0000	0.0000	-0.000300
DSZ S5..6		0.0020000v	0.0004	-0.0004	-0.001886
DLA S4		0.0000292v	-0.0008	0.0017	-0.013294
DLB S4		0.0000292v	0.0148	-0.0142	0.000000
DLA S5		0.0000510v	-0.0009	0.0009	0.000489
DLB S5		0.0000510v	-0.0018	0.0018	0.000000
DLA S6		0.0000590v	0.0007	-0.0006	0.003784
DLB S6		0.0000590v	-0.0036	0.0036	0.000000
DLX S4		0.0020000v	0.0027	-0.0027	0.000000
DLY S4		0.0020000v	0.0004	-0.0003	0.002602
DLX S5		0.0020000v	-0.0029	0.0029	0.000000
DLY S5		0.0020000v	-0.0004	0.0004	-0.002807
DLX S6		0.0020000v	0.0002	-0.0002	0.000000
DLY S6		0.0020000v	0.0001	-0.0001	0.000204
DLG S4		0.0004710v	0.0000	0.0000	0.000000
DLG S5		0.0004710v	0.0000	0.0000	0.000000
DLG S6		0.0004710v	0.0000	0.0000	0.000000
DLR S4		0.0001580v	0.0000	0.0000	0.000160
DLR S5		0.0001580v	0.0000	0.0000	-0.000088
DLR S6		0.0001580v	0.0000	0.0000	0.000030

PROBABLE CHANGE IN RMS 0.1530
PROBABLE CHANGE OF COMPENSATORS (+/-) 0.014500

FIELD (X,Y) = (1.00, 0.00)MAX, (0.50, 0.00)DEG
FIELD WEIGHT = 1.00
NOMINAL RMS = 0.1762

WAVELENGTH 632.8 NM WEIGHT 1 NO. OF RAYS 761

MANUFACTURING ERROR		CHANGES IN RMS FOR PLUS AND MINUS MANUFACTURING ERRORS		COMPENSATING PARAMETERS	
TYPE	CHANGE			DLZ S7	
ZFR S4	C5	0.1767700v	0.0273	0.0355	-0.005930
ZFR S4	C6	0.1767700v	-0.0862	0.1015	0.000000
ZFR S5	C5	0.1767700v	0.0218	0.0162	-0.002227
ZFR S5	C6	0.1767700v	0.0780	-0.0696	0.000000
ZFR S6	C5	0.1767700v	0.0092	0.0142	0.002788
ZFR S6	C6	0.1767700v	-0.0559	0.0607	0.000000
DSZ S4..5		0.0020000v	0.0000	0.0000	-0.000300
DSZ S5..6		0.0020000v	0.0000	0.0000	-0.001886
DLA S4		0.0000292v	0.0013	-0.0006	-0.013294
DLB S4		0.0000292v	0.0157	-0.0154	0.000000
DLA S5		0.0000510v	-0.0010	0.0010	0.000489
DLB S5		0.0000510v	-0.0018	0.0018	0.000000
DLA S6		0.0000590v	-0.0001	0.0002	0.003784
DLB S6		0.0000590v	-0.0038	0.0038	0.000000
DLX S4		0.0020000v	0.0029	-0.0029	0.000000
DLY S4		0.0020000v	-0.0001	0.0001	0.002602
DLX S5		0.0020000v	-0.0031	0.0031	0.000000
DLY S5		0.0020000v	0.0001	-0.0001	-0.002807
DLX S6		0.0020000v	0.0002	-0.0002	0.000000
DLY S6		0.0020000v	0.0000	0.0000	0.000204
DLG S4		0.0004710v	0.0000	0.0000	0.000000
DLG S5		0.0004710v	0.0000	0.0000	0.000000
DLG S6		0.0004710v	0.0000	0.0000	0.000000
DLR S4		0.0001580v	0.0000	0.0000	0.000160
DLR S5		0.0001580v	0.0000	0.0000	-0.000088
DLR S6		0.0001580v	0.0000	0.0000	0.000030

PROBABLE CHANGE IN RMS 0.1535
PROBABLE CHANGE OF COMPENSATORS (+/-) 0.014500

FIELD (X,Y) = (0.70, 0.70)MAX, (0.35, 0.35)DEG
FIELD WEIGHT = 1.00
NOMINAL RMS = 0.1638

WAVELENGTH 632.8 NM WEIGHT 1 NO. OF RAYS 763

MANUFACTURING ERROR		CHANGES IN RMS FOR PLUS AND MINUS MANUFACTURING ERRORS		COMPENSATING PARAMETERS	
TYPE	CHANGE			DLZ S7	
ZFR S4	C5	0.1767700v	-0.0185	0.0744	-0.005930
ZFR S4	C6	0.1767700v	-0.0715	0.0977	0.000000
ZFR S5	C5	0.1767700v	0.0544	-0.0213	-0.002227
ZFR S5	C6	0.1767700v	0.0750	-0.0606	0.000000
ZFR S6	C5	0.1767700v	-0.0207	0.0404	0.002788

ZFR S6	C6	0.1767700v	-0.0494	0.0577	0.000000
DSZ S4..5		0.0020000v	0.0000	0.0000	-0.000300
DSZ S5..6		0.0020000v	-0.0009	0.0010	-0.001886
DLA S4		0.0000292v	0.0058	-0.0053	-0.013294
DLB S4		0.0000292v	0.0145	-0.0140	0.000000
DLA S5		0.0000510v	0.0003	-0.0003	0.000489
DLB S5		0.0000510v	-0.0010	0.0010	0.000000
DLA S6		0.0000590v	-0.0020	0.0021	0.003784
DLB S6		0.0000590v	-0.0034	0.0034	0.000000
DLX S4		0.0020000v	0.0027	-0.0027	0.000000
DLY S4		0.0020000v	-0.0012	0.0012	0.002602
DLX S5		0.0020000v	-0.0029	0.0029	0.000000
DLY S5		0.0020000v	0.0013	-0.0013	-0.002807
DLX S6		0.0020000v	0.0002	-0.0002	0.000000
DLY S6		0.0020000v	-0.0001	0.0001	0.000204
DLG S4		0.0004710v	0.0000	0.0000	0.000000
DLG S5		0.0004710v	0.0000	0.0000	0.000000
DLG S6		0.0004710v	0.0000	0.0000	0.000000
DLR S4		0.0001580v	0.0000	0.0000	0.000160
DLR S5		0.0001580v	0.0000	0.0000	-0.000088
DLR S6		0.0001580v	0.0000	0.0000	0.000030

PROBABLE CHANGE IN RMS 0.1601
PROBABLE CHANGE OF COMPENSATORS (+/-) 0.014500

FIELD (X,Y) = (0.70,-0.70)MAX, (0.35, -0.35)DEG
FIELD WEIGHT = 1.00
WAVELENGTH 632.8 NM WEIGHT 1 NO. OF RAYS 758
NOMINAL RMS = 0.1963

MANUFACTURING ERROR		CHANGES IN RMS FOR PLUS AND MINUS MANUFACTURING ERRORS		COMPENSATING PARAMETERS
TYPE	CHANGE			DLZ S7
ZFR S4	C5	0.1767700v	0.0822 -0.0426	-0.005930
ZFR S4	C6	0.1767700v	-0.0197 0.0659	0.000000
ZFR S5	C5	0.1767700v	-0.0395 0.0616	-0.002227
ZFR S5	C6	0.1767700v	0.0481 -0.0204	0.000000
ZFR S6	C5	0.1767700v	0.0470 -0.0337	0.002788
ZFR S6	C6	0.1767700v	-0.0192 0.0364	0.000000
DSZ S4..5		0.0020000v	0.0000 0.0000	-0.000300
DSZ S5..6		0.0020000v	0.0013 -0.0013	-0.001886
DLA S4		0.0000292v	-0.0068 0.0073	-0.013294
DLB S4		0.0000292v	0.0083 -0.0071	0.000000
DLA S5		0.0000510v	-0.0008 0.0008	0.000489
DLB S5		0.0000510v	-0.0015 0.0015	0.000000
DLA S6		0.0000590v	0.0024 -0.0024	0.003784
DLB S6		0.0000590v	-0.0021 0.0021	0.000000
DLX S4		0.0020000v	0.0014 -0.0014	0.000000
DLY S4		0.0020000v	0.0015 -0.0015	0.002602
DLX S5		0.0020000v	-0.0015 0.0015	0.000000
DLY S5		0.0020000v	-0.0017 0.0017	-0.002807
DLX S6		0.0020000v	0.0001 -0.0001	0.000000
DLY S6		0.0020000v	0.0002 -0.0002	0.000204
DLG S4		0.0004710v	0.0000 0.0000	0.000000
DLG S5		0.0004710v	0.0000 0.0000	0.000000
DLG S6		0.0004710v	0.0000 0.0000	0.000000
DLR S4		0.0001580v	0.0000 0.0000	0.000160
DLR S5		0.0001580v	0.0000 0.0000	-0.000088
DLR S6		0.0001580v	0.0000 0.0000	0.000030

PROBABLE CHANGE IN RMS 0.1408
PROBABLE CHANGE OF COMPENSATORS (+/-) 0.014500

FIELD (X,Y) = (0.00,-0.70)MAX, (0.00, -0.35)DEG
FIELD WEIGHT = 1.00
WAVELENGTH 632.8 NM WEIGHT 1 NO. OF RAYS 764
NOMINAL RMS = 0.1948

MANUFACTURING ERROR		CHANGES IN RMS FOR PLUS AND MINUS MANUFACTURING ERRORS		COMPENSATING PARAMETERS
TYPE	CHANGE			DLZ S7
ZFR S4	C5	0.1767700v	0.0932 -0.0634	-0.005930
ZFR S4	C6	0.1767700v	0.0280 0.0280	0.000000
ZFR S5	C5	0.1767700v	-0.0549 0.0707	-0.002227
ZFR S5	C6	0.1767700v	0.0171 0.0171	0.000000
ZFR S6	C5	0.1767700v	0.0546 -0.0454	0.002788
ZFR S6	C6	0.1767700v	0.0108 0.0108	0.000000

DSZ S4..5	0.0020000v	0.0000	0.0000	-0.000300
DSZ S5..6	0.0020000v	0.0016	-0.0016	-0.001886
DLA S4	0.0000292v	-0.0087	0.0090	-0.013294
DLB S4	0.0000292v	0.0008	0.0008	0.000000
DLA S5	0.0000510v	-0.0005	0.0005	0.000489
DLB S5	0.0000510v	0.0000	0.0000	0.000000
DLA S6	0.0000590v	0.0030	-0.0029	0.003784
DLB S6	0.0000590v	0.0000	0.0000	0.000000
DLX S4	0.0020000v	0.0000	0.0000	0.000000
DLY S4	0.0020000v	0.0019	-0.0019	0.002602
DLX S5	0.0020000v	0.0000	0.0000	0.000000
DLY S5	0.0020000v	-0.0020	0.0021	-0.002807
DLX S6	0.0020000v	0.0000	0.0000	0.000000
DLY S6	0.0020000v	0.0002	-0.0002	0.000204
DLG S4	0.0004710v	0.0000	0.0000	0.000000
DLG S5	0.0004710v	0.0000	0.0000	0.000000
DLG S6	0.0004710v	0.0000	0.0000	0.000000
DLR S4	0.0001580v	-0.0001	0.0001	0.000160
DLR S5	0.0001580v	0.0000	0.0000	-0.000088
DLR S6	0.0001580v	0.0000	0.0000	0.000030

PROBABLE CHANGE IN RMS 0.1419
PROBABLE CHANGE OF COMPENSATORS (+/-) 0.014500

FIELD (X,Y) = (0.00,-1.00)MAX, (0.00, -0.50)DEG
FIELD WEIGHT = 1.00
NOMINAL RMS = 0.2416

WAVELENGTH 632.8 NM WEIGHT 1 NO. OF RAYS 760

MANUFACTURING ERROR			CHANGES IN RMS FOR PLUS AND MINUS MANUFACTURING ERRORS		COMPENSATING PARAMETERS
TYPE		CHANGE			DLZ S7
ZFR S4	C5	0.1767700v	0.0931	-0.0717	-0.005930
ZFR S4	C6	0.1767700v	0.0228	0.0228	0.000000
ZFR S5	C5	0.1767700v	-0.0593	0.0707	-0.002227
ZFR S5	C6	0.1767700v	0.0138	0.0138	0.000000
ZFR S6	C5	0.1767700v	0.0549	-0.0481	0.002788
ZFR S6	C6	0.1767700v	0.0087	0.0087	0.000000
DSZ S4..5		0.0020000v	0.0000	0.0000	-0.000300
DSZ S5..6		0.0020000v	0.0016	-0.0016	-0.001886
DLA S4		0.0000292v	-0.0091	0.0094	-0.013294
DLB S4		0.0000292v	0.0006	0.0006	0.000000
DLA S5		0.0000510v	-0.0003	0.0003	0.000489
DLB S5		0.0000510v	0.0000	0.0000	0.000000
DLA S6		0.0000590v	0.0029	-0.0029	0.003784
DLB S6		0.0000590v	0.0000	0.0000	0.000000
DLX S4		0.0020000v	0.0000	0.0000	0.000000
DLY S4		0.0020000v	0.0019	-0.0019	0.002602
DLX S5		0.0020000v	0.0000	0.0000	0.000000
DLY S5		0.0020000v	-0.0021	0.0021	-0.002807
DLX S6		0.0020000v	0.0000	0.0000	0.000000
DLY S6		0.0020000v	0.0002	-0.0002	0.000204
DLG S4		0.0004710v	0.0000	0.0000	0.000000
DLG S5		0.0004710v	0.0000	0.0000	0.000000
DLG S6		0.0004710v	0.0000	0.0000	0.000000
DLR S4		0.0001580v	-0.0001	0.0001	0.000160
DLR S5		0.0001580v	0.0000	0.0000	-0.000088
DLR S6		0.0001580v	0.0000	0.0000	0.000030

PROBABLE CHANGE IN RMS 0.1411
PROBABLE CHANGE OF COMPENSATORS (+/-) 0.014500

FIELD (X,Y) = (-0.70, 0.00)MAX, (-0.35, 0.00)DEG
FIELD WEIGHT = 1.00
NOMINAL RMS = 0.1322

WAVELENGTH 632.8 NM WEIGHT 1 NO. OF RAYS 764

MANUFACTURING ERROR			CHANGES IN RMS FOR PLUS AND MINUS MANUFACTURING ERRORS		COMPENSATING PARAMETERS
TYPE		CHANGE			DLZ S7
ZFR S4	C5	0.1767700v	0.0519	0.0271	-0.005930
ZFR S4	C6	0.1767700v	0.0987	-0.0619	0.000000
ZFR S5	C5	0.1767700v	0.0132	0.0353	-0.002227
ZFR S5	C6	0.1767700v	-0.0560	0.0755	0.000000
ZFR S6	C5	0.1767700v	0.0241	0.0061	0.002788
ZFR S6	C6	0.1767700v	0.0585	-0.0476	0.000000
DSZ S4..5		0.0020000v	0.0000	0.0000	-0.000300

DSZ S5..6	0.0020000v	0.0004	-0.0004	-0.001886
DLA S4	0.0000292v	-0.0008	0.0017	-0.013294
DLB S4	0.0000292v	-0.0142	0.0148	0.000000
DLA S5	0.0000510v	-0.0009	0.0009	0.000489
DLB S5	0.0000510v	0.0018	-0.0018	0.000000
DLA S6	0.0000590v	0.0007	-0.0006	0.003784
DLB S6	0.0000590v	0.0036	-0.0036	0.000000
DLX S4	0.0020000v	-0.0027	0.0027	0.000000
DLY S4	0.0020000v	0.0004	-0.0003	0.002602
DLX S5	0.0020000v	0.0029	-0.0029	0.000000
DLY S5	0.0020000v	-0.0004	0.0004	-0.002807
DLX S6	0.0020000v	-0.0002	0.0002	0.000000
DLY S6	0.0020000v	0.0001	-0.0001	0.000204
DLG S4	0.0004710v	0.0000	0.0000	0.000000
DLG S5	0.0004710v	0.0000	0.0000	0.000000
DLG S6	0.0004710v	0.0000	0.0000	0.000000
DLR S4	0.0001580v	0.0000	0.0000	0.000160
DLR S5	0.0001580v	0.0000	0.0000	-0.000088
DLR S6	0.0001580v	0.0000	0.0000	0.000030

PROBABLE CHANGE IN RMS 0.1530
PROBABLE CHANGE OF COMPENSATORS (+/-) 0.014500

FIELD (X,Y) = (-1.00, 0.00)MAX, (-0.50, 0.00)DEG
FIELD WEIGHT = 1.00
NOMINAL RMS = 0.1762

WAVELENGTH 632.8 NM WEIGHT 1 NO. OF RAYS 761

MANUFACTURING ERROR			CHANGES IN RMS FOR PLUS AND MINUS MANUFACTURING ERRORS		COMPENSATING PARAMETERS
TYPE		CHANGE			DLZ S7
ZFR S4	C5	0.1767700v	0.0273	0.0355	-0.005930
ZFR S4	C6	0.1767700v	0.1015	-0.0862	0.000000
ZFR S5	C5	0.1767700v	0.0218	0.0162	-0.002227
ZFR S5	C6	0.1767700v	-0.0696	0.0780	0.000000
ZFR S6	C5	0.1767700v	0.0092	0.0142	0.002788
ZFR S6	C6	0.1767700v	0.0607	-0.0559	0.000000
DSZ S4..5		0.0020000v	0.0000	0.0000	-0.000300
DSZ S5..6		0.0020000v	0.0000	0.0000	-0.001886
DLA S4		0.0000292v	0.0013	-0.0006	-0.013294
DLB S4		0.0000292v	-0.0154	0.0157	0.000000
DLA S5		0.0000510v	-0.0010	0.0010	0.000489
DLB S5		0.0000510v	0.0018	-0.0018	0.000000
DLA S6		0.0000590v	-0.0001	0.0002	0.003784
DLB S6		0.0000590v	0.0038	-0.0038	0.000000
DLX S4		0.0020000v	-0.0029	0.0029	0.000000
DLY S4		0.0020000v	-0.0001	0.0001	0.002602
DLX S5		0.0020000v	0.0031	-0.0031	0.000000
DLY S5		0.0020000v	0.0001	-0.0001	-0.002807
DLX S6		0.0020000v	-0.0002	0.0002	0.000000
DLY S6		0.0020000v	0.0000	0.0000	0.000204
DLG S4		0.0004710v	0.0000	0.0000	0.000000
DLG S5		0.0004710v	0.0000	0.0000	0.000000
DLG S6		0.0004710v	0.0000	0.0000	0.000000
DLR S4		0.0001580v	0.0000	0.0000	0.000160
DLR S5		0.0001580v	0.0000	0.0000	-0.000088
DLR S6		0.0001580v	0.0000	0.0000	0.000030

PROBABLE CHANGE IN RMS 0.1535
PROBABLE CHANGE OF COMPENSATORS (+/-) 0.014500

FIELD (X,Y) = (-0.70, 0.70)MAX, (-0.35, 0.35)DEG
FIELD WEIGHT = 1.00
NOMINAL RMS = 0.1638

WAVELENGTH 632.8 NM WEIGHT 1 NO. OF RAYS 763

MANUFACTURING ERROR			CHANGES IN RMS FOR PLUS AND MINUS MANUFACTURING ERRORS		COMPENSATING PARAMETERS
TYPE		CHANGE			DLZ S7
ZFR S4	C5	0.1767700v	-0.0185	0.0744	-0.005930
ZFR S4	C6	0.1767700v	0.0977	-0.0715	0.000000
ZFR S5	C5	0.1767700v	0.0544	-0.0213	-0.002227
ZFR S5	C6	0.1767700v	-0.0606	0.0750	0.000000
ZFR S6	C5	0.1767700v	-0.0207	0.0404	0.002788
ZFR S6	C6	0.1767700v	0.0577	-0.0494	0.000000
DSZ S4..5		0.0020000v	0.0000	0.0000	-0.000300
DSZ S5..6		0.0020000v	-0.0009	0.0010	-0.001886

DLA S4	0.0000292v	0.0058	-0.0053	-0.013294
DLB S4	0.0000292v	-0.0140	0.0145	0.000000
DLA S5	0.0000510v	0.0003	-0.0003	0.000489
DLB S5	0.0000510v	0.0010	-0.0010	0.000000
DLA S6	0.0000590v	-0.0020	0.0021	0.003784
DLB S6	0.0000590v	0.0034	-0.0034	0.000000
DLX S4	0.0020000v	-0.0027	0.0027	0.000000
DLY S4	0.0020000v	-0.0012	0.0012	0.002602
DLX S5	0.0020000v	0.0029	-0.0029	0.000000
DLY S5	0.0020000v	0.0013	-0.0013	-0.002807
DLX S6	0.0020000v	-0.0002	0.0002	0.000000
DLY S6	0.0020000v	-0.0001	0.0001	0.000204
DLG S4	0.0004710v	0.0000	0.0000	0.000000
DLG S5	0.0004710v	0.0000	0.0000	0.000000
DLG S6	0.0004710v	0.0000	0.0000	0.000000
DLR S4	0.0001580v	0.0000	0.0000	0.000160
DLR S5	0.0001580v	0.0000	0.0000	-0.000088
DLR S6	0.0001580v	0.0000	0.0000	0.000030

PROBABLE CHANGE IN RMS 0.1601
PROBABLE CHANGE OF COMPENSATORS (+/-) 0.014500

WAVELENGTH WEIGHT NO. OF RAYS
FIELD (X,Y) = (-0.70,-0.70)MAX, (-0.35, -0.35)DEG 632.8 NM 1 758
FIELD WEIGHT = 1.00
NOMINAL RMS = 0.1963

MANUFACTURING ERROR			CHANGES IN RMS FOR PLUS AND MINUS MANUFACTURING ERRORS		COMPENSATING PARAMETERS
TYPE		CHANGE			DLZ S7
ZFR S4	C5	0.1767700v	0.0822	-0.0426	-0.005930
ZFR S4	C6	0.1767700v	0.0659	-0.0197	0.000000
ZFR S5	C5	0.1767700v	-0.0395	0.0616	-0.002227
ZFR S5	C6	0.1767700v	-0.0204	0.0481	0.000000
ZFR S6	C5	0.1767700v	0.0470	-0.0337	0.002788
ZFR S6	C6	0.1767700v	0.0364	-0.0192	0.000000
DSZ S4..5		0.0020000v	0.0000	0.0000	-0.000300
DSZ S5..6		0.0020000v	0.0013	-0.0013	-0.001886
DLA S4		0.0000292v	-0.0068	0.0073	-0.013294
DLB S4		0.0000292v	-0.0071	0.0083	0.000000
DLA S5		0.0000510v	-0.0008	0.0008	0.000489
DLB S5		0.0000510v	0.0015	-0.0015	0.000000
DLA S6		0.0000590v	0.0024	-0.0024	0.003784
DLB S6		0.0000590v	0.0021	-0.0021	0.000000
DLX S4		0.0020000v	-0.0014	0.0014	0.000000
DLY S4		0.0020000v	0.0015	-0.0015	0.002602
DLX S5		0.0020000v	0.0015	-0.0015	0.000000
DLY S5		0.0020000v	-0.0017	0.0017	-0.002807
DLX S6		0.0020000v	-0.0001	0.0001	0.000000
DLY S6		0.0020000v	0.0002	-0.0002	0.000204
DLG S4		0.0004710v	0.0000	0.0000	0.000000
DLG S5		0.0004710v	0.0000	0.0000	0.000000
DLG S6		0.0004710v	0.0000	0.0000	0.000000
DLR S4		0.0001580v	0.0000	0.0000	0.000160
DLR S5		0.0001580v	0.0000	0.0000	-0.000088
DLR S6		0.0001580v	0.0000	0.0000	0.000030

PROBABLE CHANGE IN RMS 0.1408
PROBABLE CHANGE OF COMPENSATORS (+/-) 0.014500

PERFORMANCE SUMMARY
POLYCHROMATIC RMS WAVEFRONT ABERRATION

RELATIVE FIELD	WEIGHT	DESIGN	DESIGN + TOL *	COMPENSATOR RANGE (+/-) *
				DLZ S7
0.00, 0.00	1.00	0.0777	0.2326	0.014500
0.00, 0.70	1.00	0.0580	0.2291	0.014500
0.00, 1.00	1.00	0.1035	0.2642	0.014500
0.70, 0.00	1.00	0.1322	0.2852	0.014500
1.00, 0.00	1.00	0.1762	0.3297	0.014500
0.70, 0.70	1.00	0.1638	0.3239	0.014500
0.70,-0.70	1.00	0.1963	0.3371	0.014500
0.00,-0.70	1.00	0.1948	0.3368	0.014500
0.00,-1.00	1.00	0.2416	0.3828	0.014500
-0.70, 0.00	1.00	0.1322	0.2852	0.014500
-1.00, 0.00	1.00	0.1762	0.3297	0.014500
-0.70, 0.70	1.00	0.1638	0.3239	0.014500

-0.70,-0.70 1.00 0.1963 0.3371 0.014500

* The probable change and cumulative probability results are based on the assumption that the distribution of the RMS converges to a Gaussian form

The compensator range is a mean plus 2 Sigma value.
Linear compensators are in units of millimeters.
Angular compensators are in radians.

Sensitivity Analysis for Three Mirror Anastigmat using On-axis Zernike Polynomial

C O D E V

S E N S I T I V I T Y A N A L Y S I S
POLYCHROMATIC RMS WAVEFRONT ABERRATION

TMA using on-axis Zernike Surfaces

```
-----
FIELD (X,Y) = ( 0.00, 0.00)MAX, ( 0.00, 0.00)DEG    WAVELENGTH  WEIGHT  NO. OF RAYS
FIELD WEIGHT = 1.00                                632.8 NM   1         780
NOMINAL RMS = 0.0112
-----
```

MANUFACTURING ERROR			CHANGES IN RMS FOR PLUS AND MINUS MANUFACTURING ERRORS		COMPENSATING PARAMETERS
TYPE		CHANGE			DLZ S6
ZFR S3	C5	0.1767700v	0.1123	0.1088	0.000418
ZFR S3	C6	0.1767700v	0.1114	0.1106	0.000314
ZFR S4	C5	0.1767700v	0.0782	0.0815	0.000191
ZFR S4	C6	0.1767700v	0.0798	0.0806	-0.000289
ZFR S5	C5	0.1767700v	0.0524	0.0490	0.000883
ZFR S5	C6	0.1767700v	0.0513	0.0506	0.000222
DSZ S3..4		0.0020000v	0.0000	0.0000	-0.000117
DSZ S4..5		0.0020000v	0.0002	-0.0001	-0.003322
DLA S3		0.0000286v	0.0094	0.0123	0.000078
DLB S3		0.0000286v	0.0106	0.0112	-0.000045
DLA S4		0.0000556v	0.0007	0.0023	-0.003742
DLB S4		0.0000556v	0.0148	0.0141	0.000032
DLA S5		0.0000588v	0.0025	0.0008	0.005937
DLB S5		0.0000588v	0.0020	0.0016	0.000027
DLX S3		0.0020000v	0.0001	0.0002	-0.000006
DLY S3		0.0020000v	0.0011	0.0001	0.001433
DLX S4		0.0020000v	0.0001	0.0000	0.000004
DLY S4		0.0020000v	0.0002	0.0015	-0.001844
DLX S5		0.0020000v	0.0001	0.0000	0.000002
DLY S5		0.0020000v	0.0002	-0.0001	-0.000011
DLG S3		0.0000286v	0.0001	0.0001	-0.000003
DLG S4		0.0000556v	0.0003	0.0004	-0.000006
DLG S5		0.0000588v	0.0001	0.0001	0.000004
DLR S3		0.0001580v	0.0000	0.0000	0.000227
DLR S4		0.0001580v	0.0000	0.0000	-0.000146
DLR S5		0.0001580v	0.0000	0.0000	0.000036
PROBABLE CHANGE IN RMS			0.2101		
PROBABLE CHANGE OF COMPENSATORS (+/-)					0.007352
Units - linear dimensions in mm. angles in radians,					
fringes in wavelengths at 546.1 nm.					
RMS is in wavelengths at 632.8 nm.					

The probable change and cumulative probability results are based on the assumption that the distribution of the RMS converges to a Gaussian form

CUMULATIVE PROBABILITY	CHANGE IN RMS	
50.0 PCT.	0.1236	* If it is assumed that the errors can only take on the extreme values of the tolerances, the 97.7 percent probable change in RMS is 0.3570
84.1 PCT.	0.1720	
97.7 PCT.	0.2101 *	
99.9 PCT.	0.2425	

```
-----
FIELD (X,Y) = ( 0.00, 0.70)MAX, ( 0.00, 0.35)DEG    WAVELENGTH  WEIGHT  NO. OF RAYS
FIELD WEIGHT = 1.00                                632.8 NM   1         777
NOMINAL RMS = 0.0045
-----
```

MANUFACTURING ERROR			CHANGES IN RMS FOR PLUS AND MINUS MANUFACTURING ERRORS		COMPENSATING PARAMETERS
TYPE		CHANGE			DLZ S6
ZFR S3	C5	0.1767700v	0.1194	0.1155	0.000418
ZFR S3	C6	0.1767700v	0.1154	0.1151	0.000314
ZFR S4	C5	0.1767700v	0.0850	0.0889	0.000191
ZFR S4	C6	0.1767700v	0.0851	0.0854	-0.000289
ZFR S5	C5	0.1767700v	0.0592	0.0553	0.000883

ZFR S5	C6	0.1767700v	0.0563	0.0561	0.000222
DSZ S3..4		0.0020000v	-0.0002	0.0002	-0.000117
DSZ S4..5		0.0020000v	0.0005	-0.0003	-0.003322
DLA S3		0.0000286v	0.0128	0.0165	0.000078
DLB S3		0.0000286v	0.0142	0.0145	-0.000045
DLA S4		0.0000556v	0.0017	0.0054	-0.003742
DLB S4		0.0000556v	0.0180	0.0177	0.000032
DLA S5		0.0000588v	0.0044	0.0018	0.005937
DLB S5		0.0000588v	0.0033	0.0031	0.000027
DLX S3		0.0020000v	0.0003	0.0004	-0.000006
DLY S3		0.0020000v	0.0025	0.0000	0.001433
DLX S4		0.0020000v	0.0001	0.0001	0.000004
DLY S4		0.0020000v	0.0004	0.0032	-0.001844
DLX S5		0.0020000v	0.0001	0.0001	0.000002
DLY S5		0.0020000v	0.0005	-0.0004	-0.000011
DLG S3		0.0000286v	0.0002	0.0002	-0.000003
DLG S4		0.0000556v	0.0006	0.0007	-0.000006
DLG S5		0.0000588v	0.0001	0.0001	0.000004
DLR S3		0.0001580v	0.0000	0.0000	0.000227
DLR S4		0.0001580v	0.0000	0.0000	-0.000146
DLR S5		0.0001580v	0.0000	0.0000	0.000036

PROBABLE CHANGE IN RMS 0.2158
PROBABLE CHANGE OF COMPENSATORS (+/-) 0.007352

FIELD (X,Y) = (0.00, 1.00)MAX, (0.00, 0.50)DEG WAVELENGTH 632.8 NM WEIGHT 1 NO. OF RAYS 773
FIELD WEIGHT = 1.00
NOMINAL RMS = 0.0065

MANUFACTURING ERROR			CHANGES IN RMS FOR PLUS AND MINUS MANUFACTURING ERRORS		COMPENSATING PARAMETERS
TYPE		CHANGE			DLZ S6
ZFR S3	C5	0.1767700v	0.1192	0.1100	0.000418
ZFR S3	C6	0.1767700v	0.1127	0.1127	0.000314
ZFR S4	C5	0.1767700v	0.0800	0.0892	0.000191
ZFR S4	C6	0.1767700v	0.0830	0.0830	-0.000289
ZFR S5	C5	0.1767700v	0.0597	0.0504	0.000883
ZFR S5	C6	0.1767700v	0.0542	0.0542	0.000222
DSZ S3..4		0.0020000v	-0.0002	0.0002	-0.000117
DSZ S4..5		0.0020000v	0.0006	-0.0006	-0.003322
DLA S3		0.0000286v	0.0081	0.0169	0.000078
DLB S3		0.0000286v	0.0126	0.0126	-0.000045
DLA S4		0.0000556v	-0.0010	0.0061	-0.003742
DLB S4		0.0000556v	0.0159	0.0159	0.000032
DLA S5		0.0000588v	0.0054	-0.0020	0.005937
DLB S5		0.0000588v	0.0025	0.0025	0.000027
DLX S3		0.0020000v	0.0003	0.0003	-0.000006
DLY S3		0.0020000v	0.0030	-0.0018	0.001433
DLX S4		0.0020000v	0.0001	0.0001	0.000004
DLY S4		0.0020000v	-0.0018	0.0038	-0.001844
DLX S5		0.0020000v	0.0001	0.0001	0.000002
DLY S5		0.0020000v	0.0007	-0.0006	-0.000011
DLG S3		0.0000286v	0.0002	0.0001	-0.000003
DLG S4		0.0000556v	0.0003	0.0005	-0.000006
DLG S5		0.0000588v	0.0000	0.0001	0.000004
DLR S3		0.0001580v	0.0000	0.0000	0.000227
DLR S4		0.0001580v	0.0000	0.0000	-0.000146
DLR S5		0.0001580v	0.0000	0.0000	0.000036

PROBABLE CHANGE IN RMS 0.2129
PROBABLE CHANGE OF COMPENSATORS (+/-) 0.007352

FIELD (X,Y) = (0.70, 0.00)MAX, (0.35, 0.00)DEG WAVELENGTH 632.8 NM WEIGHT 1 NO. OF RAYS 768
FIELD WEIGHT = 1.00
NOMINAL RMS = 0.0045

MANUFACTURING ERROR			CHANGES IN RMS FOR PLUS AND MINUS MANUFACTURING ERRORS		COMPENSATING PARAMETERS
TYPE		CHANGE			DLZ S6
ZFR S3	C5	0.1767700v	0.1148	0.1148	0.000418
ZFR S3	C6	0.1767700v	0.1163	0.1150	0.000314
ZFR S4	C5	0.1767700v	0.0845	0.0845	0.000191
ZFR S4	C6	0.1767700v	0.0845	0.0858	-0.000289

ZFR S5	C5	0.1767700v	0.0555	0.0556	0.000883
ZFR S5	C6	0.1767700v	0.0566	0.0553	0.000222
DSZ S3..4		0.0020000v	0.0000	0.0000	-0.000117
DSZ S4..5		0.0020000v	0.0001	0.0002	-0.003322
DLA S3		0.0000286v	0.0148	0.0147	0.000078
DLB S3		0.0000286v	0.0142	0.0155	-0.000045
DLA S4		0.0000556v	0.0031	0.0029	-0.003742
DLB S4		0.0000556v	0.0195	0.0180	0.000032
DLA S5		0.0000588v	0.0032	0.0033	0.005937
DLB S5		0.0000588v	0.0041	0.0027	0.000027
DLX S3		0.0020000v	0.0001	0.0007	-0.000006
DLY S3		0.0020000v	0.0013	0.0014	0.001433
DLX S4		0.0020000v	0.0002	0.0000	0.000004
DLY S4		0.0020000v	0.0019	0.0018	-0.001844
DLX S5		0.0020000v	0.0003	-0.0001	0.000002
DLY S5		0.0020000v	0.0001	0.0001	-0.000011
DLG S3		0.0000286v	0.0002	0.0003	-0.000003
DLG S4		0.0000556v	0.0003	0.0013	-0.000006
DLG S5		0.0000588v	0.0005	0.0000	0.000004
DLR S3		0.0001580v	0.0000	0.0000	0.000227
DLR S4		0.0001580v	0.0000	0.0000	-0.000146
DLR S5		0.0001580v	0.0000	0.0000	0.000036

PROBABLE CHANGE IN RMS 0.2131
PROBABLE CHANGE OF COMPENSATORS (+/-) 0.007352

FIELD (X,Y) = (1.00, 0.00)MAX, (0.50, 0.00)DEG
FIELD WEIGHT = 1.00
NOMINAL RMS = 0.0061

WAVELENGTH 632.8 NM
WEIGHT 1
NO. OF RAYS 764

MANUFACTURING ERROR		CHANGES IN RMS FOR PLUS AND MINUS MANUFACTURING ERRORS		COMPENSATING PARAMETERS	
TYPE	CHANGE			DLZ S6	
ZFR S3	C5	0.1767700v	0.1103	0.1150	0.000418
ZFR S3	C6	0.1767700v	0.1143	0.1127	0.000314
ZFR S4	C5	0.1767700v	0.0848	0.0802	0.000191
ZFR S4	C6	0.1767700v	0.0824	0.0840	-0.000289
ZFR S5	C5	0.1767700v	0.0514	0.0560	0.000883
ZFR S5	C6	0.1767700v	0.0550	0.0534	0.000222
DSZ S3..4		0.0020000v	0.0001	-0.0001	-0.000117
DSZ S4..5		0.0020000v	-0.0003	0.0005	-0.003322
DLA S3		0.0000286v	0.0157	0.0111	0.000078
DLB S3		0.0000286v	0.0128	0.0144	-0.000045
DLA S4		0.0000556v	0.0040	0.0005	-0.003742
DLB S4		0.0000556v	0.0182	0.0166	0.000032
DLA S5		0.0000588v	0.0007	0.0042	0.005937
DLB S5		0.0000588v	0.0031	0.0025	0.000027
DLX S3		0.0020000v	0.0001	0.0005	-0.000006
DLY S3		0.0020000v	-0.0003	0.0022	0.001433
DLX S4		0.0020000v	0.0002	-0.0001	0.000004
DLY S4		0.0020000v	0.0028	-0.0001	-0.001844
DLX S5		0.0020000v	0.0002	0.0000	0.000002
DLY S5		0.0020000v	-0.0003	0.0004	-0.000011
DLG S3		0.0000286v	0.0001	0.0002	-0.000003
DLG S4		0.0000556v	0.0005	0.0007	-0.000006
DLG S5		0.0000588v	0.0002	0.0002	0.000004
DLR S3		0.0001580v	0.0000	0.0000	0.000227
DLR S4		0.0001580v	0.0000	0.0000	-0.000146
DLR S5		0.0001580v	0.0000	0.0000	0.000036

PROBABLE CHANGE IN RMS 0.2105
PROBABLE CHANGE OF COMPENSATORS (+/-) 0.007352

FIELD (X,Y) = (0.70, 0.70)MAX, (0.35, 0.35)DEG
FIELD WEIGHT = 1.00
NOMINAL RMS = 0.0070

WAVELENGTH 632.8 NM
WEIGHT 1
NO. OF RAYS 774

MANUFACTURING ERROR		CHANGES IN RMS FOR PLUS AND MINUS MANUFACTURING ERRORS		COMPENSATING PARAMETERS	
TYPE	CHANGE			DLZ S6	
ZFR S3	C5	0.1767700v	0.1142	0.1130	0.000418
ZFR S3	C6	0.1767700v	0.1091	0.1176	0.000314

ZFR S4	C5	0.1767700v	0.0830	0.0842	0.000191
ZFR S4	C6	0.1767700v	0.0874	0.0789	-0.000289
ZFR S5	C5	0.1767700v	0.0549	0.0537	0.000883
ZFR S5	C6	0.1767700v	0.0498	0.0582	0.000222
DSZ S3..4		0.0020000v	0.0000	0.0000	-0.000117
DSZ S4..5		0.0020000v	0.0001	0.0000	-0.003322
DLA S3		0.0000286v	0.0123	0.0131	0.000078
DLB S3		0.0000286v	0.0164	0.0080	-0.000045
DLA S4		0.0000556v	0.0022	0.0034	-0.003742
DLB S4		0.0000556v	0.0115	0.0199	0.000032
DLA S5		0.0000588v	0.0028	0.0018	0.005937
DLB S5		0.0000588v	-0.0014	0.0051	0.000027
DLX S3		0.0020000v	0.0013	-0.0010	-0.000006
DLY S3		0.0020000v	0.0011	0.0007	0.001433
DLX S4		0.0020000v	-0.0005	0.0006	0.000004
DLY S4		0.0020000v	0.0011	0.0016	-0.001844
DLX S5		0.0020000v	-0.0006	0.0006	0.000002
DLY S5		0.0020000v	0.0001	0.0000	-0.000011
DLG S3		0.0000286v	0.0009	-0.0007	-0.000003
DLG S4		0.0000556v	0.0010	-0.0001	-0.000006
DLG S5		0.0000588v	-0.0004	0.0005	0.000004
DLR S3		0.0001580v	0.0000	0.0000	0.000227
DLR S4		0.0001580v	0.0000	0.0000	-0.000146
DLR S5		0.0001580v	0.0000	0.0000	0.000036

PROBABLE CHANGE IN RMS 0.2126
PROBABLE CHANGE OF COMPENSATORS (+/-) 0.007352

FIELD (X,Y) = (0.70,-0.70)MAX, (0.35, -0.35)DEG
FIELD WEIGHT = 1.00
NOMINAL RMS = 0.0054

WAVELENGTH 632.8 NM
WEIGHT 1
NO. OF RAYS 767

MANUFACTURING ERROR		CHANGES IN RMS FOR PLUS AND MINUS MANUFACTURING ERRORS		COMPENSATING PARAMETERS	
TYPE	CHANGE			DLZ S6	
ZFR S3	C5	0.1767700v	0.1128	0.1141	0.000418
ZFR S3	C6	0.1767700v	0.1187	0.1120	0.000314
ZFR S4	C5	0.1767700v	0.0835	0.0822	0.000191
ZFR S4	C6	0.1767700v	0.0809	0.0877	-0.000289
ZFR S5	C5	0.1767700v	0.0534	0.0547	0.000883
ZFR S5	C6	0.1767700v	0.0583	0.0515	0.000222
DSZ S3..4		0.0020000v	0.0000	0.0000	-0.000117
DSZ S4..5		0.0020000v	-0.0001	0.0003	-0.003322
DLA S3		0.0000286v	0.0152	0.0140	0.000078
DLB S3		0.0000286v	0.0111	0.0178	-0.000045
DLA S4		0.0000556v	0.0026	0.0013	-0.003742
DLB S4		0.0000556v	0.0220	0.0153	0.000032
DLA S5		0.0000588v	0.0024	0.0036	0.005937
DLB S5		0.0000588v	0.0054	0.0001	0.000027
DLX S3		0.0020000v	-0.0010	0.0014	-0.000006
DLY S3		0.0020000v	0.0008	0.0015	0.001433
DLX S4		0.0020000v	0.0007	-0.0006	0.000004
DLY S4		0.0020000v	0.0020	0.0012	-0.001844
DLX S5		0.0020000v	0.0007	-0.0005	0.000002
DLY S5		0.0020000v	0.0000	0.0002	-0.000011
DLG S3		0.0000286v	-0.0005	0.0008	-0.000003
DLG S4		0.0000556v	-0.0006	0.0021	-0.000006
DLG S5		0.0000588v	0.0013	-0.0008	0.000004
DLR S3		0.0001580v	0.0000	0.0000	0.000227
DLR S4		0.0001580v	0.0000	0.0000	-0.000146
DLR S5		0.0001580v	0.0000	0.0000	0.000036

PROBABLE CHANGE IN RMS 0.2120
PROBABLE CHANGE OF COMPENSATORS (+/-) 0.007352

FIELD (X,Y) = (0.00,-0.70)MAX, (0.00, -0.35)DEG
FIELD WEIGHT = 1.00
NOMINAL RMS = 0.0062

WAVELENGTH 632.8 NM
WEIGHT 1
NO. OF RAYS 772

MANUFACTURING ERROR		CHANGES IN RMS FOR PLUS AND MINUS MANUFACTURING ERRORS		COMPENSATING PARAMETERS
TYPE	CHANGE			DLZ S6

ZFR S3	C5	0.1767700v	0.1175	0.1134	0.000418
ZFR S3	C6	0.1767700v	0.1135	0.1132	0.000314
ZFR S4	C5	0.1767700v	0.0821	0.0862	0.000191
ZFR S4	C6	0.1767700v	0.0825	0.0829	-0.000289
ZFR S5	C5	0.1767700v	0.0567	0.0527	0.000883
ZFR S5	C6	0.1767700v	0.0538	0.0535	0.000222
DSZ S3..4		0.0020000v	-0.0001	0.0001	-0.000117
DSZ S4..5		0.0020000v	0.0004	-0.0002	-0.003322
DLA S3		0.0000286v	0.0124	0.0164	0.000078
DLB S3		0.0000286v	0.0138	0.0142	-0.000045
DLA S4		0.0000556v	0.0008	0.0027	-0.003742
DLB S4		0.0000556v	0.0182	0.0179	0.000032
DLA S5		0.0000588v	0.0045	0.0008	0.005937
DLB S5		0.0000588v	0.0030	0.0028	0.000027
DLX S3		0.0020000v	0.0003	0.0004	-0.000006
DLY S3		0.0020000v	0.0021	-0.0001	0.001433
DLX S4		0.0020000v	0.0001	0.0001	0.000004
DLY S4		0.0020000v	0.0002	0.0026	-0.001844
DLX S5		0.0020000v	0.0001	0.0001	0.000002
DLY S5		0.0020000v	0.0003	-0.0002	-0.000011
DLG S3		0.0000286v	0.0002	0.0002	-0.000003
DLG S4		0.0000556v	0.0007	0.0008	-0.000006
DLG S5		0.0000588v	0.0003	0.0003	0.000004
DLR S3		0.0001580v	0.0000	0.0000	0.000227
DLR S4		0.0001580v	0.0000	0.0000	-0.000146
DLR S5		0.0001580v	0.0000	0.0000	0.000036

PROBABLE CHANGE IN RMS 0.2125
PROBABLE CHANGE OF COMPENSATORS (+/-) 0.007352

FIELD (X,Y) = (0.00,-1.00)MAX, (0.00, -0.50)DEG WAVELENGTH 632.8 NM WEIGHT 1 NO. OF RAYS 773
FIELD WEIGHT = 1.00
NOMINAL RMS = 0.0047

MANUFACTURING ERROR		CHANGES IN RMS FOR PLUS AND MINUS MANUFACTURING ERRORS		COMPENSATING PARAMETERS	
TYPE	CHANGE			DLZ S6	
ZFR S3	C5	0.1767700v	0.1169	0.1169	0.000418
ZFR S3	C6	0.1767700v	0.1153	0.1153	0.000314
ZFR S4	C5	0.1767700v	0.0853	0.0853	0.000191
ZFR S4	C6	0.1767700v	0.0843	0.0843	-0.000289
ZFR S5	C5	0.1767700v	0.0559	0.0559	0.000883
ZFR S5	C6	0.1767700v	0.0551	0.0551	0.000222
DSZ S3..4		0.0020000v	0.0000	0.0000	-0.000117
DSZ S4..5		0.0020000v	0.0001	0.0001	-0.003322
DLA S3		0.0000286v	0.0159	0.0158	0.000078
DLB S3		0.0000286v	0.0153	0.0153	-0.000045
DLA S4		0.0000556v	0.0017	0.0022	-0.003742
DLB S4		0.0000556v	0.0196	0.0196	0.000032
DLA S5		0.0000588v	0.0032	0.0037	0.005937
DLB S5		0.0000588v	0.0035	0.0035	0.000027
DLX S3		0.0020000v	0.0004	0.0004	-0.000006
DLY S3		0.0020000v	0.0013	0.0014	0.001433
DLX S4		0.0020000v	0.0001	0.0001	0.000004
DLY S4		0.0020000v	0.0018	0.0019	-0.001844
DLX S5		0.0020000v	0.0001	0.0001	0.000002
DLY S5		0.0020000v	0.0001	0.0000	-0.000011
DLG S3		0.0000286v	0.0002	0.0002	-0.000003
DLG S4		0.0000556v	0.0011	0.0011	-0.000006
DLG S5		0.0000588v	0.0004	0.0004	0.000004
DLR S3		0.0001580v	0.0000	0.0000	0.000227
DLR S4		0.0001580v	0.0000	0.0000	-0.000146
DLR S5		0.0001580v	0.0000	0.0000	0.000036

PROBABLE CHANGE IN RMS 0.2142
PROBABLE CHANGE OF COMPENSATORS (+/-) 0.007352

FIELD (X,Y) = (-0.70, 0.00)MAX, (-0.35, 0.00)DEG WAVELENGTH 632.8 NM WEIGHT 1 NO. OF RAYS 768
FIELD WEIGHT = 1.00
NOMINAL RMS = 0.0044

MANUFACTURING ERROR		CHANGES IN RMS FOR PLUS AND MINUS		COMPENSATING PARAMETERS
---------------------	--	-----------------------------------	--	-------------------------

TYPE	CHANGE	MANUFACTURING ERRORS		DLZ S6	
ZFR S3	C5	0.1767700v	0.1146	0.1146	0.000418
ZFR S3	C6	0.1767700v	0.1159	0.1163	0.000314
ZFR S4	C5	0.1767700v	0.0844	0.0844	0.000191
ZFR S4	C6	0.1767700v	0.0857	0.0853	-0.000289
ZFR S5	C5	0.1767700v	0.0555	0.0555	0.000883
ZFR S5	C6	0.1767700v	0.0561	0.0564	0.000222
DSZ S3..4		0.0020000v	0.0000	0.0000	-0.000117
DSZ S4..5		0.0020000v	0.0001	0.0002	-0.003322
DLA S3		0.0000286v	0.0149	0.0148	0.000078
DLB S3		0.0000286v	0.0152	0.0148	-0.000045
DLA S4		0.0000556v	0.0030	0.0030	-0.003742
DLB S4		0.0000556v	0.0186	0.0192	0.000032
DLA S5		0.0000588v	0.0032	0.0033	0.005937
DLB S5		0.0000588v	0.0031	0.0038	0.000027
DLX S3		0.0020000v	0.0005	0.0004	-0.000006
DLY S3		0.0020000v	0.0013	0.0014	0.001433
DLX S4		0.0020000v	0.0001	0.0001	0.000004
DLY S4		0.0020000v	0.0019	0.0019	-0.001844
DLX S5		0.0020000v	0.0000	0.0002	0.000002
DLY S5		0.0020000v	0.0001	0.0001	-0.000011
DLG S3		0.0000286v	0.0002	0.0003	-0.000003
DLG S4		0.0000556v	0.0012	0.0005	-0.000006
DLG S5		0.0000588v	0.0001	0.0004	0.000004
DLR S3		0.0001580v	0.0000	0.0000	0.000227
DLR S4		0.0001580v	0.0000	0.0000	-0.000146
DLR S5		0.0001580v	0.0000	0.0000	0.000036

PROBABLE CHANGE IN RMS 0.2133
PROBABLE CHANGE OF COMPENSATORS (+/-) 0.007352

FIELD (X,Y) = (-1.00, 0.00)MAX, (-0.50, 0.00)DEG
FIELD WEIGHT = 1.00
NOMINAL RMS = 0.0061

WAVELENGTH 632.8 NM
WEIGHT 1
NO. OF RAYS 764

MANUFACTURING ERROR	CHANGES IN RMS FOR PLUS AND MINUS		COMPENSATING PARAMETERS		
TYPE	CHANGE	MANUFACTURING ERRORS	DLZ S6		
ZFR S3	C5	0.1767700v	0.1103	0.1150	0.000418
ZFR S3	C6	0.1767700v	0.1131	0.1140	0.000314
ZFR S4	C5	0.1767700v	0.0848	0.0802	0.000191
ZFR S4	C6	0.1767700v	0.0836	0.0827	-0.000289
ZFR S5	C5	0.1767700v	0.0514	0.0560	0.000883
ZFR S5	C6	0.1767700v	0.0537	0.0546	0.000222
DSZ S3..4		0.0020000v	0.0001	-0.0001	-0.000117
DSZ S4..5		0.0020000v	-0.0003	0.0005	-0.003322
DLA S3		0.0000286v	0.0157	0.0111	0.000078
DLB S3		0.0000286v	0.0140	0.0132	-0.000045
DLA S4		0.0000556v	0.0040	0.0006	-0.003742
DLB S4		0.0000556v	0.0170	0.0178	0.000032
DLA S5		0.0000588v	0.0007	0.0042	0.005937
DLB S5		0.0000588v	0.0028	0.0028	0.000027
DLX S3		0.0020000v	0.0004	0.0002	-0.000006
DLY S3		0.0020000v	-0.0003	0.0022	0.001433
DLX S4		0.0020000v	0.0000	0.0002	0.000004
DLY S4		0.0020000v	0.0028	-0.0001	-0.001844
DLX S5		0.0020000v	0.0000	0.0001	0.000002
DLY S5		0.0020000v	-0.0003	0.0004	-0.000011
DLG S3		0.0000286v	0.0001	0.0002	-0.000003
DLG S4		0.0000556v	0.0007	0.0005	-0.000006
DLG S5		0.0000588v	0.0003	0.0001	0.000004
DLR S3		0.0001580v	0.0000	0.0000	0.000227
DLR S4		0.0001580v	0.0000	0.0000	-0.000146
DLR S5		0.0001580v	0.0000	0.0000	0.000036

PROBABLE CHANGE IN RMS 0.2105
PROBABLE CHANGE OF COMPENSATORS (+/-) 0.007352

FIELD (X,Y) = (-0.70, 0.70)MAX, (-0.35, 0.35)DEG
FIELD WEIGHT = 1.00
NOMINAL RMS = 0.0071

WAVELENGTH 632.8 NM
WEIGHT 1
NO. OF RAYS 772

MANUFACTURING ERROR CHANGES IN RMS FOR COMPENSATING PARAMETERS

TYPE	CHANGE	PLUS AND MINUS		DLZ S6	
		MANUFACTURING ERRORS			
ZFR S3	C5	0.1767700v	0.1136	0.1126	0.000418
ZFR S3	C6	0.1767700v	0.1174	0.1087	0.000314
ZFR S4	C5	0.1767700v	0.0827	0.0837	0.000191
ZFR S4	C6	0.1767700v	0.0785	0.0873	-0.000289
ZFR S5	C5	0.1767700v	0.0545	0.0535	0.000883
ZFR S5	C6	0.1767700v	0.0582	0.0494	0.000222
DSZ S3..4		0.0020000v	0.0000	0.0000	-0.000117
DSZ S4..5		0.0020000v	0.0002	0.0000	-0.003322
DLA S3		0.0000286v	0.0123	0.0129	0.000078
DLB S3		0.0000286v	0.0078	0.0164	-0.000045
DLA S4		0.0000556v	0.0021	0.0034	-0.003742
DLB S4		0.0000556v	0.0199	0.0112	0.000032
DLA S5		0.0000588v	0.0027	0.0018	0.005937
DLB S5		0.0000588v	0.0052	-0.0016	0.000027
DLX S3		0.0020000v	-0.0010	0.0013	-0.000006
DLY S3		0.0020000v	0.0011	0.0007	0.001433
DLX S4		0.0020000v	0.0006	-0.0006	0.000004
DLY S4		0.0020000v	0.0011	0.0016	-0.001844
DLX S5		0.0020000v	0.0006	-0.0006	0.000002
DLY S5		0.0020000v	0.0001	0.0000	-0.000011
DLG S3		0.0000286v	-0.0007	0.0009	-0.000003
DLG S4		0.0000556v	-0.0002	0.0010	-0.000006
DLG S5		0.0000588v	0.0005	-0.0004	0.000004
DLR S3		0.0001580v	0.0000	0.0000	0.000227
DLR S4		0.0001580v	0.0000	0.0000	-0.000146
DLR S5		0.0001580v	0.0000	0.0000	0.000036

PROBABLE CHANGE IN RMS 0.2120
PROBABLE CHANGE OF COMPENSATORS (+/-) 0.007352

FIELD (X,Y) = (-0.70,-0.70)MAX, (-0.35, -0.35)DEG
FIELD WEIGHT = 1.00
NOMINAL RMS = 0.0053
WAVELENGTH 632.8 NM
WEIGHT 1
NO. OF RAYS 768

TYPE	CHANGE	CHANGES IN RMS FOR		DLZ S6	
		PLUS AND MINUS			
		MANUFACTURING ERRORS		COMPENSATING PARAMETERS	
ZFR S3	C5	0.1767700v	0.1134	0.1144	0.000418
ZFR S3	C6	0.1767700v	0.1121	0.1186	0.000314
ZFR S4	C5	0.1767700v	0.0837	0.0827	0.000191
ZFR S4	C6	0.1767700v	0.0876	0.0811	-0.000289
ZFR S5	C5	0.1767700v	0.0538	0.0548	0.000883
ZFR S5	C6	0.1767700v	0.0517	0.0582	0.000222
DSZ S3..4		0.0020000v	0.0000	0.0000	-0.000117
DSZ S4..5		0.0020000v	-0.0001	0.0003	-0.003322
DLA S3		0.0000286v	0.0152	0.0143	0.000078
DLB S3		0.0000286v	0.0177	0.0113	-0.000045
DLA S4		0.0000556v	0.0026	0.0014	-0.003742
DLB S4		0.0000556v	0.0156	0.0219	0.000032
DLA S5		0.0000588v	0.0025	0.0035	0.005937
DLB S5		0.0000588v	0.0003	0.0054	0.000027
DLX S3		0.0020000v	0.0014	-0.0009	-0.000006
DLY S3		0.0020000v	0.0009	0.0014	0.001433
DLX S4		0.0020000v	-0.0006	0.0007	0.000004
DLY S4		0.0020000v	0.0019	0.0013	-0.001844
DLX S5		0.0020000v	-0.0005	0.0006	0.000002
DLY S5		0.0020000v	0.0000	0.0002	-0.000011
DLG S3		0.0000286v	0.0008	-0.0005	-0.000003
DLG S4		0.0000556v	0.0021	-0.0006	-0.000006
DLG S5		0.0000588v	-0.0008	0.0013	0.000004
DLR S3		0.0001580v	0.0000	0.0000	0.000227
DLR S4		0.0001580v	0.0000	0.0000	-0.000146
DLR S5		0.0001580v	0.0000	0.0000	0.000036

PROBABLE CHANGE IN RMS 0.2123
PROBABLE CHANGE OF COMPENSATORS (+/-) 0.007352

PERFORMANCE SUMMARY
POLYCHROMATIC RMS WAVEFRONT ABERRATION

```

-----
--

```

RELATIVE FIELD	WEIGHT	DESIGN	DESIGN + TOL *	COMPENSATOR RANGE (+/-) *
				DLZ S6
0.00, 0.00	1.00	0.0112	0.2213	0.007352
0.00, 0.70	1.00	0.0045	0.2203	0.007352
0.00, 1.00	1.00	0.0065	0.2194	0.007352
0.70, 0.00	1.00	0.0045	0.2176	0.007352
1.00, 0.00	1.00	0.0061	0.2166	0.007352
0.70, 0.70	1.00	0.0070	0.2196	0.007352
0.70, -0.70	1.00	0.0054	0.2174	0.007352
0.00, -0.70	1.00	0.0062	0.2187	0.007352
0.00, -1.00	1.00	0.0047	0.2189	0.007352
-0.70, 0.00	1.00	0.0044	0.2177	0.007352
-1.00, 0.00	1.00	0.0061	0.2166	0.007352
-0.70, 0.70	1.00	0.0071	0.2191	0.007352
-0.70, -0.70	1.00	0.0053	0.2177	0.007352

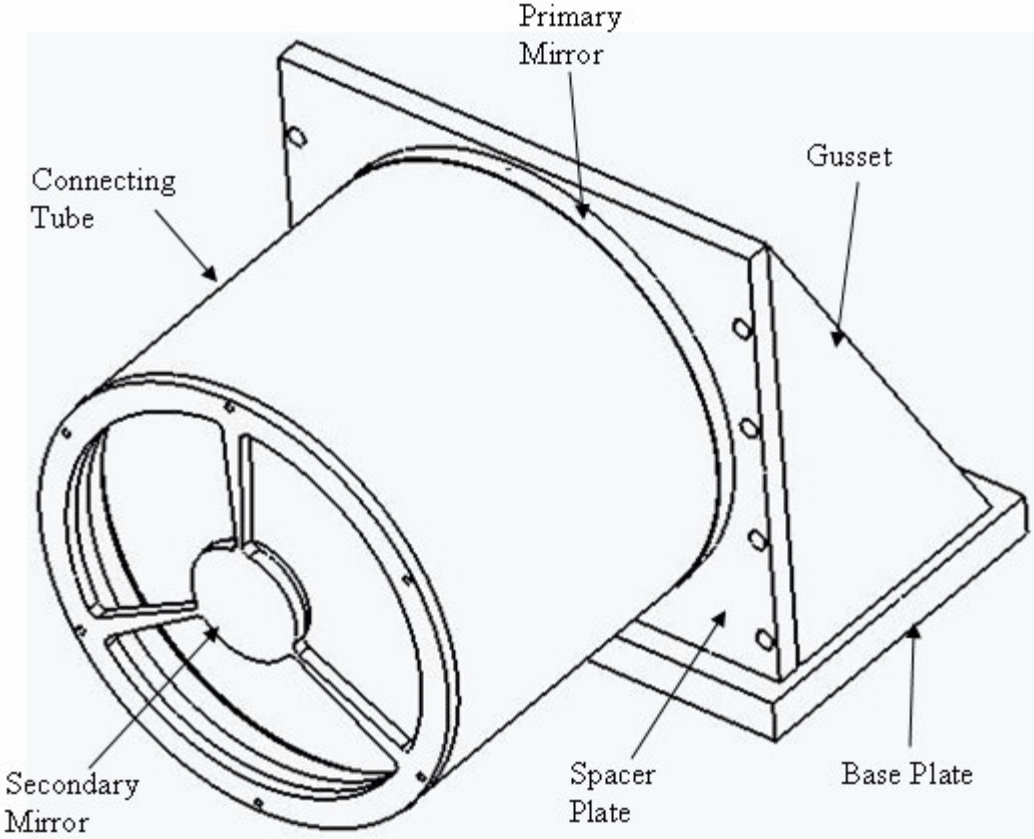
```

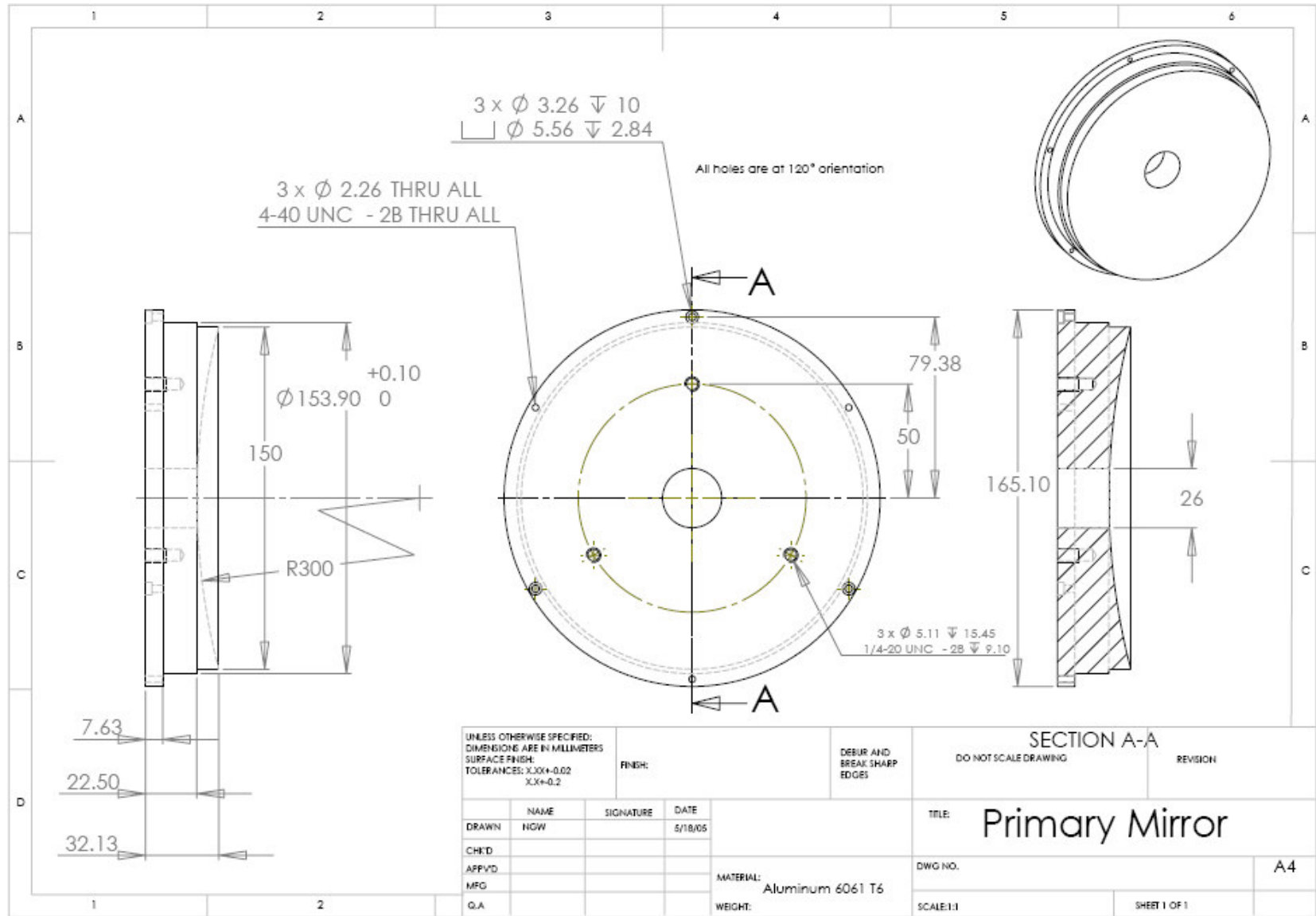
-----
--

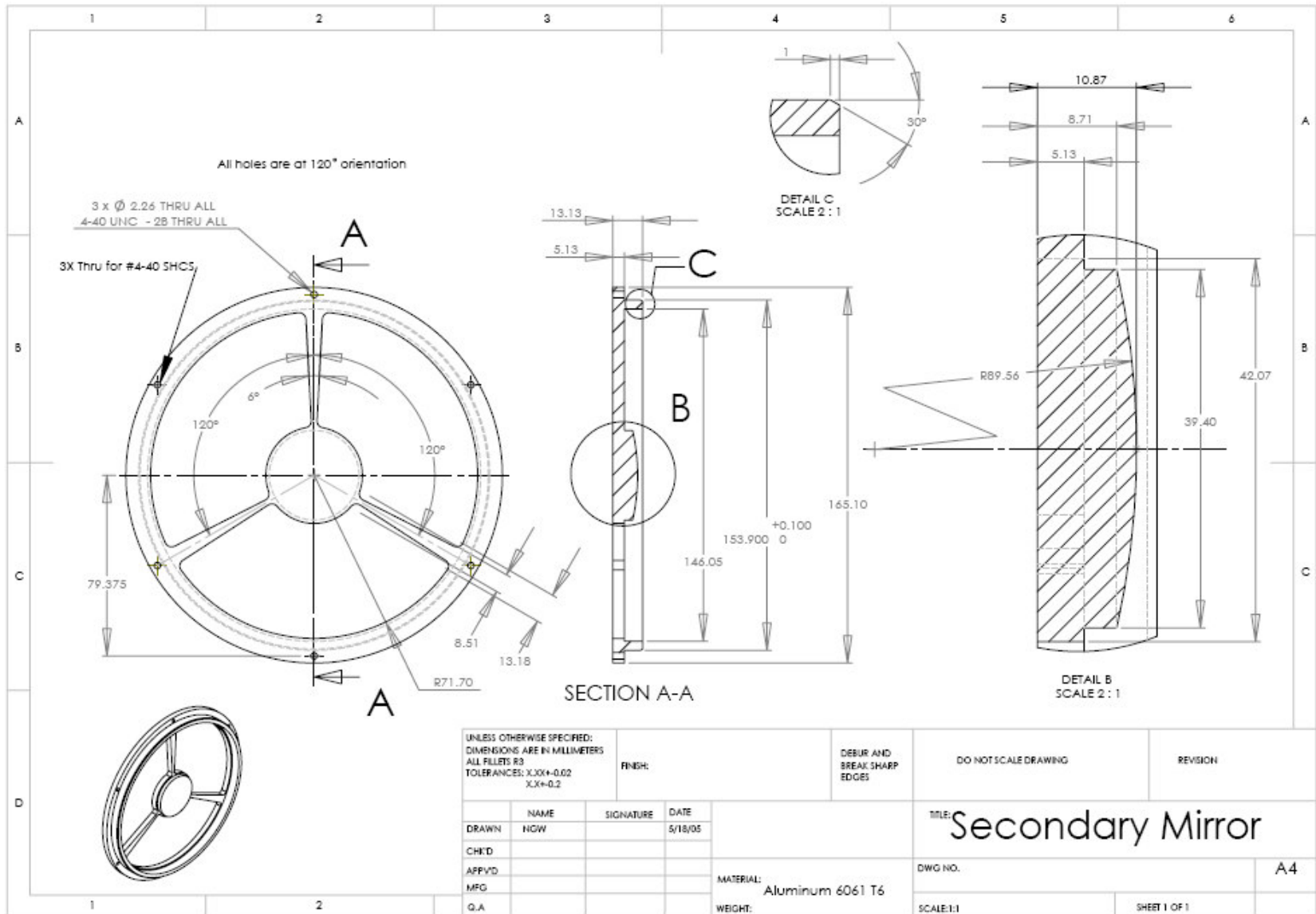
```

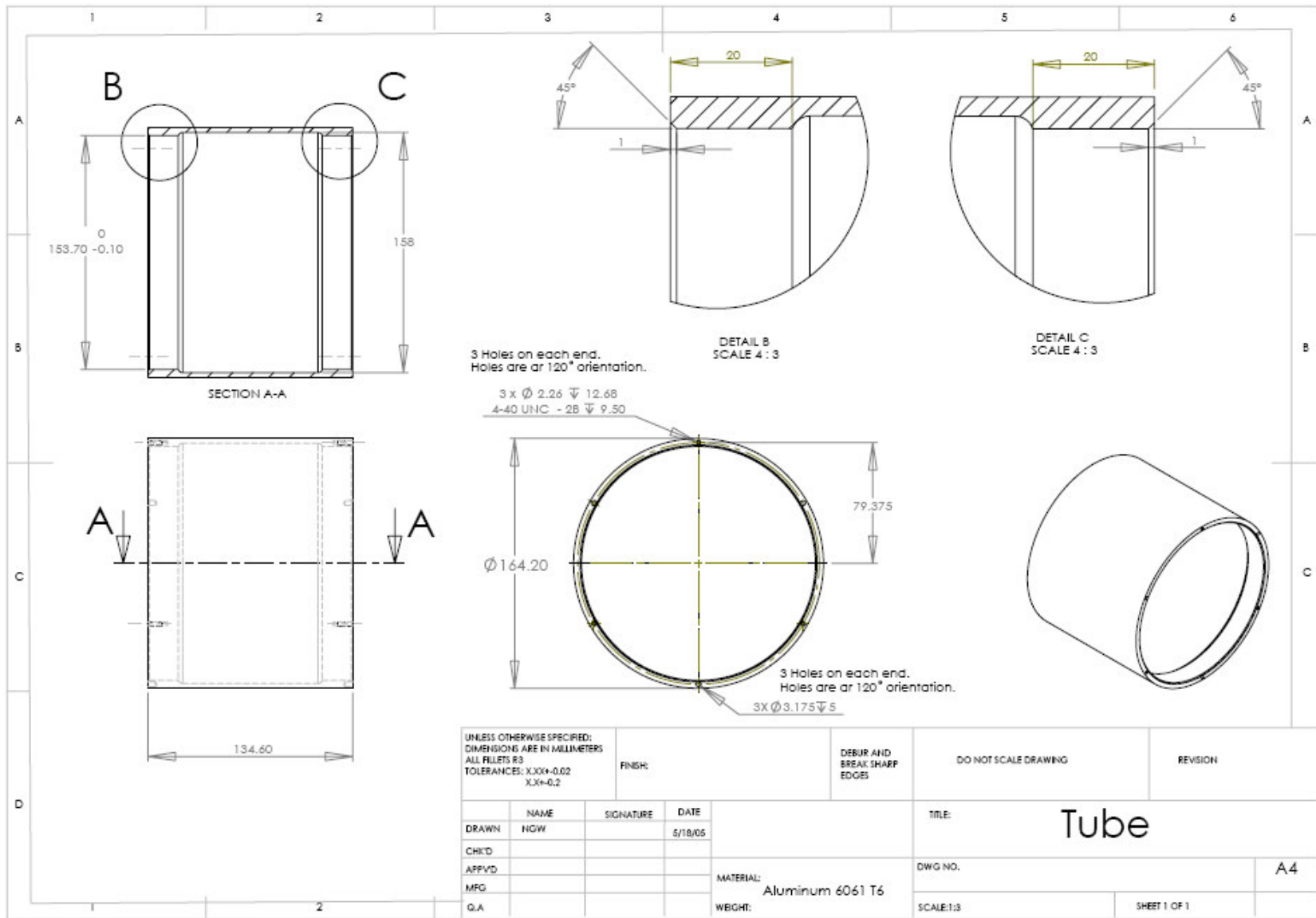
APPENDIX C – Detail Drawings of the Two Mirror Telescope

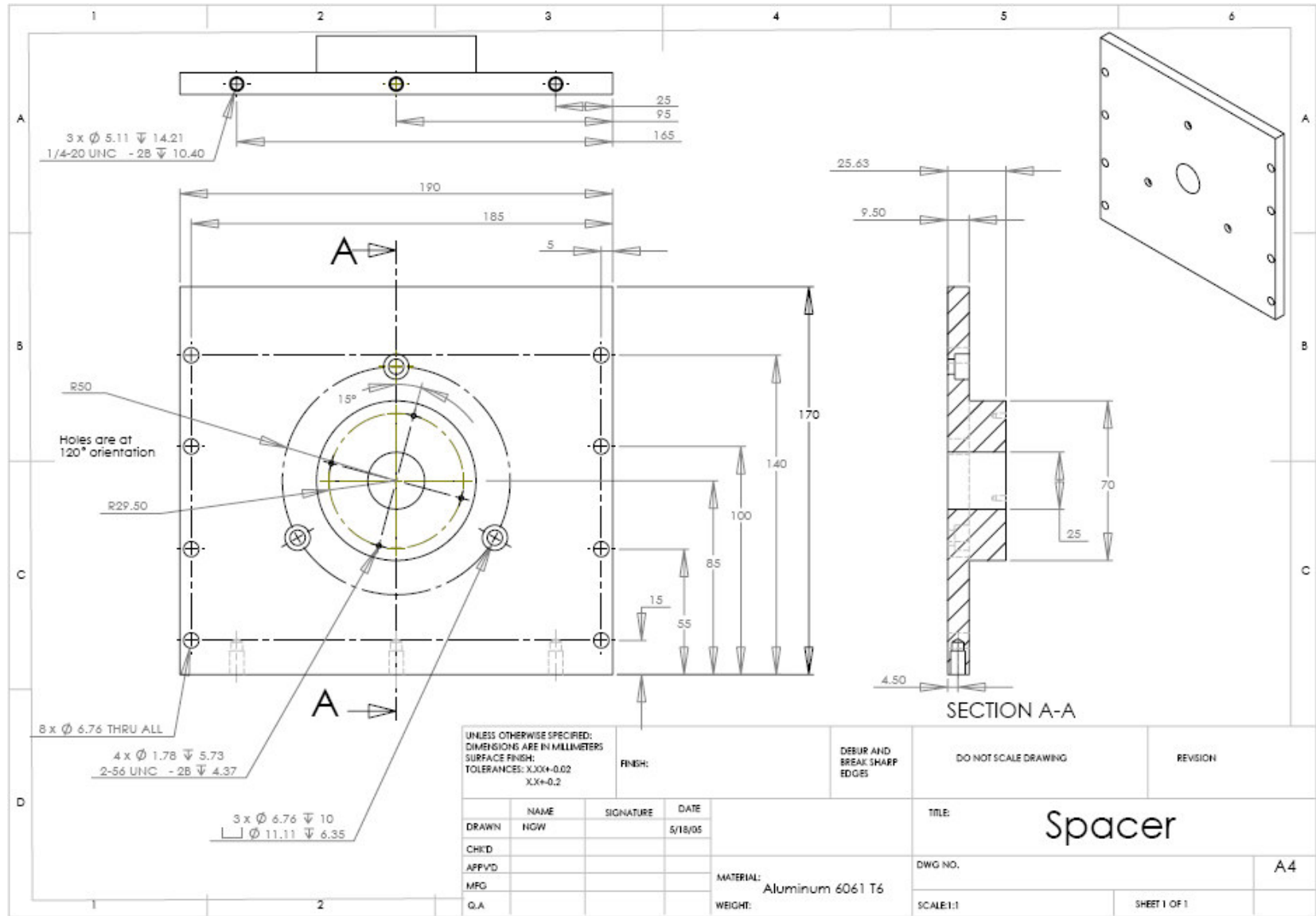
Two Mirror Telescope Components

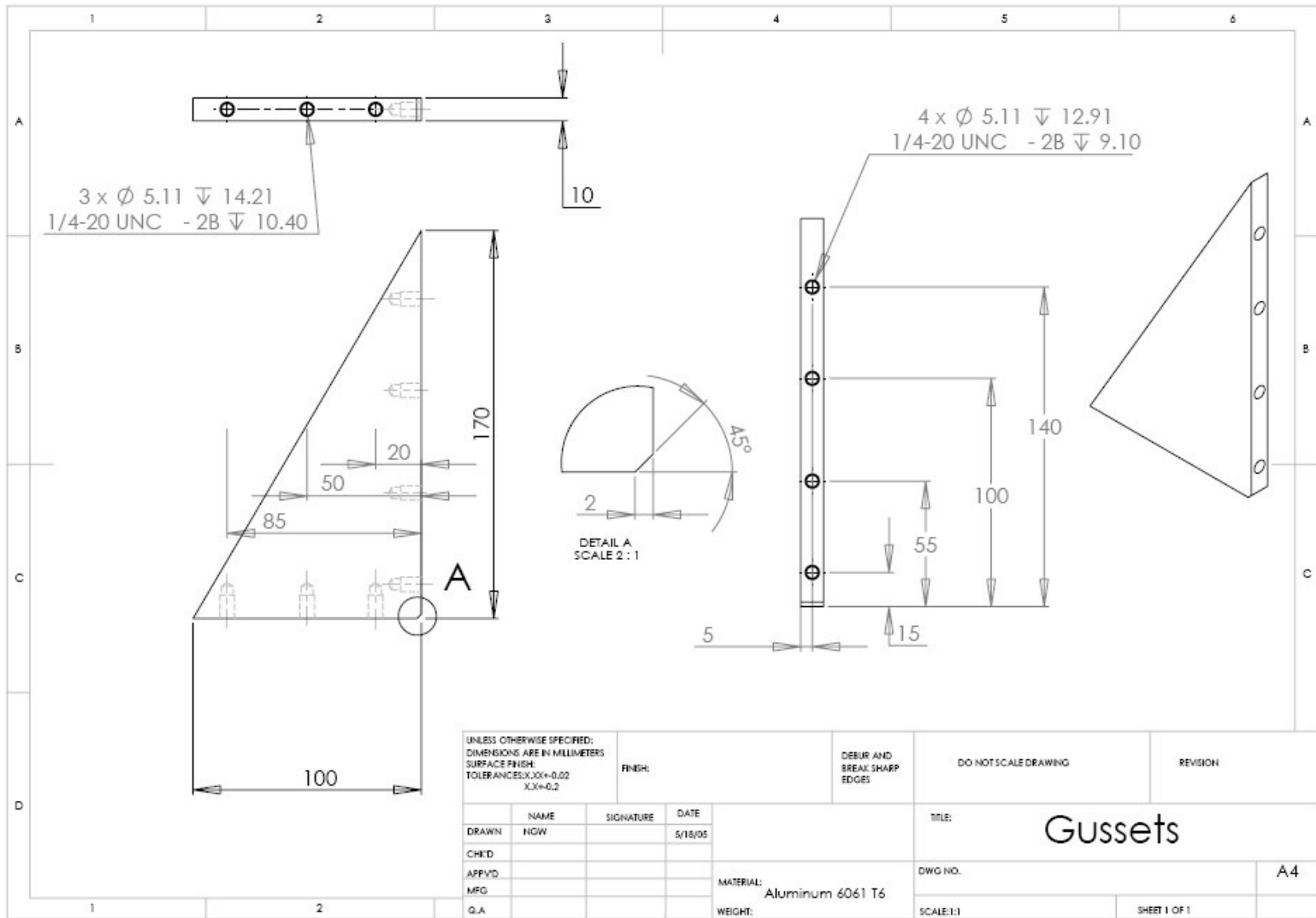


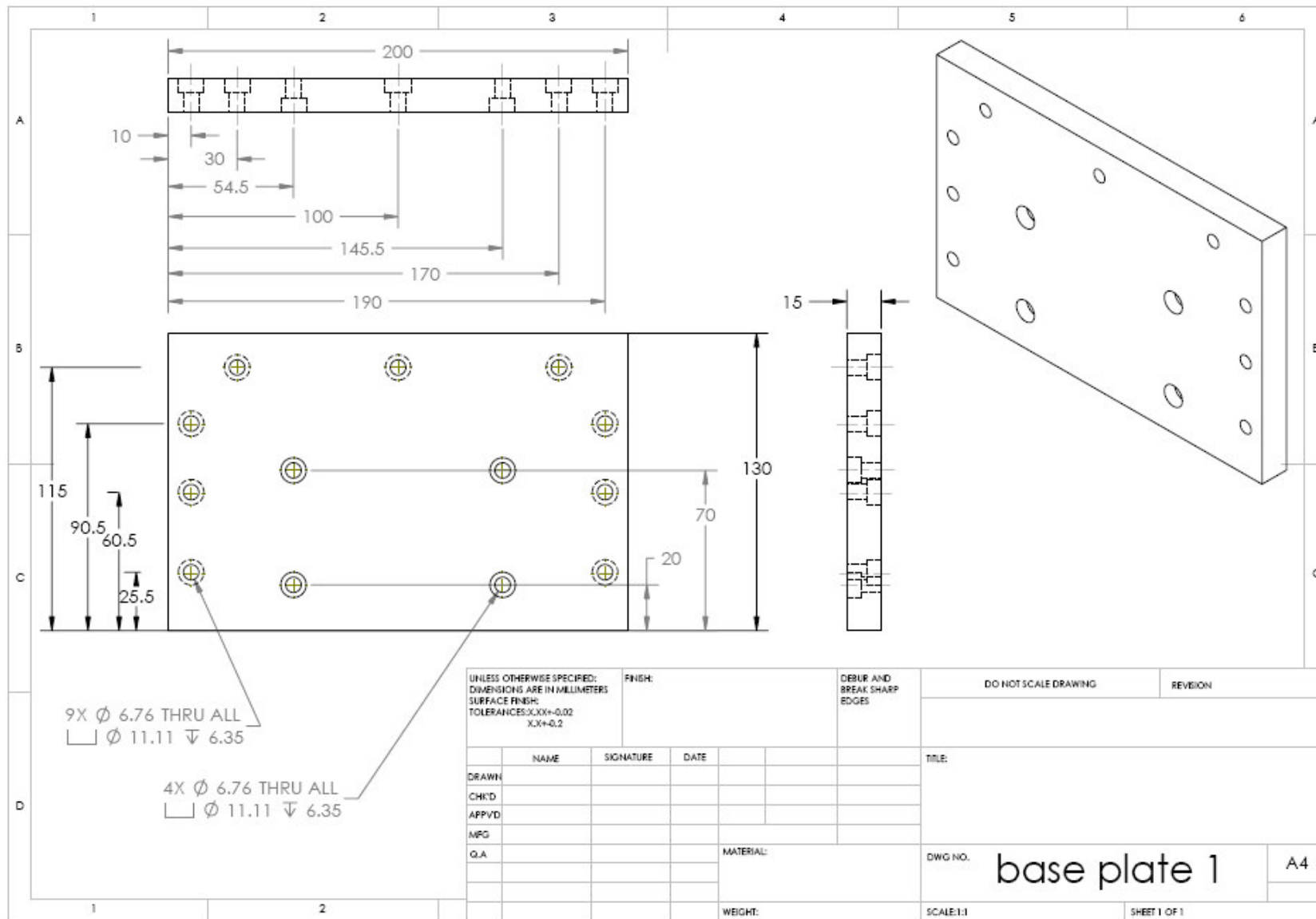




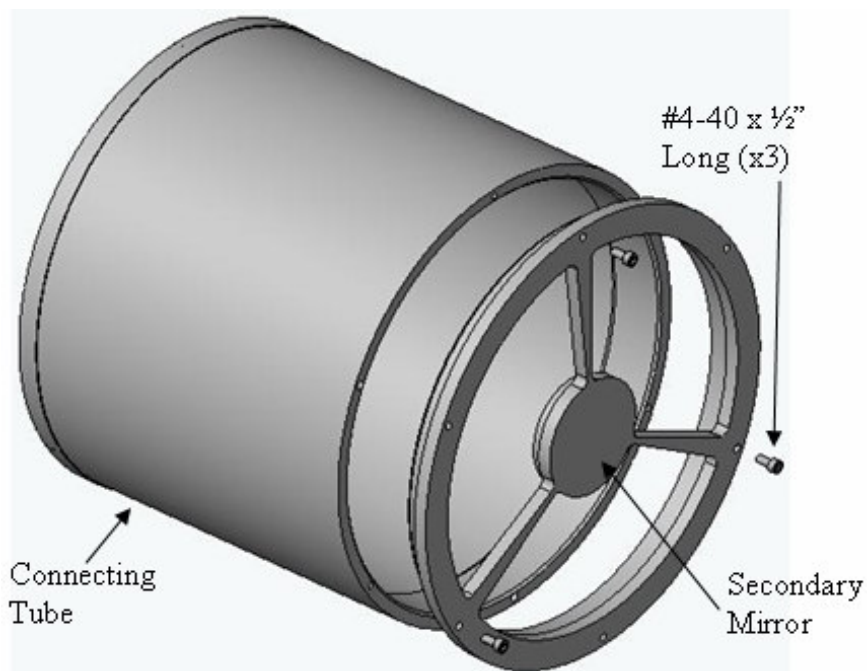
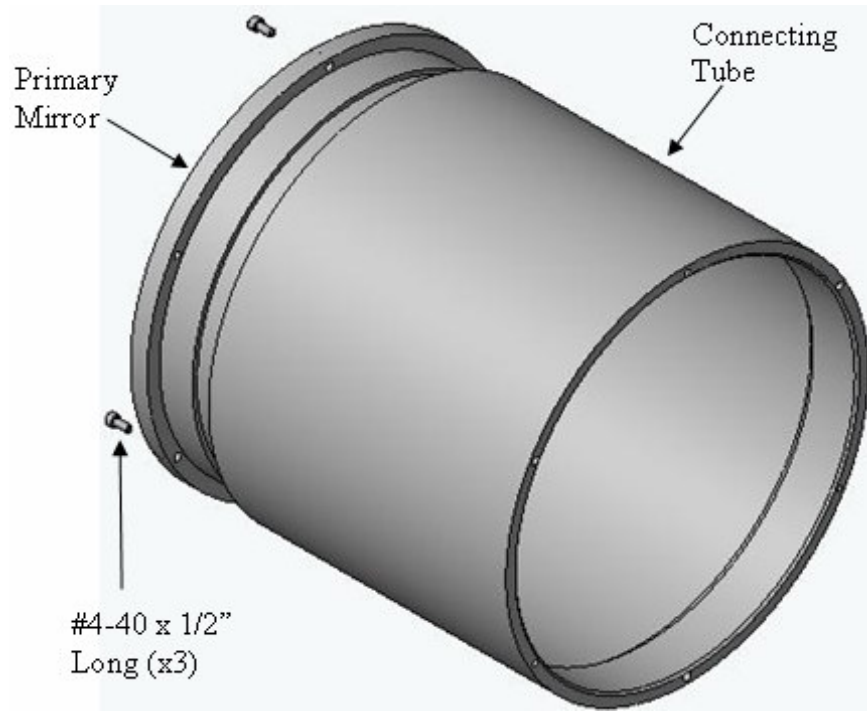


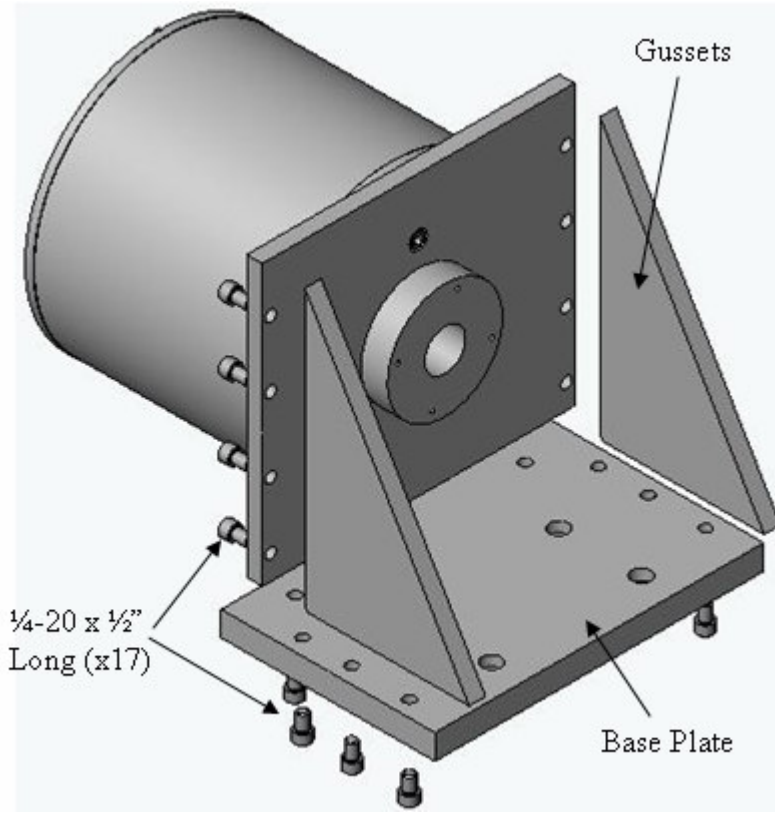
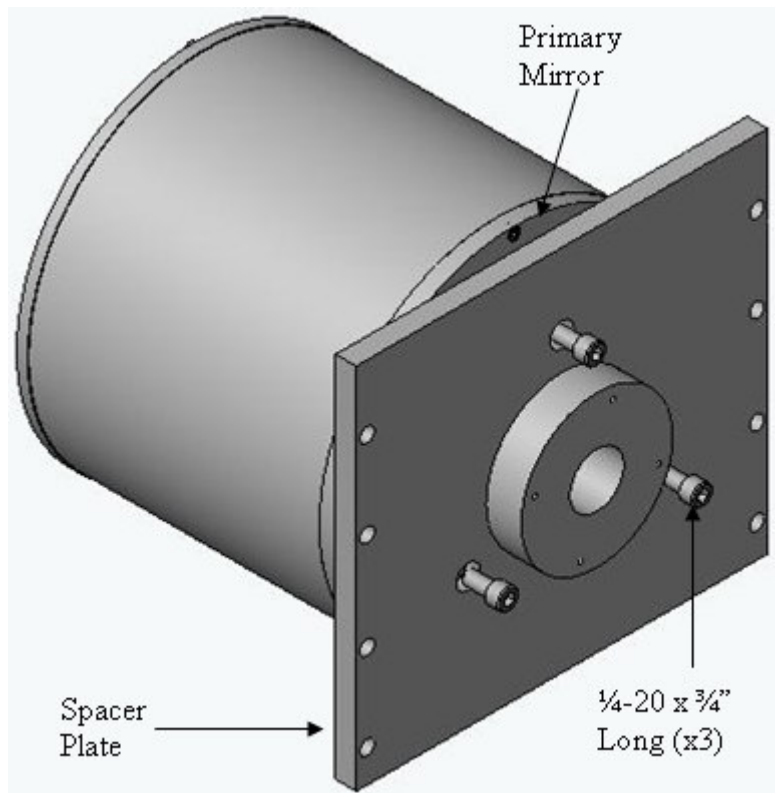






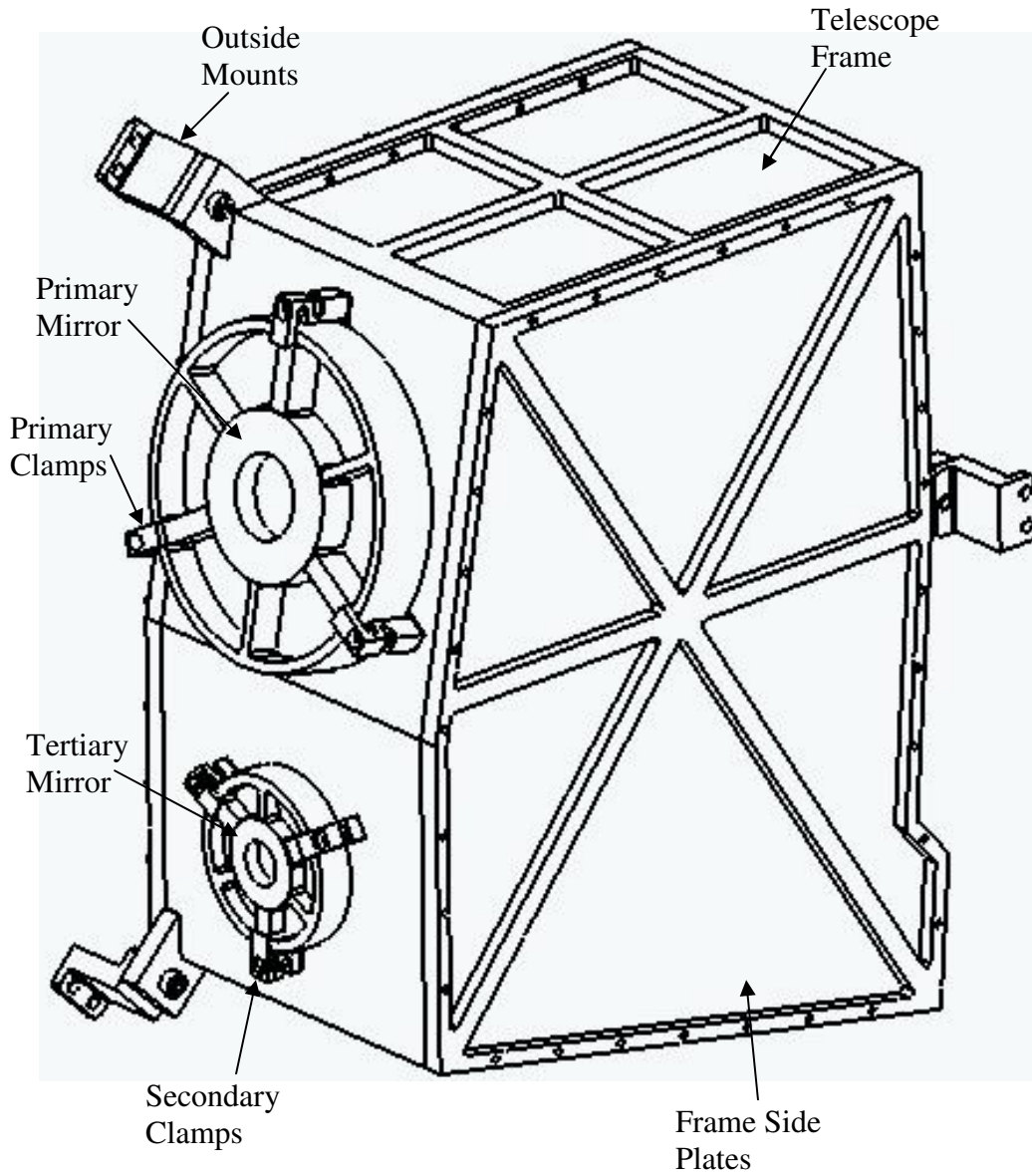
Two Mirror Assembly Steps

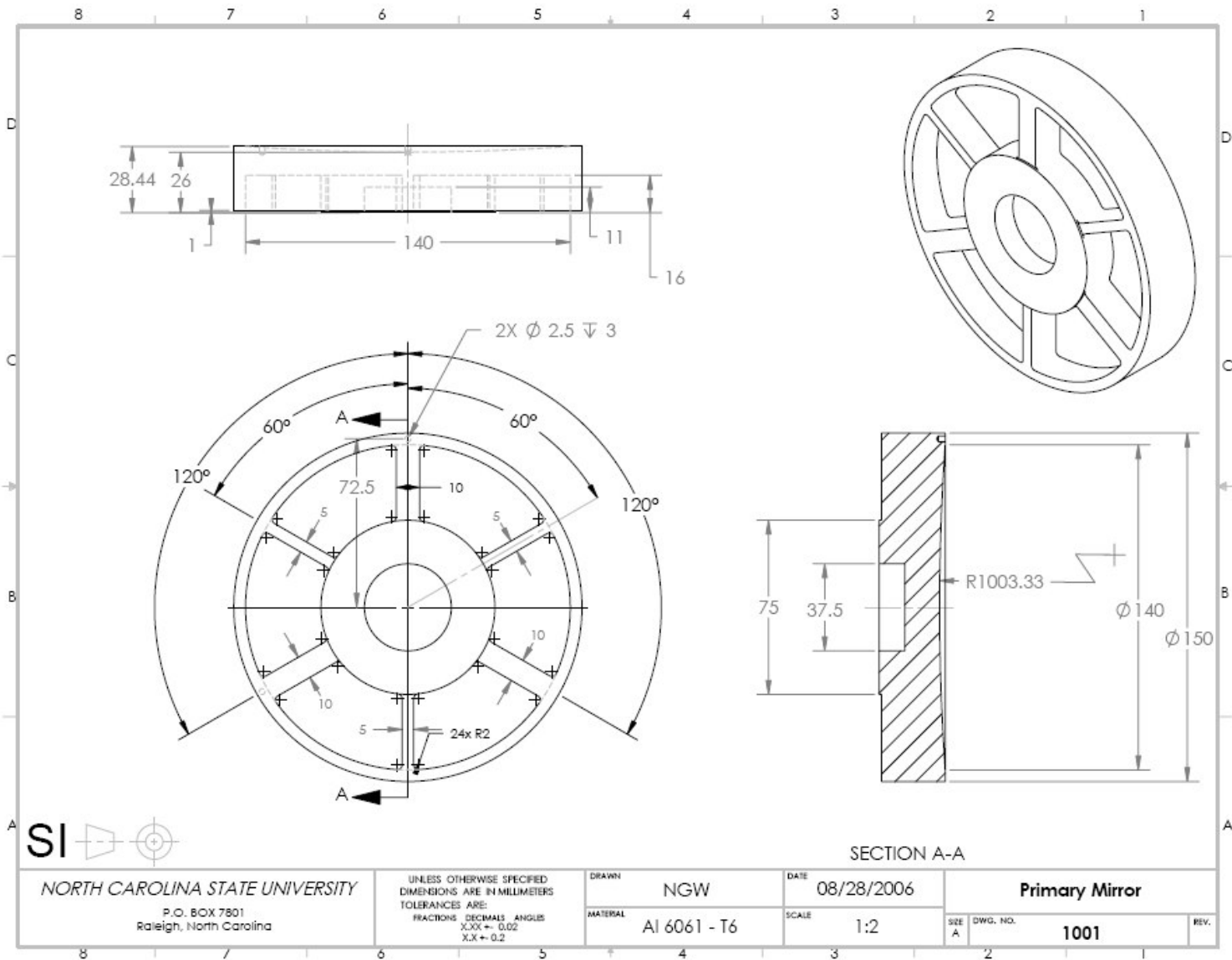


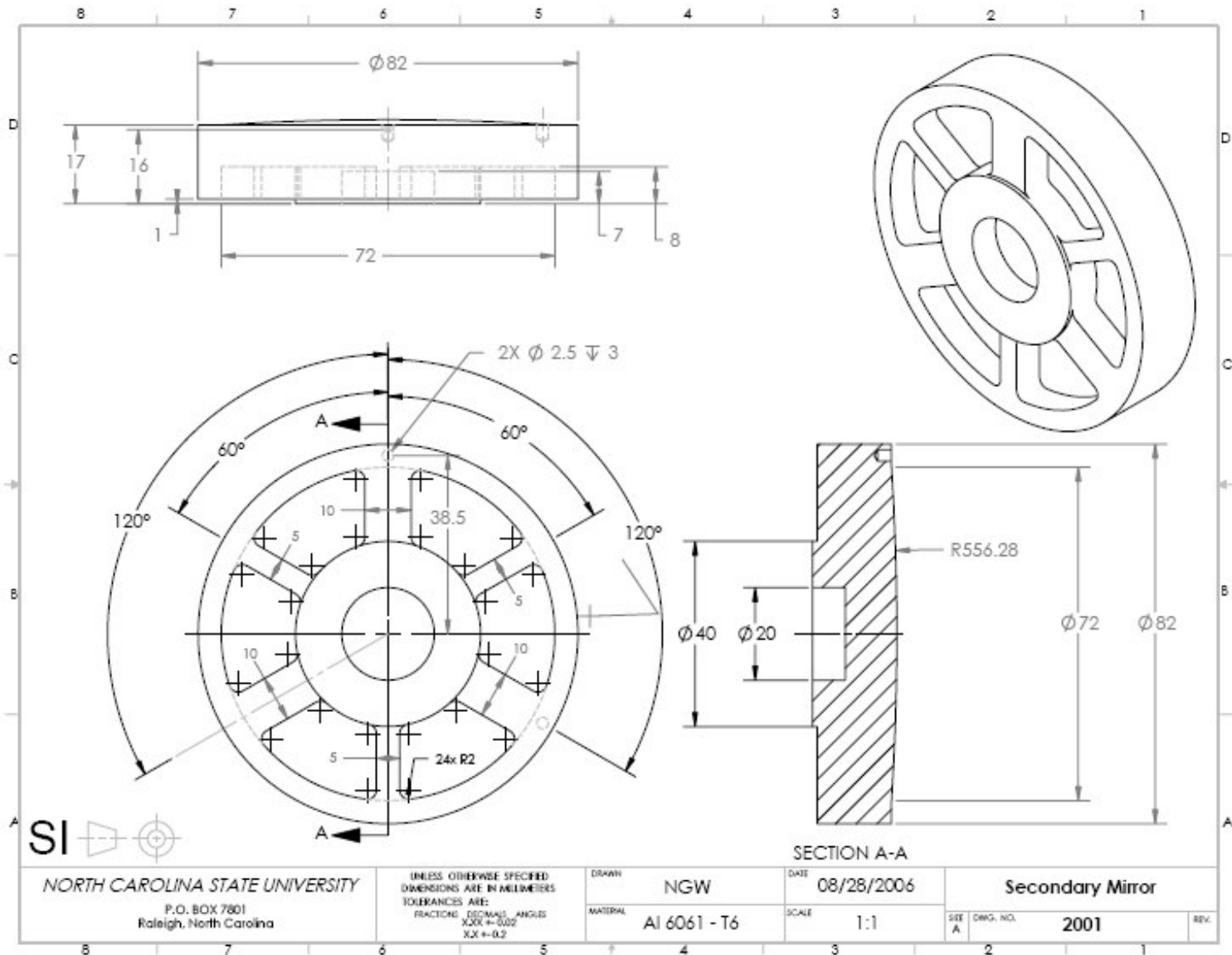


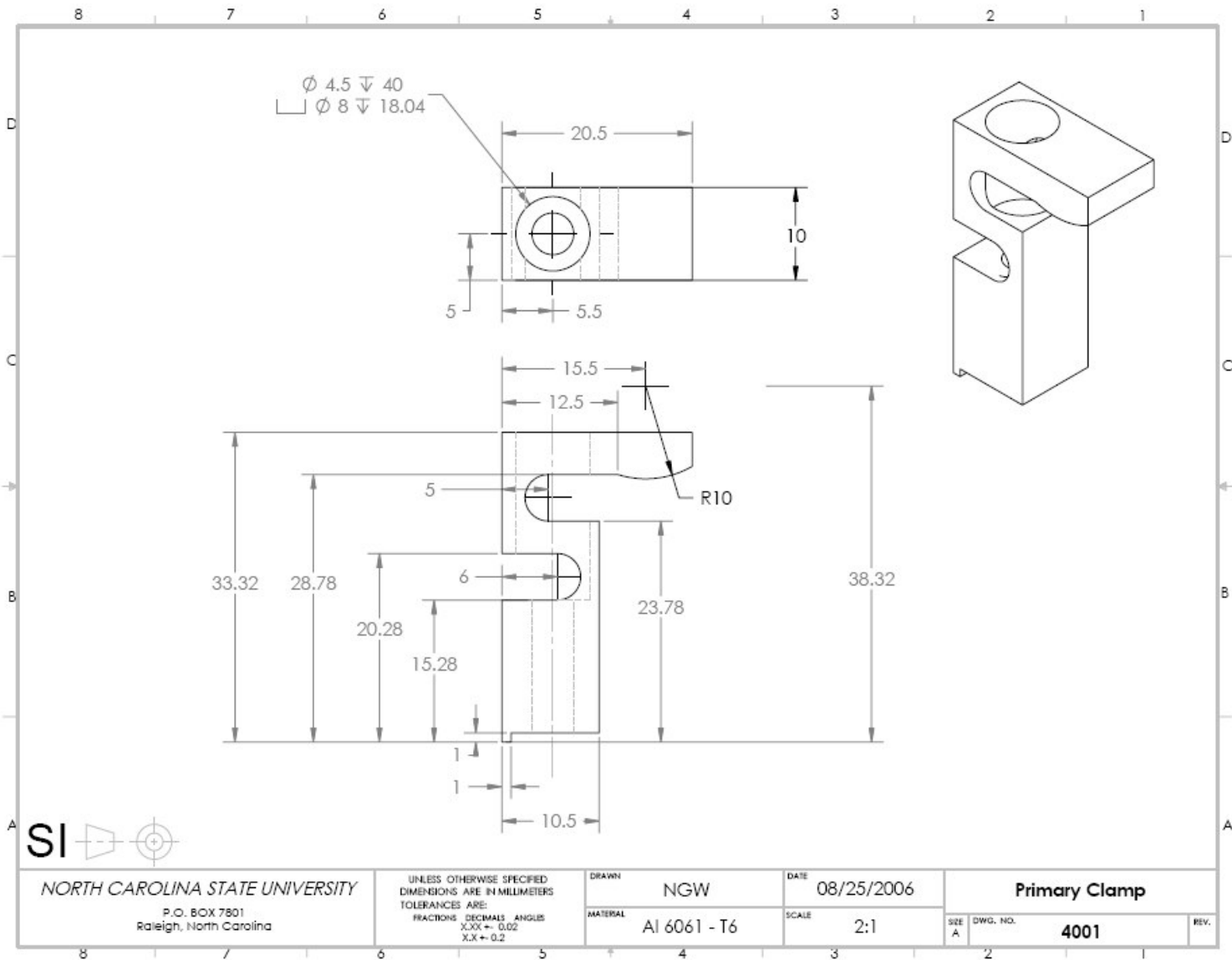
APPENDIX D – Detail Drawings of the Three Mirror Anastigmat

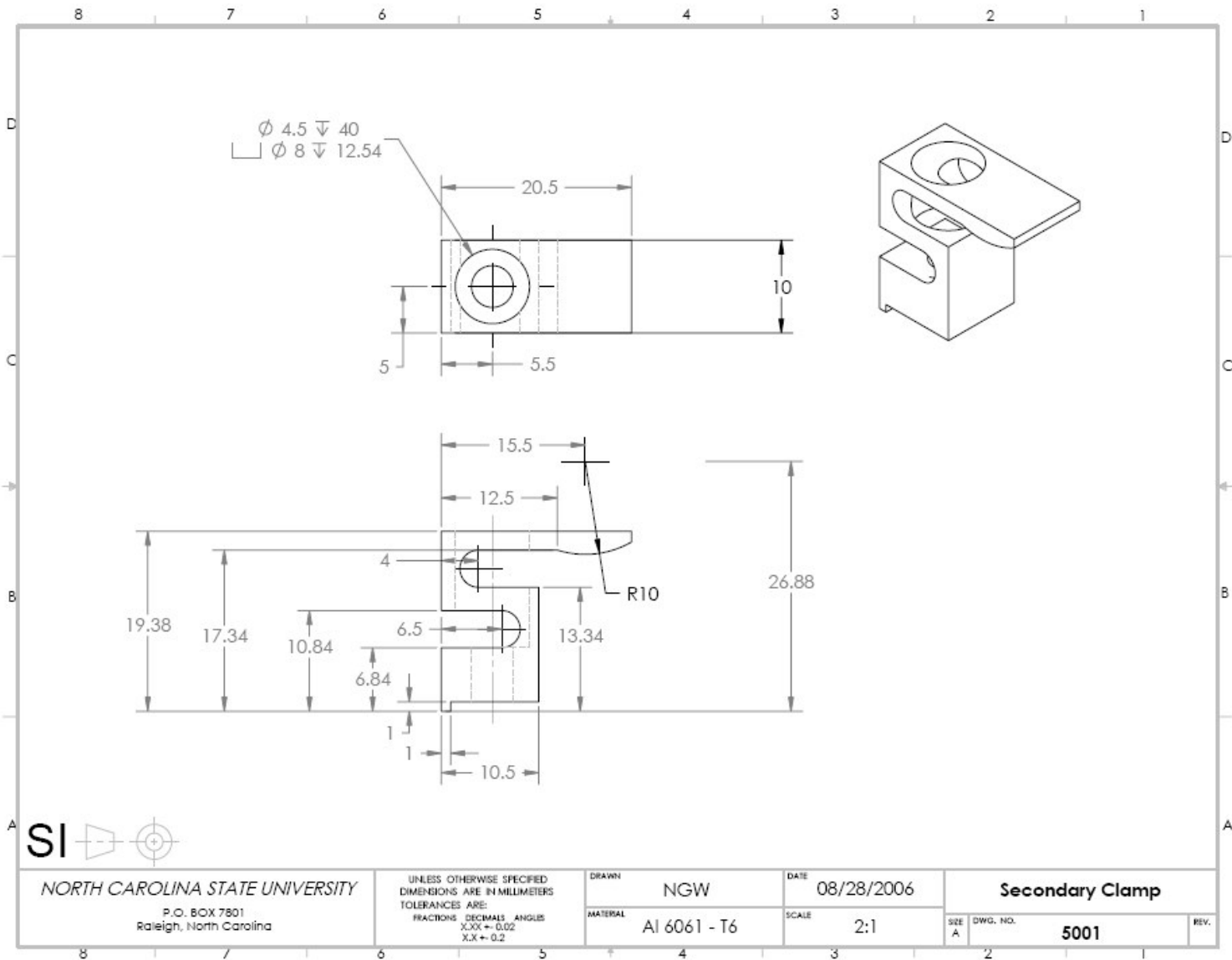
TMA Telescope Components

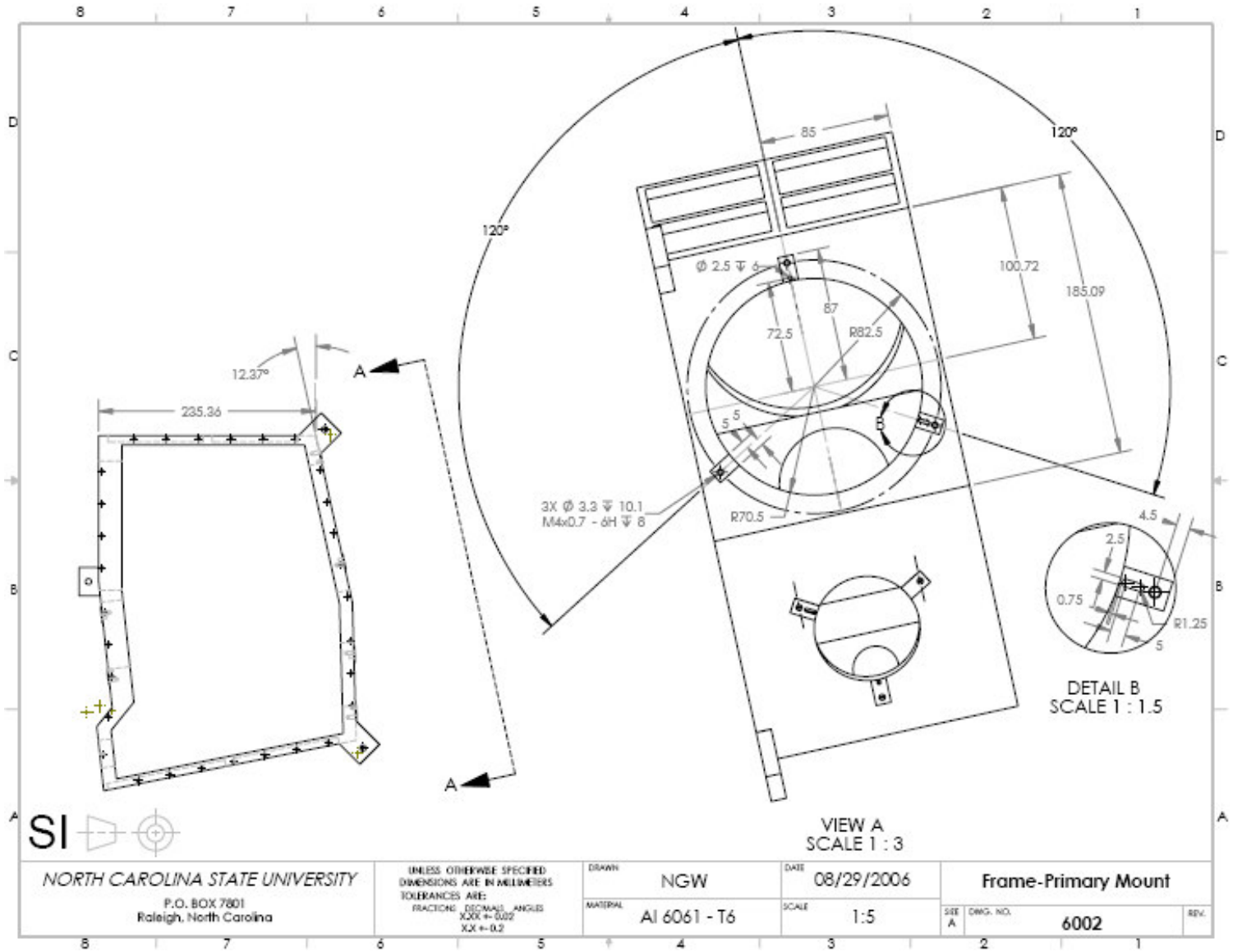


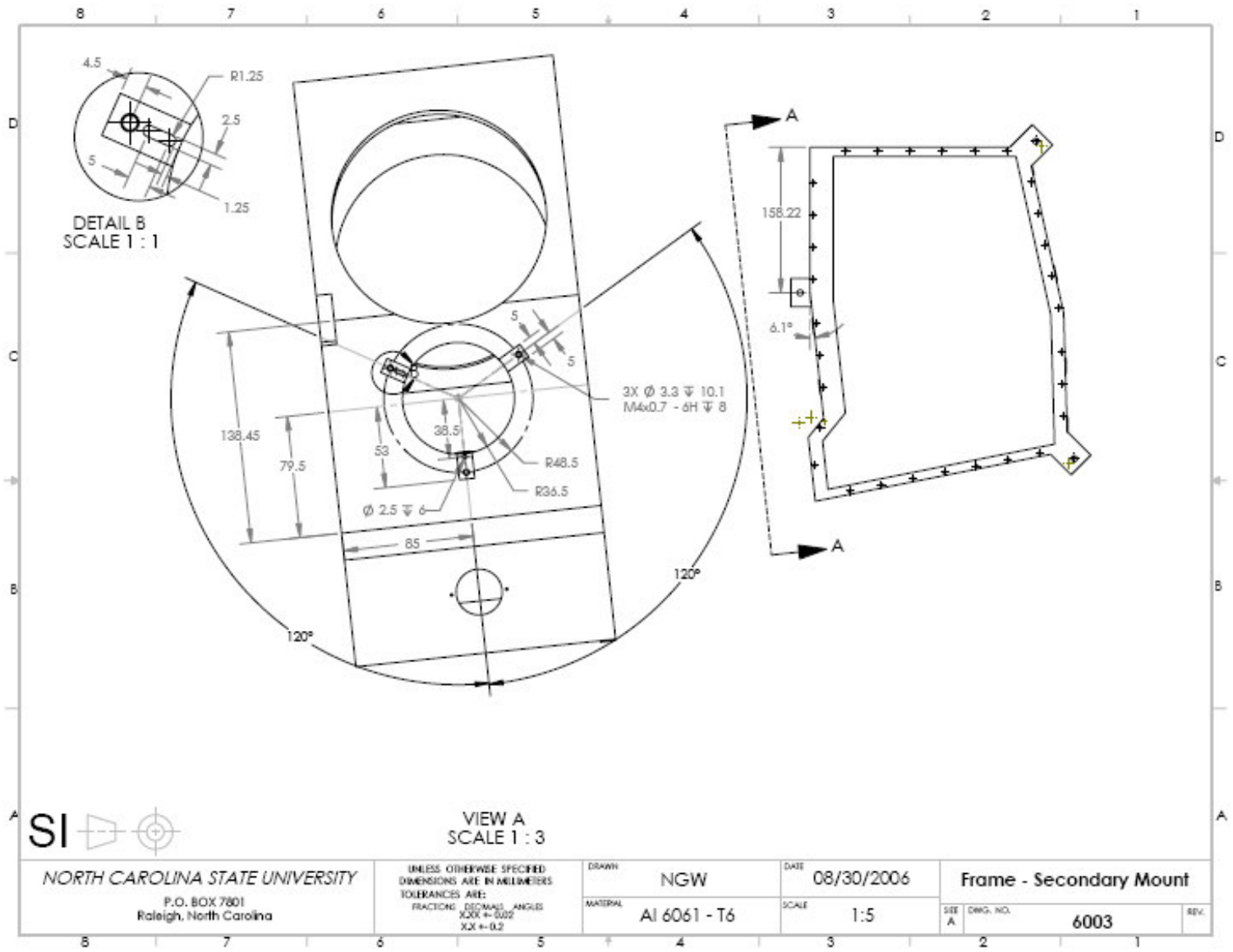


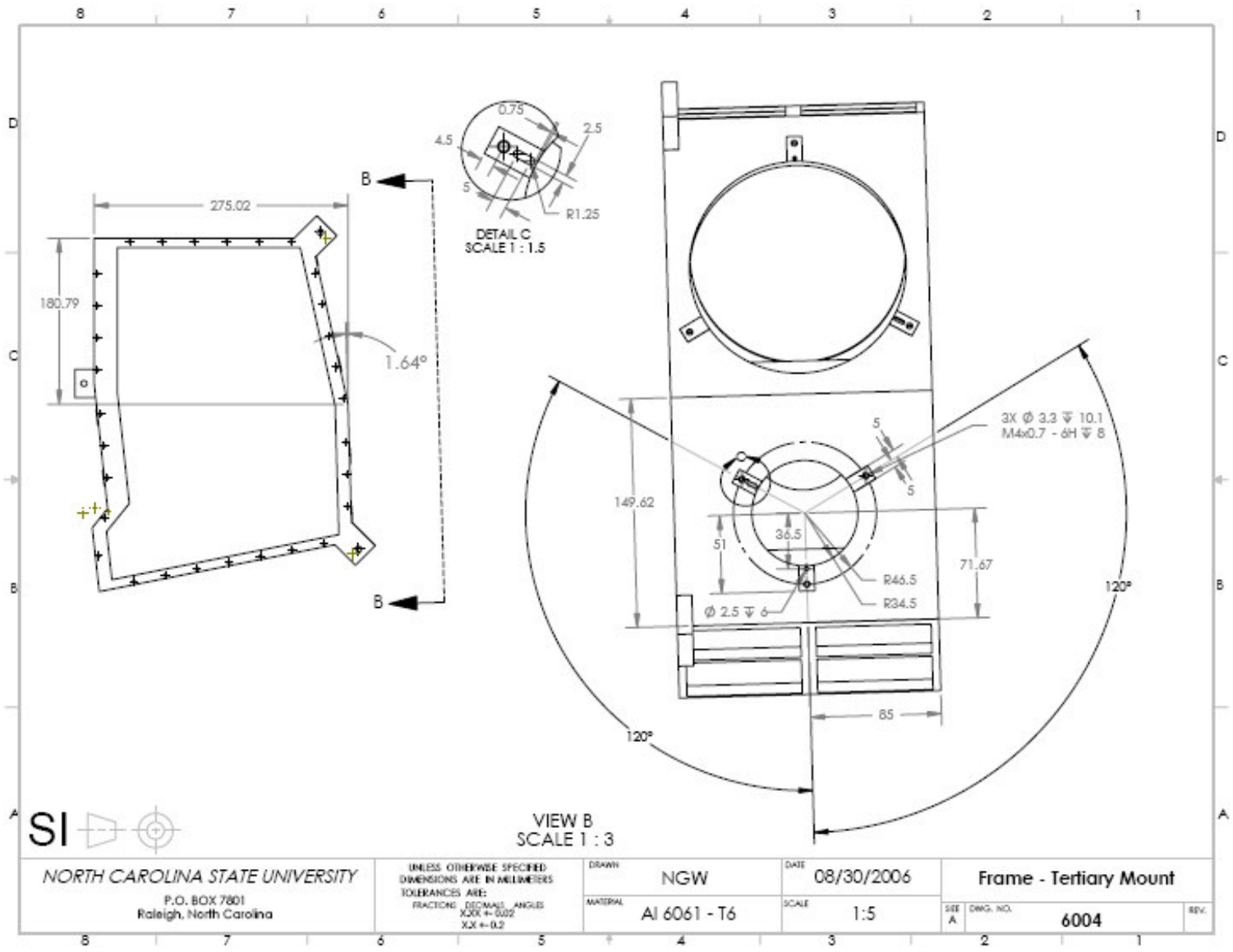


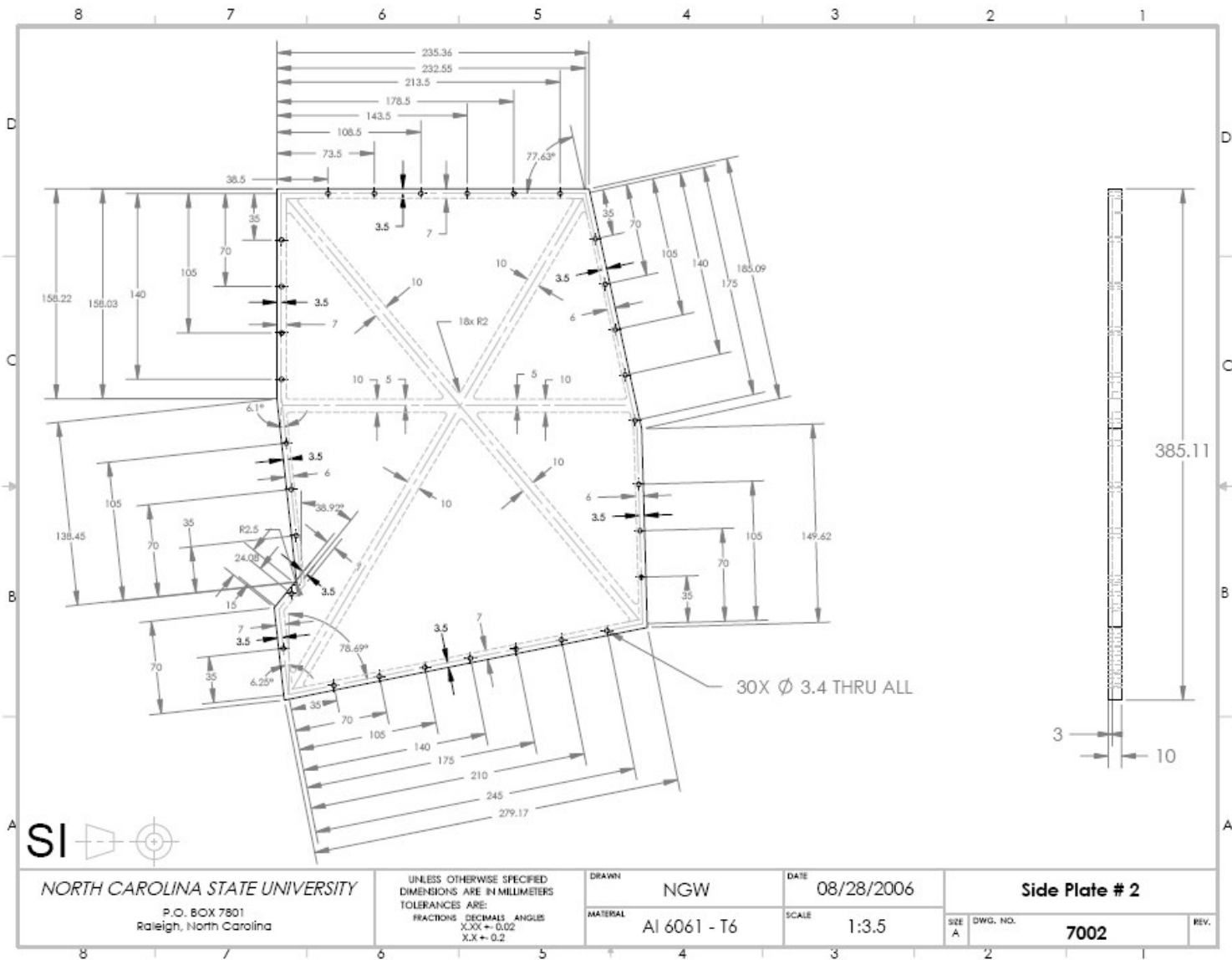


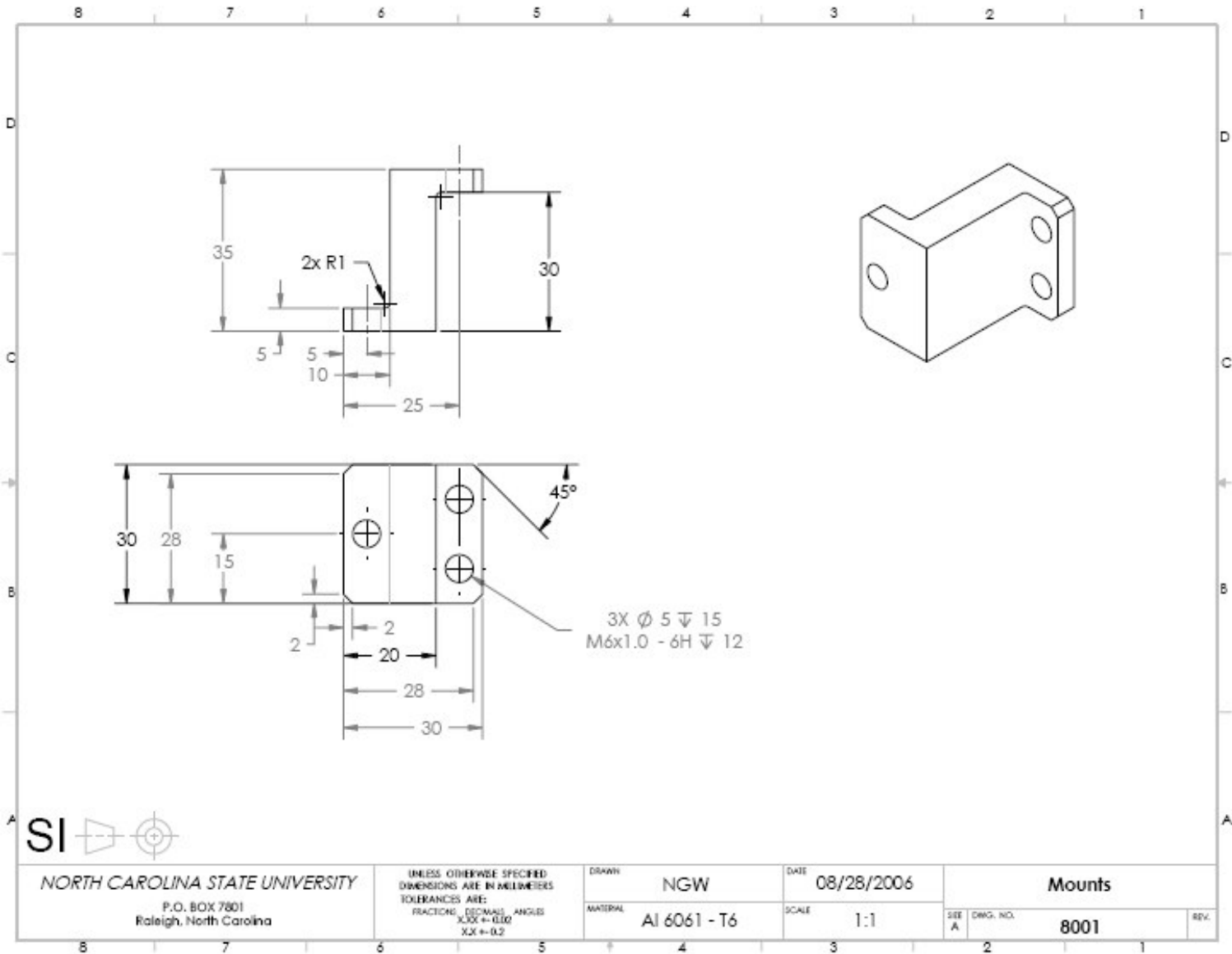




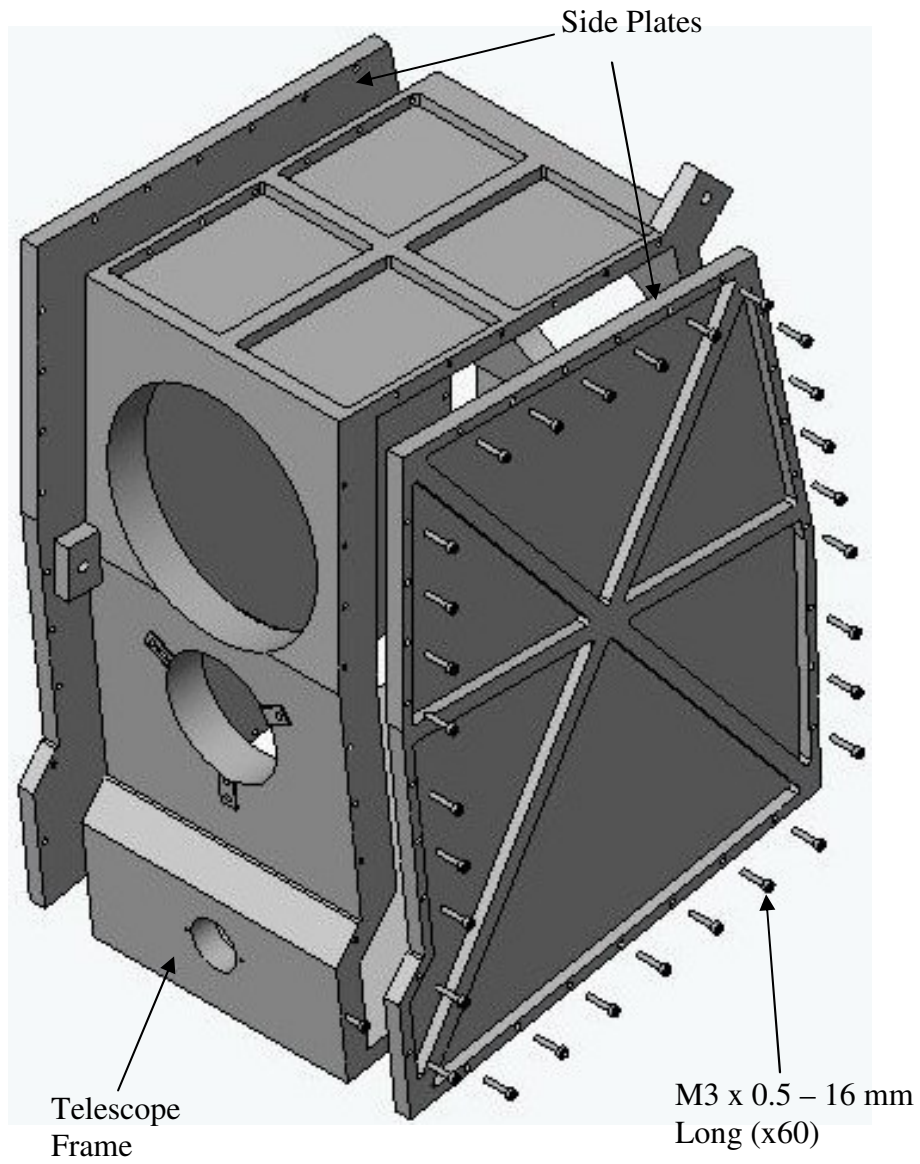


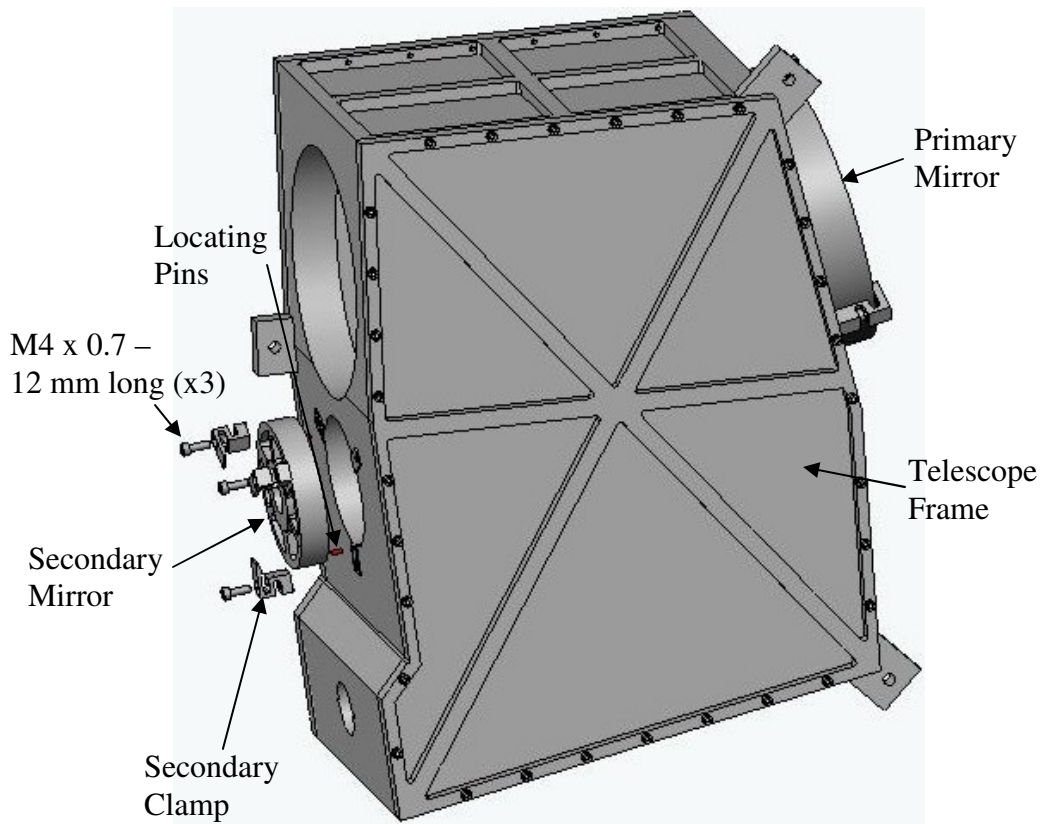
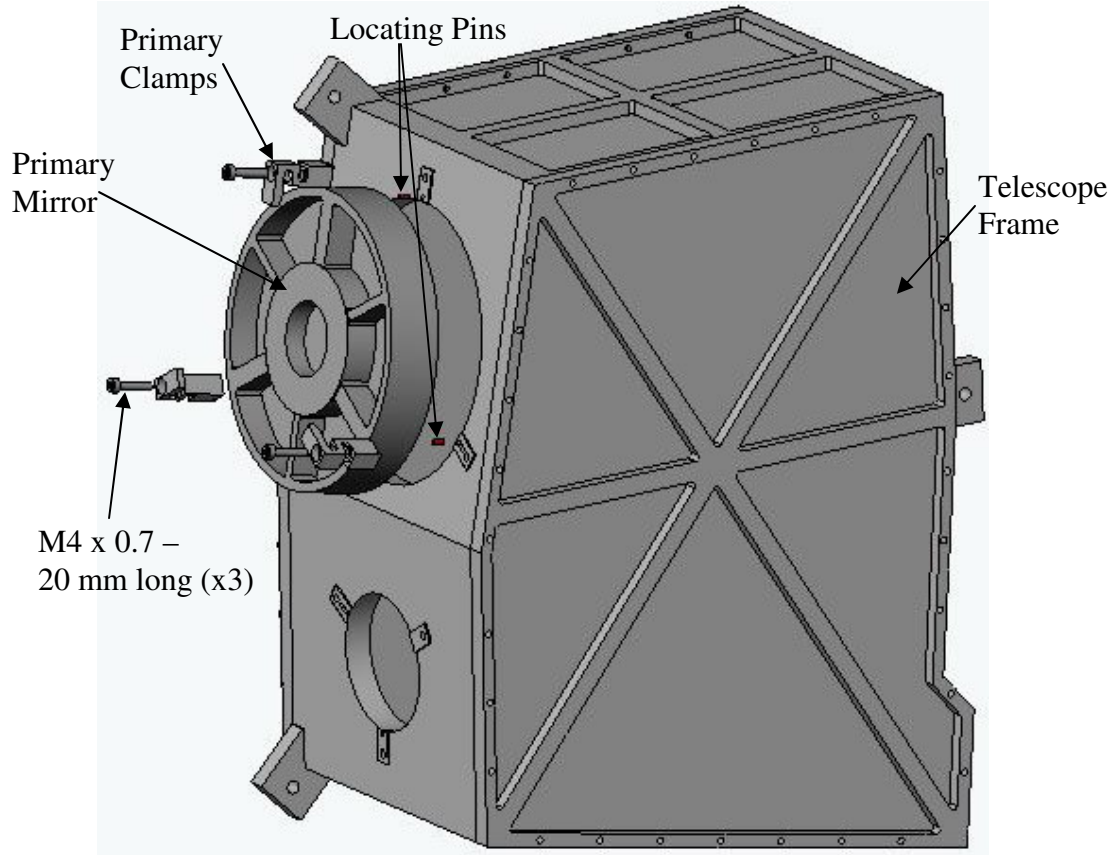


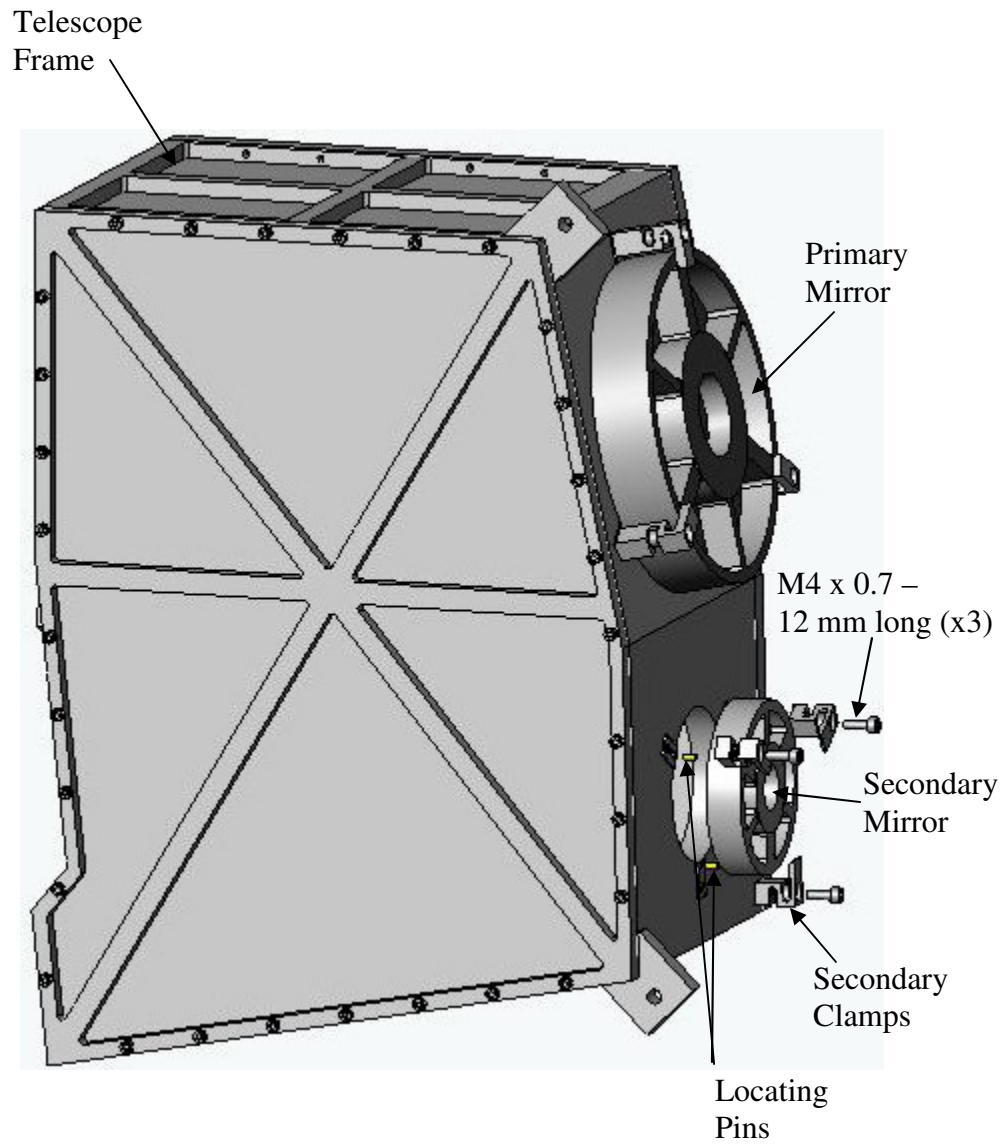


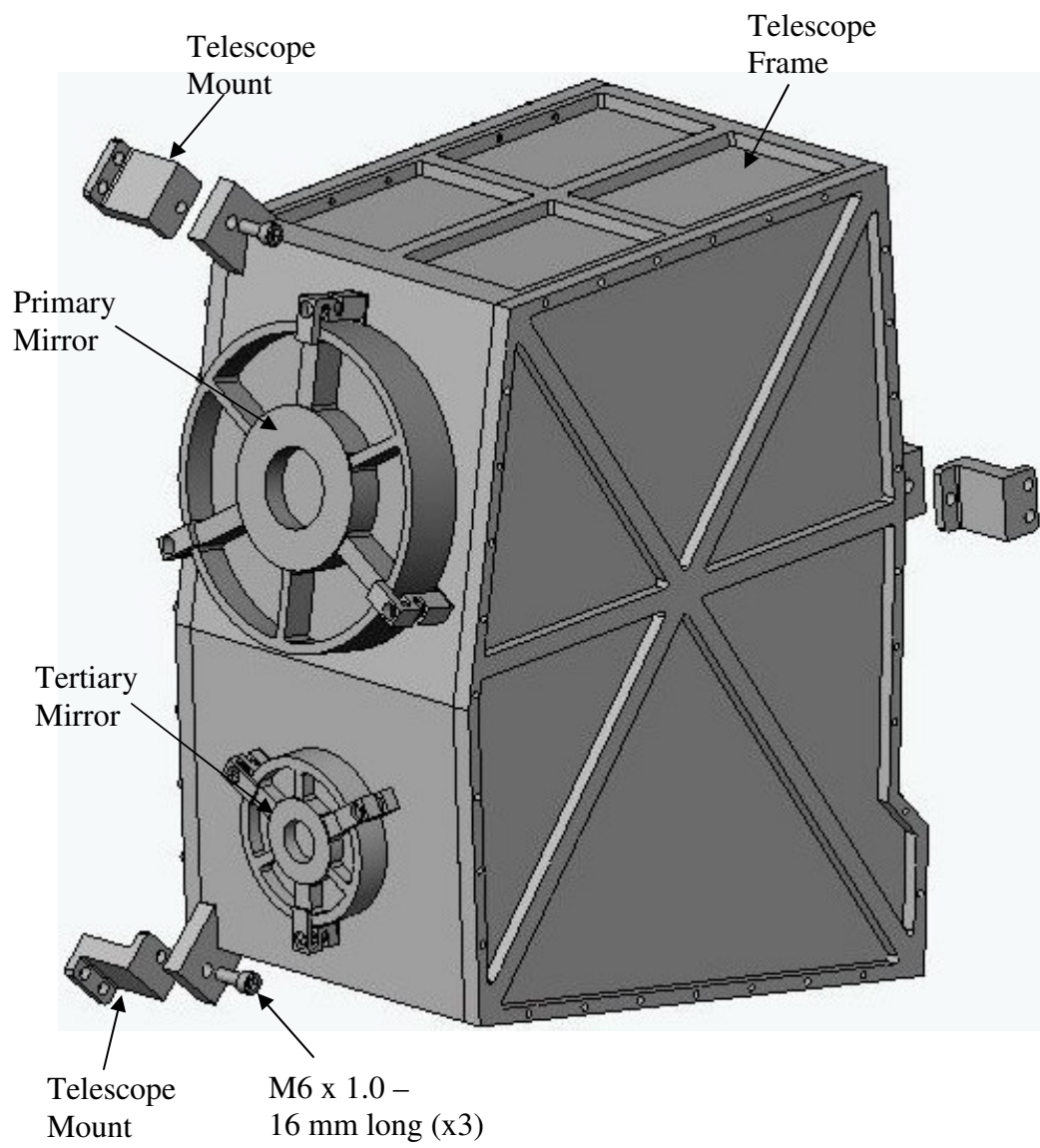


Three Mirror Anastigmat Assembly Steps









APPENDIX E – Zernike Polynomial Surface

The Zernike surface is a 10th-order standard Zernike polynomial added to a base conic.

The equation used is:

$$z = \frac{cr^2}{1 + \sqrt{1 - (1+k)c^2r^2}} + \sum_{j=1}^{66} C_{j+1}Z_j \quad (13)$$

where z is the sag of the surface parallel to the z-axis

c is the vertex curvature

k is the conic constant

Z_j is the j-th Zernike polynomial (range of j: 1 to 66)

C_{j+1} is the coefficient for Z_j

$$r^2 = x^2 + y^2$$

Zernike polynomials are polynomials in radial coordinates (R and θ) over a unit circle.

Table 8-1 gives the set of Zernike polynomials through the 10th order [9].

Table 8-1: Standard Zernike polynomials

Z1	1
Z2	$R\cos\theta$
Z3	$R\sin\theta$
Z4	$R^2\cos2\theta$
Z5	$2R^2 - 1$
Z6	$R^2\sin2\theta$
Z7	$R^3\cos3\theta$
Z8	$3R^3\cos\theta - 2R\cos\theta$
Z9	$3R^3\sin\theta - 2R\sin\theta$
Z10	$R^3\sin3\theta$
Z11	$R^4\cos4\theta$
Z12	$4R^4\cos2\theta - 3R^2\cos2\theta$
Z13	$6R^4 - 6R^2 + 1$
Z14	$4R^4\sin2\theta - 3R^2\sin2\theta$
Z15	$R^4\sin4\theta$
Z16	$R^5\cos5\theta$
Z17	$5R^5\cos3\theta - 4R^3\cos3\theta$
Z18	$10R^5\cos\theta - 12R^3\cos\theta + 3R\cos\theta$
Z19	$10R^5\sin\theta - 12R^3\sin\theta + 3R\sin\theta$
Z20	$5R^5\sin3\theta - 4R^3\sin3\theta$
Z21	$R^5\sin5\theta$
Z22	$R^6\cos6\theta$
Z23	$6R^6\cos4\theta - 5R^4\cos4\theta$
Z24	$15R^6\cos2\theta - 20R^4\cos2\theta + 6R^2\cos2\theta$
Z25	$20R^6 - 30R^4 + 12R^2 - 1$
Z26	$15R^6\sin2\theta - 20R^4\sin2\theta + 6R^2\sin2\theta$
Z27	$6R^6\sin4\theta - 5R^4\sin4\theta$
Z28	$R^6\sin6\theta$

Z29	$R^7 \cos 7\theta$
Z30	$7R^7 \cos 5\theta - 6R^5 \cos 5\theta$
Z31	$21R^7 \cos 3\theta - 30R^5 \cos 3\theta + 10R^3 \cos 3\theta$
Z32	$35R^7 \cos \theta - 60R^5 \cos \theta + 30R^3 \cos \theta - 4R \cos \theta$
Z33	$35R^7 \sin \theta - 60R^5 \sin \theta + 30R^3 \sin \theta - 4R \sin \theta$
Z34	$21R^7 \sin 3\theta - 30R^5 \sin 3\theta + 10R^3 \sin 3\theta$
Z35	$7R^7 \sin 5\theta - 6R^5 \sin 5\theta$
Z36	$R^7 \sin 7\theta$
Z37	$R^8 \cos 8\theta$
Z38	$8R^8 \cos 6\theta - 7R^6 \cos 6\theta$
Z39	$28R^8 \cos 4\theta - 42R^6 \cos 4\theta + 15R^4 \cos 4\theta$
Z40	$56R^8 \cos 2\theta - 105R^6 \cos 2\theta + 60R^4 \cos 2\theta - 10R^2 \cos 2\theta$
Z41	$70R^8 - 140R^6 + 90R^4 - 20R^2 + 1$
Z42	$56R^8 \sin 2\theta - 105R^6 \sin 2\theta + 60R^4 \sin 2\theta - 10R^2 \sin 2\theta$
Z43	$28R^8 \sin 4\theta - 42R^6 \sin 4\theta + 15R^4 \sin 4\theta$
Z44	$8R^8 \sin 6\theta - 7R^6 \sin 6\theta$
Z45	$R^8 \sin 8\theta$
Z46	$R^9 \cos 9\theta$
Z47	$9R^9 \cos 7\theta - 8R^7 \cos 7\theta$
Z48	$36R^9 \cos 5\theta - 56R^7 \cos 5\theta + 21R^5 \cos 5\theta$
Z49	$84R^9 \cos 3\theta - 168R^7 \cos 3\theta + 105R^5 \cos 3\theta - 20R^3 \cos 3\theta$
Z50	$126R^9 \cos \theta - 280R^7 \cos \theta + 210R^5 \cos \theta - 60R^3 \cos \theta + 5R \cos \theta$
Z51	$126R^9 \sin \theta - 280R^7 \sin \theta + 210R^5 \sin \theta - 60R^3 \sin \theta + 5R \sin \theta$
Z52	$84R^9 \sin 3\theta - 168R^7 \sin 3\theta + 105R^5 \sin 3\theta - 20R^3 \sin 3\theta$
Z53	$36R^9 \sin 5\theta - 56R^7 \sin 5\theta + 21R^5 \sin 5\theta$
Z54	$9R^9 \sin 7\theta - 8R^7 \sin 7\theta$
Z55	$R^9 \sin 9\theta$
Z56	$R^{10} \cos 10\theta$
Z57	$10R^{10} \cos 8\theta - 9R^8 \cos 8\theta$
Z58	$45R^{10} \cos 6\theta - 72R^8 \cos 6\theta + 28R^6 \cos 6\theta$

APPENDIX F – Kinematic Coupling Design Table

Values of m and n for various values of θ are given in Table 8-2 where θ is found using Equation 11 [22].

Table 8-2: Constants (m and n) for different θ values

θ	30°	35°	40°	45°	50°	55°	60°
m	2.731	2.397	2.136	1.926	1.754	1.611	1.486
n	0.493	0.530	0.567	0.604	0.641	0.678	0.717

θ	65°	70°	75°	80°	85°	90°
m	1.378	1.284	1.202	1.128	1.061	1.000
n	0.759	0.802	0.846	0.893	0.944	1.000